MASTER OF SURGERY THESIS

1999

DEVELOPMENT AND EVALUATION OF IMAGE-GUIDED NEUROENDOSCOPY, WITH INVESTIGATION OF POST-IMAGING BRAIN DISTORTION AND ACCURACY OF FRAMELESS STEREOTAXY

Neil Lawrence Dorward BSc, MB BS, FRCS(SN)

University Department of Neurosurgery,

Institute of Neurology, University College, University of London

ProQuest Number: U129798

ProQuest U129798

ABSTRACT

Neuroendoscopy enables a surgeon to operate deep within the brain whilst limiting morbidity through a minimally invasive approach. Technical advances in illumination, instrumentation and camera design, along with evidence for improved clinical outcome, have increased the indications for this technique and have ensured widespread popularity. However, broader application of neuroendoscopy is restricted by the necessity for direct vision of targets and by spatial disorientation. The aim of this investigation was to overcome these limitations by combining neuronavigation with neuroendoscopy to develop Image-Guided Neuroendoscopy (IGN). The strategy adopted for this was firstly to select, assess and validate a neuronavigation system, secondly to develop methods of endoscope tracking and frameless stereotactic implantation. Thirdly, to assess the impact of post-imaging brain distortion upon neuronavigation, fourthly to correct distortion of the endoscope image and finally to assess the use of graphics overlay in IGN.

Laboratory phantom accuracy assessments revealed a mean point localisation error for the navigation system pointers of 0.8mm (SD 0.4mm) with CT imaging, for the tracked endoscope of 1.5mm (SD 0.8mm) and for frameless stereotaxy of 1.3mm (SD 0.6mm). An in vivo study revealed a mean Euclidean error of 4.8mm (SD 2.0mm) for frameless stereotactic biopsy. The navigation system was evaluated through a clinical series of 100 cases, the frameless stereotactic technique was employed in 21 brain biopsy procedures and IGN evaluated in 5 procedures. The magnitude of post-imaging

brain distortion was determined and correlations discovered with pre-operative image characteristics.

The conclusions of this thesis are that IGN can be accomplished with acceptable accuracy, including frameless stereotactic implantation, and that the impact of post-imaging brain distortion will not negate the value of IGN in most cases. Thus, the method developed for IGN has overcome both major constraints of neuroendoscopy, enabling endoscopic surgery to pass through and beyond the ventricular wall, to be undertaken safely in cases with distorted anatomy and opening the potential for wider application of these minimally invasive techniques.

CONTENTS

LIST OF FIGURES

13

LIST OF TABLES

INTRODUCTION

1.1 STATEMENT OF THE PROBLEM ADDRESSED

The recent introduction of minimally invasive techniques to several surgical sub-specialities has been rewarded by reduced morbidity rates. In the field of neurosurgery improved optics, instrumentation and light sources have enabled the successful application of neuroendoscopy to a number of conditions occurring within the cerebral ventricles. The associated patient benefits of this minimally invasive approach have ensured widespread adoption of the technique. However, passage of the neuroendoscope through the brain is blind, the field of view is restricted, the image is distorted, the surgeon is easily disorientated and only structures visible within the ventricles may be tackled safely. These constraints have limited the general application of neuroendoscopy to simple cases with relatively normal anatomy and to pathology within the ventricles.

In order for the advantages of minimally invasive neurosurgery to be realised in a wider group of cases the intrinsic limitations of neuroendoscopy must be overcome. The aim of this investigation was to achieve this through the provision of guidance during endoscope insertion, real-time display of the regional anatomy during surgery and correction of image distortion for image co-registration, without restricting the freedom of endoscope movement. The method selected for this was the combination of neuroendoscopy and neuronavigation. The union of these technologies required the development of a system for frameless stereotactic implantation, a method for endoscope tracking, correction of the distortion inherent in an endoscope image, investigation of the impact of post-imaging brain distortion and clinical evaluation of the resultant technique.

1.2 HISTORICAL BACKGROUND

The history of modern neurosurgery begins with the pioneering work of Dandy and Cushing whose results, despite the undoubted pre-eminence and skill of these surgeons, included many devastating post-operative neurological deficits and deaths. Succeeding generations of neurosurgeons experienced similar, and frequently worse, results until relatively recently. This catalogue of morbidity reflects the peculiar properties of the brain including sensitivity to manipulation, high vascularity, the profound deficits produced by injury and restricted powers of recovery. In addition, the encasing skull carries few surface landmarks to direct the surgeon, the brain itself is relatively homogeneous and anatomy is frequently distorted by the pathological process. Furthermore, mobilisation of the brain is restricted by the vessels and nerves coursing between brain and skull base. In order to overcome these restrictions neurosurgeons have developed special techniques, many of which are unique to neurosurgery. In particular frame-based stereotaxy, neuronavigation and neuroendoscopy have revolutionised the surgical approach to cerebral lesions.

1.2.1 Neuroendoscopy

When he inspected the ventricular cavity with a cystoscope in 1910, Espinasse was probably the first to perform a neuroendoscopic procedure and, whilst the optical characteristics of the lens and power of illumination were woefully inadequate in this instrument, the dim vision he gained of the living ventricle with floating fronds of choroid plexus must have been impressive. Dandy (1918) also adopted this technique and, as with

so much in neurosurgery, he introduced novel surgical procedures with unparalleled success despite the limitations of his instruments. A contemporary neurosurgeon actually performed the first endoscopic third ventriculostomy for obstructive hydrocephalus (Mixter 1923), but either the importance of this advance was not recognised or the instrumentation barred wider use for this procedure remained neglected for many years. During the half century following these pioneering endoscopic procedures the ventriculoscope was periodically revived, with uniformly disappointing results (Griffith 1986). For example, in 1934 Putnam developed an endoscopic method of choroid plexus coagulation, which offered a treatment for hydrocephalus, with some success, at a time when this was generally a terminal condition.

The history of ventriculostomy (both open and endoscopic) is a long and miserable story of high mortality and poor results for a condition which is now treated lightly. The essential principles for successful ventriculostomy were described by Dandy in 1922 and he pioneered open third ventriculostomy, describing the procedure thus;

"This consists in removing the floor of the third ventricle. A small opening is made in the skull and dura in the frontal region. The frontal lobe is elevated until the bulging third ventricle is well exposed. Usually, it is necessary to divide one of the optic nerves, for in hydrocephalus these nerves are very short; usually the chiasm lies directly on the anterior border of the sella turcica."

Sadly, the operative difficulties and poor results led to the abandonment of this approach, but by 1933 Dandy had achieved some success with a subtemporal approach for third ventriculostomy. By 1945 Dandy was able to report on the outcome of 92 such cases, revealing an operative mortality of 12%, a mean survival of 7 years and arrest of hydrocephalus in 50%. Concurrently Stookey and Scarff described the relief of hydrocephalus via open surgical puncture of the lamina terminalis in 1936. The results for this procedure, described by Scarff in 1951, were similar to Dandy's with a 15% mortality and 54% arrest of the hydrocephalus. Despite the obvious advantages of endoscopic third ventriculostomy, as performed by Mixter in 1922, the bulky scope, poor illumination and instrumentation prohibited acceptance of this method.

Subsequent technical advances, including the introduction of external light sources, the Hopkins lens and fibre-optics have contributed to the reversal of this trend. Concurrent advances in imaging and neuroanaesthesia have enhanced the safety and effectiveness of neuroendoscopy and indeed third ventriculostomy has become widely accepted as the treatment of choice in triventricular hydrocephalus (Cohen 1994, Drake 1993, Jones et al 1994). The development of the flexible endoscope, first used by Fukushima in 1973, opened new possibilities for endoscopic inspection of tortuous and narrow CSF pathways and was later applied to spinal inspection by Huewel (1992). The scope of neuroendoscopy was further expanded, by Auer in 1985, to include intraparenchymal surgery with his endoscopic evacuation of intracerebral haematomata. Such intraparenchymal applications have also been explored for tumour resection (Hellwig et al 1995), but the difficulties of obscuration of vision until a cavity is created appear to have blocked further progress in this area. Meanwhile the flexible viewing endoscope has

been employed to many regions, from inspection of the cerebello-pontine angle for vascular indentation of the Trigeminal nerve to assessment of thecal compression in the spine (Tutino 1996).

Enthusiasm for neuroendoscopy is currently widespread and diverse clinical indications have been reported including the revival of choroid plexus coagulation for hydrocephalus (Bucholz & Pittman 1991, Pople & Ettles 1995), simplification of loculated hydrocephalus (Lewis et al 1995), dilatation of aqueduct stenosis (Oka et al 1993), surgery for craniopharyngioma (Abdullah & Caemaert 1995) and resection of intraventricular tumours (Heal 1995, Lewis et al 1994). Endoscopic evacuation has even been proposed to be superior to open surgery for intracerebral haematomas (Auer et al 1989). However, further development of novel endoscopic approaches has been limited by the fundamental requirements of direct visualisation of ventricular anatomy for orientation and visualisation of pathology for intervention (Fukushima 1978, Hellwig & Bauer 1991, Walker et al 1992). In addition, the wider use of endoscopic techniques by less experienced surgeons has inevitably increased the incidence of disorientation during endoscopic surgery and a higher incidence of avoidable complications (Teo et al 1996).

In contemporary neurosurgical practice the endoscope has also been introduced into the field of open neurosurgery, so called endoscope-assisted micro-neurosurgery (Cohen at al 1995). This enables a lens and light source to be advanced into the surgical field, enabling detailed inspection and guiding further surgery on regions obscured from the microscope view. Similarly, endoscopy has been introduced to pituitary surgery with good effect (Jho et al 1997). In future, with the advent of image-guided neuroendoscopy,

many of these procedures may be accessible to a minimally invasive endoscopic approach alone.

During the recent renaissance of neuroendoscopy the technique of frame-based stereotactic endoscopy was introduced, which improved the accuracy of endoscope insertion (Hellwig et al 1995). However, this technique removed the freedom of movement from the endoscope, which is a necessary attribute in neuroendoscopic surgery. This restriction led to the development of ultrasound-guided neuroendoscopy (Yamakawa et al 1994) but as yet this has limited resolution and provides two-dimensional guidance only. The union of neuronavigation and neuroendoscopy has also been attempted employing arm-based navigation systems (Drake et al 1994). However, the combined weight of the arm, endoscope, camera and light source inevitably creates an awkward instrument with limited freedom of movement. In addition, no adequate assessment of accuracy has been described and whilst the endoscope trajectory could be tracked the tip position was unknown. The combination of a sonic digitiser with an endoscope has also been reported (Rhoten et al 1997), but this suffered from tracking interference (Bucholz & Smith 1993) and required the pointer to occupy the instrument channel, precluding guidance during endoscopic surgery.

1.2.2 Frame-Based Stereotaxy

The origins of frame-based stereotaxy can be traced to 19th century neuro-anatomists and neuro-physiologists. The earliest instruments developed by these scientists were simple encephalometers; metal cages allowing the surface morphology of skull or brain to be measured. The first recorded clinical use of such a frame is the

measurement of skull shape by Harting, at the University of Utrecht in 1861 (Redfern 1989). Not long after, in 1889, an encephalometer designed by the Russian anatomist Zernov was used to successfully place a burr hole over the motor strip of a man (Kandel & Schavinsky 1972). However, the transition from encephalometer to stereotactic system is usually attributed to the innovative frame described by the British engineer Richard Clarke and neurosurgeon Sir Victor Horsley in 1906. A series of modifications resulted in an equatorial system enabling accurate targeting with a wide choice of entry point and trajectory (Horsley & Clarke 1908). This apparatus proved highly successful for lesioning experiments in animals, when used in conjunction with standard brain atlases. However, the variation found between human brains precluded such atlas-based stereotaxy in man. For this, individual anatomical information would be required, combined with averaged atlas measurements. Thus, when ventricular imaging became available with the introduction of pneumoencephalography this was exploited in the first human stereotactic apparatus developed by Spiegel and Wycis (1947). Leksell, Riechert and Talairach, the founders of modern stereotaxy, soon described improved frame designs, surgical techniques were steadily refined and functional neurosurgery blossomed for over two decades.

A significant landmark in the evolution of stereotactic frames was the introduction of the concentric ring system by Lars Leksell in 1950. Whilst previous and contemporary systems were frame-centred, Leksell produced a target-centred system in which the operating arc and instrument cradle could be rotated freely whilst the target remained at the geometric centre of the frame (Figure 1.1). This not only simplified trajectory calculation but also allowed the surgeon to approach any target within the
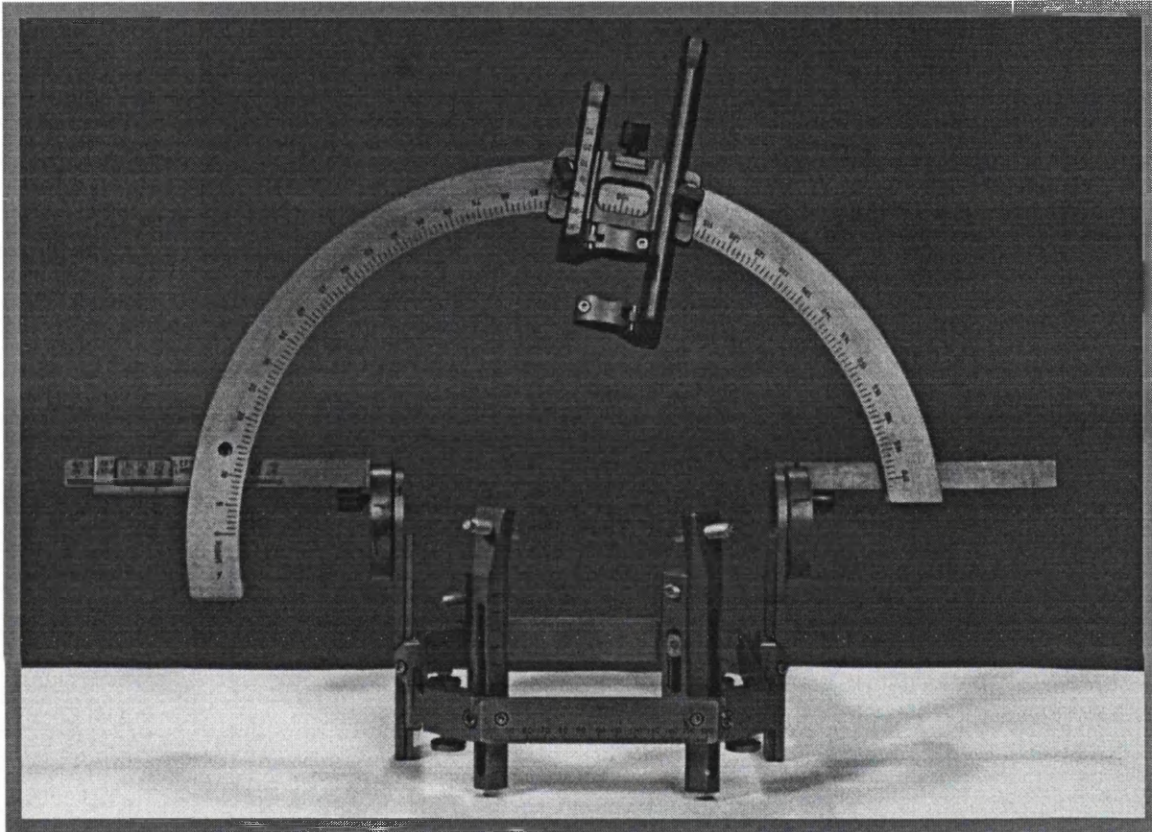
Figure 1.1: Photograph of a modern Leksell stereotactic frame. The side rings allow the arc to rotate forwards and backwards, and the instrument carrier slides around the arc, whilst the target remains fixed. This is the concentric ring design, which has become widely adopted in contemporary frame-based stereotactic systems.

cranium through any desired entry point, either pre-selected or chosen freehand. However, pneumoencephalography and ventriculography remained indirect imaging techniques that could not visualise the actual target and therefore limited stereotaxy to peri-ventricular functional procedures until direct radiological imaging became available in the early 1970's with the introduction of CT scanning. Initially CT was employed only to modify calculated target co-ordinates in functional procedures but, with the introduction of the Brown-Roberts-Wells frame (BRW, Radionics Inc., USA) in 1979 (Figure 1.2), CT-directed stereotaxy was finally realised (Brown 1979, Brown et al 1979). The BRW also incorporated the landmark innovation of N-fiducials, thereby becoming the original scanner-independent system (Figure 1.3). Recent advances in radiological imaging have been accommodated in such frame systems by the introduction of MRI-compatible equipment (Bradford & Thomas 1987) and non-invasive relocatable frames, such as the Gill-Thomas-Cosman (GTC, Radionics Inc., USA) frame (Gill et al 1991). The latter may be used in combination with CT, angiography or PET and these frames are also compatible with the XKnife (Radionics Inc., USA) for post-operative radiotherapy or stereotactic radiosurgery.

In contemporary neurosurgery stereotactic frames are in widespread use both for biopsy and functional procedures. The advantages of stereotactic biopsy over freehand procedures are well documented, demonstrating both improved diagnostic yield and reduced morbidity (Apuzzo et al 1987, Thomas & Nouby 1989), making stereotactic biopsy the current gold standard in this field. The complication rates of published series of stereotactic biopsy reveal a management mortality of between 0 and 2.3% and a diagnostic yield of over 90%. Haemorrhage is reported in 0.4 - 5% of cases, transient
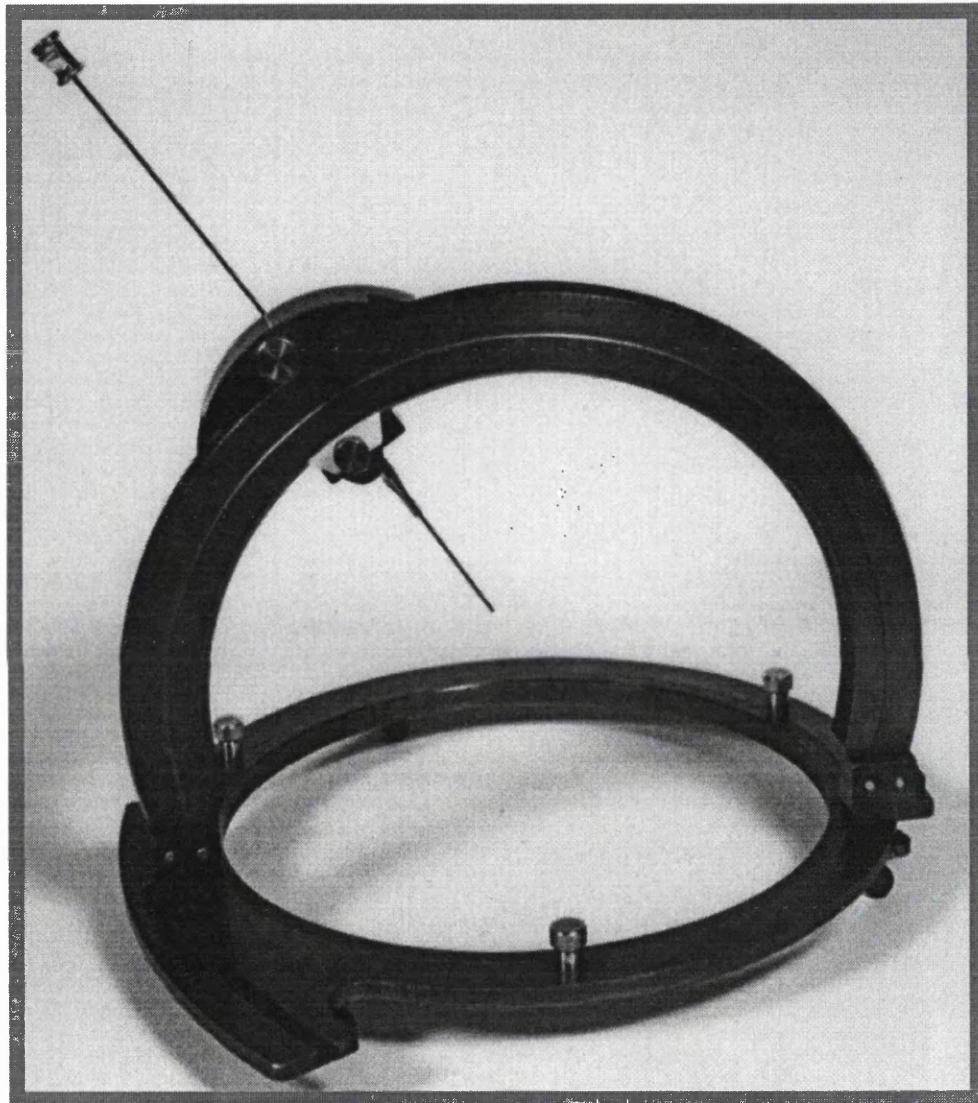
Figure 1.2: Photograph of the Brown-Roberts-Wells stereotactic frame. This system was the first to be designed specifically for CT-directed procedures and, although target-centred, the BRW achieved widespread popularity.
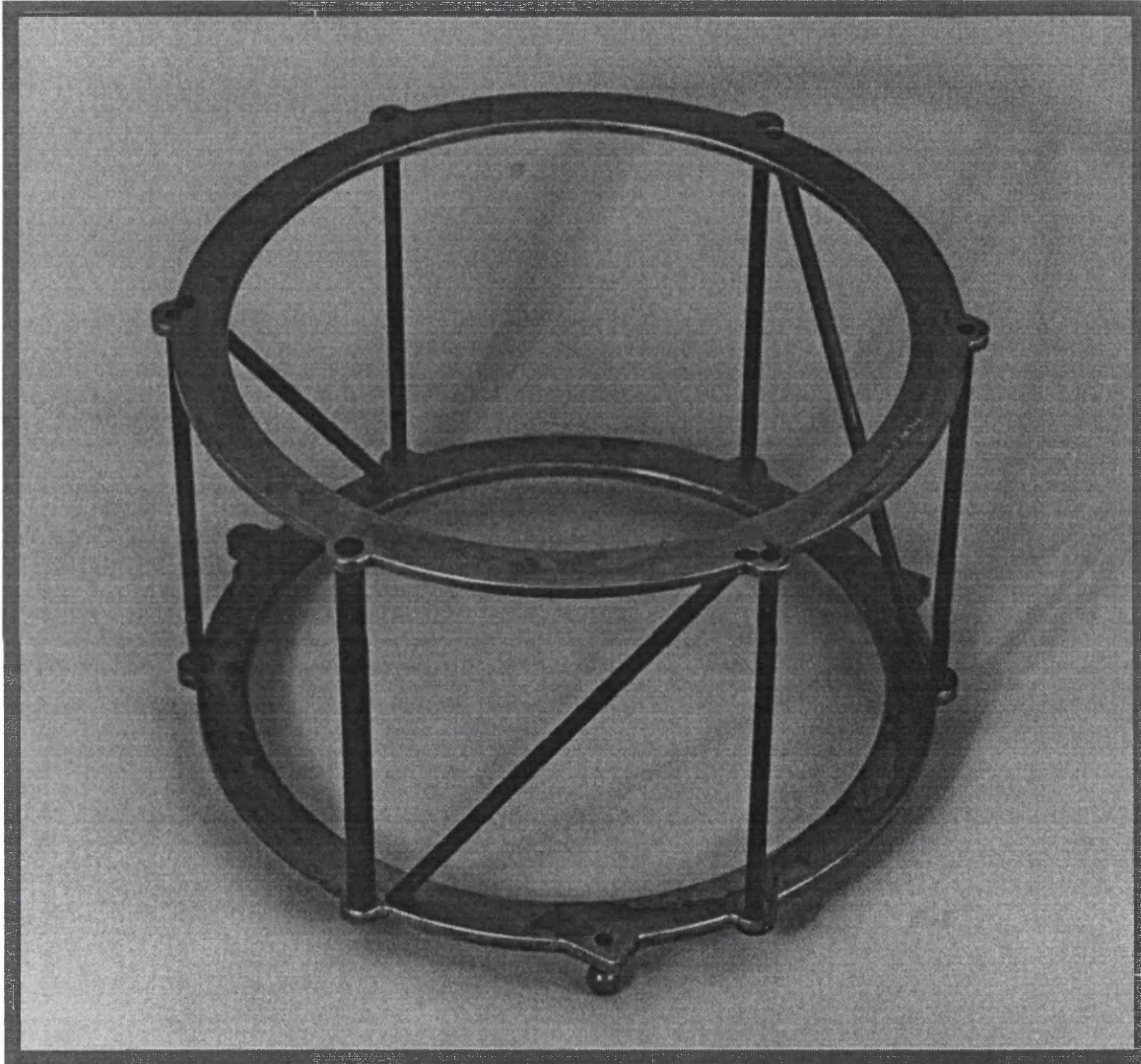
Figure 1.3: Photograph of the N-fiducial localiser for the BRW/CRW system. This ingenious device enables the scan plane to be derived from the rod positions independent of the scanner and has since been adopted by many frame-based systems.

neurological deterioration in 0.2 - 5%, permanent neurological deficit in 1%, epilepsy in 0.2 - 2% and infection in 0.1 - 0.5% (Apuzzo et al 1987, Ostertag et al 1980, Regis et al 1996, Thomas & Nouby 1989, Wild et al 1990).

1.2.3 Neuronavigation

By the 1980's CT-directed stereotaxy for functional neurosurgery and burr hole biopsy had achieved a high degree of sophistication and accuracy. The introduction of stereotactic craniotomy, whereby the frame was employed to localise the desired flap position and selected operative targets, provided the first method for intra-operative guidance in open neurosurgery. Further development began with the important recognition by Sheldon (1980) that sequential CT images formed a volume, that a computer could reconstruct these images in any plane and that such reconstructions could be employed to direct stereotactic surgery. With rapidly increasing processing speeds 3D reconstructions could soon be performed on commercially available computers and volumetric stereotactic frame-based methods were quickly developed. Whilst these heralded the birth of computer-assisted neurosurgery the hardware required was expensive, surgery was impeded by the stereotactic frame and the intraoperative calculation and frame adjustments were tedious in the extreme.

In 1986 whilst Kelly described his complete frame-based computer-assisted volumetric tumour excision method, two independent groups were developing frameless systems for intraoperative guidance (Roberts 1986, Watanabe 1987). These systems defined a co-ordinate system for physical space and registered this with the scan co-ordinate system, just as the stereotactic frame did, but in a revolutionary manner. In

addition, they provided real-time display of scan reconstructions corresponding to any anatomical structure encountered during surgery. To achieve these facilities both systems required a method for tracking a pointer in space. Watanabe's group developed an articulated arm with potentiometers at each joint that enabled rapid calculation of the arm configuration and thus determination of tip position (Kosugi et al 1988). Roberts' group attached ultrasound-emitting spark gaps to an operating microscope in a specific pattern. Microphones detected the sound, thus triangulating the position of each spark gap (and therefore the microscope) in space. In each case registration of physical and scan co-ordinate systems was achieved through the identification and matching of surface structures in the scans and the same structures localised on the patient with the system pointer. Having registered the patient these systems provided real-time image reconstructions of the patients own image data in three planes corresponding to whichever structure the system pointer was placed upon. Thus, interactive image-directed neurosurgery was achieved and although many developments have occurred since, the basic structure of neuronavigation systems and the principles of guidance have not altered.

Although the ultrasonic tracking employed by Roberts' group was highly accurate in theory and in laboratory tests, interference in the operating theatre environment made this method unsuitable for widespread clinical use (Bucholz & Smith 1993). In contrast the submillimetric mechanical accuracy of the potentiometer-based arms determined in laboratory accuracy assessments was not severely affected by the operating theatre environment (Galloway et al 1992). Thus, the first commercially available neuronavigation system, the Viewing Wand (ISG Technologies, Canada), incorporated

an articulated arm with potentiometers (Figure 1.4) and considerable experience in image-guided surgery rapidly accrued with this device. Thus, Golfinos et al (1995) reported 325 consecutive cases with the ISG Wand, Sandeman and Gill (1995) reported 305 cases and Gomez et al (1993) reported 501. Whilst the guidance was reported to be beneficial, the bulk of the arm was found to obstruct access to the surgical field, the working volume was limited, the six joints were difficult to manoeuvre and the weight of the arm precluded simple fixation. These limitations propelled the investigation of alternative tracking technologies including electromagnetic field distortion (Kato et al 1991), video tracking (Colchester et al 1996) and triangulation of infra-red light emitted by pointer LED's (Zamorano et al 1994). Whilst several tracking technologies continued to be used by isolated groups, infrared optical tracking emerged as the superior technology for pointer localisation (Rohling et al 1995). This provided high levels of accuracy in the hostile operating theatre environment and ergonomic intra-operative localisation of hand-held pointers. Alternative methods of registration were also investigated, from surface mapping (Henderson et al 1994) and cortical vessel matching (Nakajima et al 1997) to dental attachments (Bale et al 1997). However, accuracy assessments have consistently revealed that the fiducial-based method is the more accurate (Sipos et al 1996, Tan et al 1993).

Ironically, the major drawback of the successful hand-held pointer based navigation systems was found to be obstruction of the line of sight by the microscope. Similarly, in arm-based systems the bulk of the device was found to hinder pointer insertion with the microscope in position. Thus the navigating microscope was rediscovered, with tracking of the focal point by infrared technology (Westermann et al
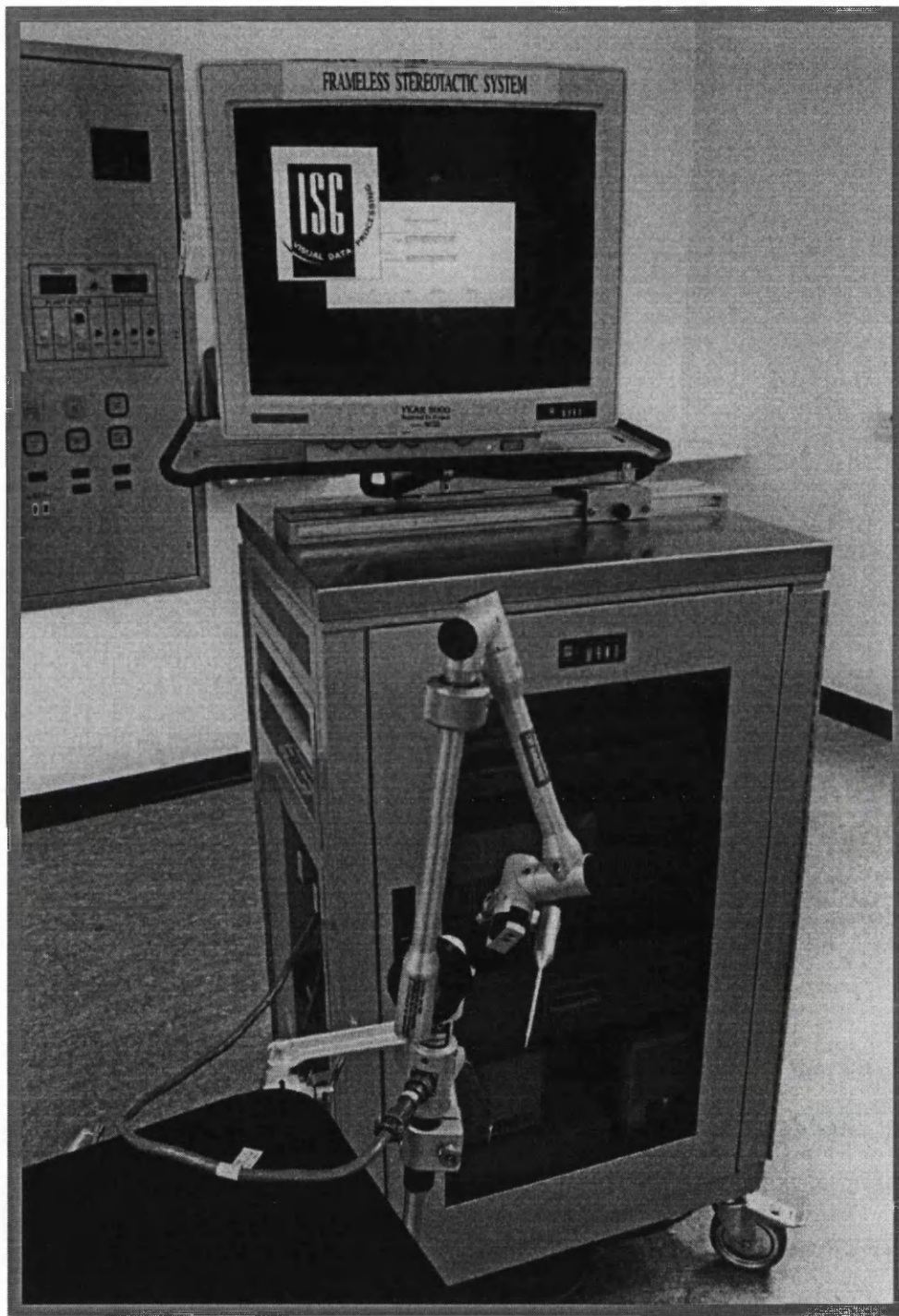
Figure 1.4: Photograph of the ISG Viewing Wand neuronavigation system. The position of the steel pointer tip is calculated by the computer workstation from the potentiometer outputs for each of the six arm joints. This is displayed on the monitor in triplanar image reformats.

32

1995). Later developments of this included the addition of motorised microscopes, which could position automatically over a defined target, and image projection into the eyepieces (Zeiss MKM, Surgiscope). Whilst such innovations provided real advantages for microsurgical procedures, the registration process was cumbersome and such systems could not be employed for macroscopic procedures. The latest evolution is the combination of pointer tracking and microscope guidance by the same system. These infra-red systems circumvent the line of sight restriction through tracking either the pointer or the microscope.

Although interest in neuronavigation was at first limited to the development research groups, the potential clinical value of these devices gradually became apparent and the ISG Wand became available commercially in 1990. Combined with dramatic increases in computer power, this heralded the onset of a rapid increase in neuronavigation-assisted operations performed, the number of surgeons using such systems and the choice of systems on the market. Large series of open neurosurgical operations were performed over subsequent years, establishing the place of neuronavigation in neurosurgical practice (Golfinos 1995, Gomez 1993). Whilst stringent clinical trials of the efficacy of neuronavigation have not been conducted, this is widely accepted to confer advantages and some clinical benefits have been observed. These include reduced hospital stay, reduced anaesthetic time and shorter operations (Henderson et al 1997, Ungersböck et al 1996). In addition, there are associated advantages of enhanced surgical planning, simulation, teaching, intraoperative plan execution and documentation (Maciunas 1993). However, the absolute indications for and particular advantages of neuronavigation have yet to be established. Surgeons with

considerable experience of such devices regard the main benefit of image-guidance variously as the reduction in morbidity, improvement in extent of resection achieved for intraventricular tumours (Vinas et al 1996) and improved superficial tumour margin delineation (Reinhardt et al 1993).

The occurrence of brain distortion subsequent to imaging has been widely portrayed as a serious limit upon the accuracy of intra-operative guidance for the localisation of anatomical structures. Whilst brain distortion is an everyday experience for the neurosurgeon and is concomitant with the practice of neurosurgery, the magnitude of such distortion, the influence of pathology and the imaging characteristics that predict shift have received scant attention. Furthermore, the impact of brain shift on image-guidance, the need for intra-operative image-updating and the resolution necessary for such updating are controversial and unresolved issues (Barnett et al 1993a, Bucholz et al 1993, Drake et al 1994, Golfinos et al 1995, Kelly et al 1988). Despite this dearth of quantitative information several groups are already pursuing a variety of avenues for intra-operative image updating and re-registration.

1.2.4 Frameless Stereotaxy

Whilst neuronavigation has become an established adjunct to open neurosurgery, image-guidance has had little impact on the traditionally frame-based stereotactic procedures of burr-hole biopsy, functional neurosurgery and guided endoscope insertion. In these fields neuronavigation has the potential to detach image acquisition from surgery, improve surgical access, increase flexibility, introduce interactive target selection, reduce operation times and avoid the need for MRI-compatible stereotactic

equipment. For such advances to be realised a technique for true frameless stereotaxy would be required.

To be truly stereotactic a technique must fulfil certain criteria. These include the precise guidance of a delicate instrument to a pre-selected discrete target at any site within the cranium, without deviation or collateral brain injury. Whilst image-guidance of a tracked instrument has been achieved relatively simply (Barnet et al 1996, Laborde et al 1993, Smith et al 1994), hand-held devices cannot satisfy these rigorous requirements of stereotaxy. Indeed, hand-held frameless biopsy, even performed live in an interventional MRI scanner, has been shown to have disappointingly low accuracy and a poor diagnostic yield (Silverman et al 1997). One method developed to overcome this limitation has been the re-introduction of an arc system to the operating field, but this defeats the objective of improved access and ergonomics of frameless stereotaxy (Yeh et al 1993). Other increasingly elaborate have been developed to overcome these problems including intra-operative micro-electrode recordings to define the tumour margin during hand-held navigation and biopsy (Hirato et al 1994).

Thus, for true frameless stereotaxy to be realised an instrument guide was required which would reach all parts of the vault, lock in place rigidly to provide robust support, allow fine correction of trajectory settings, adapt to a variety of instruments and be compatible with image-guidance tracking, whilst allowing full surgical access. Attempts to adapt traditional neurosurgical devices to this task have been reported (Drake et al 1994) but none has been satisfactory due to either excessive movement, inflexibility or obstruction of the surgical field.

1.3 OBJECTIVES

The objective of this investigation was to develop and evaluate a novel surgical instrument, the Image-Guided Neuroendoscope. This required methods to be devised for the tracking of an endoscope by a navigation system and for frameless stereotactic guidance during endoscope insertion. In addition, image fusion would require the correction of endoscope optical distortion and the impact of post-imaging brain distortion on accuracy would need investigation.

1.3.1 Envisaged Outcome

The envisaged instrument was a rigid operating endoscope, coupled to a neuronavigation system. The aim was firstly that blind insertion of the endoscope may be accurately guided, either through interactive feedback or by frameless stereotactic guidance, along a pre-selected trajectory to a specific target position. Secondly, that spatial information be supplied to the surgeon continuously regarding the position of the tip of the endoscope and orientation of the shaft, in the pre-operative images, during an endoscopic procedure. Thirdly, that visible structures may be identified and non-visible structures, beyond the ventricular wall or obscured by ventricular adhesions, may become accessible targets for surgical intervention. Fourthly, that the optical distortion of the endoscopic view may be corrected to improve surgical intervention and enable injection of graphics overlays of important structures into the endoscope video image. Finally, that the value of 3D reconstructions of the endoscope image, derived from the pre-operative data sets, could be determined.

1.3.2 Predicted Clinical Impact of Image-Guided Neuroendoscopy

Technical advances in neuroendoscopy and concurrent advances in imaging and neuroanaesthesia have contributed to the enhanced safety and effectiveness of contemporary neuroendoscopy. Enthusiasm for this technique is widespread and diverse clinical indications have been reported. However, further dissemination and the application of minimally invasive procedures to intraparenchymal lesions is limited by the fundamental requirement of direct visualisation, both for orientation and for intervention, and by disorientation. These restrictions may be circumvented by the provision of intra-operative anatomical and spatial orientation, both of endoscope position and peri-ventricular anatomy. Thus, the combination of a neuronavigation system with a rigid endoscope would provide continuous accurate interactive and ergonomic image-guided neuroendoscopy. This would incorporate the advantages of the continuous provision of orientation information, guidance during endoscope insertion and the facility to identify structures beyond the endoscope field of view. Such guidance could be further enhanced through the injection of graphics depicting the outlines of pre-selected targets and anatomical structures.

An influence on surgical outcome might be expected if the extent of lesion resection were to be enhanced or the morbidity associated with such surgery were reduced in some cases. In addition, the development of a valid technique for frameless stereotaxy could facilitate, for example, the safe biopsy of brain lesions (with either CT or MR guidance), implantation of electrodes and stereotactic catheter placement with reduced surgical and anaesthetic time and potentially improved accuracy. Furthermore, the analysis of factors influencing post-imaging brain distortion and quantification of

this phenomenon has implications for the whole practice of image-directed surgery, whether frame-based or frameless.

1.3.3 Strategy for Development and Evaluation of IGN

In the development of Image-Guided Neuroendoscopy the first requirement was the selection of a neuronavigation system which would readily adapt to the role of endoscope tracking whilst maintaining the freedom of movement intrinsic to endoscopic surgery. In addition the system would require software tools for pointer view reconstructions, virtual tip elongation and path planning whilst having the facility to enhance these features with video input and distortion correction algorithms. Thus, a suitable neuronavigation system would be a novel late stage prototype system that employs infrared optical tracking technology. The accuracy and clinical validity of the system would require full investigated with laboratory phantom studies and validation through clinical application to a variety of open neurosurgical operations. In addition, the impact of post-imaging brain distortion on neuronavigation would need to be addressed in a wide range of pathologies to determine the likely impact of this upon the accuracy of IGN.

The envisaged method of instrument insertion would be a frameless stereotactic procedure whereby the entry point and trajectory are pre-defined in the image data set and the instrument is passed through the brain under rigid stereotactic guidance. This would require a technique for true frameless stereotaxy, including the development of an adjustable, locking instrument holder. This technique would also require assessment

through a series of laboratory phantom studies of accuracy, validation through a clinical series of frameless stereotactic biopsies and assessment of the in vivo accuracy.

In order to allow tracking of the endoscope during insertion and intervention a method of LED attachment to the instrument would be required. Again, both laboratory phantom accuracy assessments and clinical validation of this method would be required. Following the development, assessment and validation of image-guided neuroendoscopy the possibilities of graphics enhancement could be explored. This would involve both the projection of selected graphics outlines of anatomical structures into the video image, reconstruction of endoscope views from the data sets and simulation of endoscopic approaches. This would first require correction of the optical distortion inherent in an endoscope to enable co-registration of the endoscope view and the image data.

MATERIALS AND METHODS

2.1 THE NEURONAVIGATION SYSTEM

The requirements of the neuronavigation system for this investigation were; that the system employed an accurate and reliable method for intra-operative guidance, that the system software would allow brain shift measurement and the introduction and integration of novel techniques (namely Frameless Stereotaxy and Image-Guided Neuroendoscopy), and that the system had approval for introduction into clinical practice. At the time of planning this investigation the superior method, among the available tracking technologies, was provided by infrared LED / camera systems and the most accurate and reliable registration method was fiducial-based. Thus, the preferred system was a late development version of an optical image guidance system requiring clinical validation and development. These requirements were fulfilled by the prototype of EasyGuide Neuro (Philips Medical Systems, the Netherlands) under development with the European Union funded EASI Project in the University Department of Neurosurgery at the Institute of Neurology, London. Thus, Image Guided Neuroendoscopy came to form a small but significant part of this development project and this system was able to be employed for the associated development of frameless stereotaxy and in the investigation of post-imaging brain distortion.

2.1.1 Components and Principles of Operation

The neuronavigation system comprised a mobile computer workstation with high-resolution monitor, a table-mounted detector array incorporating two infrared cameras (Figure 2.1) and a selection of hand-held pointers. The handle of each pointer was fitted with three embedded light-emitting diodes in a non-colinear arrangement (Figure 2.2) and the steel shafts were shaped into a short straight pointer, a long
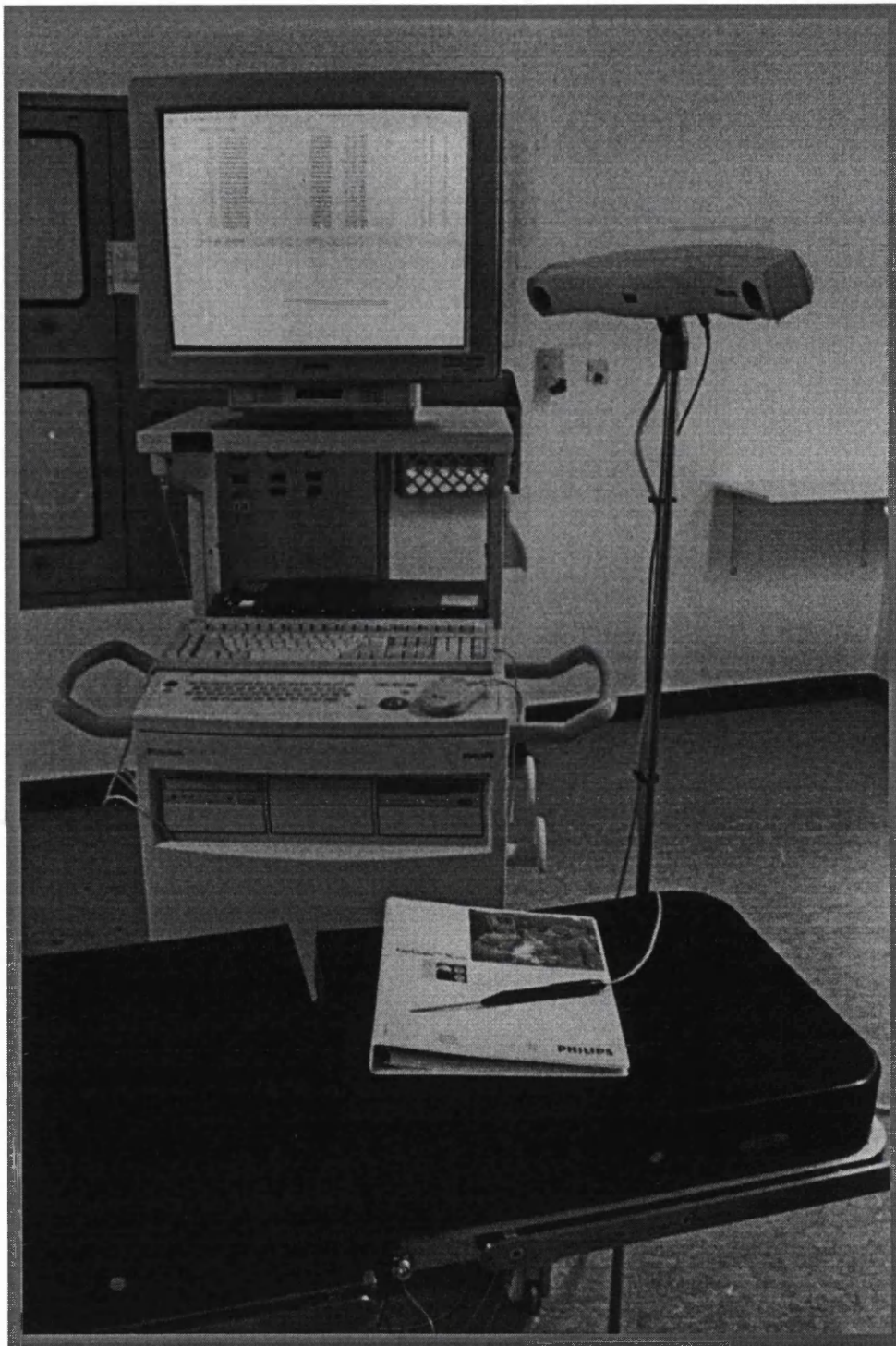
Figure 2.1: The EasyGuide Neuro infrared-based neuronavigation system. The main components are the mobile workstation with high resolution monitor, detector array (mounted on the operating table) and a hand-held pointer. Attachment of the cameras to the table allows registration to be maintained during height and tilt adjustments.
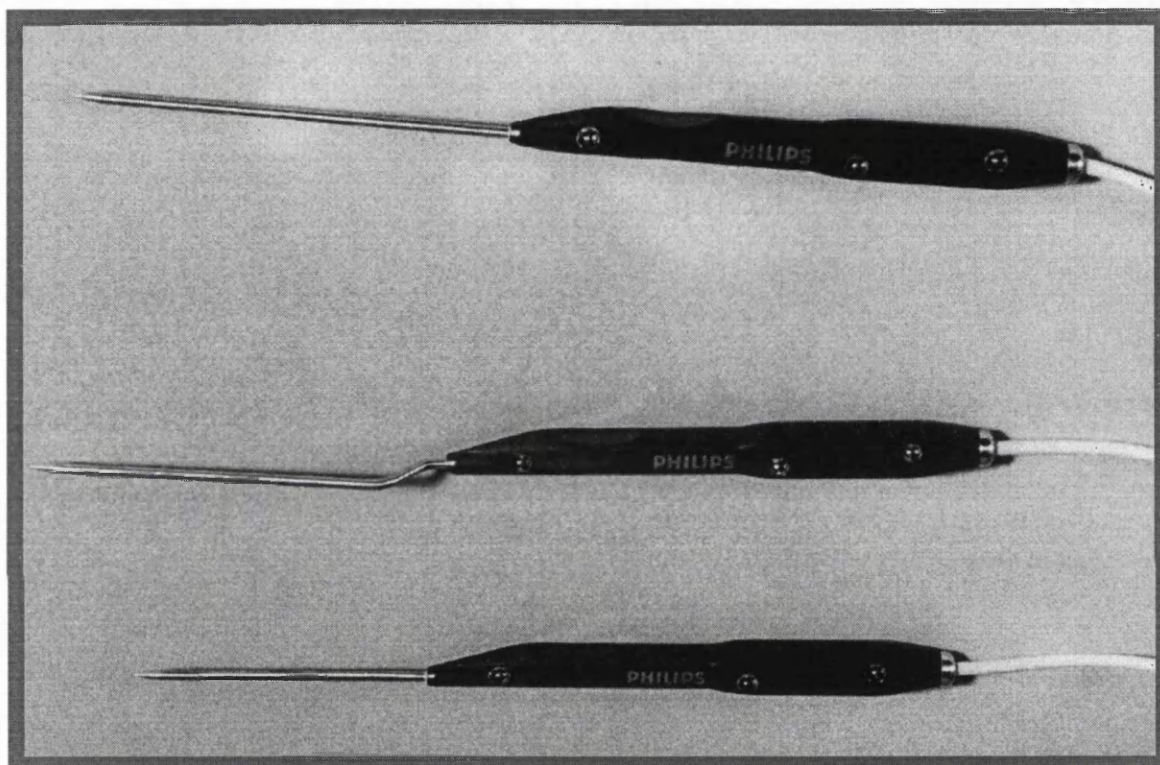
Figure 2.2: The standard selection of short straight, long straight and long bayonet hand-held pointers. Note that each pointer handle is identical, having three LED's mounted in an asymmetric pattern. The phase alignment/power cables are seen entering the top of each pointer.

straight pointer and a long bayonet pointer. These pointers were rigid and connected to the detector array via a power and phase-alignment cable that enabled sequenced pulses of infrared light to be emitted by the LED's. This sequencing ensured the correct detection of each pulse of light by the camera array and rejection of reflections and interference. The detector array comprised two solid state two-dimensional infrared cameras mounted on a rigid pole that fixed to the table via an adjustable block. Within the detector array the cameras were separated by 0.5 metres and their angle of convergence were preset to provide an optimal working distance of 1.0-1.5 metres from the array. Within this range each pulse of infrared light emitted by an LED could be detected by both cameras and the three dimensional position of this LED determined. Thus, when the position of each of the three LED's in a pointer handle was detected the tip position, orientation and rotation of the pointer could be derived. For this purpose the table-mounted camera array was connected via a separate power/signal cable to the mobile workstation.

The navigation system workstation incorporated a SunSparc5 computer with additional hard disc memory, a generic Philips processing unit (PPU), an optical disc drive, a CD-ROM drive, keyboard, mouse and high definition monitor. The detected position of each LED within the camera fields of view was input to the generic PPU and the position of each LED in space, relative to the cameras, calculated from this. A model of each pointer was loaded into the PPU describing the spatial relationship between each LED and the pointer tip. Thus, by fitting the model to the detected LED positions the PPU determined the pointer orientation and tip position, in camera co-ordinates. This enabled the system to display the pointer tip position in the image data

set reformats in virtual real time, once registration of the radiological images with physical space (defined as camera co-ordinates) had been accomplished.

The image data set co-ordinates of the skin fiducials were defined via manual identification of each fiducial position in the images. The co-ordinates of each fiducial in physical space were defined by placement of the pointer tip in the centre of each fiducial and capture of this localised position. These two co-ordinate sets were matched by the system through rigid body transformations, namely; scaling, rotation and translation. The solution to this co-registration that was accepted by the system was that with the lowest root mean square error (RMSE). This method of registration applied equal weight to each fiducial. Following registration the pointer position could be converted to image co-ordinates and displayed in the pre-operative image data set as the intersection of three standard orthogonal views (axial, coronal and sagittal).

Image data sets were loaded either on re-writeable optical disc in PMS format or via ethernet in DICOM III format. At the start of the project network connections were only available between the MRI scanners and the imaging workstations. A laboratory SunSparc5 workstation was enabled with the EasyVision CT/MR software (Philips Medical Systems), which allowed MR images to be transferred to the CT/MR workstation via ethernet in DICOM III format and converted to PMS format for optical disc transfer to the navigation system. The network was later completed to connect the scanners, laboratory and operating theatres, simplifying the transfer of image data sets.

2.1.2 Standard Neuronavigation Software Tools

The basic navigation system interface provided separate windows for data handling, registration and intraoperative guidance functions. The data handling tools

enabled image data set input, transfer to connected devices or optical disc and data set editing. The registration tool included the facility to capture surface fiducial positions in the image data sets, automatic definition of CT markers of know Hounsfield value, capture of the fiducial positions localised with a pointer, measurement of distance from pointer to nearest fiducial, deletion of fiducials, fallback marker definition and re-registration. The error associated with each registration was automatically displayed by the system as the RMSE. In the intra-operative guidance window were tools for path planning, virtual pointer elongation and calliper measurement. The path-planning tool allowed an entry point and target points along a path to be defined in the image data set for reference during image-guided surgery. The virtual pointer elongation tool enabled the localised pointer tip position to be advanced along the pointer trajectory to a known distance beyond the physical tip position. The software calliper tool enabled measurements to be made either between stored pointer locations or between structures visible in the images. The real time display of pointer tip position could also be frozen and reactivated in this window.

2.1.3 Supplementary Navigation Tools

During the project additional tools were developed and integrated into the navigation system software. Firstly, the facility to employ pre-prepared segmentations and surface renderings during navigation was introduced. Powerful segmentation tools were available with the CT/MR workstation software but, whilst such methods could enhance the understanding of anatomical relationships, the images could only be viewed on this workstation. The facility that was developed enabled surface renderings to be transferred to a gallery in the mobile workstation, which was available for viewing

during intra-operative navigation. In addition, the segmented structures could be highlighted in the real-time orthogonal display of reformatted radiological images. Secondly, a craniotomy planning tool was developed that allowed pre-operative definition of burr hole sites, craniotomy flap, target lesion and trajectory of approach. Having defined these parameters a movie of sequential image slices along the planned path from skin surface to lesion could be viewed, with the craniotomy window overlaid. This tool also provided the facility to transfer the plan to the patient with an interactive display of pointer position on a 3D surface reconstruction. Thirdly, the facility to grab video frames and present these in the fourth view port was introduced. This would later enable the simultaneous display of endoscope tip position and trajectory in the reformatted radiological images alongside the captured endoscope view on the navigation monitor. Fourthly, a pointer learning tool was introduced whereby the configuration of any rigid instrument, with an attached LED carrier, could be detected and thence tracked by the system. To learn the configuration of a novel instrument the tip was placed in a fixed position and the handle swung around this until the relationship between the LED's and tip was solved by the computer.

2.1.4 Imaging Protocols for Neuronavigation

The imaging protocols employed during the investigations were identical for both phantom and clinical studies. Volumetric data acquisition was employed throughout for the greater accuracy achieved in stereotactic procedures with such image protocols (Walker et al 1997). These images were either Gadolinium-enhanced MRI (General Electric 0.5 Tesla Vectra and 1.5 Tesla Signa scanners) or contrast-enhanced CT scans (Siemens Somatom 4 scanner). In each case adhesive fiducials were applied to

the scalp prior to imaging, spread widely across the vault, with a cluster overlying the region of interest. Imaging protocols were employed which achieved a suitable compromise between the desire for high resolution and the duration of acquisition, which was associated with movement artefacts when prolonged. For the Signa MR scanner the imaging protocol was a SPGR sequence with minimum TR and TE, flip 50°, matrix 256 x 256, FOV 24cm and slice thickness 1.5mm. For the Vectra MR scanner the standard imaging protocol was TR 42, TE 15, flip 50°, matrix 192 x 256, FOV 24cm and slice thickness 2.0mm. During the project a longer sequence fine Vectra scan was employed for phantom accuracy studies with the parameters TR 42, TE 15, FOV 24cm, slice thickness 1.5mm and matrix 256 x 256. For sequential axial CT scans the matrix was 512 x 512, FOV 23cm, gantry tilt 0° and slice thickness was either 2 mm with 2mm slice separation or 3mm with 3mm slice separation. The parameters for helical CT scans was a matrix of 512 x 512, FOV 20.5cm, gantry tilt 0° and slice thickness 3mm. The resultant voxel dimensions for the Signa MR images were X=0.93mm, Y=0.93mm, Z=1.5mm. Those for the standard Vectra MR images were X=1.25mm, Y=0.93mm, Z=2.0mm. The fine Vectra MR voxel dimensions were X=0.93mm, Y=0.93mm and Z=1.5mm. For sequential axial CT scans the voxel dimensions were X=0.45mm, Y=0.45mm and Z either 2.0mm or 3.0mm. The voxel dimensions for helical CT images were X=0.40mm, Y=0.40mm, Z=3.0mm.

Registration of the image data sets with physical space was performed with a fiducial-based method. The patient or phantom was positioned and held rigidly in place with the Mayfield head clamp (Figure 2.3). The location of each fiducial was identified in the pre-operative images and stored in the navigation workstation memory as the image marker set. A hand-held pointer was used to localise the position of each fiducial
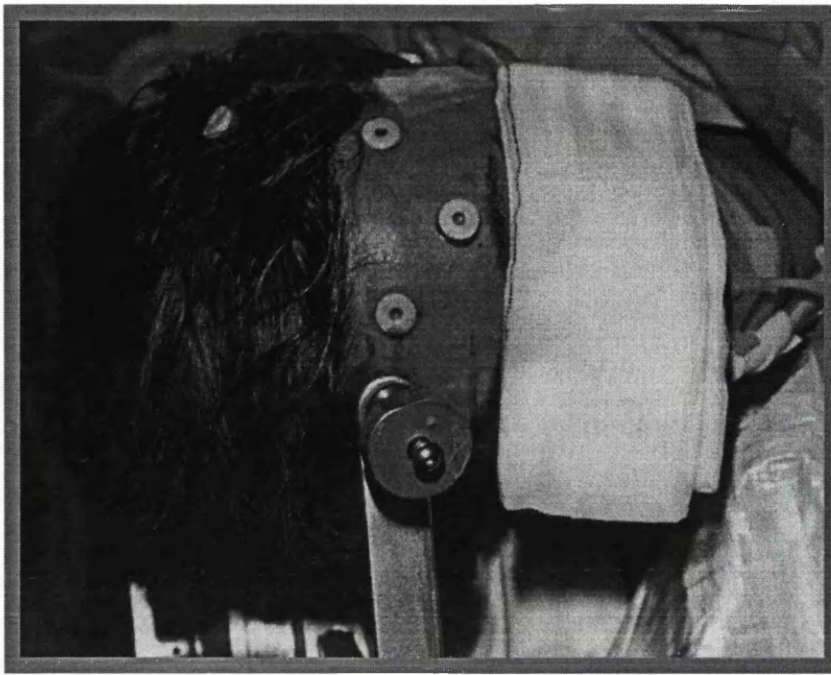
Figure 2.3: Photograph of a patient prepared for fiducial registration. The adhesive

fiducials are is situ and the head is fixed in a Mayfield clamp.
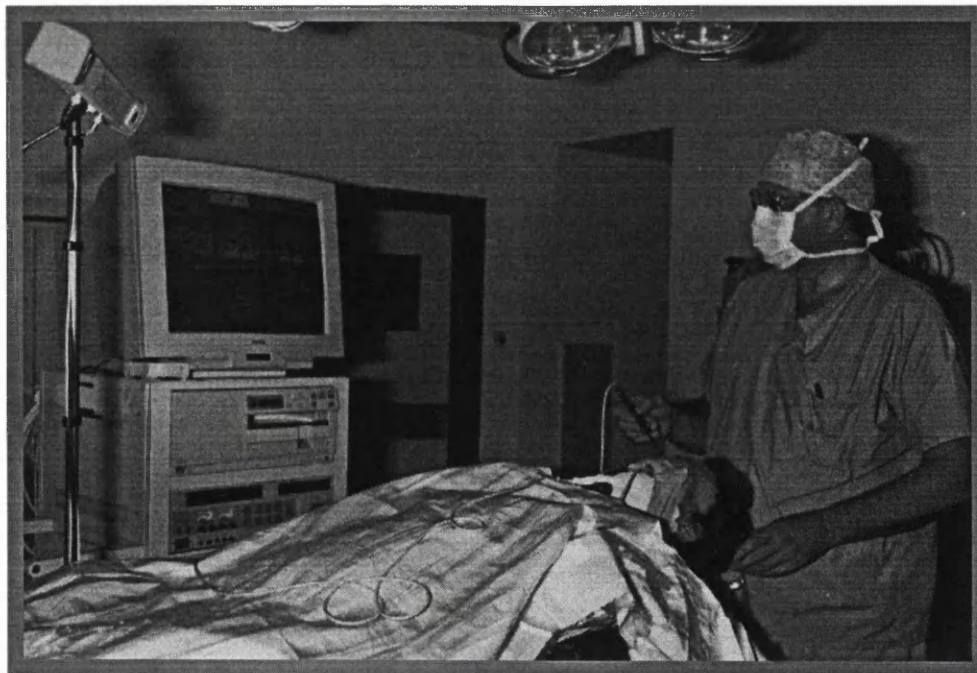
Figure 2.4: The prototype neuronavigation system in clinical use. The table-mounted

camera array, mobile workstation and hand-held pointer are shown.

in space and these points were captured as the patient marker set (Figure 2.4). Registration was performed via the least squares method and the resultant RMSE of registration displayed. The error associated with each fiducial position was checked through the "Nearest Marker" output and any fiducial with a markedly elevated value was deleted.

2.2 LABORATORY STUDIES OF NEURONAVIGATION

SYSTEM ACCURACY

A review of the literature describing the introduction and dissemination of neuronavigation reveals a remarkable paucity of accuracy data. Some papers describe the sensitivity of movement detection in the tracking system and some employ the RMSE of registration as an indicator of system error (Fuchs et al 1996, Roessler et al 1997) but none provide a detailed assessment of system accuracy. Until relatively recently this situation applied equally to the allied field of frame-based stereotaxy. Thus, for many years the figures for mechanical frame accuracy were confused with application accuracy resulting in the millimetre myth (the incorrect belief that frames were accurate to within a millimetre in clinical practice). This situation was corrected through publication of the seminal works of Maciunas and Galloway describing their detailed laboratory phantom investigations of stereotactic frame accuracy (Maciunas et al 1992, Maciunas et al 1994). The essential features of these experiments were; firstly that a phantom was employed which contained targets clearly identifiable both in CT images and in physical space, secondly that the clinical situation was reproduced as closely as possible, thirdly that multiple measurements were taken and finally that the offset of the frame target from the physical target was determined. Thus, the laboratory investigations of neuronavigation system accuracy described here were designed to rigorously test the system accuracy following the same principles. This was both to ensure that meaningful results were obtained and to enable comparison with the frame accuracy results.

2.2.1 The Phantom

The phantom employed during the laboratory studies of system accuracy comprised a plastic moulded skull with removable vault, mounted on a perspex base (Radionics Inc, USA) that was CT and MR compatible (Figure 2.5). For MR imaging a hexagonal perspex box was placed over the skull and secured to the base to produce a watertight seal (Figure 2.6). Two screw holes in the top of the box allowed the instillation of copper sulphate solution. The skull itself was composed of two parts, the detachable vault and the fixed skull base. Within the phantom skull base was a perspex baseplate, with peripherally placed 2mm drill holes separated by 15mm, surmounted by finely engineered geometric shapes (Figure 2.7). Plastic strips were attached to the under surface of the baseplate to close off the drill holes, enabling the system pointers to be inserted and to accurately locate the centre of the lower margin of each drill hole. The internal features were supplemented by the insertion of 20 imaging localisers (Figure 2.7). These comprised titanium screws of two lengths onto which were fitted cups to accept a variety of attachments (Leibinger, Freiburg, Germany). The imaging attachments for use with CT and plain film radiology comprised perspex balls with a central gold sphere mounted on a stalk. The attachments for MR imaging comprised perspex balls with a hollow centre, which were filled with Copper Sulphate solution prior to scanning. An intra-operative attachment was employed for position localisation, which comprised a flat cap with a central dimple (Figure 2.8). These attachments were manufactured such that the position of the central dimple of the intra- operative cap corresponded precisely with the centre of the imaging spheres.

The base on which the phantom was mounted was designed to fit within the inner ring of a CRW MR-compatible stereotactic frame, which could itself be attached
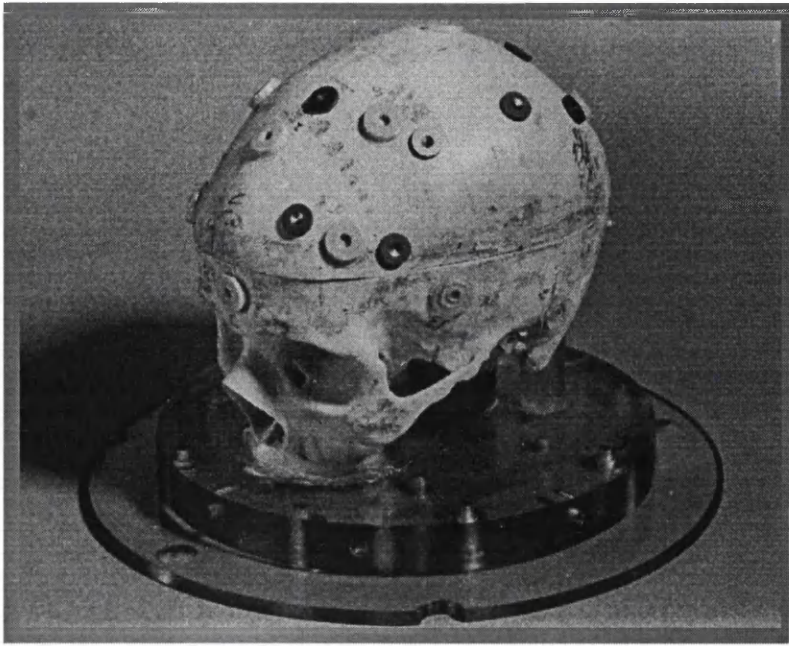
Figure 2.5: The skull phantom external appearance. Standard position fiducials and additional markers are visible across the removable vault and skull base.

Figure 2.6: The phantom prepared for MR imaging. A perspex cover was secured with nylon screws to form a watertight seal and copper sulphate solution instilled.

Figure 2.7: Internal features of the skull phantom comprising a perspex plate with drill holes surmounted by geometric shapes with implanted image localiser screws. The whole range of screw components and attachments are visible.
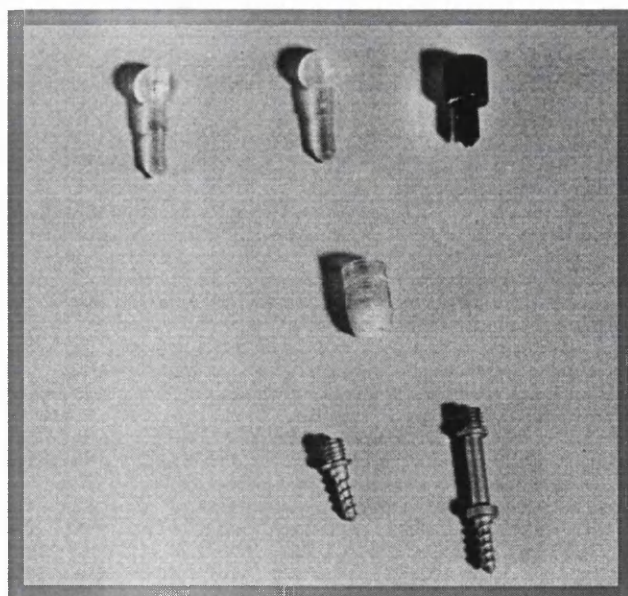
Figure 2.8: The image localiser screw system. CT, MRI and intra-operative localiser attachments are shown above. The universal cup attachment lies in the centre and screws of two lengths are shown below.

to a Mayfield head clamp. However, a small amount of residual movement between the frame and the phantom remained possible with this arrangement. This was eliminated through the construction of a fixing plate, which was screwed onto both the phantom and the CRW base ring. This arrangement enabled the phantom skull to be mounted on the operating table with a Mayfield head holder, in the clinical supine position.

2.2.2 Registration

The accuracy of image to physical space registration was assessed, as well as the impact of imaging modality, imaging protocol and the number of fiducials employed, in a series of phantom studies. The method employed was designed to closely reproduce the clinical procedure for registration with this system. The phantom was imaged according to the described neuronavigation protocols with the Signa MR scanner, the Vectra MR scanner and CT scanner, following application of surface fiducials in the standard clinical positions. Thus, the data sets comprised a Signa MRI, Standard Vectra MRI, Fine Vectra MRI, 2mm Sequential axial CT, 3mm Sequential axial CT and 3mm Helical CT. Five copies of each data set were transferred to the neuronavigation workstation and fiducial positions defined manually in each. The phantom and camera array were mounted on an operating table in the standard clinical arrangement. The fiducial-based registration was performed five times for each data set in turn with recording of the resultant registration RMSE and the Nearest Marker error output for each fiducial. These registration tests were repeated for each of the standard system pointers, namely the short straight, long straight and bayonet pointers.

The impact of the number of fiducials employed on registration error was also investigated. The five registrations performed for each imaging modality employed

eleven fiducials for registration. These registrations were repeated a further five times but employing six of the previous fiducials. The same fiducials were employed in the registrations for each imaging modality and the subset of six were evenly spread across the phantom vault.

2.2.3 Point Localisation

The error of point localisation by the navigation system, the impact of imaging on this and the differences between pointers was assessed through a series of phantom experiments. Prior to imaging of the phantom the appropriate localiser attachments were inserted into the screw cups. The standard MR and CT image data sets were acquired and five copies transferred to the Navigation system database. Three groups of target structures were employed in these experiments, comprising the image localiser screws, spare surface fiducials not employed for registration and the baseplate drill holes. The position of each target was defined manually in the image data sets and captured as a registration point. The intra-operative localiser caps, with the central dimple, were then substituted for the imaging attachments and the phantom mounted on the operating table. Following registration the error of point localisation was determined for each of the physical targets. Thus, the pointer tip was placed on each target in turn and the distance of the localised pointer tip from the defined image marker recorded from the Nearest Marker output (Figure 2.9). These measurements were repeated for each of the five copies of each data set, on the nineteen implanted image localisers, the four spare surface fiducials and the twenty base plate drill holes. These error assessments were duplicated in full with each of the short, long and bayonet pointers.
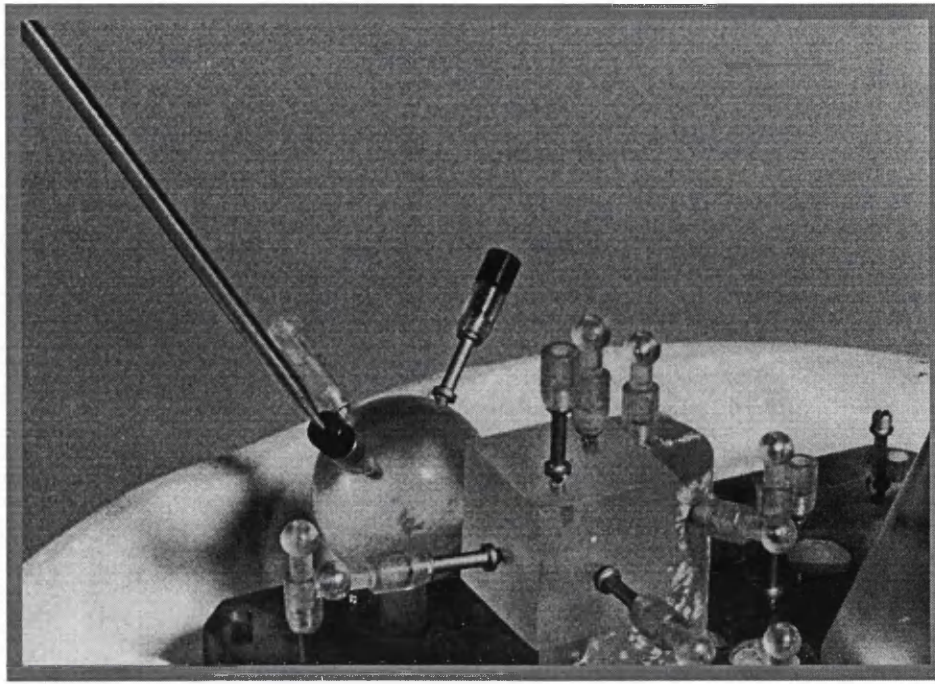
Figure 2.9: The long pointer docked with the central dimple of an image localiser cap

for point localisation error assessment.
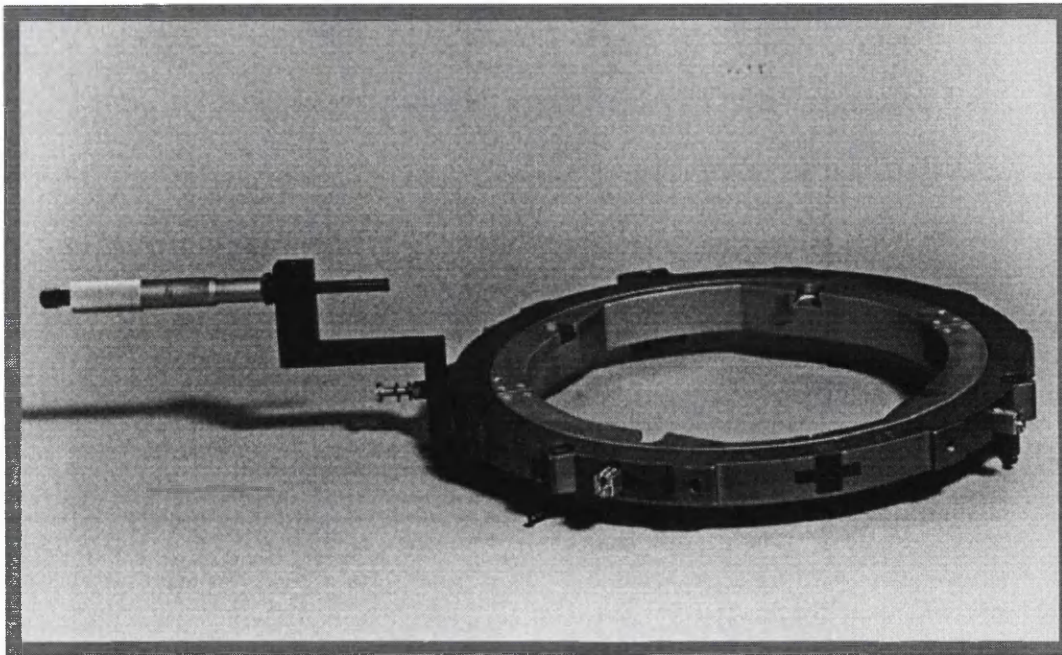
Figure 2.10: Mounting of the micrometer on a stereotactic base ring enabled rigid

fixation to the table for the detection of pointer movement experiments.

2.2.4 Reproducibility of Point Localisation

The congruence with which a physical point was localised by the system was investigated with the phantom apparatus. The phantom was imaged, mounted on the operating table and registered with the image data sets as described above. Following phantom registration a frameless stereotactic block (see Section 2.5.1) was locked rigidly in position to allow the pointer to repeatedly locate the same target, with the same camera alignment. The pointer was introduced into the block and the localisation error recorded for each event as the distance to the Nearest Marker output. These measurements were repeated in excess of sixty times for each of the short, long and bayonet pointer types.

2.2.5 Detection of Pointer Movement

The sensitivity of the system for movement was examined through determination of the magnitude of pointer movement required for the system to detect a new position. For these experiments a micrometer was mounted onto a stereotactic base ring, which could be fixed rigidly to the operating table (Figure 2.10). The camera array was mounted on the table, phantom registration performed and the skull replaced by the micrometer apparatus. The system pointer was held horizontally, with the tip abutting the micrometer, by a frameless stereotactic block supported by the adjustable locking arm (see Section 2.5.1). The pointer handle was maintained perpendicular to the camera line of sight with the LED's facing the cameras directly, providing the optimum arrangement for tracking. The Nearest Marker output was recorded and the micrometer slowly advanced, thereby pushing the pointer through the block, until a different

position was registered by the guidance system. The micrometer reading was recorded for each localised position to determine the distance advanced.

2.2.6 Effect of Pointer Rotation on Localisation

The variation in point localisation with angle of rotation relative to the camera array was examined. Following registration of the phantom with the images, the pointer was placed in a steel block and locked in position in the frameless stereotactic arm (see Section 2.5.1). The top of the block had previously been marked with angles of rotation at 45° intervals and the axis of the LED's marked on the pointer tip. One of the block marker lines was aligned perpendicular to the camera array by ensuring that the line lay in the path of a laser light source, which was mounted midway between the cameras in the detector array. This was designated the 0° position and the distance to Nearest Marker output recorded for repeated localisations at this position. The pointer was rotated to align with each of the angular lines from 90° left through to 90° right and the distance to nearest marker recorded. These measurements were repeated twenty times for each position.

2.3 CLINICAL EVALUATION OF THE NEURONAVIGATION SYSTEM

As a novel prototype, the navigation system required evaluation in clinical use and this was achieved through application to a wide variety of surgical pathologies, approaches and procedures. For each case the clinical findings, imaging details and registration data were recorded in an evaluation protocol, the surgeon ranked the usefulness of the system on a visual analogue scale and the duration of the operation and total time of system usage was determined.

The formidable issue of clinical accuracy in neuronavigation was partly addressed through the RMSE of registration, which was recorded for each case and could be compared with the phantom registration results. But while this has been the mainstay of clinical accuracy assessment in most large series of neuronavigation (Doshi et al 1995, Roessler et al 1997) the meaning of these values is severely restricted. The major impediment in deriving clinical accuracy measurements is the difficulty of defining precise physical points in vivo and in scan images. This is compounded by the difficulty in reliably measuring the offset of the two. Several investigators have attempted to address this problem, some relying simply on a surgeon's estimate of error (Golfinos et al 1995) and others employing anatomical landmarks selected by the surgeon and later segmented from the images (Ryan et al 1996). However, neither method provides a reliable or robust measure of application accuracy. Thus, in this study two techniques were employed to address this issue. Firstly the offset of the localised pointer tip from a readily defined and inflexible surface (the skull) was determined (see Section 2.3.5) and secondly a method was developed to determine the

in vivo error of frameless stereotactic biopsy where the target and biopsy site should, by definition, be identical (see Section 2.55).

2.3.1 Clinical Evaluation Protocol

An evaluation protocol pamphlet was produced for the purpose of data collection during clinical validation of the navigation system (Appendix I). This ensured that a complete set of data was collected and stored for each navigation case undertaken. The parameters recorded were details of and time required for case preparation (fiducial application, scan acquisition, data transfer and image marker identification for registration) and the operation details (date, surgeon, duration, patient positioning, layout of the operating room equipment and personnel, the pointers used, registration RMSE, nearest marker results and fallback marker location errors). The clinical details were also recorded in the evaluation protocol pamphlet, including the presenting history and examination, hospital stay and condition on discharge. In addition a précis of each procedure was written including details of the impact of navigation on all the aspects of surgery (planning, execution of the operation and a surgeon's perception of the benefits and failings of the system).

2.3.2 Visual Analogue Scales

Upon completion of each surgical procedure the operating surgeon was asked to complete a short questionnaire in the evaluation protocol and to score the system on a series of issues using visual analogue scales. These required the surgeon to rate the system in response to 10 questions concerning the impact of the system on the surgical

operation and on the functioning of the system, from detrimental at one extreme, through no impact to highly beneficial at the other extreme.

VISUAL ANALOGUE SCALE QUESTIONNAIRE

How would you describe the effect of the navigation system on –

1) - your appreciation of the surgical anatomy?
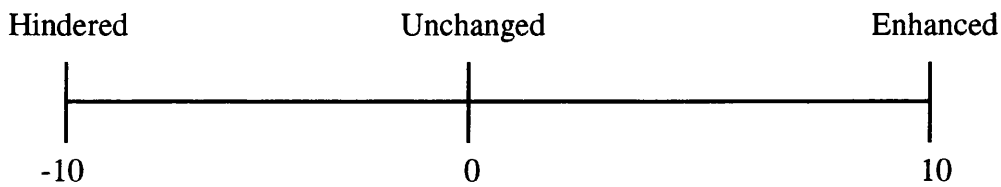
Hindered	Unchanged	Enhanced
-10	0	10

2) – your surgical planning ?

Hindered	Unchanged	Enhanced
-10	0	10

3) - localisation of the lesion ?

Hindered	Unchanged	Enhanced
-10	0	10
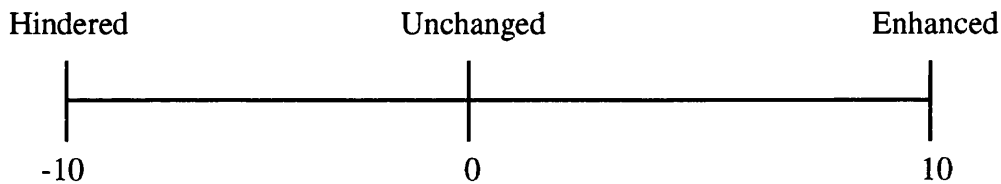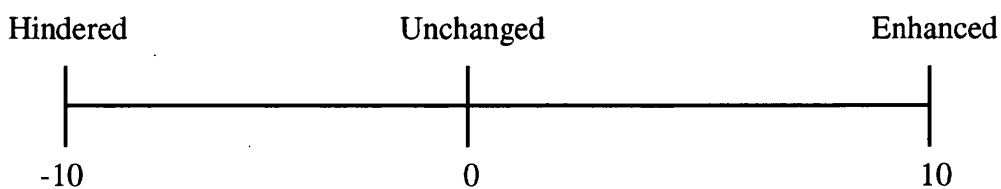
How would you describe the effect of the navigation system on –

4) - the extent of appropriate resection accomplished?

Hindered	Unchanged	Enhanced
-10	0	10

5) - the safety of surgery?

Hindered	Unchanged	Enhanced
-10	0	10
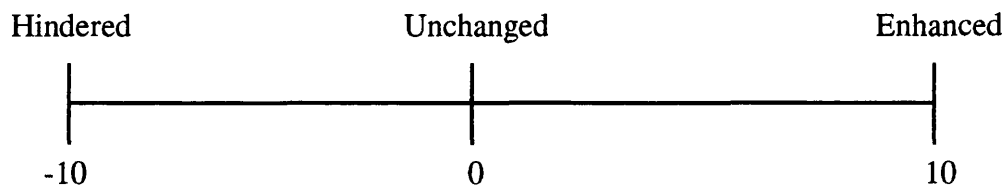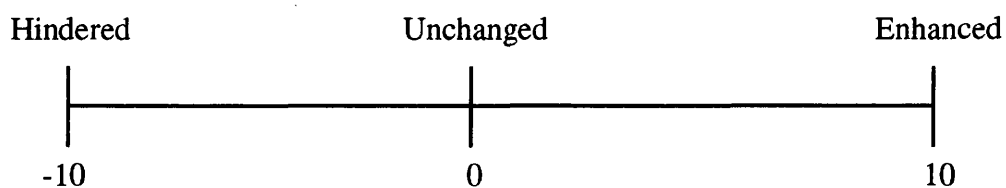
6) - your confidence during surgery?

Hindered	Unchanged	Enhanced
-10	0	10

7) - the duration of surgery?

Prolonged	Unchanged	Shortened
-10	0	10
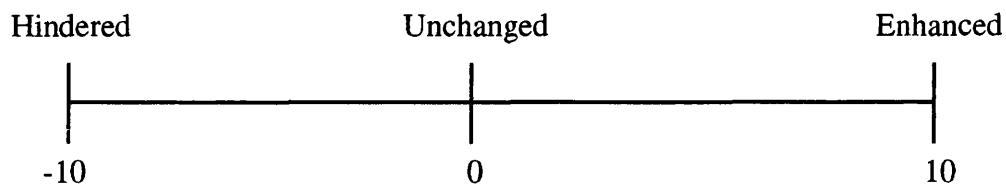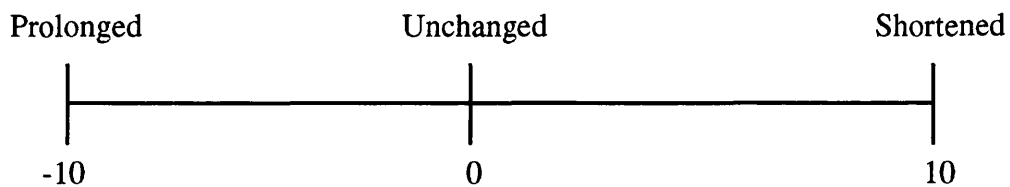
8) What is your overall opinion of the navigation system?

Detrimental   Ambivalent   Advantageous

```
|----------------------|----------------------|
-10                    0                     10
```
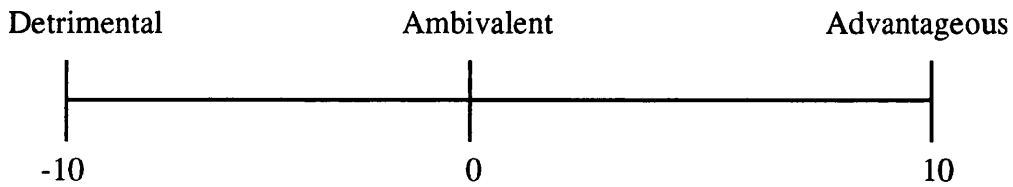
9) What is your opinion of the user interface?

Detrimental   Ambivalent   Advantageous

```
|----------------------|----------------------|
-10                    0                     10
```
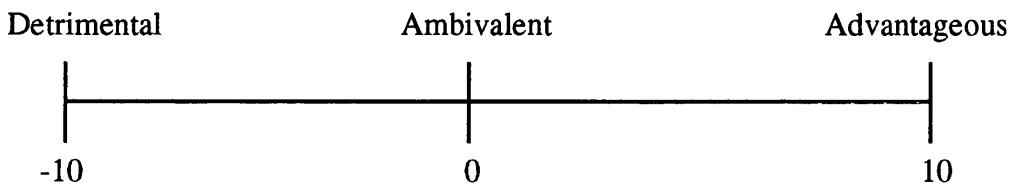
10) What is your opinion of the instrument guide for frameless stereotaxy?

Detrimental   Ambivalent   Advantageous

```
|----------------------|----------------------|
-10                    0                     10
```
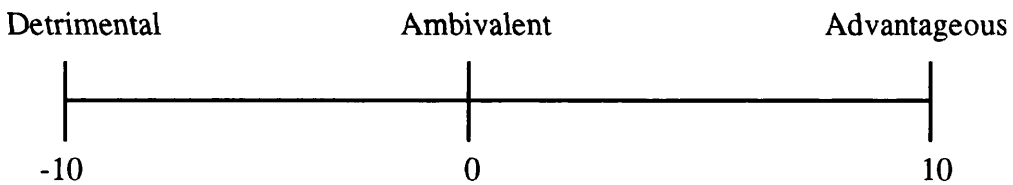
2.3.3 Patient Populations

The prototype neuronavigation system was employed to provide intra-operative guidance during 100 open neurosurgical operations between June 1996 and August 1997. These cases provided experience with intra-operative image guidance, enabled the neuronavigation system to be evaluated and allowed clinical studies to be undertaken. These studies comprised measurement of post-imaging brain distortion in 48 of the

cases (Section 2.4) and analysis of both frequency and duration of intra-operative system usage in 39 cases (Section 2.3.4).

Cases were proposed by the operating surgeon, according to perceived clinical need, and the navigation system used provided the patient could comply with the navigation system protocol. Four proposed cases were excluded from the study for failure to fulfil the protocols. Of these, one patient was unable to undergo MRI scanning due to a metal fragment within the globe, one refused scanning due to claustrophobia and two confused patients removed the fiducials between scanning and surgery. The patients who fulfilled the protocol comprised 60 men and 40 women with a median age of 44 years (range 15–77 years, interquartile range 22 years).

The most frequent pathological indication for surgery was glioma, followed by meningioma, then epilepsy and vascular malformations. A variety of miscellaneous other diagnoses including cavernoma, haemangioblastoma, chordoma and ependymoma constituted the remaining cases. The performance of the navigation system during each case was recorded in the Evaluation Protocol booklet and assessed in the case summary compiled subsequently.

2.3.4 Duration of Surgery and Navigation Time Analysis

The duration of each operation was recorded prospectively for the consecutive series of 100 patients undergoing a broad range of image-guided neurosurgical interventions. The impression of the surgeon of the effect of the neuronavigation system on the duration of surgery was also ascertained immediately after the procedure, by means of the visual analogue scale questionnaire (see Section 2.3.2). Comparison was

made between the duration of surgery in image-guided cases and matched conventional cases, selected from a pool of contemporary operations derived from the theatre log books. Pairs of operations were matched for type of pathology, procedure, lesion location (supratentorial or infratentorial) and for the grade of the operating surgeon. Duration of surgery, from positioning on the table to completion, was determined from the computerised theatre records and verified by comparison with that derived from the anaesthetic log. The duration of anaesthesia was also obtained from the anaesthetic record.

Within this series a detailed prospective analysis of the frequency and duration of intraoperative usage of the neuronavigation system was undertaken in thirty-nine of the cases. In these cases, timings were recorded manually in the operating room during thirty-five procedures and via analysis of a wall camera video recording of the procedure in the remaining four. The duration of each stage of the procedure, the frequency of intra-operative system usage and the duration of each usage were determined.

2.3.5 Accuracy in the Clinical Environment

Image to patient registration was performed via the fiducial-based method described previously. Following registration the RMSE and the Nearest Marker distance for each fiducial was recorded in the evaluation protocol. Any fiducial with a markedly elevated Nearest Marker distance (when compared with the entire fiducial set and in the context of the fiducial position and surgical pathology) was deleted from the registration

set and re-registration performed. The resultant RMSE and Nearest Marker distance for each fiducial was again recorded in the evaluation protocol and this was repeated until the registration accuracy was acceptable. In 43 cases no fiducials were deleted, in 48 cases one fiducial was removed from the registration and in 9 cases two fiducials required deletion.

In the subset of 48 cases where post-imaging brain distortion measurements were made, the application accuracy of the system was determined through bone surface offset measurements (Section 2.4.3). The outer surface of the skull provided a well-defined structure, which was accessible and would not distort between imaging and surgery. Thus, the position of the bone surface, at the centre of the scalp flap, was localised with the system pointer and captured on the workstation. The offset of the pointer tip from this surface was then measured in each of the orthogonal views with the software calliper tool, providing a measure of system application accuracy (see Figure 2.12).

2.4 POST-IMAGING BRAIN DISTORTION

Neuronavigation systems employ pre-operative images for surgical guidance. Thus, alterations to the morphology of the brain during surgery will not be reflected in the images, leading to potentially erroneous guidance. Intra-operative brain distortion has been proposed to occur as a result of pressure changes on skull opening, cerebral oedema, unopposed gravity, surgical resection and CSF withdrawal (Bucholz et al 1996). However, no reliable quantitative assessments of such distortions were available in the literature. Therefore, the magnitude of brain shift during neurosurgical operations was examined and the correlations between shift and features evident in the pre-operative images were determined.

In the absence of any comparable study data, a method was designed to determine the maximal deviation of the brain from the pre-operative position. Thus, the measurement position was defined as the centre of the craniotomy opening, the deviation of readily identifiable surfaces from their image position was determined and registration skew corrected for.

2.4.1 Study Population

During the period from June 1996 to August 1997 the neuronavigation system was employed in 100 open neurosurgical operations (see Section 2.3.3). The male to female ratio of these patients was 1.5:1 and the median age 44.7 years (Table 2.1). Brain shift and bone offset data were obtained in 48 of these image-guided cases. Of the remaining 52 cases in which complete shift measurement data was not obtained 23 were burr hole procedures (biopsy and shunt insertion), which precluded the acquisition of the deep shift measurements, in 12 cases the lesion margins were poorly demarcated,

69

TABLE 2.1

Comparison of patient population characteristics for the study group

vs. all patients undergoing image-guided surgery (no statistical difference)

	All Patients	Data Group
Number of cases	100	48
Male : Female ratio	1.5 : 1	1.0 : 1
Median age (range)	45 (15 - 77)	47 (20 - 77)
Mean registration RMSE	3.6 (SD 1.1)	3.6 (SD 1.0)
Pathological Group I (%)	21	(13) 27%
Pathological Group II (%)	29	(18) 38%
Pathological Group III (%)	27	(11) 23%
Pathological Group IV (%)	23	(6) 12%

TABLE 2.2

Pathological classification of study group diagnoses. Breakdown of the study

population according to histological diagnosis and allocation to pathological groups

for data analysis

Pathological Group	Histological Diagnosis	Frequency
I Vault meningiomas	Meningioma	13
II Cerebral gliomas	Glioma	18
III Non-gliomatous intra-axial lesions	Colloid cyst of IIIrd ventricle	2
	Metastasis	1
	Haemangioblastoma	1
	DNT	1
	Choroid plexus papilloma	1
	Ependymoma	1
	Cavernoma	1
	Granuloma	1
	Abscess	1
	Epileptic focus	1
IV Skull base lesions	Meningioma	2
	Chordoma	1
	Neurilemmoma	1
	Epidermoid	1
	Arachnoid cyst	1

surgical time constraints did not allow for full data collection in 13 operations and in 4 cases registration was lost prior to completion of data acquisition through table break adjustments. The median age of the 48 patients in the study group was 47.1 years and the male to female ratio 1:1. There were no statistically significantly differences between the study subgroup and the total patient population (Table 2.1). The surgical pathologies were divided into four groups for data analysis. Group I; convexity and parasagittal meningiomas, Group II; cerebral gliomas, Group III; non-glial intra-axial lesions and Group IV; skull base lesions (Table 2.2).

2.4.2 Pre-operative Image Analysis

All patients in the study group underwent pre-operative imaging with Gadolinium-enhanced T1-weighted volumetric MRI. Each image data set was transferred both to the CT/MR image-processing workstation for evaluation and to the navigation system for intra-operative guidance. The images were examined on the CT/MR workstation to determine the maximal extent of midline shift, lesion volume, depth of the lesion below the skin surface and presence or absence of oedema. Midline shift was determined as the maximum diversion of the midline structures from a line joining the anterior and posterior origins of the falx cerebri in the axial plane.

In determining the depth and volume of the lesion the centre of the abnormality was first defined and displayed in the standard three orthogonal views. The distance from this centre of density to the nearest skin surface was then measured in millimetres with the software calliper tool (Figure 2.11). The volume of the lesion was estimated via determination of the three perpendicular radii (x, y and z). These were measured from the defined centre of the lesion to the surface of the lesion along the axes of the
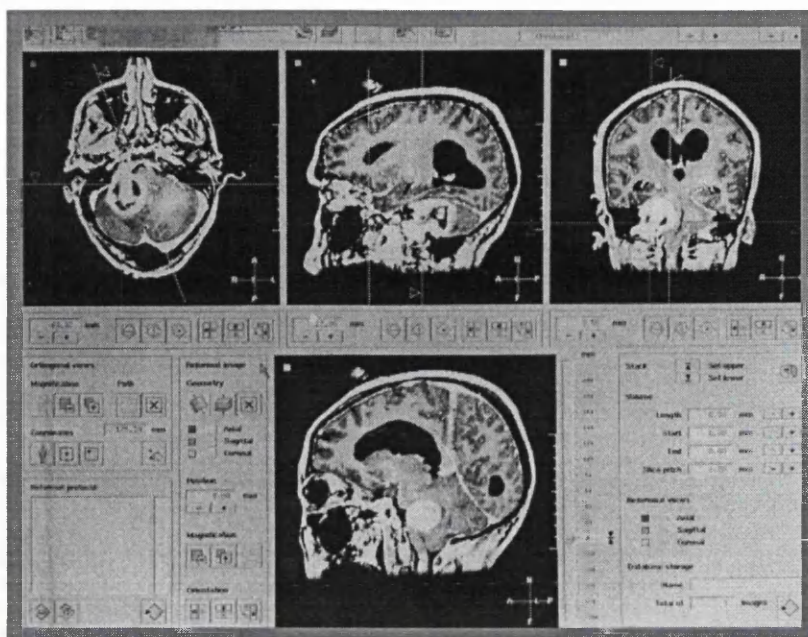
Figure 2.11: The CT/MR workstation image reformat window. The lesion centre was defined with cross hairs and the three diameters (in the x, y and z axes) measured.
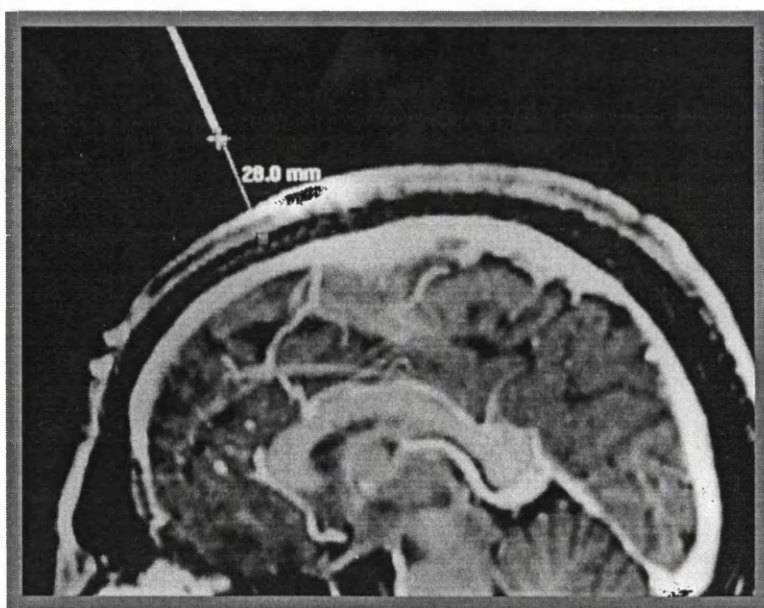
Figure 2.12: The technique of bone offset and shift measurement. The distance between the localised pointer tip position and target structure in the pre-operative images is determined (exaggerated for clarity in this example).

orthogonal planes. The x radius was defined as the distance from the centre to the anterior margin along the sagittal plane line in the axial view. The y radius was defined as the distance from the centre to the left margin along the axial plane line in the coronal view. The z radius was defined as the distance from the centre to the superior margin along the coronal plane line in the sagittal view. Lesion volume was calculated from these measurements by employing the formula for the volume of an ellipsoid:

$$volume = 4/3\pi r_x r_y r_z$$

2.4.3 Brain Shift Measurement Technique

The structures examined in this study were the skull surface at the centre of the planned craniotomy, the cortical surface at the centre of the dural opening (or, in the case of surface lesions, the most central cortex adjacent to the tumour), the deep tumour margin and the cortical surface at completion, adjacent to the resection margin. The method employed to detect and measure post-imaging brain distortion was for the surgeon first to identify the required surface and then to gently touch this with a pointer. The localised position of the pointer tip was captured on the system monitor and, when shift was present, the pointer tip position appeared to lie at a distance from the chosen structure in the images. This distance was measured with the software calliper tool (Figure 2.12) in each orthogonal plane in which the surface was visible. Measurement of shift of the deep tumour margin was only undertaken when the surgeon could identify this structure with confidence.

2.5 FRAMELESS STEREOTAXY

An integral part of the investigation into Image-Guided Neuroendoscopy was the development of a frameless stereotactic method for the insertion and guidance of the endoscope through a small skull opening, directly into the desired ventricular position without causing collateral brain injury. This necessitated the introduction of a novel technique for true frameless stereotaxy. Thus, assessments were required of the accuracy of this new method in both phantom simulations and in vivo, as well as evaluation of the technique in clinical practice. The model employed for these assessments was that of frameless stereotactic biopsy as the target, biopsy site and error could be rigidly defined in this way.

2.5.1 Development of the Stereotactic Instrument Guide

To achieve a truly stereotactic method of guidance with an optical navigation system required that a delicate instrument could be advanced to a pre-selected discrete target at any site within the cranium, without deviation or collateral brain injury. Whilst image-guidance of a tracked instrument could have been achieved relatively simply, hand-held devices would not satisfy these requirements of stereotaxy. Therefore, a frameless stereotaxy instrument guide was needed. The requirements of this device were the ability to reach all possible entry sites across the cranium, to adjust finely to select a target, to fix rigidly to define a trajectory and to provide accurate instrument guidance. Whilst support required strength and rigidity, guidance required flexibility in positioning and adaptability to a variety of instruments. For reasons of accuracy the arm was designed to be as short as possible without restricting access to the cranium and to mount rigidly on the Mayfield head holder.

The instrument holder that was developed (Figure 2.13) fulfilled the requirements of frameless stereotactic guidance and comprised a mounting block, a triple-jointed arm and a locking trapped ball. The configuration of the mounting block enabled fixation to either the operating table or Mayfield head holder. The three joints of the arm (mounting block to proximal limb, proximal to distal limb, distal limb to trapped ball block) were simultaneously stiffened by turning the single central handle, without torsional movement of the arm. The distal trapped ball contained a large central channel (Figure 2.14) into which instrument-holding blocks could be introduced. A selection of instrument-blocks was produced with inner bores of 2.0mm to 5.25mm calibre (Figure 2.15), allowing for guidance of a wide variety of instruments including standard stereotactic biopsy needles and the neuroendoscope. An instrument-block was developed specifically for use with the navigation system pointers that had an incomplete inner bore, which placed the pointer tip at the geometric centre of the trapped ball (Figure 2.16).

2.5.2 The Technique of Frameless Stereotaxy

During planning and development of the technique of frameless stereotaxy, biopsy of intracerebral lesions was employed as the model procedure. Thus, enabling comparisons to be drawn with frame-based stereotactic biopsy. The latter was an established technique, the accuracy had been thoroughly investigated and this represented the gold standard in clinical practice. The aim in developing frameless stereotaxy was to develop a method which not only compared favourably with the accuracy and simplicity of frame-based stereotactic biopsy but which would also apply to a wide variety of stereotactic procedures, in particular Image-Guided
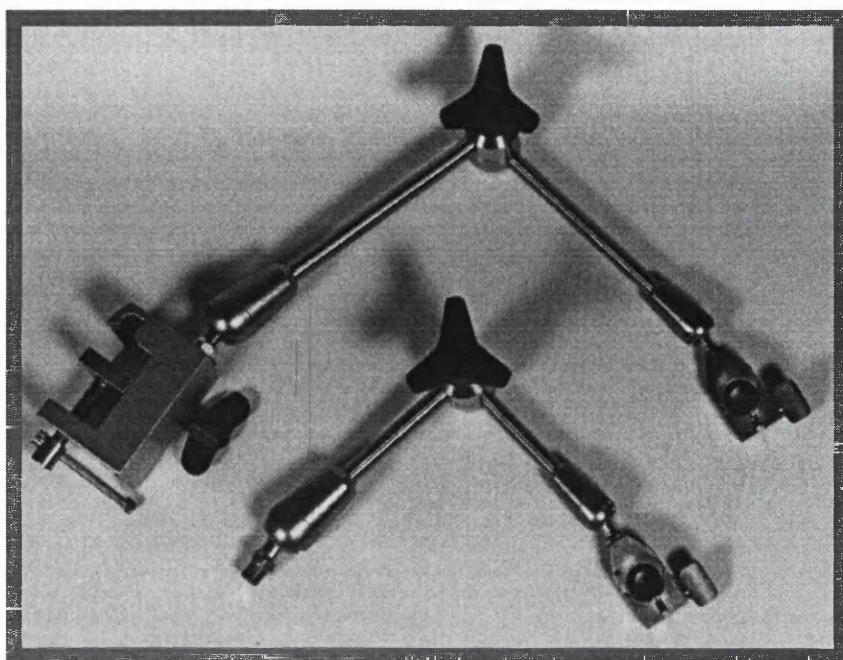
Figure 2.13: The frameless stereotaxy instrument guides. Two arms are shown of different lengths. The clamp on the longer arm (above) enables attachment of the arms to the head-holder or table and the central handle locks all three joints rigidly.
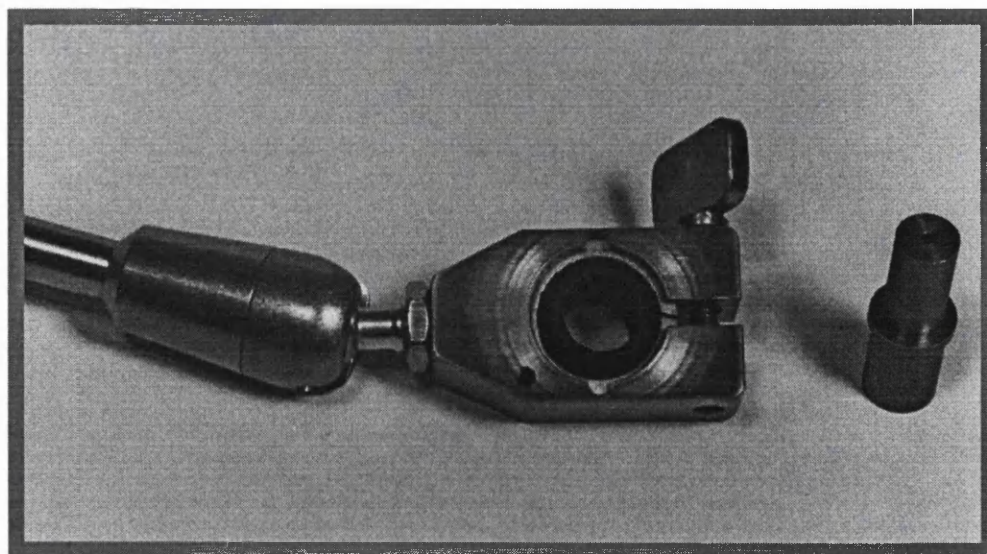
Figure 2.14: The trapped ball and an instrument block. The block fits the central channel of the trapped ball, enabling fine adjustment of the instrument trajectory.
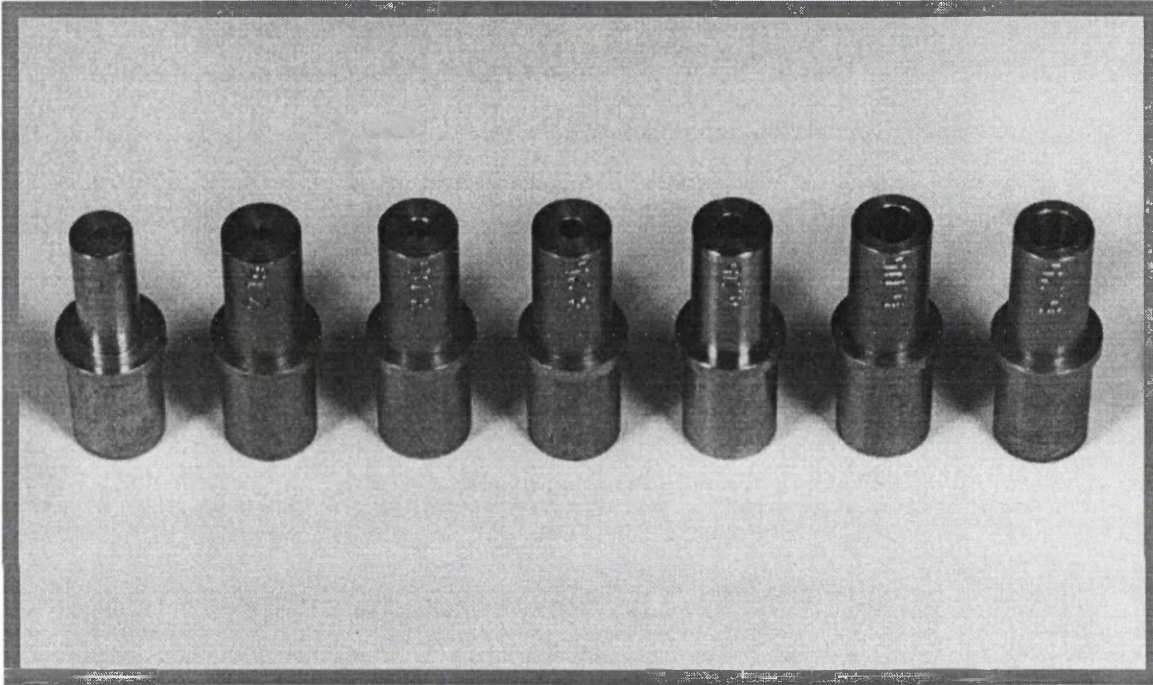
Figure 2.15: The selection of instrument guide blocks. The blocks have inner bores of 2.0mm, 2.16mm, 3.15mm, 3.25mm, 4.04mm, 5.05mm and 5.25mm corresponding to the outer diameters of some widely used biopsy instruments, aspiration needles, recording electrodes, and an endoscope.

Figure 2.16: A pointer of the prototype system docked with the pointer guide block in the trapped ball. Fine adjustment of pointer trajectory and of the extent of virtual elongation enables interactive target selection .

Neuroendoscopy. Thus, the principle requirements for frameless stereotactic biopsy were analysed, resulting in the identification of five stages in the process. These stages were; i) image acquisition, ii) image to patient registration, iii) entry point selection, iv) target and trajectory definition and v) biopsy retrieval. The method by which each stage would be accomplished was then developed. Thus, for frameless stereotactic procedures images were acquired with either Gadolinium-enhanced MRI or contrasted CT, following application of adhesive fiducials to the scalp, with the standard neuronavigation imaging protocols (see Section 2.1.3). Image to patient registration was performed with the fiducial-based method, following positioning in a Mayfield head clamp, and the RMSE of registration and Nearest Marker values for each fiducial were recorded (Section 2.1.3).

Two alternative methods were developed for entry point and target selection. These could either be defined peri-operatively by the surgeon in the images with the path-planning tool or could be selected per-operatively by interactive planning with the hand-held pointer. In the pre-planned method the entry point and trajectory were transferred to the patient via manual alignment of the pointer to match the localised position and trajectory to the pre-selected ones.

For interactive planning pointer elongation was used to display structures along the pointer trajectory from surface to target. As the pointer tip position was altered the trajectory and target were displayed in the images in real time. An appropriate entry site was selected, the area prepared for surgery and a burr hole constructed. The instrument guide was clamped to the vertical portion of the Mayfield head clamp and locked in position with the trapped ball over the burr hole. A pointer was inserted into the trapped ball (Figure 2.17) and virtual elongation used again to display the trajectory and target.

Figure 2.17: The stereotactic instrument guide arm mounted on a head clamp. The prototype system pointer is seen locked in position by the trapped ball. For frameless stereotactic biopsy the pointer block and pointer were replaced by a 2.0mm block and biopsy needle.

Fine adjustment of both the trapped ball position and length of virtual elongation enabled the optimum target site and trajectory to be selected. The trapped ball was then locked in position and the pointer block exchanged for the appropriate instrument-guide block.

Biopsy retrieval was performed with a standard Sedan-Nashold side cutting needle of 2mm outer diameter and 10mm side window (Figure 2.18). The depth to target was calculated from the length of virtual elongation used (displayed automatically by the system) plus 28mm (the distance into the block to which the pointer tip passed). A ruler was then used to measure this distance from the centre of the side-window to position a stop (Figure 2.19) such that the target would be expected to lie at the centre of the biopsy core. The needle was guided to the target by the appropriate instrument block and specimens retrieved from each quadrant (Figure 2.20). Following biopsy retrieval the needle was removed, the pointer was replaced in the trapped ball and the trajectory again captured to detect any movement of the arm.

2.5.3 Phantom Accuracy Measurements

The phantom employed in these studies was the moulded plastic skull mounted on a perspex base described previously (Section 2.2.1) and the image data sets were the Signa MRI, Standard Vectra MRI, Fine Vectra MRI, 2mm sequential CT, 3mm Sequential CT and 3mm Helical CT scans of this phantom (Section 2.2.2). The protocol for the phantom accuracy assessments adhered closely to those described by Maciunas' group for the assessment of stereotactic frame accuracy (Maciunas et al 1992, Maciunas et al 1994), such that comparisons could later be made with frame system accuracy results. Thus, the phantom was mounted on the operating table in a Mayfield clamp and
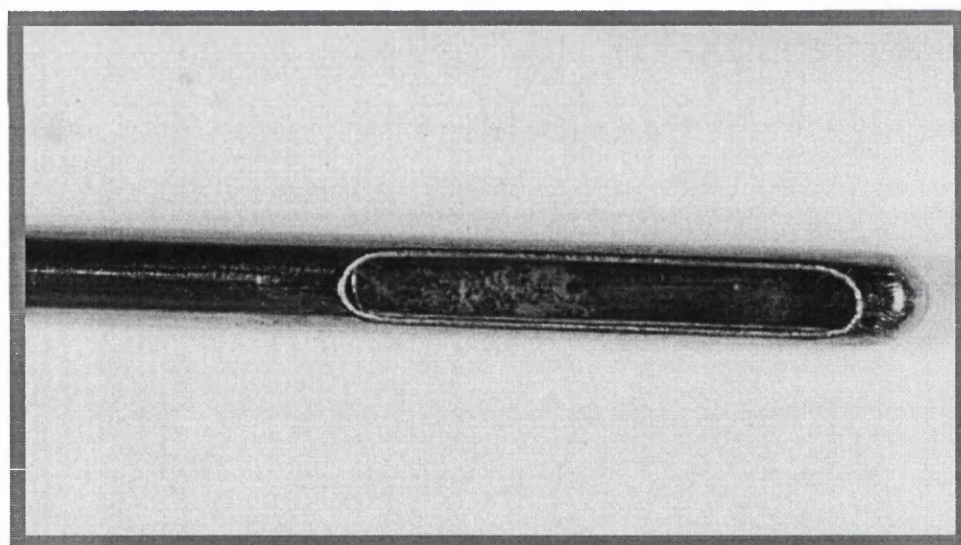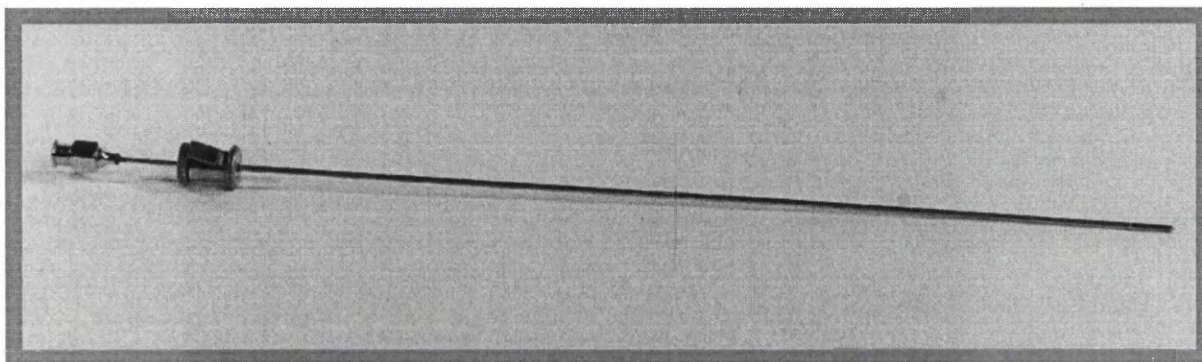
Figure 2.18: The Sedan-Nashold side-cutting needle used for brain biopsy. This is the

2mm diameter biopsy needle employed by the CRW frame system. The close-up shows

the double layers of the 10mm long window.
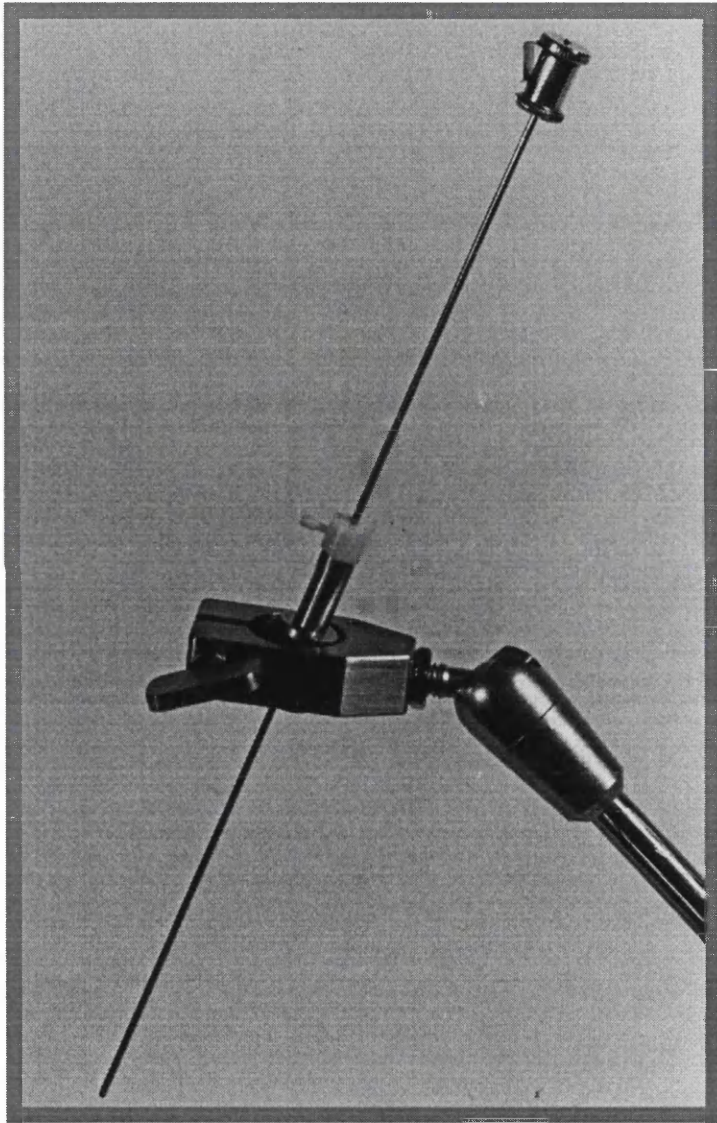
Figure 2.19: The biopsy needle held in the instrument guide block. The nylon depth stop was positioned such that the biopsy target should fall at the centre of the side-cutting window.
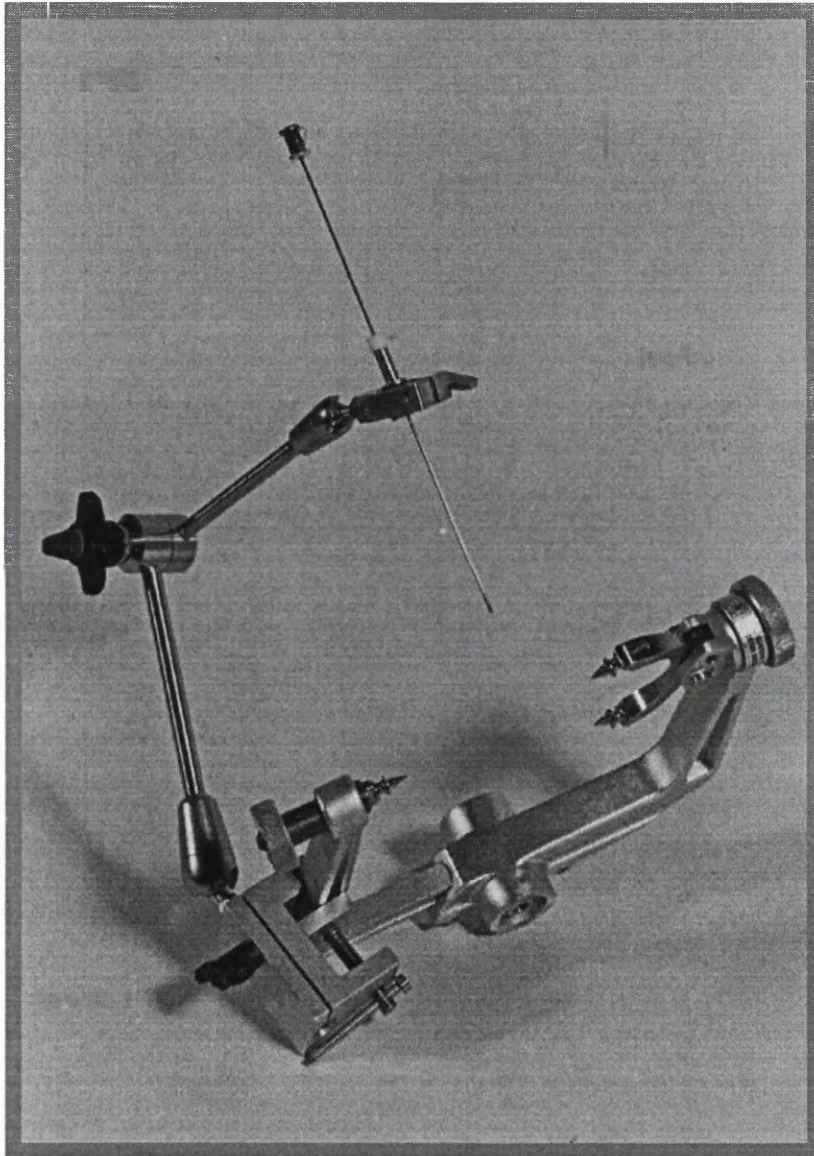
Figure 2.20: The stereotactic arm and biopsy needle mounted on a head clamp. This arrangement provided rigid instrument guidance and fixation during specimen retrieval.

the camera array attached to the table in the standard position. Fiducial-based registrations were performed and each image localiser screw attachment selected in turn as the target for frameless stereotaxy. The procedure for phantom frameless stereotaxy reproduced the entire clinical method. Thus, the entry point was selected with the pointer and the arm locked in position, virtual elongation adjusted to identify the target and the trajectory finely altered with the trapped ball. Once the instrument holder was positioned, the depth to target was calculated and a depth stop set on a sharp rigid needle. The pointer block was exchanged for the appropriate guide block, the vault of the phantom skull removed and the needle inserted. The distance from the needle tip to the central dimple of the localiser cap was then measured with micro-callipers. By this means the accuracy of localisation was ascertained for each of the 19 implanted image localisers available. This entire process, from fiducial definition and registration through to error measurement, was repeated five times for each data set.

The mean inter-voxel distance (MID) for each imaging protocol was calculated, for later comparison with the accuracy assessments, for each image data set. The MID was defined as the mean of the distances from the centre of any voxel to the centre of all adjacent voxels. In the volumetric data sets employed, each voxel was neighboured by 26 others and the mean intervoxel distance was calculated from the formula (where x, y and z represent the antero-posterior, lateral and vertical voxel dimensions respectively):

$$MID = \frac{2x + 2y + 4(\sqrt{x^2 + y^2}) + 2z + 4(\sqrt{x^2 + z^2}) + 4(\sqrt{y^2 + z^2}) + 4(\sqrt{x^2 + y^2 + z^2})]}{26}$$

2.5.4 Clinical Evaluation of Frameless Stereotaxy

The developed method of frameless stereotaxy was evaluated through a clinical series of frameless stereotactic biopsies (Figure 2.21, 2.22). A total of 21 biopsy sites were sampled in 19 consecutive patients presenting with cerebral mass lesions of unknown pathology. The patients comprised 8 females and 11 males aged between 25 and 76 years (Table 2.3). The procedures were conducted according to the protocol

TABLE 2.3

General characteristics of patients undergoing frameless stereotactic biopsy

Case No.	Age	Sex	Site	No. of fiducials	Lesion Diameter (mm)	MRI/ CT
1	43	F	Rt Parietal	11	27.4	MRI
2	50	M	Lt Temporal	7	60.0	MRI
3	56	F	Rt Parietal	9	17.0	MRI
4	25	M	Rt Parietal	11	26.4	MRI
5	73	M	Rt Thalamic	11	42.9	MRI
6	55	M	Lt Temporal	10	46.9	MRI
7	53	F	Lt Frontal	10	53.3	MRI
8	53	F	Lt Occipital	9	54.8	MRI
9	68	F	Rt Parietal	16	39.7	CT
10	57	F	Rt Parietal	10	59.0	CT
11	63	M	Cb Peduncle	9	22.0	CT
12	70	M	Rt Frontal	8	37.8	CT
12	70	M	Rt Frontal	8	37.8	CT
13	25	M	Lt Frontal	11	60.5	MRI
14	76	M	Lt Parietal	8	29.0	CT
15	38	M	Lt Parietal	11	23.6	CT
16	28	F	Lt Frontal	9	13.2	MRI
17	69	F	Lt Parietal	9	40.2	MRI
18	57	M	Rt Thalamic	8	36.2	MRI
19	53	M	Rt Temporal	9	22.6	MRI
19	53	M	Rt Temporal	9	26.7	MRI

described above. The burr hole, target and trajectory planning was performed by the interactive method for 19 of the targets and by pre-planning in the image data set for the
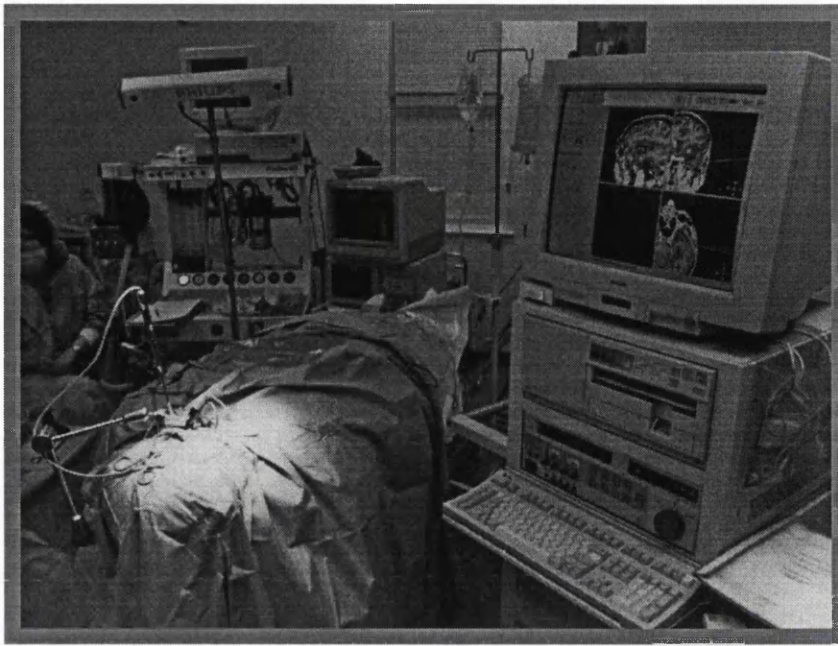
Figure 2.21: Clinical photograph of a frameless stereotactic biopsy with the prototype neuronavigation system.
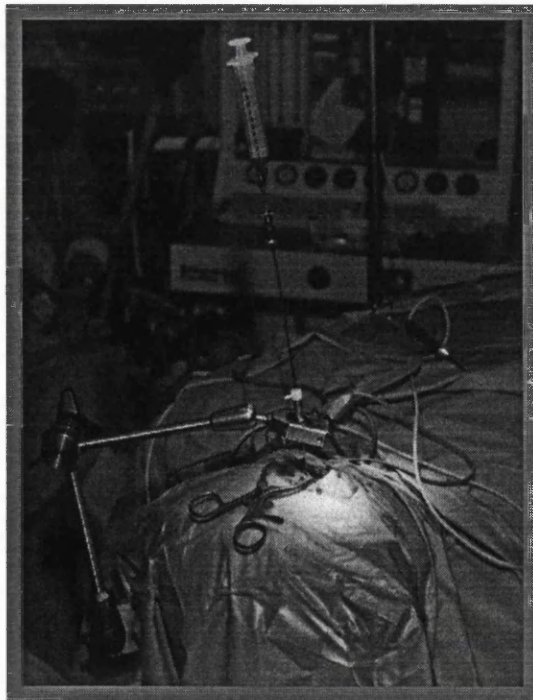
Figure 2.22: Clinical photograph of the biopsy needle in situ, supported by the stereotactic arm, and specimen retrieval by the syringe vacuum method.

remaining 2 target sites. Six patients underwent pre-operative imaging with 3mm sequential axial CT and 13 underwent pre-operative MRI scanning.

2.5.5 In Vivo Accuracy Assessment

Although the accuracy of frameless stereotaxy determined through the phantom accuracy studies would be directly comparable with similar studies reported in the literature, such studies necessarily underestimate the errors experienced in clinical practice. Therefore, in vivo accuracy of frameless stereotactic biopsy was determined directly for cases in the clinical series. The method devised for this involved firstly, transfer of the pre-operative data sets to the EasyVision CT/MR Workstation. Secondly, the intra-operative biopsy target (three orthogonal views) was captured in the navigation system database and also transferred to the EasyVision CT/MR Workstation following surgery. Thirdly, a post-operative volumetric MRI (image-guidance protocol) was acquired within 24 hours of surgery and again transferred to the EasyVision CT/MR Workstation (Figure 2.23). Fourthly, the data sets were registered through manual selection of identical structures in the pre-operative and post-operative images (Figure 2.24, 2.25). This aligned the co-ordinate system of the post-operative images with that for the pre-operative data set, allowing the intra-operative target position to be compared with the position of the actual biopsy site. This method of image registration with the CT/MR software has previously been assessed and validated through comparison studies (West et al 1997).

In the post-operative MR images the biopsy site was clearly identifiable as a low-signal ellipsoid in all but one case. The dimensions of the imaged ellipsoid correlated well with those of the biopsy needle window and were therefore accepted as
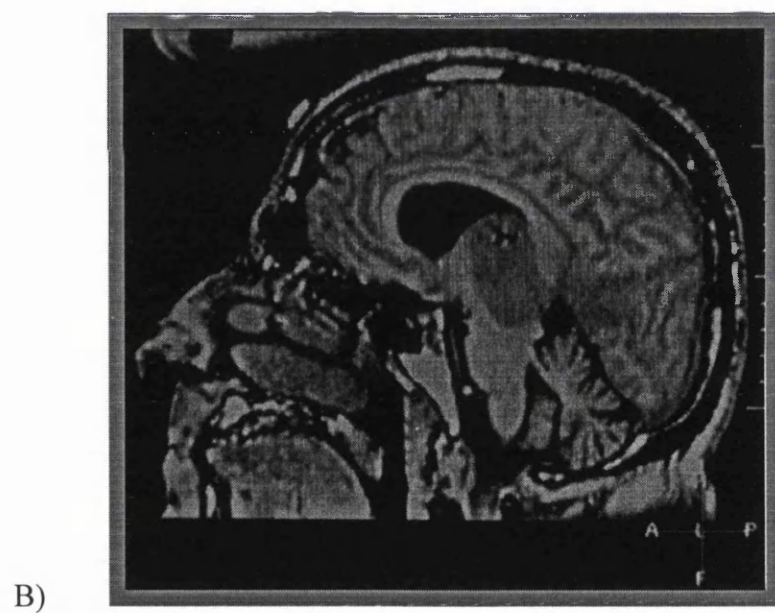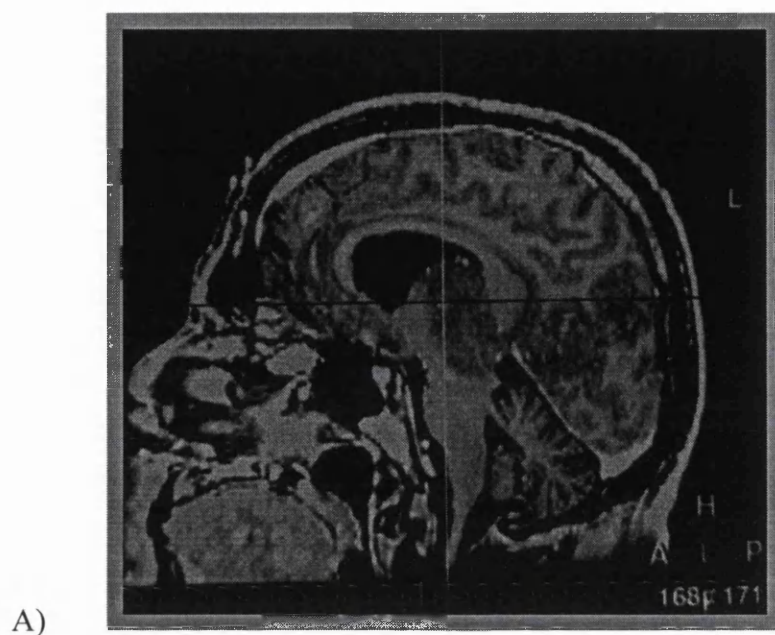
Figure 2.23: MR images acquired during the frameless stereotactic biopsy study. These sagittal images, of case 5 in the clinical series, demonstrate a) the captured intra-operative target and b) the post-operative appearance of the biopsy site.
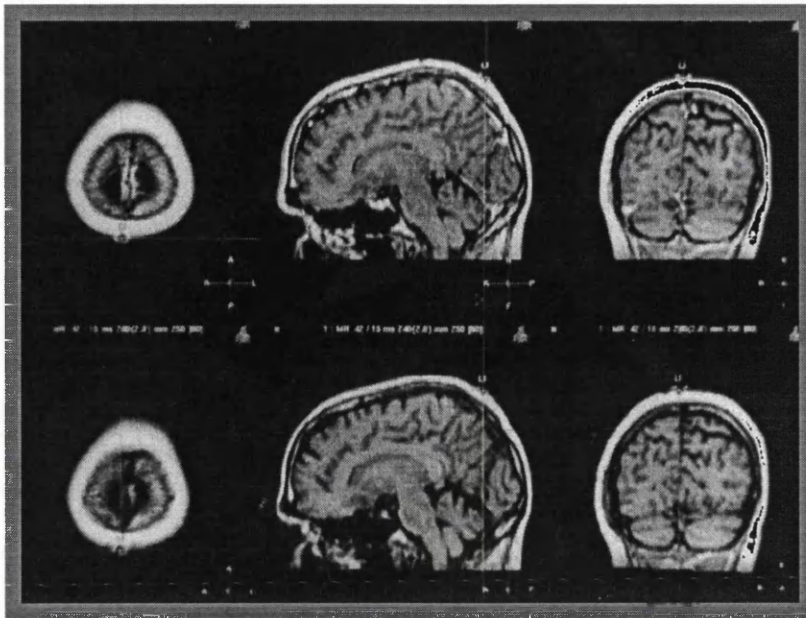
Figure 2.24: The landmark method of image data set fusion. Identical imaging protocols simplified the selection of landmarks in the pre- and post-operative image data sets on the CT/MR workstation.
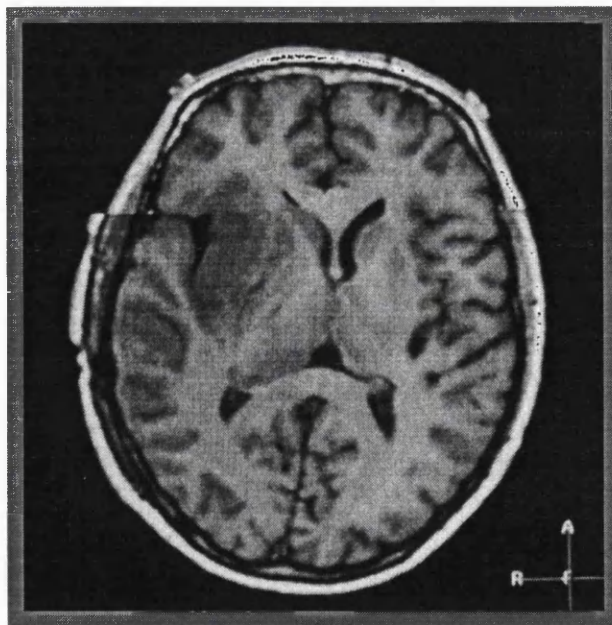
Figure 2.25: The moving curtain overlay of fused pre- and post-operative MRI scans. Note how well the cerebral structures and skull match and that post-operative swelling has distorted the skin in the lower image.

the position from which the biopsy core had been retrieved. In each case the needle stop had been positioned so as to bring the target to the centre of the side window, so the biopsy site co-ordinates were taken as the centre of this elliptical cavity. The difference between the target and biopsy site co-ordinates was calculated in millimetres, providing the error of localisation in linear x, y and z values. Euclidean errors were calculated from these according to the formula:

$$V = \sqrt{(x^2 + y^2 + z^2)}$$

2.6 IMAGE-GUIDED NEUROENDOSCOPY

The envisaged method of IGN was analysed and five stages identified in the development process. These were firstly, to establish near real time tracking of the endoscope by the optical navigation system. Secondly, assessment of the accuracy of endoscope tip localisation in laboratory phantom experiments. Thirdly, evaluation of the novel instrument through a small clinical series. Fourthly, incorporation of a method for correction of the intrinsic endoscope image distortion and finally, assessment of the value of virtual endoscopy and graphic overlays on the IGN images.

2.6.1 Description of the Endoscope Equipment

The endoscope employed in this investigation was a rigid, solid lens neuroendoscope (Aesculap, Tüttlingen, Germany) of 2.6mm outer diameter (Figure 2.26). The endoscope fitted tightly into an operating carrier of 5.6mm outer diameter and locked in position, with the tip protruding from the carrier by 2-3mm. The carrier had four channels; two 1.5mm irrigation channels, the 2.6mm endoscope channel and a 2.2mm instrument channel. For insertion of the carrier into the ventricle each channel was blanked off with a trocar. The tip of each trocar was smoothed off to conform with the rounded contour of the carrier nose, to avoid snagging cerebral tissues or vessels during insertion. A coupler attached to the eyepiece of the endoscope and enabled linkage to a single chip video camera for visualisation on a TV monitor. The coupler enabled a limited range of focus with a wide depth of field. The whole carrier fitted into the channel of a frameless stereotactic instrument block, enabling the adjustable locking arm to be employed for stereotactic guidance.
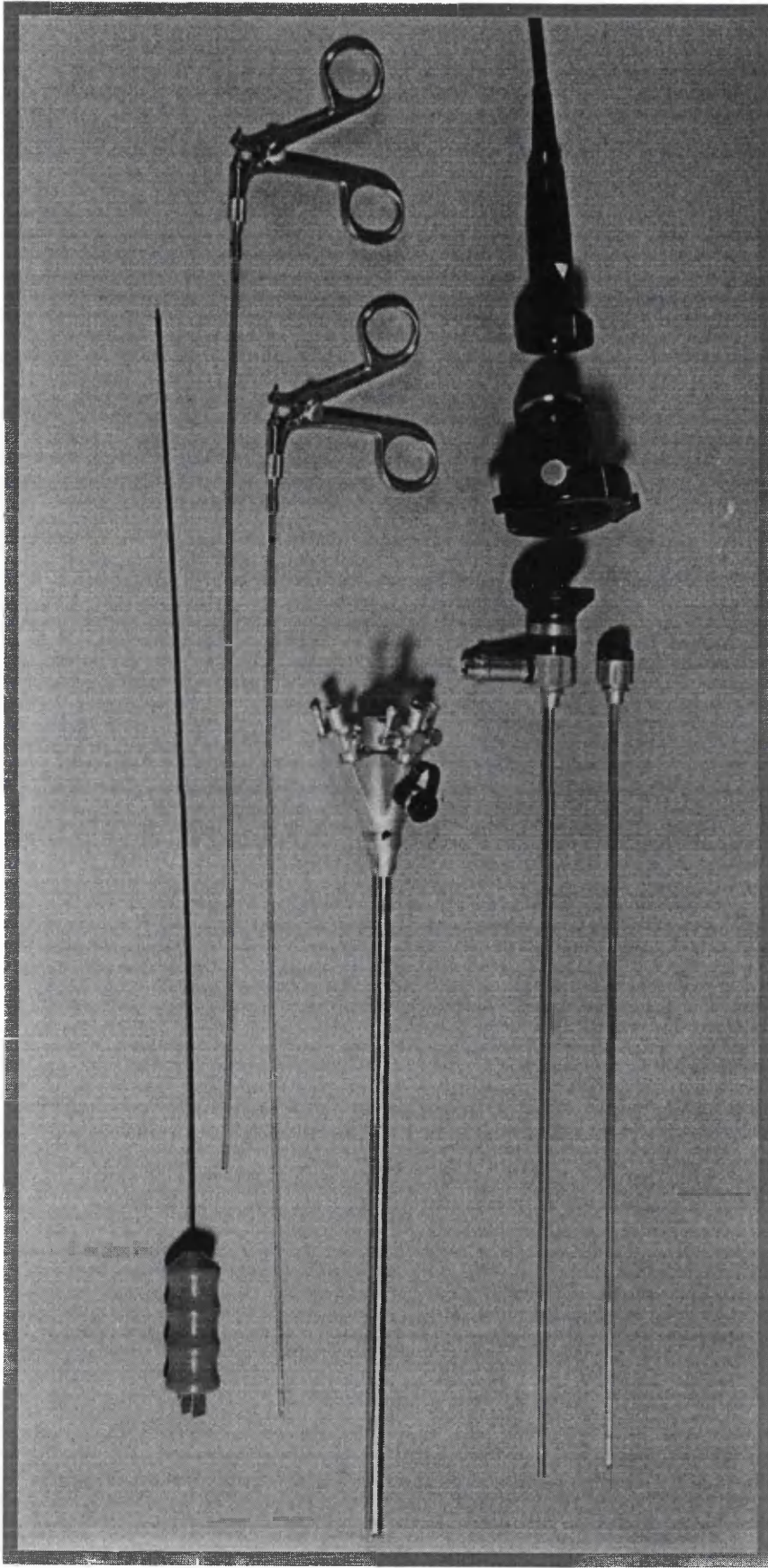
Figure 2.26: The rigid neuroendoscope set. The endoscope carrier is seen in the centre with the endoscope and trocar below. The etched white lines are visible on the coupler and camera. A selection of forceps and diathermy instruments lie above the carrier.

2.6.2 Development of the Method for Endoscope Tracking

Tracking of the endoscope tip and calculation of the orientation by the navigation system required the attachment of LED's to the endoscope. In designing the method of attachment the considerations included the need for guidance during insertion as well as during surgery, the ability to attach to a variety of rigid endoscopes and the need to accurately localise a long tip. Thus, a prototype relocatable block was designed and manufactured which carried LED's at known positions and could be attached to any rigid endoscope carrier (Figure 2.27). A model of the relationship between the LED's and the endosope tip was installed on the guidance system workstation to enable the tip position and orientation to be calculated and displayed in real time. However, this required the prototype block to be replaced on the endoscope carrier at a pre-determined position and orientation accurately whenever the system was used.

Whilst the prototype block demonstrated the ability of the system to accurately locate the endoscope tip the block was heavy, sharp edged and cumbersome, making clinical acceptance unlikely. Therefore, a second prototype LED block was developed which was constructed of plastic, was smoothly contoured, lightweight and could be sterilised in an autoclave (Figure 2.28). However, whilst the second prototype LED block was a significant improvement, replacement of either of these blocks in precisely the same position and alignment could not be guaranteed, potentially leading to errors in tip localisation and rotational orientation.

Development of the pointer learning software tool (Section 2.1.4) enabled the introduction of a method by which the relationship between the endoscope tip and LED's could be determined following each reapplication, overcoming difficulties of accurately repositioning the block. This tool require the endoscope tip to be placed in a
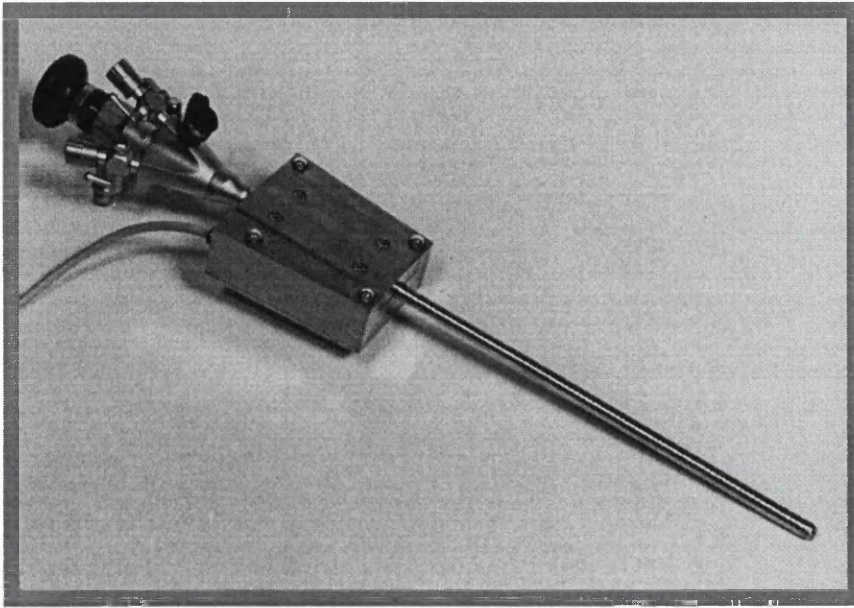
Figure 2.27: The prototype LED block mounted on the endoscope. Although this enabled accurate localisation of the endoscope tip the block was very cumbersome.
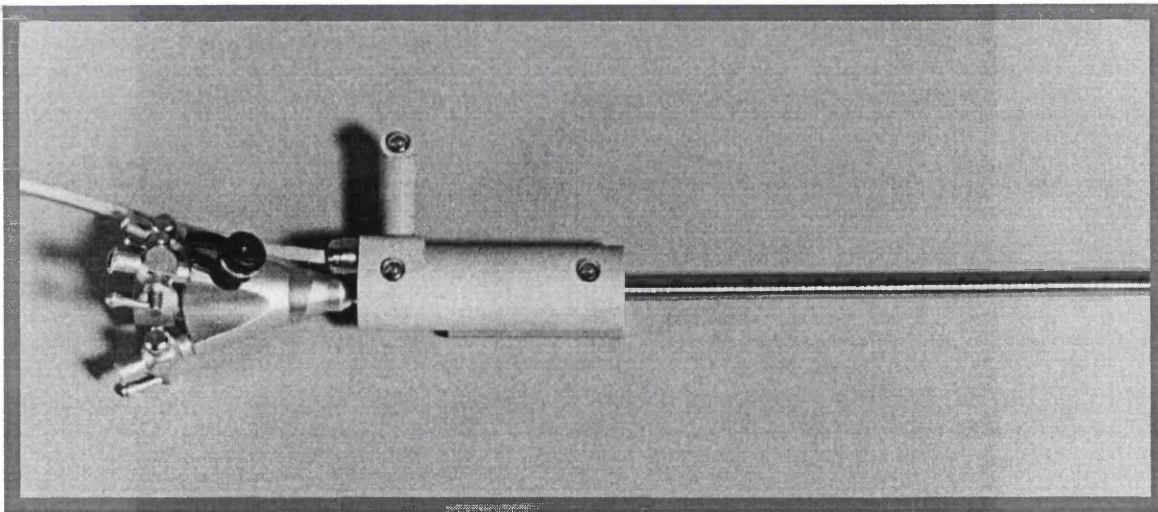
Figure 2.28: The second generation endoscope block. This was lightweight and low profile enabling tip localisation without hindering the operative procedure. The pointer-learning software tool enabled the relationship between the LED's and the endoscope tip to be derived on each occasion the block was reattached.

divot and for the endoscope to be swung around this isocentre, whilst tracked by the cameras, until the geometric relationship was solved by the computer. Because the endoscope tip was flat and such a manoeuvre could damage the delicate lens, a sharp trocar was manufactured which would lock into the endoscope channel to perform this process. The trocar dimensions ensured that the tip position corresponded precisely with the centre of the endoscope lens position (Figure 2.29).

2.6.3 Phantom Assessment of Endoscope Tracking Accuracy

The accuracy with which physical points could be localised with the tracked endoscope was determined in a series of laboratory phantom experiments. The image data sets employed were the Signa MRI, Standard Vectra MRI, Fine Vectra MRI, 2mm Sequential CT, 3mm Sequential CT and 3mm Helical CT studies of the skull phantom (Section 2.1.3). For these experiments the endoscope was replaced by the sharpened trocar to enable more precise error measurements and the targets employed were the image localiser screw attachments (Figure 2.29). The method employed was identical to that previously described for the assessment of point localisation with the standard system pointers (Section 2.2.3).

2.6.4 Clinical Evaluation of IGN

The technique of IGN was employed in five consecutive adult cases (the University Department of Neurosurgery treats an exclusively adult population) in which a neuroendoscopic approach was considered appropriate. These cases were proposed by the surgeon in charge as suitable for IGN due to their complexity and the necessity for accurate guidance (Section 3.6.4).
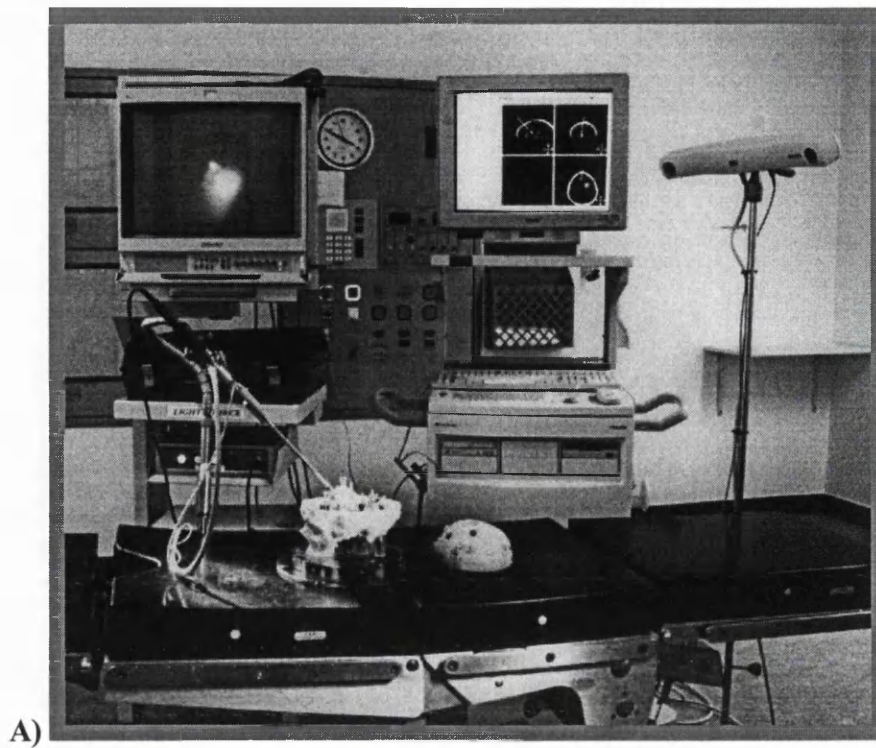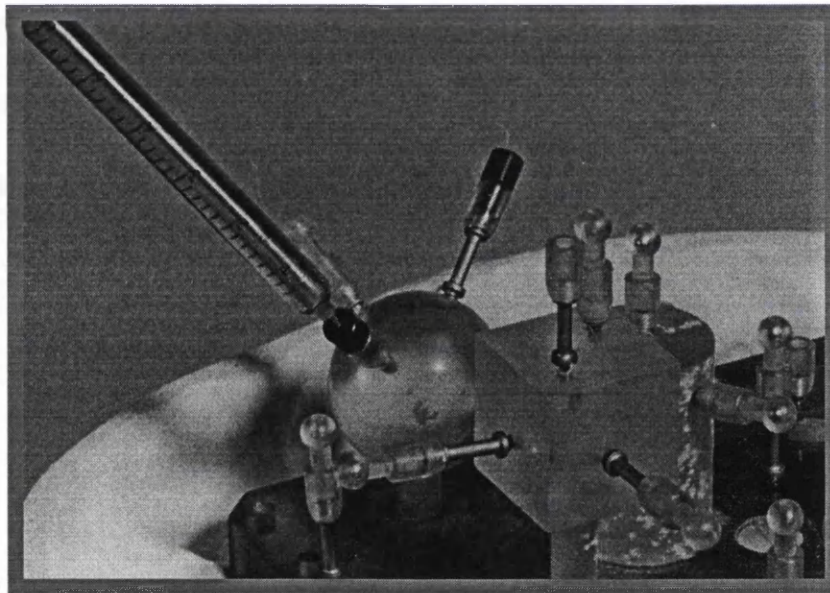
Figure 2.29: Point localisation error assessment for the tracked endoscope. A) The operating theatre layout showing the phantom, endoscope, video stack and navigation system. B) The sharpened endoscope trocar docked with a localiser cap.

2.6.5 Correction of Optical Distortion

In order to achieve precise registration between the pre-operative image data set and an intra-operative endoscopic image the distortion inherent in the endoscope image required correction. The method adopted for this was to apply the Haneishi algorithm (Haneishi et al 1995), which employs the crossing points of lines in a viewed grid pattern to reconstruct straight grid lines. Thus, a series of experiments was performed in which a regular 1mm grid was viewed with the rigid neuroendoscope.

In the first set of experiments, the endoscope was clamped perpendicular to the grid and the distance from the endoscope tip to the grid measured with micro-callipers. The endoscopic video image was captured on a PC Frame Grabber and stored as a TIFF file for later analysis. This procedure was repeated for several endoscope positions, throughout the working range of the endoscope, in air and in physiological saline. The resultant endoscope images were analysed to determine the optical axis of the endoscope. This was located through measurement of the number of pixels between intersections along each line of the grid. In addition, a graphical plot of these intersection distances over a regular grid pattern was employed to determine the nature of the optical distortion of the endoscope. This method has been widely used for the assessment of optical distortion (Smith et al 1992).

The second stage was to determine whether the algorithm would accurately correct the distorted grid image. For this purpose the intersection points in the TIFF images were detected by an intensity thresholding technique. The distortion correction algorithm was run on these points and the least cost solution that resulted in straight lines joining the intersections was determined. The resultant corrected images were assessed for regularity and symmetry by repetition of the intersection pixel distance

98

measurements and plotting of these over a regular grid. This procedure was repeated for images acquired at different distances from the grid, in air, in physiological saline and for an endoscopic image acquired at 45° to the grid.

2.6.6 Graphic Overlays and Image Reconstructions

Graphic overlays were intended to provide the surgeon with information not readily available in the endoscopic image during IGN. Such overlays could be of widely varying complexity and number. Therefore, a collection of graphical representations of anatomical and pathological features were devised, including attempts to provide three-dimensional information. For this purpose a selection of clinical images and reconstructions, derived from the data sets employed for image-guidance during the clinical evaluation phase (Section 2.3), were transferred to a computer as TIFF files. This enabled the designed graphics to be overlaid and assessed in a variety of views, structures and colours and the most appropriate solutions selected.

The accuracy with which a simple graphical overlay could represent an anatomical feature was determined in a laboratory phantom experiment. A phantom skull with internal anatomical features was imaged with 2mm Sequential axial CT and the centre of each optic nerve identified in these images. A simple graphical line representation of the optic nerves was constructed and the phantom registered with the navigation system. The tracked endoscope was brought in to visualise the internal features of the phantom and the resultant endoscope images captured with the frame grabber. The distortion correction algorithm was applied and the graphics overlay applied to the corrected image. The distance of this line from the centre of the optic nerves was estimated to determine the accuracy of this method.

In addition to the overlay experiments, segmentations of the ventricular surface anatomy were performed, on the laboratory CT/MR image workstation, for a number of pre-operative image data sets. This enabled the usefulness of constructing a virtual endoscopic view to be assessed.

2.7 STATISTICAL METHODS EMPLOYED IN THE

ANALYSIS OF RESULTS

The raw data derived from the experiments described were entered into spread sheets for analysis (Microsoft Excel 97). Simple descriptive statistics were derived for each test, imaging modality and subgroup. The distribution of the results in each of these data sets was also displayed via a frequency histogram. The descriptive statistics employed are the mean and standard deviation for normally distributed, continuous data and the median with range otherwise.

Results were analysed for correlations and significance as a whole and when segregated according to subgroups. The statistical tests of significance employed were the unpaired two-tailed t-tests for normally distributed data and Wilcoxon Ranked-Sum test for non-continuous data (significance was regarded to have been established when $p < 0.05$). The Levene test was employed to determine whether there was equal variance between the two sets to be compared for significance. If the Levene test was significant, and the hypothesis of equal variance was therefore rejected, the Wilcoxon ranked sum test was employed. If the Levene test was not significant and the data was continuous, the two-tailed T-test was employed. Correlations were recognised when the r-value exceeded 0.5 and the p-value was less than 0.05. Standard statistical computer software packages were employed namely; Minitab for Macintosh, Microsoft Excel 97 and SPSS.

RESULTS

3.1 LABORATORY STUDIES OF NAVIGATION SYSTEM ACCURACY

Investigations was undertaken to determine the accuracy and suitability of the chosen prototype neuronavigation system prior to clinical introduction and adaptation for the task of image-guided neuroendoscopy. These experiments were designed to reproduce the planned clinical processes, to determine the magnitude of localisation error and to assess the impact of imaging modality, pointer design and pointer orientation on localisation accuracy.

3.1.1 Registration

The accuracy of image data set to phantom registration and the impact of imaging modality on this were assessed via the resultant RMSE of registration. Six registrations were performed for each of the image data sets, comprising the standard protocol Signa, standard Vectra and fine Vectra MR images and 2mm sequential axial, 3mm sequential axial and 3mm helical CT images. The mean RMSE of registration for all image data sets and tests was 1.4mm (SD 0.2mm).

When the imaging modalities were compared the mean RMSE of registration with CT data was found to be significantly lower than for MR data ($p<0.0001$). Furthermore, when each of the imaging data set subtypes was compared significant differences were found. Thus, the registration RMSE for 2mm sequential axial CT was found to be significantly lower than that for 3mm helical CT images ($p=0.48$), the RMSE of registration with the Signa data was significantly higher than with either the

Standard Vectra (p<0.0001) or the Fine Vectra data (p=0.002) and registration with the Standard Vectra was significantly more accurate than with the Fine Vectra data sets (p<0.0001) (Appendix II.i.i, Appendix III.i.i).

The lowest mean registration RMSE for any image subtype (0.73mm) was achieved with 2mm sequential axial CT images (Table 3.1, Figure 3.1). Whilst within the CT subgroups error rose with slice thickness, the same pattern was not evident with

TABLE 3.1

Phantom registration accuracy results according to imaging modality.

Imaging Protocol	Mean RMSE (mm)	S D (mm)	Range (mm)	Mean No. Fiducials	Mean Nearest Fiducial (mm)
Standard Vectra MRI	1.06	0.15	0.9-1.3	9.0	1.0
Fine Vectra MRI	1.42	0.19	0.9-1.7	7.7	1.3
Signa MRI	1.67	0.20	1.2-1.9	8.7	1.5
All MRI	1.39	0.31	0.9-1.9	8.47	1.3
2mm axial CT	0.73	0.19	0.4-1.0	7.0	0.5
3mm axial CT	0.91	0.20	0.6-1.3	7.0	0.8
3mm helical CT	0.89	0.14	0.7-1.1	7.0	0.6
All CT	0.84	0.19	0.4-1.3	7.0	0.6
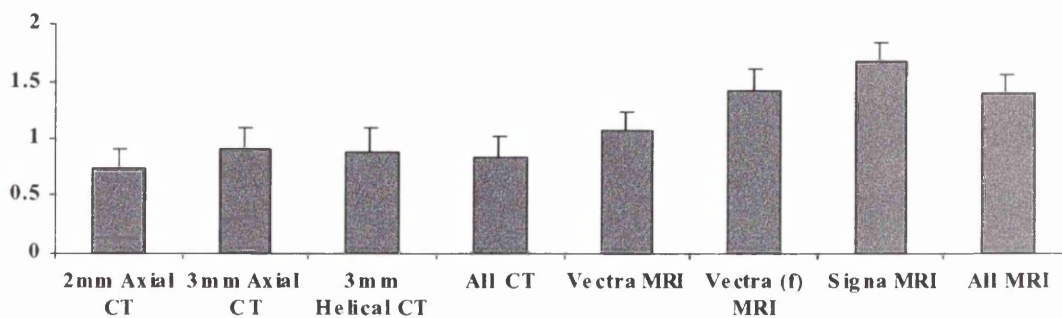
Figure 3.1: Histogram of mean registration RMSE according to image protocol.

MRI. Although each MRI data set subtype produced significantly different results the expected rise in RMSE with increasing voxel size was reversed.

When the RMSE of registration was examined for the number of fiducial markers employed in the registration process no significant difference was found between the accuracy of registration with 6 versus 11 fiducials within any of the MRI imaging data subsets (Table 3.2).

TABLE 3.2

Results of registration with 6 and 11 fiducials. The mean RMSE of registration is given in each case in millimetres.

Imaging Protocol	6 Fiducials	11 Fiducials
Standard Vectra	1.1	1.1
Fine Vectra	1.6	1.5
Signa	1.8	1.8

3.1.2 Point Localisation

In these experiments the error of point localisation was determined for three sets of physical targets in the phantom. These were the implanted image localisers, the base plate holes and the spare fiducials (not employed for registration). The mean overall error of point localisation for all target types and all data sets was found to be 1.6mm (SD 0.7mm). The mean error for all CT-directed localisation tests (0.8mm, SD 0.4mm) was significantly lower ($p < 0.0001$) than that for all MRI-directed tests (1.8mm, SD 0.7mm). When the mean error of localisation for image subtypes was analysed the 2mm Sequential CT images were found to be significantly more accurate than either the 3mm

Sequential (p=0.012) or the 3mm Helical CT data sets (p=0.009). Similarly, comparison of the MRI subtypes showed that the mean error of localisation with Standard Vectra images was significantly lower than that associated with both Fine Vectra (p<0.0001) and Signa data sets (p<0.0001) (Appendix III.i.ii).

Examination of the results for determination of localisation error with the implanted image markers (Table 3.3, Figure 3.2) revealed that the mean error of

TABLE 3.3

Results of the image marker point localisation assessments.

Imaging Protocol	Pointer	Mean Error (mm)	SD (mm)
Signa	S	1.5	0.5
	L	1.9	0.4
	B	2.0	0.6
	All	1.8	0.6
Standard Vectra	S	2.0	0.5
	L	2.2	0.5
	B	2.4	0.6
	All	2.1	0.6
Fine Vectra	S	1.5	0.6
	L	1.7	0.6
	B	2.4	0.7
	All	1.9	0.7
All MRI	All	1.9	0.6
2mm Axial CT	S	0.7	0.4
3mm Axial CT	S	0.8	0.5
3mm Helical CT	S	0.8	0.5
All CT	S	0.8	0.4
All Data Sets	All	1.6	0.8

S = Short straight pointer
L = Long straight pointer
B = Bayonet pointer (long)
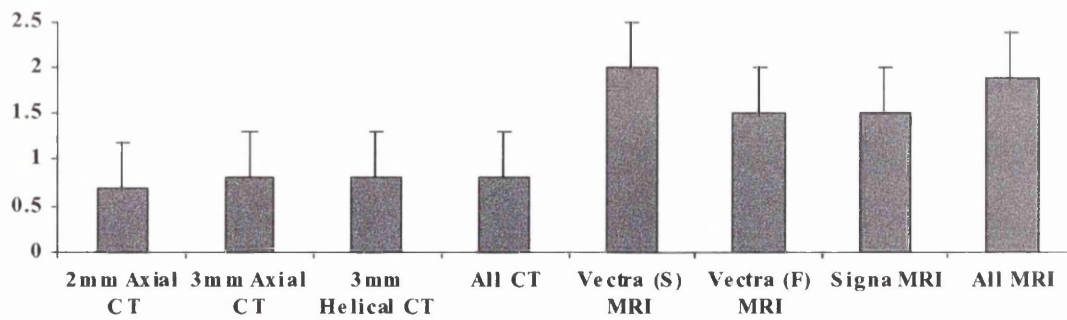
Figure 3.2: Point localisation results; image localiser screws.

localisation with MRI was again significantly greater than that for CT (p<0.0001). As would be expected analysis of the localisation errors within the CT-directed sets showed that localisation with the 2mm Sequential scans was significantly more accurate than with either the 3mm Sequential (p=0.012) or the 3mm Helical data sets (p=0.009). Similarly, examination of the results for MRI-directed localisation revealed that the errors associated with Signa and Fine Vectra data sets were significantly lower than that accompanying Standard Vectra localisation (p<0.001 and p=0.001 respectively) (Appendix II.i.ii).

Analysis of the error of localisation of the image markers for individual pointer types also proved informative. Thus, across all scan subtypes the mean error of localisation was significantly lower when the short pointer was employed compared to both the long straight pointer (p=0.015) and the bayonet pointer (p=0.0012). However, whilst the mean error of localisation with the bayonet pointer was greater than with the long pointer in each test, this did not reach statistical significance. This pattern of pointer accuracies was also evident within individual scan subtype results.

The tests of localisation error employing spare fiducial markers revealed a slightly different pattern to the image marker experiments (Table 3.4, Figure 3.3). In

TABLE 3.4

Results of spare fiducial localisation error assessments.

Imaging Protocol	Pointer	Mean Error (mm)	SD (mm)
Signa MRI	S	1.7	0.8
	L	1.4	0.8
	B	1.6	0.9
	All	1.6	0.8
Fine Vectra MRI	S	1.7	0.6
	L	1.6	0.7
	B	1.4	0.9
	All	1.6	0.7
Standard Vectra MRI	S	0.9	0.5
	L	0.9	0.3
	B	1.4	0.5
	All	1.1	0.5
All MRI	All	1.4	0.7

S = Short straight pointer; L = Long straight pointer; B = Bayonet pointer (long)
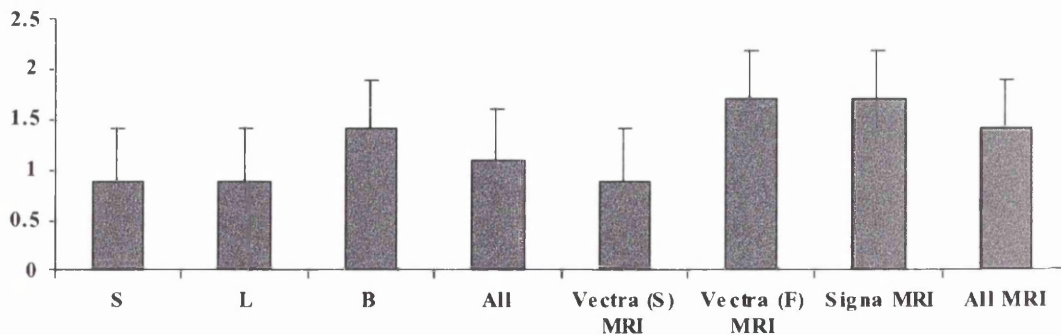
Figure 3.3: Point Localisation results; spare fiducial tests.

both fine Vectra-guided and Signa-guided experiments the registration error was significantly greater than in standard Vectra guided ones (p<0.0001 in each case). In addition, localisation error was found to be significantly greater in fine Vectra-guided cases than Signa-guided ones (p<0.0001). The pattern of localisation errors for individual pointer types was also somewhat different for this series. Whilst the mean error of localisation with the bayonet pointer was found to be greater than that for either the long or the short pointer there was no significant difference between the latter pointer subtypes (Appendix II.i.iv).

The series of tests of localisation accuracy employing the baseplate holes as targets and with MRI guidance revealed an overall mean error of localisation of 1.7mm (Table 3.5, Figure 3.4). Analysis of the results according to imaging subtype revealed that the standard Vectra images were associated with the lowest mean localisation error and the fine Vectra images with the highest. Comparison of the image subtypes revealed that localisation errors were significantly lower for standard Vectra-guided localisation than Signa-guided tests (p<0.0001) and that Signa-guided localisation was significantly more accurate than fine Vectra localisation (p<0.0001). Thus, standard Vectra guidance was significantly more accurate than fine Vectra guidance (p<0.0001). Within each imaging data set for the baseplate holes localisation series accuracy was significantly better with the short pointer than with either the long (p<0.0001) or bayonet pointers (p<0.0001). In addition the error of localisation with the long pointer was found to be significantly lower than that for the bayonet pointer in each image subtype examined (p<0.001) (Appendix II.i.iii).

TABLE 3.5

Results of baseplate hole localisation error assessments.

Imaging Protocol	Pointer	Mean Error (mm)	SD(mm)
Signa MRI	S	1.3	0.2
	L	1.6	0.3
	B	2.2	0.3
	All	1.7	0.5
Standard Vectra MRI	S	0.9	0.4
	L	0.9	0.3
	All	0.9	0.3
Fine Vectra MRI	S	1.7	0.3
	L	2.0	0.3
	B	2.6	0.4
	All	2.1	0.5
All MRI	All	1.7	0.6

S = Short straight pointer

L = Long straight pointer

B = Bayonet pointer (long)
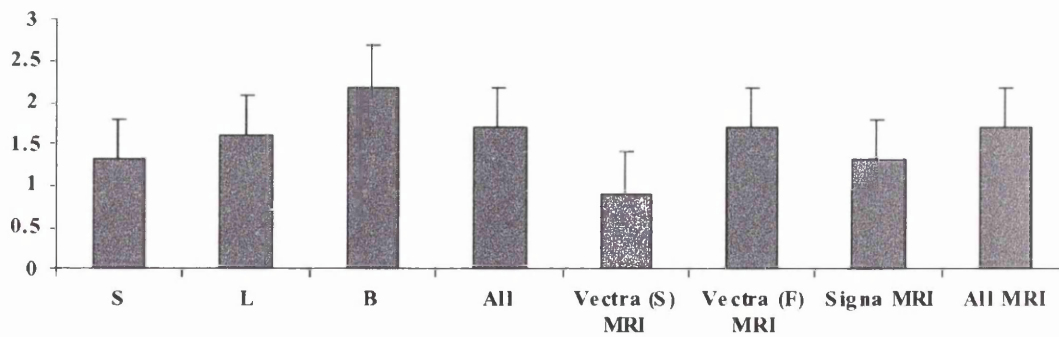
Figure 3.4: Point localisation results; baseplate hole experiments.

3.1.3 Reproducibility of Point Localisation

Repeated localisation of the same physical point revealed a remarkably low spread of values for each of the pointer subtypes (Table 3.6, Appendix III.i.iii). However, the bayonet pointer showed a significantly greater spread of values than

either the short or long pointers (p=0.03 and p<0.0001 respectively), and the long

pointer showed a significantly wider spread than the short pointer (p<0.0001)

(Appendix II.i.v).

TABLE 3.6

Results of reproducibility test according to pointer type

Pointer	S D (mm)	Number of Tests
Short Straight	0.02	63
Long Straight	0.05	138
Bayonet	0.06	105

3.1.4 Detection of Pointer Movement

The mean micrometer advance required to alter the detected pointer position was

found to be 0.4mm (SD 0.1mm). No significant difference was detected for this value

when measurements were carried out at different parts of the working volume of the

cameras. Similarly, there was no significant difference between the pointer subtypes, the

handles and LED arrangements of the pointers being identical (Appendix II.i.vi,

Appendix III.i.iv).

3.1.5 Effect of Pointer Rotation upon Localisation

The effect of pointer rotation upon position detection was assessed through

repeated pointer localisation at rotations of 45° and 90° in each direction from a reference

position (Table 3.7, Figure 3.5). This reference position was defined as the

perpendicular alignment of pointer and camera in the centre of the working volume.

Repeated pointer localisation determined the reference position to be 50.44mm from the

nearest defined image marker with a SD of 0.8mm. Although the discrepancy between

the reference position and the mean localisation position for each angle of

TABLE 3.7

Results of pointer rotation assessment.

Angle of Rotation	Mean Position	SD (mm)	Offset (mm)
0°	50.44	0.08	N/A
45° Clockwise	50.63	0.06	0.19
45° Anti clockwise	50.60	0.06	0.16
90° Clockwise	51.41	0.11	0.97
90° Anticlockwise	50.98	0.05	0.54
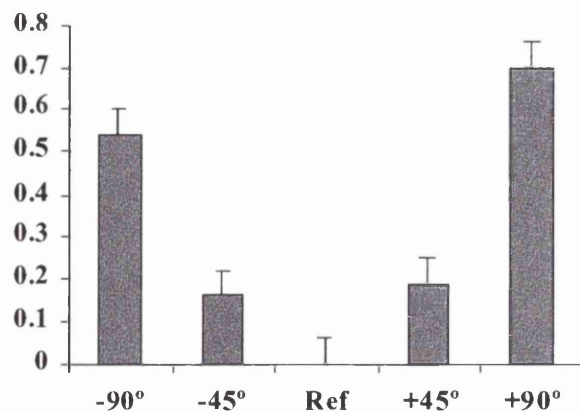
Figure 3.5: Graph of pointer rotation experiment results. The mean pointer

localised position with rotation away from a reference position.

rotation was found to be small (0.16-0.97mm) the SD of each was very low. Thus, for

each rotation the mean localised position was significantly different from the reference

position (p<0.0001 in all cases).

3.2 CLINICAL EVALUATION OF THE NEURO-

NAVIGATION SYSTEM

The prototype neuronavigation system was evaluated as a clinical instrument via a series of 100 image-guided neurosurgical procedures. These operations were undertaken for diverse surgical pathologies, were performed by several different surgeons and a variety of surgical approaches were employed. Data pertaining to clinical status, imaging, operating time, system accuracy and clinical outcome were collected in the Evaluation Protocol booklet.

3.2.1 Patient Data

The 100 consecutive image-guided cases were performed on 60 males and 40 females (Table 3.8). The median age of these patients was 44 years (range 15-77 years). The pathological diagnosis was glioma in 27 cases, meningioma in 26, epilepsy in 12, vascular malformations in 7 and metastasis in 5 (Appendix II.ii.i, Appendix III.ii.i). A variety of miscellaneous others including chordomas, neuromas, haemangioblastomas, cysts and inflammatory granulomas constituted the remaining 23 cases. The median number of fiducials applied for registration was 9 (range 5-13) , which resulted in a mean registration RMSE of 3.7mm (SD 1.1mm). The median lesion diameter was 39.6mm (range 2.5-105.6mm, IQR 31.6mm) and the median duration of surgery was 2.25hrs (range 0.83-8.83hrs, IQR 1.50hrs). The operations were supratentorial in 77, posterior fossa in 22 and cervical in 1. There were no intra-operative system failures or evidence of gross system inaccuracy. The operating surgeons comprised 5 Consultant

Neurosurgeons, 1 Consultant ENT Surgeon, 4 Senior Registrars and 2 Registrars in Neurosurgery.

TABLE 3.8

General characteristics of 100 image-guided surgery cases.

Operations	100
Median Age	44
Mean Registration RMSE (mm)	3.7
Median number of fiducials	9
Male : Female Ratio	1.5 : 1
Glioma (%)	27
Meningioma (%)	26
Epilepsy (%)	12
Vascular Malformation (%)	7
Metastasis (%)	5
Miscellaneous (%)	23

3.2.2 Visual Analogue Scales

The visual analogue scale ratings, defined by the operating surgeon after each case, were converted into numerical values from −5, indicating dissatisfaction or perceived disadvantage to +5, denoting satisfaction or advantage (Appendix II.ii.ii, Appendix III.ii.ii). The resultant median score for each question over the 100 clinical cases is displayed in table 3.9 and the proportion of positive, negative and equivocal values are demonstrated in the pie charts for each question (Figure 3.6). Thus, the questions, and therefore the perceived attributes of the system, could be ranked in order of median value. The highest median score was given in reply to question 3, next highest

to question 6, then questions 8, 2, 1, 5, 10, 9, 7 and lastly 4. This indicates a good impression of the system for lesion localisation, enhancing surgical confidence, overall usefulness, surgical planning and appreciation of surgical anatomy. The scores indicate a moderate perceived advantage with navigation for the safety of surgery, for the frameless stereotaxy tool holder and the user interface and a minimal advantage in the duration of surgery. Overall the use of neuronavigation was thought not to have altered the extent of tumour removal.

TABLE 3.9

Visual Analogue Scale results.

Question	Median Score	IQR	Min Score	Max Score	Ranking
1	2.0	2.4	-0.8	5.0	5
2	2.5	2.5	-1.3	5.0	4
3	3.0	2.4	-2.0	5.0	1
4	0.0	2.6	-3.0	5.0	10
5	2.0	1.8	-2.7	5.0	6
6	2.7	2.8	-1.0	5.0	2
7	0.2	2.1	-3.2	4.6	9
8	2.6	2.2	-3.9	5.0	3
9	1.6	1.9	0.0	4.8	8
10	1.6	2.6	0.0	4.7	7

3.2.3 Duration of Surgery and Navigation Time Analysis

In the subset of 39 cases for which detailed measurement of time requirements for neuronavigation was undertaken the median duration of setting up in the operating theatre was found to be 3.5min (Table 3.10). The median time required for patient

Figure 3.6: Pie charts of visual analogue scale questionnaire results. Proportions of positive, negative and equivocal responses are given.

☐ Advantageous   ▨ Ambivalent   ■ Detrimental

1. Appreciation of Anatomy
89%
1% 10%

2. Effect on surgical planning
88%
2% 10%

3. Localisation of the lesion
91%
1% 8%

4. Extent of resection
52%
46%
2%

5. Safety of surgery
90%
2% 8%

6. Effect upon confidence
85%
6% 9%

7. Duration of surgery
53%
12%
35%

8. Overall opinion
95%
1%4%
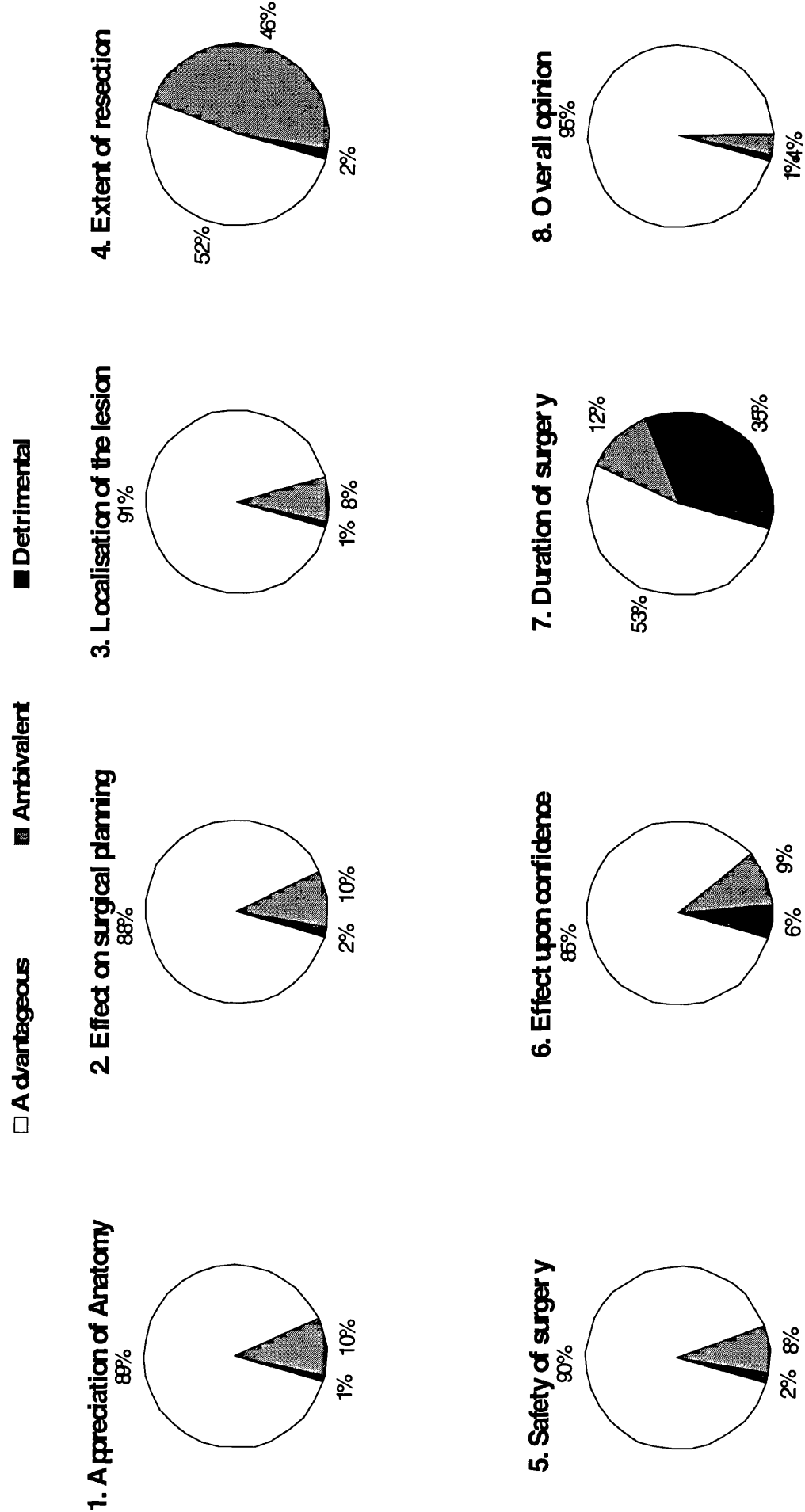
registration, following positioning by the surgeon, was 5.0min. Planning of the skin

incision by the surgeon with the navigation pointer took a median of 1.2min. During

surgery, i.e. from skin incision to skin closure, the neuronavigator was used by the

surgeon for guidance with a median frequency of 7 episodes. The median duration of

TABLE 3.10

Comparison of Image-Guided Vs Conventional Operations.

	Median	Range
Neuronavigation:		
Set-up Time	3.5min	2-6min
Registration time	5.0min	2-12min
Incision Planning	1.2min	0.4-3.3min
Fallback Marker Storage	1.7min	0.6-9.2min
Number of Uses by Surgeon	7	2-15
Duration of Each Usage	1.1min	0.2-6min
Total Use By Surgeon	7.0min	1.2-29.5min
Total Theatre Time	199min	55-590min
Matched Conventional Cases:		
Total Theatre Time	208min	60-470min

each episode was 63sec resulting in a median total duration of intraoperative

navigational assistance of 7.0min. Registration and verification of the intraoperative

fallback markers required an additional 1.7min.

The median duration of the surgical procedures alone in the 39 image-guided

cases was 173 min. Therefore, neuronavigation represented a median 5.2% of the

surgical operation time. This percentage of operation time was found to significantly

lower in meningioma surgery (3.2 min) than in all other operations together (8.8 min,

p<0.0001). The frequency of intraoperative usage was also significantly lower in meningioma operations (median 4.7 occasions) than in other cases (median 7.6 occasions, p<0.05).

The results of the matched control comparison between duration of surgery with neuronavigation and without showed some remarkable similarities between the two groups. The median duration of surgery for the whole series of 100 image-guided cases was 3 hrs 19 min. The median duration of surgery for the matched conventional cases was 3 hrs 28 min. No statistically significant difference was found between the duration of neuronavigational and conventional cases.

3.2.4 Accuracy in the Clinical Environment

Analysis of the registration RMSE, mean nearest marker test results and number of fiducials employed for registration in the 100 clinical cases (Table 3.11) revealed little difference between the imaging modalities of Signa and standard Vectra which

TABLE 3.11

Clinical registration RMSE according to imaging modality.

Imaging Protocol	Mean RMSE (mm)	Mean Nearest Marker (mm)	No. cases	Median No. Fiducials
Vectra MRI	3.6	3.1	53	9
Signa MRI	3.7	3.3	46	8
2mm Axial CT	3.3	3.3	1	9
All	3.6	3.2	100	9

were employed. Thus, the overall mean RMSE of registration was 3.6mm (SD 1.1), with no significant difference between the image types. The manual check of the error associated with each registration fiducial, the nearest image marker output, revealed a mean error of 3.2mm (SD 1.2). However, when the error associated with each individual fiducial position, as described in the Clinical Evaluation Protocol (Appendix I), was examined some marked variations were revealed (Table 3.12, Figure 3.7). Thus, the lowest errors were found in the standard positions of vault and forehead fiducial

TABLE 3.12

Nearest Marker results according to fiducial number.

Fiducial No.	Mean Offset (mm)	SD (mm)
1	2.9	1.2
2	2.4	1.1
3	2.7	1.4
4	2.7	1.2
5	3.2	1.4
6	3.2	1.6
7	3.3	1.7
8	3.6	1.7
9	3.6	1.6
10	3.3	1.6
11	3.7	1.5
12	3.7	1.7
13	3.7	2.1
14	3.7	1.6
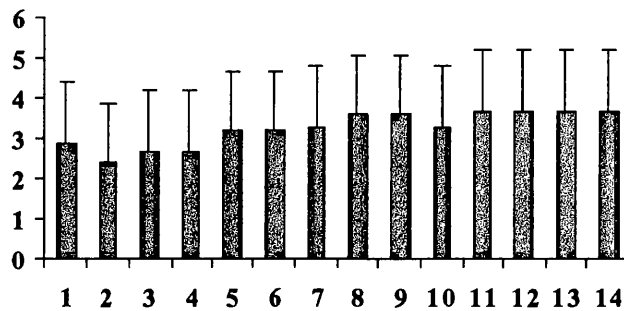
Figure 3.7: Graph of mean error associated with each fiducial position.

occipital placements (positions 6-9) and the greatest errors with unusually low and

posterior placements (positions 11-14). The low error associated with position 10 is

placement (positions 1-5), intermediate errors with the standard mastoid and explicable

through recognition that this fiducial was usually placed on the vault, overlying the

region of interest, a relatively immobile and easily defined site.

3.3 POST-IMAGING BRAIN DISTORTION

This study was undertaken to quantify brain shifts during open cranial surgery, determine correlations between these shifts and pre-operative image characteristics and to assess the impact of post-imaging brain distortion on Image-Guided Neuroendoscopy. Shift of the cortex on opening, the deep tumour margin and the cortex at completion were measured during 48 operations. Pre-operative images were examined for the presence of oedema and for measurement of tumour volume, midline shift and depth of the lesion below the skin surface. Results were analysed for all cases together and separately for four pathological groups comprising 13 meningiomas (Group I), 18 gliomas (Group II), 11 non-glial intra-axial lesions (Group III) and 6 skull base lesions (Group IV).

3.3.1 Pre-Operative Image Analysis

The measurements of lesion volume, midline shift, distance below skin surface and incidence of oedema, determined from the pre-operative MR images, revealed patterns particular to each pathological Group (Table 3.12, Figure 3.8, Appendix II.iii.i, Appendix III.iii.i). Thus, the volume of Group III (non-gliomatous intra-axial) lesions was found to be significantly lower than the volume of all other lesions together (p=0.021) and the extent of midline shift was found to be significantly lower in these non-gliomatous lesions than in meningiomas (p=0.011). The magnitude of midline shift was also significantly greater in meningiomas than in all other groups together

TABLE 3.13 *Pre-operative image characteristics by pathological group.*

		All 48 (n=48)	I (n=13)	II (n=18)	III (n=11)	IV (n=6)
Volume (ml)	Median Range IQR	13.4 0.5 – 140.5 33.7	27.0 5.3 – 76.4 31.0	8.6 0.9 – 140.5 37.3	3.9 0.5 – 40.3 10.5	8.5 4.7 – 47.5 25.0
Midline shift (mm)	Median Range IQR	3.6 0.0 – 19.9 7.25	6.8 1.8 – 19.9 5.0	3.3 0.0 – 12.9 7.6	0.0 0.0 – 7.6 3.9	3.6 0.0 – 8.3 1.8
Depth below skin (mm)	Median Range IQR	36.5 14.1 – 71.9 21.4	30.5 14.1 – 43.6 12.3	33.8 23.8 – 53.3 14.3	58.3 22.9 – 71.9 22.0	52.6 21.1 – 66.1 17.7
Oedema	% with	60	100	67	36	17
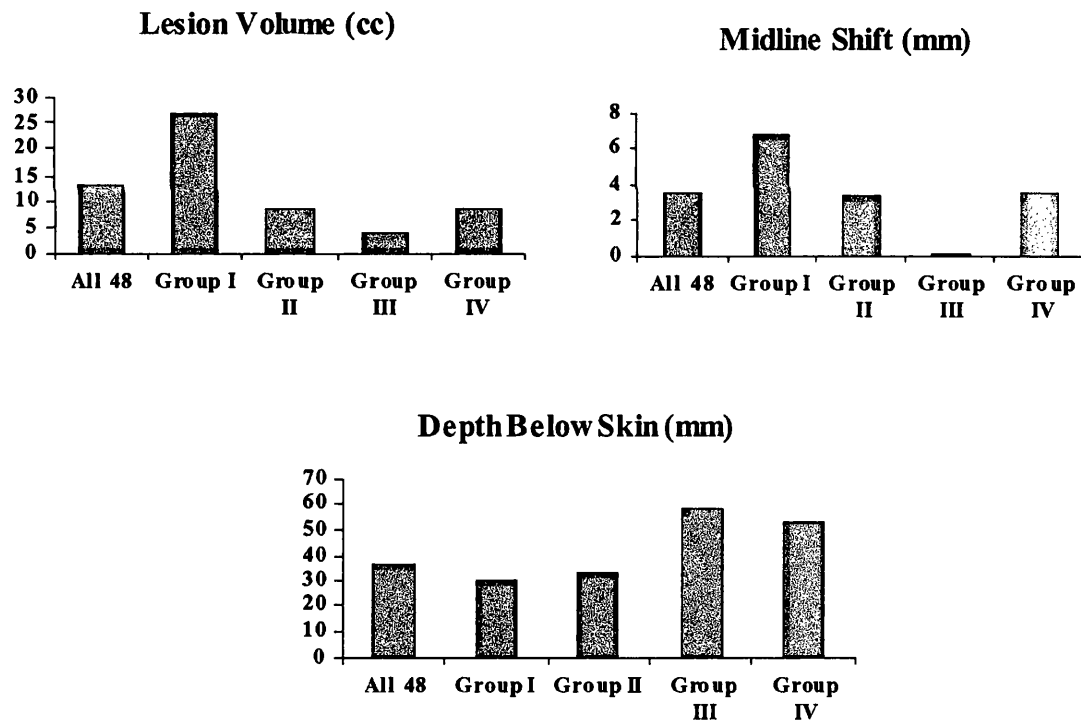
Figure 3.8: Bar charts of the median values for the pre-operative imaging characteristics

analysis. Values are displayed according to pathological group.

124

(p=0.031). Not surprisingly, the distance below the skin surface was found to be significantly lower in meningiomas than in all other groups together (p=0.0007). Similarly, the frequency of reactive oedema was significantly greater in meningiomas than gliomas (p<0.02) and in meningiomas when compared with all other groups together (p<0.001).

3.3.2 Magnitude of Post-Imaging Brain Distortion

Intra-operative measurement of brain shift revealed a mean corrected shift of the cortex on opening for all 48 cases of 4.6mm (SD 4.0mm), mean shift of the deep tumour margin of 5.1mm (SD 5.8mm) and mean shift of the cortex at completion of 6.7mm (SD 5.7mm) for all 48 cases (Table 3.13, Appendix II.iii.ii, Appendix III.iii.ii).

TABLE 3.14

Magnitude of post-imaging brain distortion according to pathological group.

	All (n=48)	I (n=13)	II (n=18)	III (n=11)	IV (n=6)
Shift of cortex on opening	4.6	4.3	5.8	3.7	2.0
S D	4.0	3.2	5.1	2.9	1.4
Shift of deep tumour margin	5.1	10.0	3.5	2.4	1.2
S D	5.8	6.5	4.2	4.3	1.5
Shift of cortex at completion	6.7	9.4	4.2	9.4	1.1
S D	5.7	6.9	3.0	4.8	1.9

Thus, the overall magnitude of post-imaging brain distortion was found to rise through the course of the operations. However, starkly different patterns were revealed when the shift data was analysed separately for each pathological group (Figure 3.9, 3.10).

Shift of cortex on opening

Shift at depth

Shift of cortex at completion
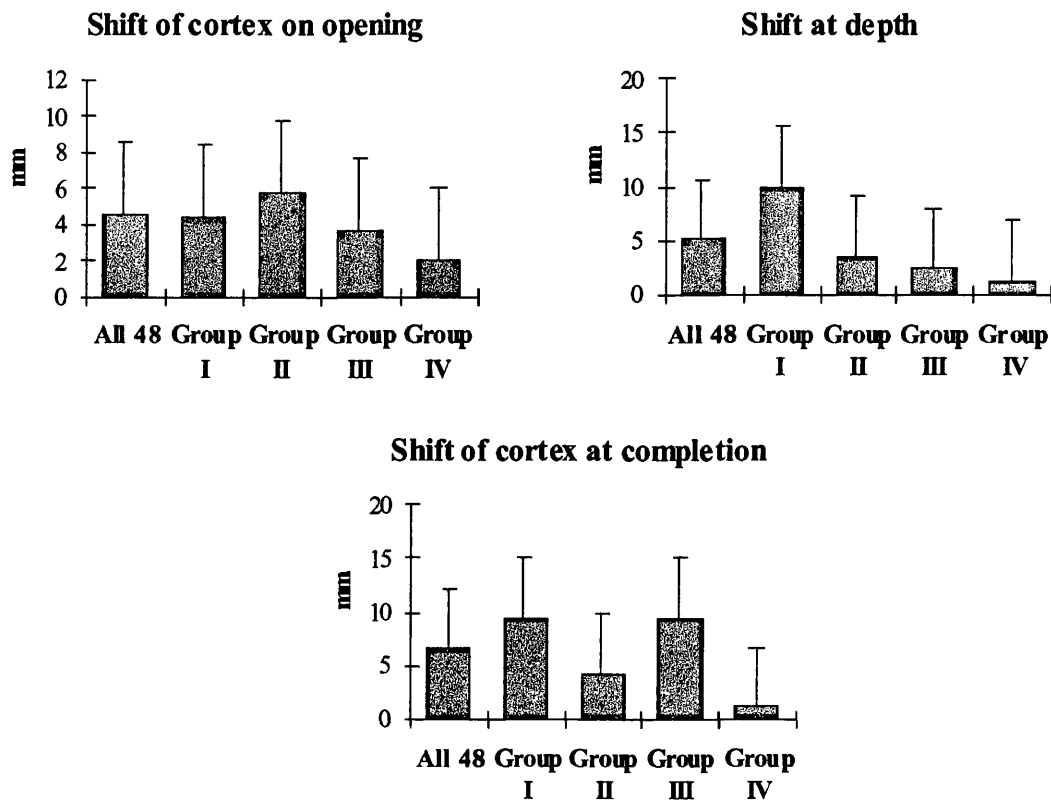
Figure 3.9: Bar charts of mean brain shifts according to pathological group. These demonstrate the differences in shifts revealed for the cortex and depth measurements.
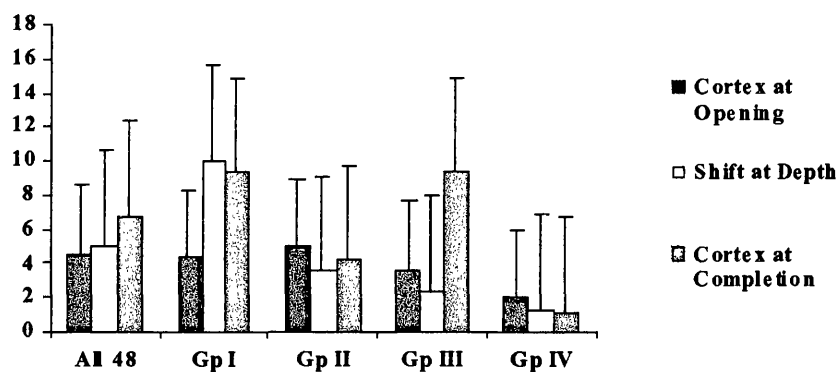
Figure 3.10: Bar chart of brain shift data to demonstrate the different patterns of shift within pathological groups.

Thus, the greatest of all shifts (mean 10.0mm) was found to be that for shift of the deep

tumour margin in meningiomas. This was significantly greater than both deep shift in all

other groups together (p=0.032) and shift of the cortex on opening in gliomas (p=0.015)

(Table 3.15). Shift of the cortex at completion in meningiomas was also significantly

greater than shift of the cortex on opening in that group (p=0.041).

Table 3.15

Summary of the differences in brain shift between pathological groups.

Pathology Group	Larger Variable	Vs.	Pathology Group	Smaller Variable	p value
I	Shift at depth	Vs.	II	Shift at depth	0.007
I	Shift at depth	Vs.	All others	Shift at depth	0.0032
I	Cortex shift at completion	Vs.	II	Cortex shift at completion	0.04
All others	Cortex shift on opening	Vs.	IV	Cortex shift on opening	0.047
All others	Shift at depth	Vs.	IV	Shift at depth	0.003
All others	Cortex shift at completion	Vs.	IV	Cortex shift at completion	0.0006
III	Cortex shift at completion	Vs.	III	Cortex shift on opening	0.014
III	Cortex shift at completion	Vs.	III	Shift at depth	0.012
I	Shift at depth	Vs.	I	Cortex shift on opening	0.015
I	Cortex shift at completion	Vs.	I	Cortex shift on opening	0.041

Importantly, in gliomas shift of the deep tumour margin and shift of the cortex at

completion were both lower than cortical shift on opening. In the non-gliomatous group

cortical shift on opening and shift at depth were significantly lower than shift of the cortex at completion (p=0.014 and p=0.012 respectively). In base of skull lesions shift at depth and shift of the cortex at completion were found to be significantly lower than in all other groups together (p=0.003 and p=0.0006 respectively).

3.3.3 Direction of Brain Shifts

The direction of each measured shift was recorded and ascribed to one of three groups comprising bulging, infalling and no shift categories. When these directions of shift were examined for each pathological group at each stage of surgery striking differences were again found between groups (Figure 3.11). The pattern for all 48 cases together was of outward bulging of the cortex on opening in 67%, infalling in 30% and remaining level in 3%. At the tumour bed there was an outward shift of the brain in 72%, infalling in 23% and no shift in 5%. At completion the direction of cortex shift was bulging in 26%, infalling in 69% and level in 5%.

Pathological groups showed differences in the pattern of direction of shifts at each stage. In Meningiomas the same pattern as for all 48 was seen in exaggerated form with bulging in 73% at opening, bulging in 100% at the deepest tumour margin and infalling of the cortex in 82% at completion. In gliomas and non-gliomatous lesions the pattern was similar to that for all 48 together and in skull base lesions, with the smallest recorded shifts, infalling of the cortex at opening was seen in the majority, minimal bulging at depth and slight infalling at completion (Figure 3.11).

Figure 3.11: Bar charts displaying the direction of brain shift at opening, at depth and at completion according to pathological group.
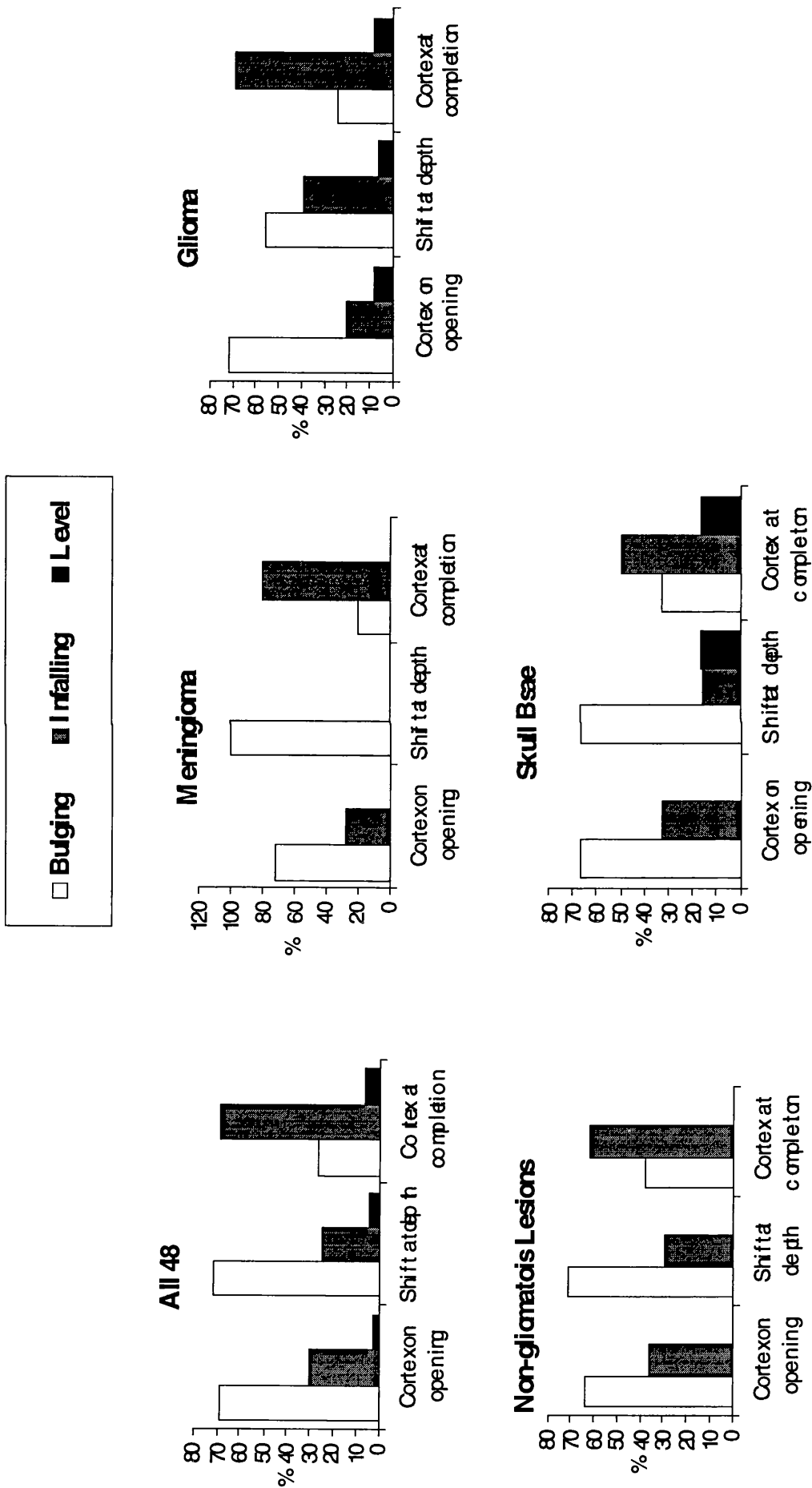
3.3.4 Correlations of Brain Shift

Analysis of the pre-operative image characteristics and brain shift measurements revealed a number of important correlations. Thus, for all 48 cases together shift of the cortex on opening was negatively correlated with distance of the lesion below the skin surface ($r=-0.41$, $p=0.012$) and was positively correlated with the presence of oedema ($p=0.013$). Shift of the deepest tumour margin was positively correlated with lesion volume ($r=0.51$, $p=0.001$), midline shift ($r=0.52$, $p=0.001$) and the presence of oedema ($p=0.035$). When each group was analysed individually further correlations were revealed. In meningiomas shift of the cortex at completion was positively correlated with tumour volume ($r=0.61$, $p=0.046$) and midline shift ($r=0.64$, $p=0.045$), and negatively correlated with distance below the skin surface ($r=0.69$, $p=0.018$). In gliomas shift of the cortex on opening was positively correlated with midline shift ($r=0.53$, $p=0.043$) and negatively correlated with distance below the skin surface ($r=0.55$, $p=0.033$). Shift at depth was positively correlated with midline shift ($r=0.56$, $p=0.024$) and tumour volume ($r=0.68$, $p=0.004$). In the non-gliomatous intra-axial lesions shift of the cortex on opening and shift at depth showed a strong positive correlation with tumour volume ($r=0.8$, $p=0.017$ and $r=0.94$, $p=0.002$ respectively) and shift of the cortex at completion was positively correlated with midline shift ($r=0.8$, $p=0.017$). In addition when the relationships between each of the shift parameters were examined shift of the cortex on opening was found to be positively correlated with shift at the deepest tumour margin ($r=0.5$, $p=0.006$) both for all 48 cases and for individual pathological groups (Figure 3.12).
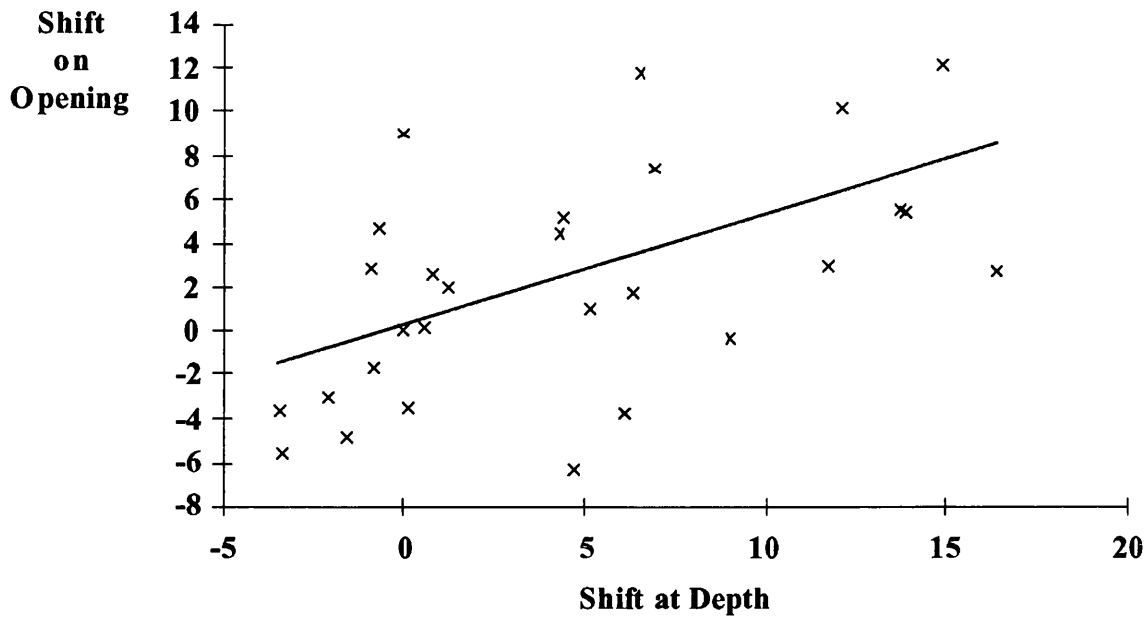
Figure 3.12: Correlation between shift of the cortex on opening and shift of the deepest

tumour margin (r=0.5, p=0.006, n=28).

3.4 FRAMELESS STEREOTAXY

During this investigation the technique of frameless stereotaxy was developed, through the design and manufacture of an adjustable, locking, adaptable instrument holder. Laboratory phantom investigations were performed to assess the accuracy of this technique. A clinical series of frameless stereotactic biopsies was undertaken, enabling the introduction of frameless methods to traditionally frame-based procedures. In addition, the in vivo accuracy of the frameless stereotactic method was examined in a series of frameless stereotactic biopsies.

3.4.1 Phantom Accuracy Measurements

A total of 258 phantom frameless stereotactic procedures were performed (Table 3.15, Figure 3.13, Appendix II.iv.i, Appendix III, iv.i) and these revealed an overall mean error of 1.3mm (SD 0.6mm). Of these tests 120 were CT-directed and 138 were MRI-directed. The mean error for CT-guided phantom frameless stereotaxy was 1.1mm (SD 0.5mm) and for MRI-guided phantom frameless stereotaxy was 1.4mm (SD 0.7mm). Thus, the accuracy of CT-directed frameless stereotaxy was found to be significantly better than that directed by MRI (p=0.0001).

The 120 CT-directed measurements comprised 40 procedures with 2mm sequential axial CT images, 40 procedures directed by 3mm sequential axial CT images and 40 directed by 3mm helical CT images. The mean error for phantom frameless stereotaxy directed by the 2mm axial CT images was found to be 1.1mm (SD 0.5mm). The comparable mean error for 3mm axial CT images was 1.3mm (SD 0.6mm) and that

for the 3mm helical images was 0.9mm (SD 0.5mm). Therefore, frameless stereotaxy

directed by the finer cut 2mm axial CT and the 3mm helical CT were both significantly

TABLE 3.16

Results of the phantom frameless stereotaxy accuracy studies.

Imaging Protocol	n	Mean Error (mm)	S D (mm)	MID (mm)
Standard Vectra MRI	43	1.7	0.6	1.7
Signa MRI	95	1.3	0.6	1.3
All MRI	138	1.4	0.7	1.4
2mm Axial CT	40	1.1	0.5	1.3
3mm Axial CT	40	1.3	0.6	1.8
3mm Helical CT	40	0.9	0.5	1.6
All CT	120	1.1	0.5	1.6
All Modalities	258	1.3	0.6	1.5
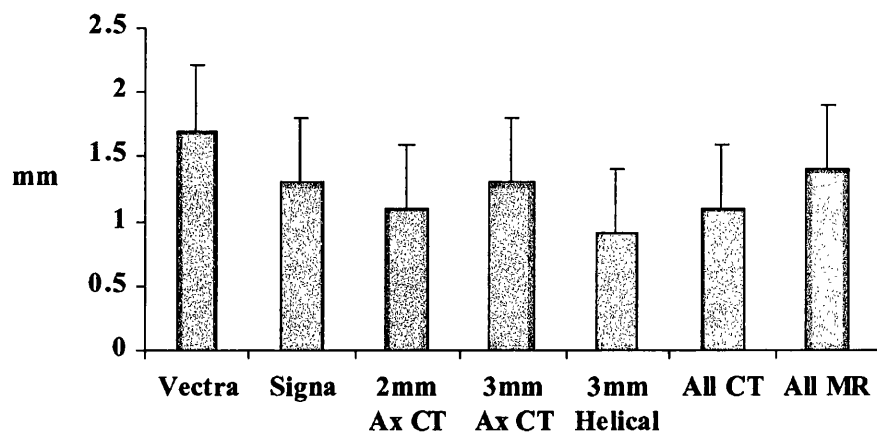
Figure 3.13: Bar graph demonstrating the mean errors of phantom frameless stereotaxy

according to imaging modality.

more accurate than when directed by the 3mm axial CT scans (p=0.025 and p=0.0006 respectively).

Of the 138 MRI-directed phantom frameless stereotaxy measurements 95 employed images from the 1.5 Tesla Signa scanner and 43 employed images from the 0.5 Tesla Vectra scanner. The mean error for Signa-guided phantom frameless stereotaxy was shown to be 1.3mm (SD 0.6mm) whilst that for Vectra-guided stereotaxy was 1.7mm (SD 0.6mm). Thus, frameless stereotaxy with images from the Signa machine was significantly more accurate than that conducted with images from the Vectra one (p=0.0074).

3.4.2 Clinical Validation

The clinical series of 21 frameless stereotactic biopsies was performed in 19 consecutive patients presenting with cerebral mass lesions of unknown pathology (Table 3.17). The patients comprised 8 females and 11 males aged between 25 and 76 years of age (median 55 years). The median number of self-adhesive skin fiducials applied to the scalp prior to imaging was 9 (range 7–16) and the mean registration RMSE was 3.1mm (SD 1.1mm). The lesions measured between 13.2mm and 60.5mm in diameter (median 37.8mm) and were situated in a variety of cerebral structures. The duration of the surgical procedure, from positioning on the operating table to reversal of anaesthesia, was between 20 minutes and 1 hour 45 minutes (median 45 min) and the depth of the biopsy target below the locked instrument holder ranged from 40mm to 120mm (median 77mm). In each case the final histological diagnosis corroborated that

made from the smear specimen, being high grade glioma in 17 cases, metastasis in 1 and

neurocytoma in 1. There were no intra-operative or post-operative complications and

the movement check did not show drift of the instrument guide in any case.

TABLE 3.17

Summary of clinical characteristics for the series of 21 frameless stereotactic biopsies.

Case No.	Age	Sex	Site of lesion	Lesion Diameter (mm)	Op Time (Hrs)	Depth to target (mm)	Pathology
1	43	F	Rt Parietal	27.4	1.08	71	Metastasis
2	50	M	Lt Temporal	60.0	0.83	69	Glioma
3	56	F	Rt Parietal	17.0	0.75	75	Glioma
4	25	M	Rt Parietal	26.4	1.75	40	Glioma
5	73	M	Rt Thalamic	42.9	0.83	77	Glioma
6	55	M	Lt Temporal	46.9	1.00	100	Glioma
7	53	F	Lt Frontal	53.3	0.75	72	Glioma
8	53	F	Lt Occipital	54.8	0.70	60	Glioma
9	68	F	Rt Parietal	39.7	0.70	77	Glioma
10	57	F	Rt Parietal	59.0	0.50	77	Glioma
11	63	M	Cb Peduncle	22.0	0.75	77	Glioma
12	70	M	Rt Frontal	37.8	0.75	78	Glioma
	70	M	Rt Frontal	37.8	0.75	82	Glioma
13	25	M	Lt Frontal	60.5	0.58	50	Neurocytoma
14	76	M	Lt Parietal	29.0	0.33	85	Glioma
15	38	M	Lt Parietal	23.6	0.50	55	Glioma
16	28	F	Lt Frontal	13.2	1.00	78	Glioma
17	69	F	Lt Parietal	40.2	0.33	65	Glioma
18	57	M	Rt Thalamic	36.2	0.83	120	Glioma
19	53	M	Rt Temporal	22.6	0.75	88	Glioma
	53	M	Rt Temporal	26.7	0.75	103	Glioma

3.4.3 In Vivo Accuracy Assessment

Of the 19 patients in the series of frameless stereotactic biopsies, 14 underwent follow-up MRI within 24 hours of surgery (Table 3.18). Sixteen biopsies had been performed in these 14 patients and of these 15 could be clearly identified in the post-operative images (aspiration of one cystic lesion precluded comparison). Fusion of the remaining 15 useful post-operative studies with their corresponding pre-operative scan was performed with a mean RMSE of 1.1mm (SD 0.6mm). Thereafter, simple subtraction of the co-ordinates for the intra-operative targets from those for the centre of the actual biopsy sites revealed a mean linear error of localisation of 2.3mm (SD 2.0mm, Appendix II.iv.ii, Appendix III.iv.ii). The mean linear error for the 9 MRI-directed frameless stereotactic biopsies was 2.6mm (SD 1.9mm) and for the 6 CT-directed biopsies was 2.5mm (SD 0.7mm). When the three linear errors (x, y and z) were transformed into a vector, the resultant mean Euclidean error of localisation was 4.8mm (SD 2.0mm). The mean Euclidean error for the 9 MRI-directed biopsies was 4.4mm (SD 2.1mm) and for the 6 CT-directed biopsies was 5.4mm (SD 1.5mm). No statistically significant difference was found between the imaging modalities and there was no correlation found between the length of pointer extension employed and biopsy error ($r=0.35$).

TABLE 3.18

Summary of in vivo accuracy assessment for frameless stereotactic biopsy

Case Number	Pre-op Imaging	Post-op Imaging	RMSE of Image Fusion (mm)	Linear Error (mm)	Euclidean Error (mm)
3	MRI (S)	MRI (S)	1.0	2.4	4.6
6	MRI (S)	MRI (S)	0.8	3.9	8.1
7	MRI (S)	MRI (S)	0.8	3.6	6.5
8	MRI (S)	MRI (S)	1.5	2.0	4.0
9	CT	MRI (S)	1.8	2.5	6.1
10	CT	MRI (V)	0.8	3.2	6.0
12	CT	MRI (V)	0.5	2.9	6.3
12	CT	MRI (V)	0.5	1.4	3.0
13	MRI (S)	MRI (S)	1.3	0.7	1.8
14	CT	MRI (S)	1.5	1.7	3.9
15	CT	MRI (V)	2.4	3.1	7.1
16	MRI (V)	MRI (V)	0.4	0.6	1.2
17	MRI (V)	MRI (V)	0.7	1.2	2.6
19	MRI (V)	MRI (V)	0.5	2.9	5.2
19	MRI (V)	MRI (V)	0.5	2.4	5.7

MRI (S) = Signa 1.5Tesla MRI
MRI (V) = Vectra 0.5Tesla MRI

3.5 IMAGE-GUIDED NEUROENDOSCOPY

Development of the endoscope LED blocks resulted in a lightweight, ergonomic method of endoscope tracking. This was assessed for accuracy in laboratory phantom studies and was validated through a series of clinical cases. In addition, correction of endoscope image distortion was employed to enable accurate registration of the endoscope view with the pre-operative images. This allowed graphic overlays to be assessed, image injection evaluated and the associated error to be determined in laboratory phantom studies.

3.5.1 Phantom Accuracy Assessment

The accuracy of point localisation was determined for the endoscope when employed as a pointer, with the LED block attached and the sharpened trocar providing the tip. The physical targets employed in these studies were the implanted image localisers within the phantom skull. The mean overall error of point localisation for the image-guided endoscope was 1.5mm (SD 0.8mm) (Table 3.18, Appendix II.v.i, Appendix III.v.i). The overall mean error for CT-directed point localisation was 0.9mm (SD 0.5mm) and that for MRI-directed tests was 2.1mm (SD 0.6mm). Thus, CT-guided endoscope tracking was found to be significantly more accurate than MRI-guided tracking ($p < 0.0001$).

When the errors associated with each image subtype were analysed localisation with 2mm sequential axial CT was found to be significantly more accurate than with either 3mm sequential axial CT ($p < 0.0001$) or the 3mm helical CT ($p < 0.001$).

Furthermore, the mean error of localisation with standard Vectra images was found to significantly lower than that with either fine Vectra imaging (p=0.0011) or Signa data (p<0.0014).

TABLE 3.19

Results of the laboratory phantom assessment of localisation error for the image-guided neuroendoscope.

Imaging Protocol	Mean Error (mm)	SD (mm)
Signa	2.1	0.6
Standard Vectra	2.3	0.6
Fine Vectra	2.0	0.4
All MRI	2.1	0.6
2mm Axial CT	0.8	0.5
3mm Axial CT	0.9	0.6
3mm Helical CT	0.9	0.5
All CT	0.9	0.5
All Studies	1.5	0.8

3.5.2 Clinical Evaluation of IGN

The novel image-guided neuroendoscopy tool was clinically validated through a short series of carefully selected cases. The instrument was simple to assemble, register and handle in the clinical setting. Image-guidance during endoscopic surgery was found to be both intuitive and of considerable assistance.

139

<u>Case Report 1</u>

The first case was that 38 year old man who presented with a 4 month history of headache and deteriorating vision. His initial presentation was in childhood with a low-grade astrocytoma of the cerebellum and obstructive hydrocephalus. Multiple shunt revisions had been required and, in 1994, he developed life-threatening ventriculitis secondary to faecal peritonitis. Examination on this admission revealed bilateral papilloedema and impaired higher cortical function. A MRI scan demonstrated triventricular hydrocephalus with contracted and scarred anterior horns of both lateral ventricles (Figure 3.14). Post-meningitic adhesions obstructed the foramina of Munro and encased the bilateral ventricular catheters.

In this case shunt revision would have been complex, requiring bilateral and third ventricle catheters to be placed in the loculated cavities, and would certainly have entailed some risk. Endoscopic simplification of the loculi and third ventriculostomy would be a superior treatment but, with the anterior horns and foramina of Munro filled with adhesions, freehand endoscopy would be somewhat hazardous and unlikely to succeed. However, the addition of IGN enabled direct insertion of the endoscope into the narrow right lateral ventricle under continuous guidance, puncture of the obscuring membranes over the foramen of Munro and construction of a third ventriculostomy at a safe site. The patient made an uneventful recovery and remained shunt-independent at six months follow-up.
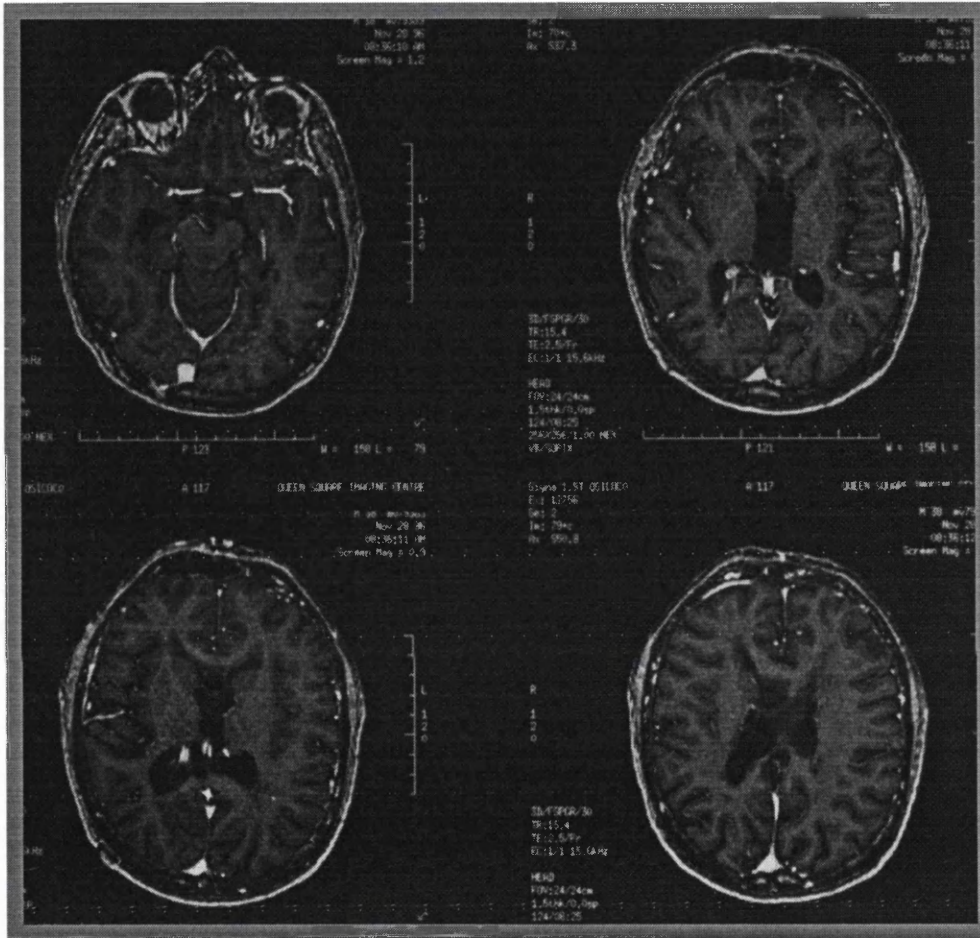
Figure 3.14: Axial MR images of IGN case 1. The dilated third ventricle, wide occipital horns and narrowed anterior horns are shown. Thus, the potential difficulties of freehand endoscope insertion and operation can be appreciated.

Case Report 2

The second case to undergo Image-Guided Neuroendoscopy was that of a 53 year old man who present with a 2 month history of increasing diplopia, blurring of vision, headaches and intermittent confusion. A vascular, infiltrating, enhancing periventricular lesion was seen on MRI (Figure 3.15). Examination on admission revealed a fluctuating conscious level, a mental test score of 3/10, visual acuity of 6/18, midsized unreactive pupils, ophthalmoplegia, a right upper motor neurone facial palsy, ataxia and a mild right hemiparesis.

The surgical alternatives in this case were frame-based stereotactic biopsy and freehand endoscopic biopsy. Whilst stereotactic biopsy would be feasible in such a situation the site and appearance on MRI predicted an above average risk of negative biopsy and of deep haemorrhage. The alternative procedure of transventricular biopsy could provide the possibility to retrieve biopsies under direct vision. However, the freehand endoscopic view may have revealed a featureless ependymal lining making safe and diagnostic biopsy retrieval difficult.

Image-Guided Neuroendoscopic biopsy was performed in this case. Image-guidance enabled the most favourable biopsy site to be defined in the pre-operative images, located via intra-operative navigation and biopsies were retrieved under direct vision. The patient made an uneventful post-operative recovery and the final diagnosis was of cerebral lymphoma that responded to radiotherapy.
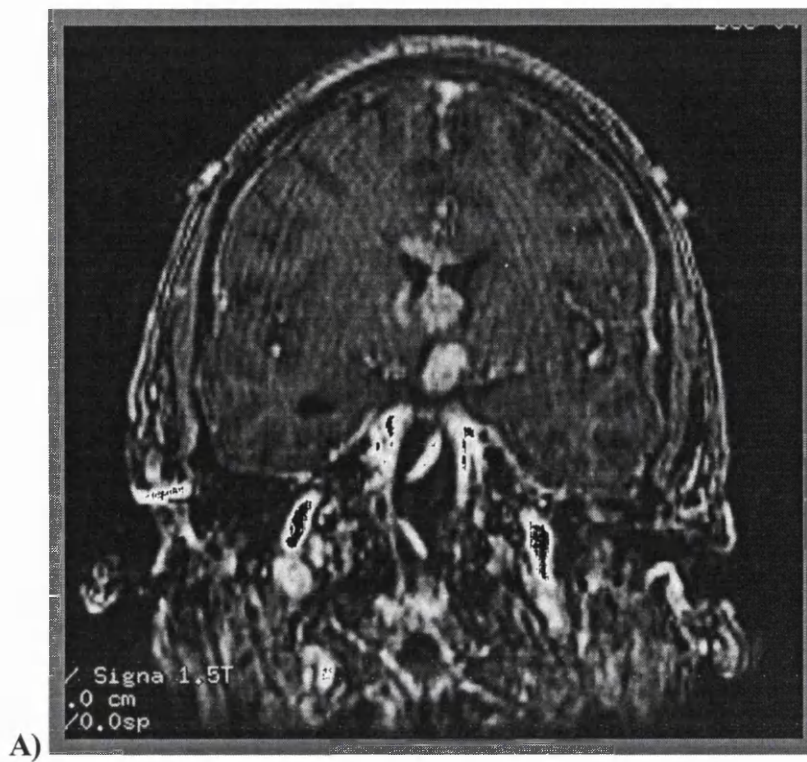
Figure 3.15: MR images of IGN Case 2 showing the vascular periventricular tumour from which transventricular biopsies were retrieved. A) Coronal and B) Sagittal views.

Case Report 3

The third case was that of a 38 year old man who presented with a three month history of progressive ataxia. His cognitive and communication abilities had also been noted to deteriorate prior to admission. At the age of two he had suffered a significant head injury resulting in developmental delay. CT and MRI scans revealed a large multi-loculated left hemisphere cyst with gross cerebral atrophy and compression of the right cerebral hemisphere (Figure 3.16). Freehand endoscopic fenestration and simplification of the cyst had been attempted previously without benefit and with recurrence of the symptoms.

Whilst shunt drainage of such a cyst may be performed the multiple loculations were likely to make this unrewarding. Image-Guided Neuroendoscopy was employed to identify the optimum entry site and trajectory to reach all loculi, an appropriate site for fenestration and for the intra-operative localisation of these targets. The procedure was successfully performed with little shift of the adhesive bands evident during surgery. At follow-up the cyst remained decompressed and the patient had been restored to his pre-morbid condition.

Case Report 4

The fourth case was that of a 67 year old woman presenting with headaches, nausea and drowsiness. A ventriculo-peritoneal shunt had been inserted previously for post-operative hydrocephalus. On admission she was drowsy, irritable and pyrexial. The CSF was found to be infected and the VP shunt was therefore removed. During this
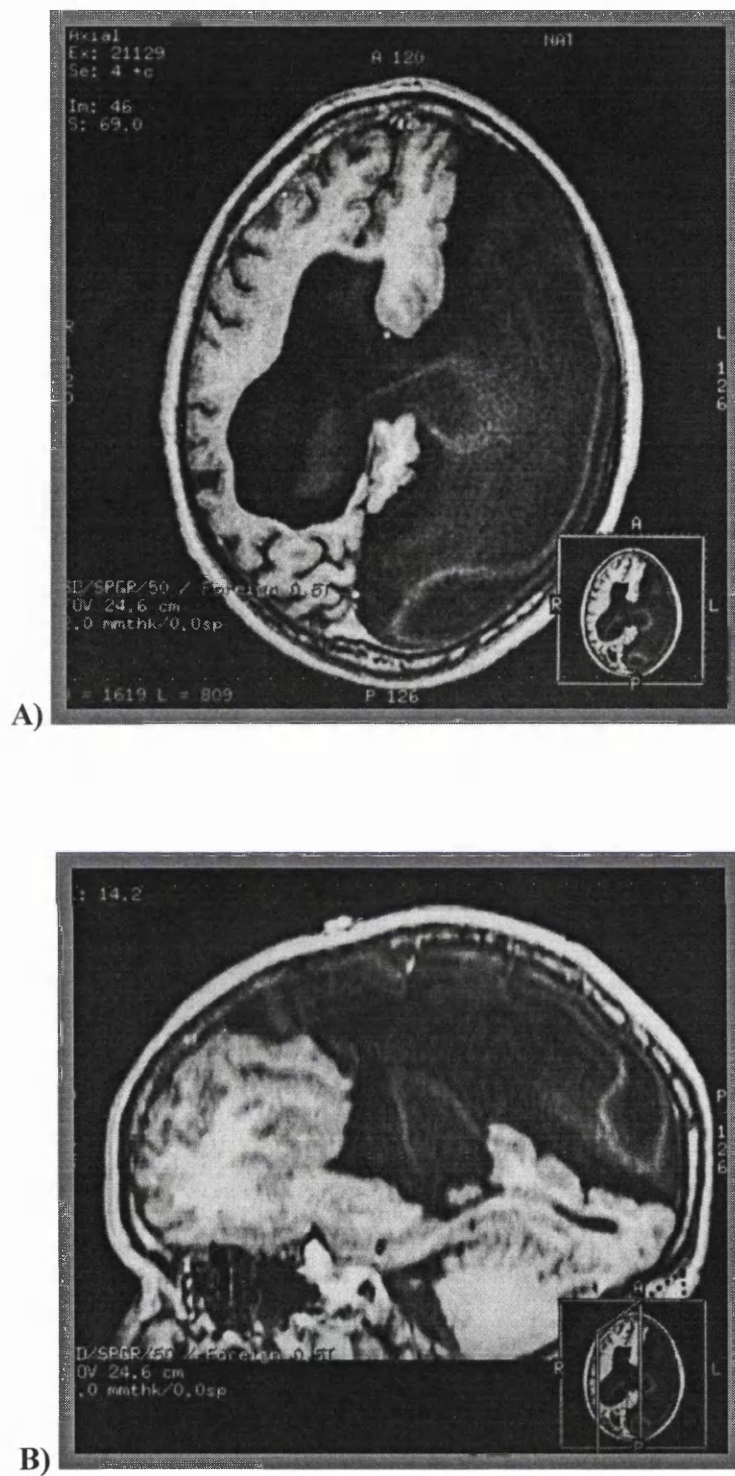
Figure 3.16: Pre-operative MRI for IGN case 3. The loculated collections, left-right shift of the midline and disorganised cerebral anatomy can be apprectiated in these A) Axial and B) Sagittal views.

operation the ventricular catheter was noted to be missing from the system. Further imaging revealed that the catheter had become detached, had migrated through the ventricular wall and was lying within the thalamus and below the floor of the third ventricle (Figure 3.17).

In the presence of infection total shunt removal was desired and endoscopic retrieval would provide the only relatively safe approach for this. However, this would be technically challenging in the presence of inflammatory exudate and with the catheter buried in the tissues. Image-Guided Neuroendoscopy was employed and, as predicted, the ependyma of the ventricle was featureless with the catheter completely obscured. The site of ventricular perforation was identified in the images and the endoscope guided to this point. The membrane was pierced at the target site, the end of the catheter revealed, grasped with forceps and removed with ease. The infection rapidly resolved following surgery and the shunt system was replaced 10 days later.

Case Report 5

The fifth case was a 25 year old man with a 9 month history of progressive visual failure and headaches. Examination revealed severe papilloedema and reduced higher cortical function. A MRI scan revealed an arachnoid cyst of the third ventricle with narrowed anterior horns of the lateral ventricles. Whilst stereotactic shunt insertion could have been performed bilateral VP shunts would have been necessary and the preferred solution was to fenestrate the cyst and perform a third ventriculostomy. However, this would be a difficult procedure through the narrow
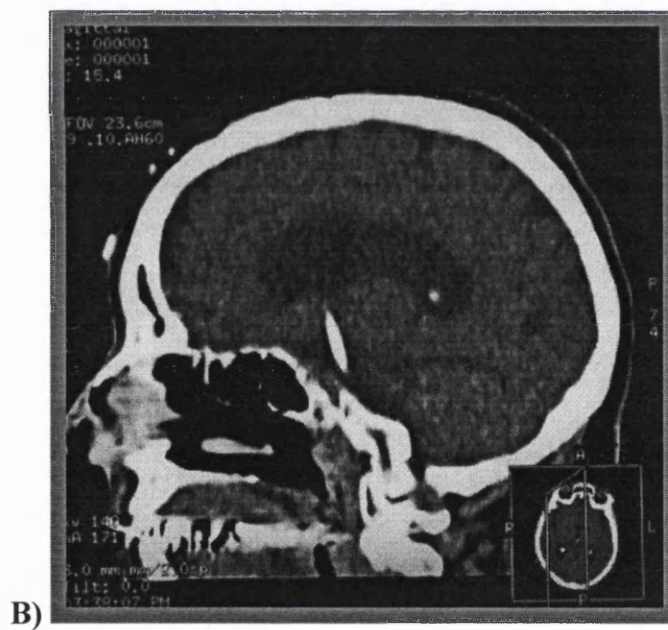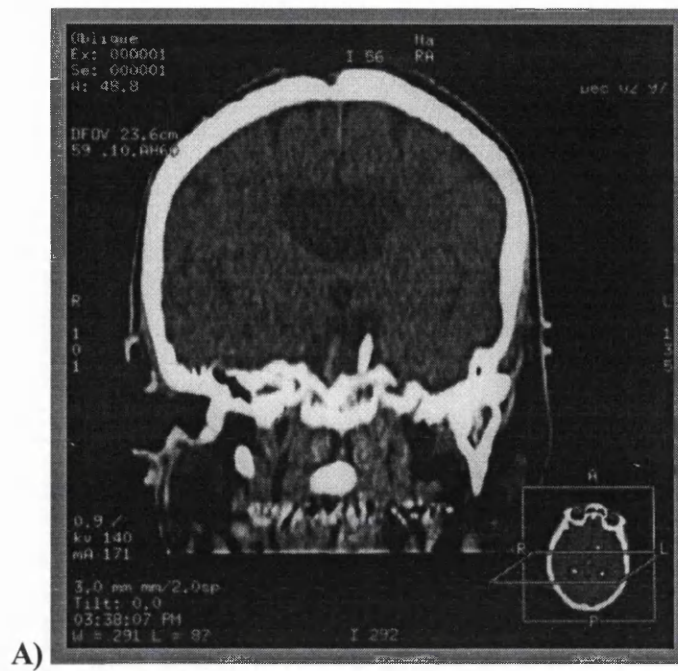
Figure 3.17: The pre-operative CT scans from IGN case 4 show how the ventricular catheter had migrated through the ventricular wall, coming to lie in the interpeduncular fossa. A) Coronal and B) sagittal views.

anterior horns and with a thick inferior wall of the cyst. In this case Image-Guided Neuroendoscopy was helpful in planning the entry site with precision, with guided insertion to the narrow ventricle and for safe perforation of the thickened and opaque floor of the third ventricle.

3.5.3 Correction of Optical Distortion

In these experiments the neuroendoscope was clamped both perpendicular to and at 45 degrees tilt to a regular 1mm grid. The endoscopic images of the grid were captured with a video frame-grabber and stored as standard TIFF files for later analysis. This procedure was repeated at several measured distances from the grid, encompassing the working range of the endoscope, in air and in physiological saline.

The endoscope images were analysed to determine the number of pixels between intersections along each line of the grid (Table 3.20, 3.21, Figure 3.18, 3.19). This data revealed that the greatest distance between intersections for the horizontal lines occurred at the third intersection and on the vertical lines the greatest intersection distance was found at the fourth intersection. This revealed the position of least distortion, which corresponded with the optical axis of the endoscope. When this point was taken as the origin of the grid and the position of each intersection plotted for both the regular grid and the distorted endoscope image the pattern of distortion was revealed to be radial (Figure 3.20)

TABLE 3.20

Mean number of pixels between each intersection along the horizontal lines in endoscope

images acquired at a distance of 15mm and perpendicular to the grid.

Intersection	Line 1	Line 2	Line 3	Line 4	Line 5	Line 6
1	44	47	48	46		41
2	50	51	52	51	49	48
3	53	52	53	54	52	51
4	50	51	52	52	50	50
5	49	48	50	50	47	48
6	47	47	47	46	45	46
7	41	44	44	44	41	42
8	38	37	39	36	37	38
9	32	31	30	32		30

TABLE 3.21

Mean number of pixels between each intersection along the vertical lines in endoscope

images acquired at a distance of 15mm and perpendicular to the grid.

Intersection	Line 1	Line 2	Line 3	Line 4	Line 5	Line 6	Line 7
1	45	47	48	47	48	46	
2	49	50	50	49	49	48	48
3	51	52	52	51	50	49	50
4	52	53	54	53	51	50	51
5	51	51	52	51	49	49	50
6	49	49	50	49	48	47	47
7	47	48	47	46	46	46	45
8	45	46	43	44	44	43	
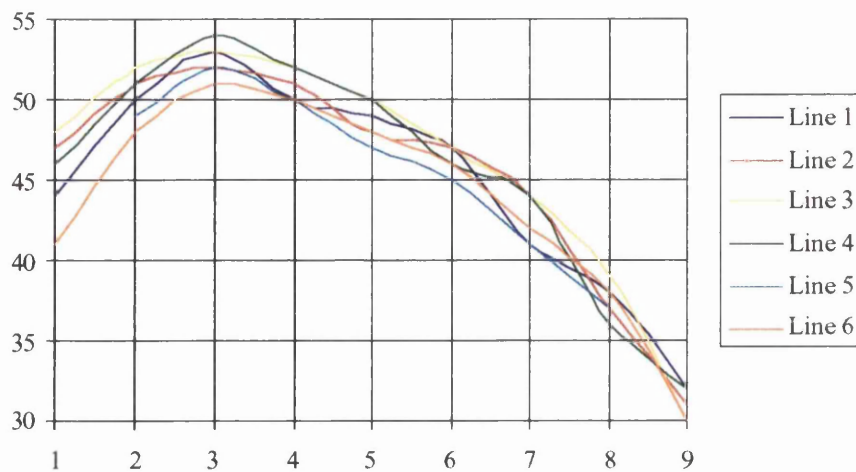
Figure 3.18: Graph displaying the mean number of pixels between each intersection along the horizontal lines in the endoscope images acquired at a distance of 15mm and perpendicular to the grid.
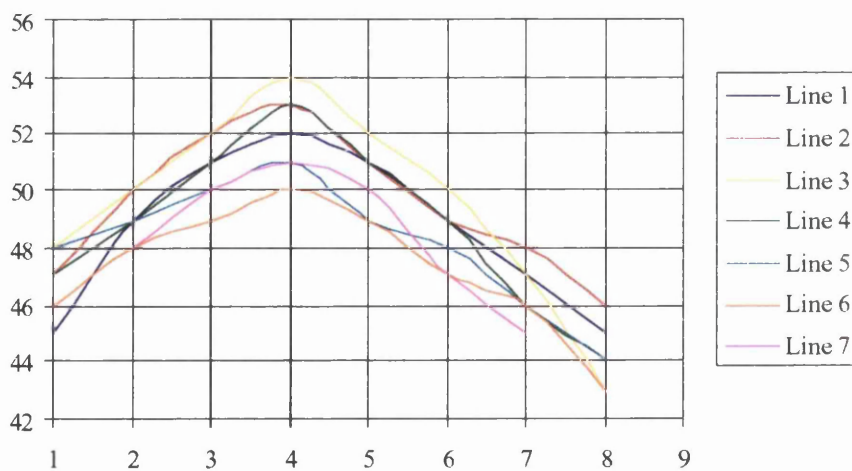
Figure 3.19: Graph displaying the mean number of pixels between each intersection along the horizontal lines in the endoscope images acquired at a distance of 15mm and perpendicular to the grid.
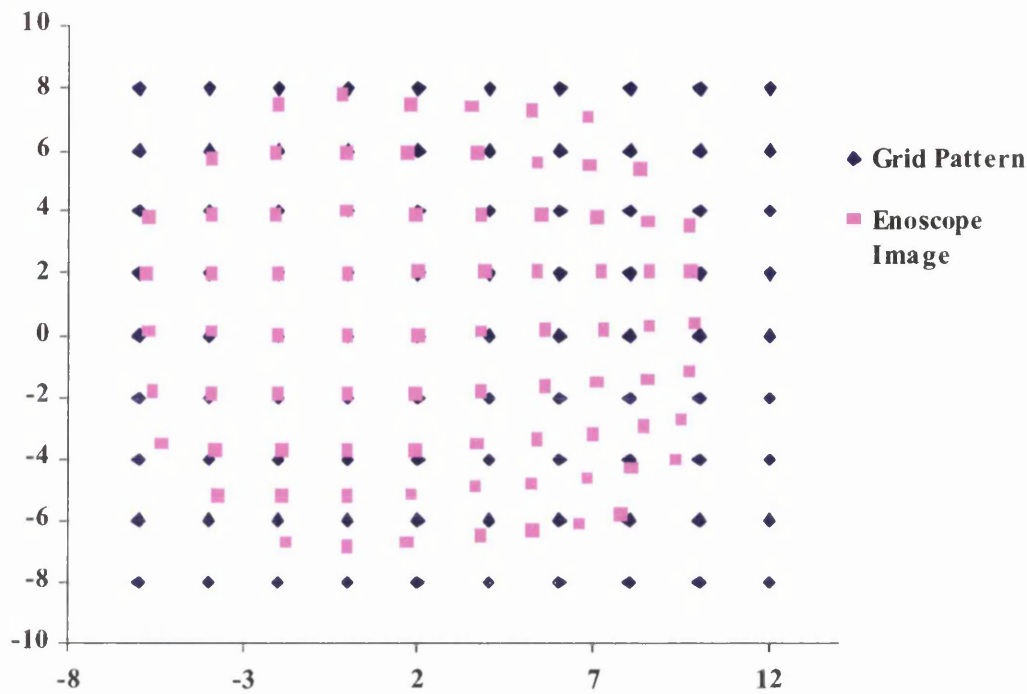
Figure 3.20: Graph of the intersection positions in the regular grid and the distorted endoscope images, acquired at a distance of 15mm and perpendicular to the grid. This displays the radial nature of the endoscope image distortion.

The radial pattern of distortion in the endoscope images was suitable for correction with the Haneishi algorithm. Therefore, the algorithm was run on the points of intersection in each of the endoscope images and the least cost solution that resulted in straight lines joining these intersections was accepted. The distortion evident in the uncorrected images (Figure 3.21) was thus removed from the corrected images (Figure 3.22). These corrected images were analysed for intersection distances and were found to be regular and symmetrical indicating that an appropriate solution had been achieved.
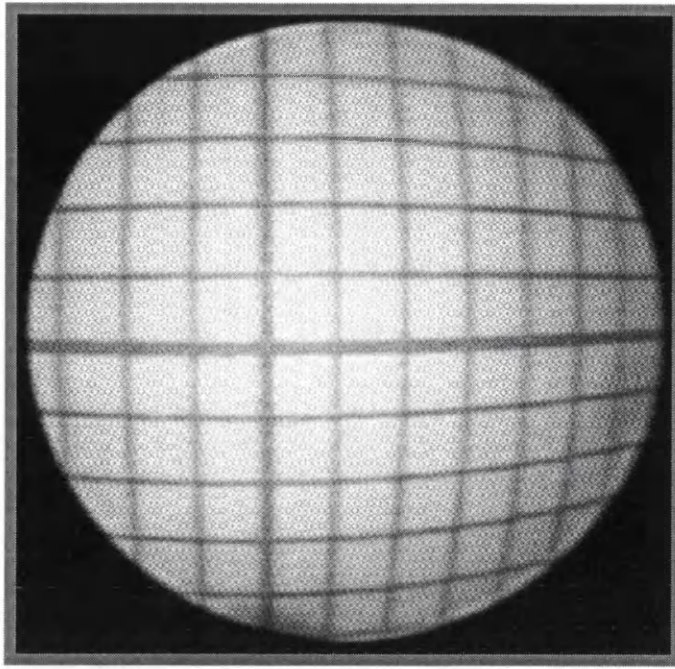
Figure 3.21: Captured endoscope image of a regular 1mm grid pattern. Optical distortion is evident from the curvature of the grid lines.
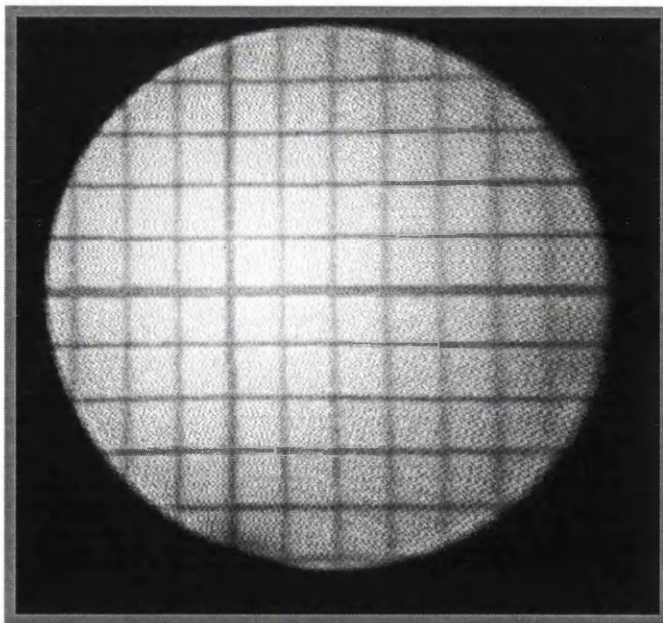
Figure 3.22: Corrected endoscope image of the regular 1mm grid derived from the endoscope view in figure 3.21
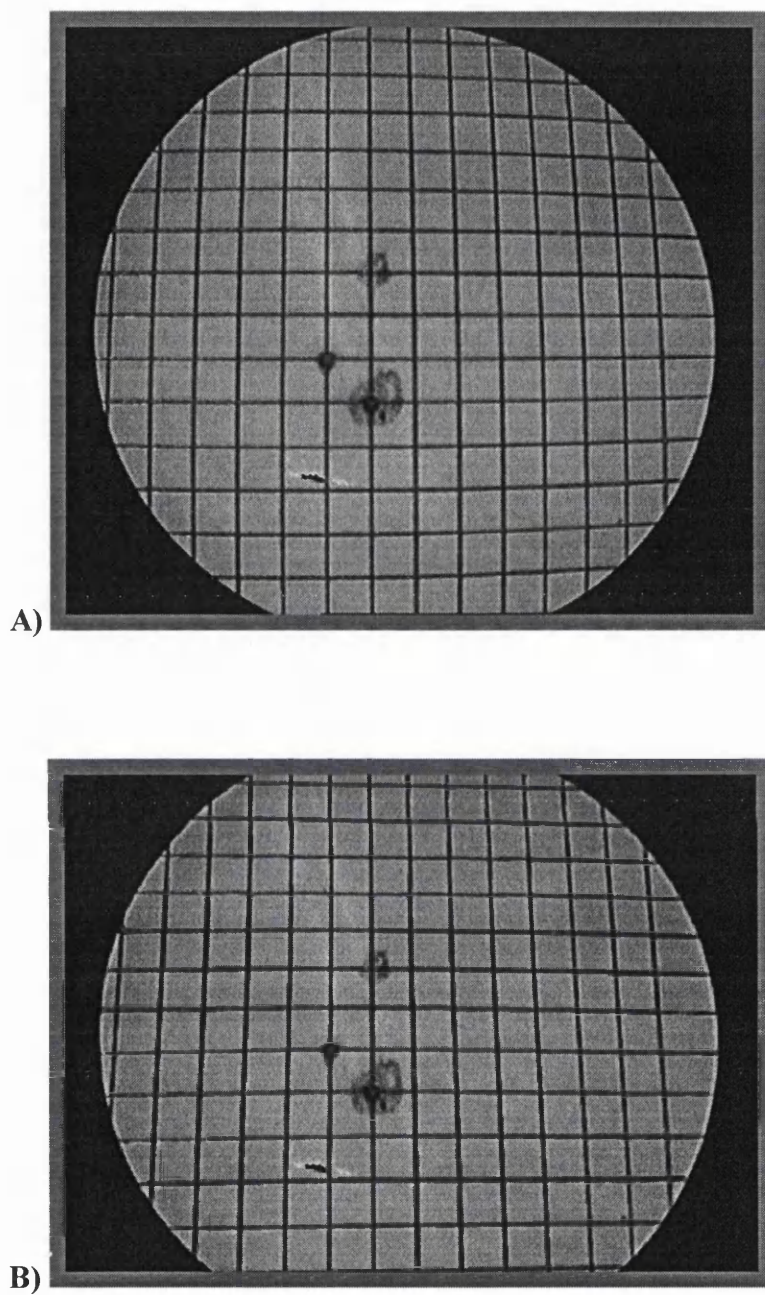
Figure 3.23: Endoscopic images of the regular 1mm grid acquired at 45° to the surface. A) Distortion of the grid is evident when the grid lines are examined closely in the uncorrected image. B) The grid lines are straight in the corrected image whilst the perspective of the 45 degree tilt is retained.

Repetition of the experiment for an endoscopic image viewed at 45° revealed that the algorithm could appropriately correct images other than at the perpendicular (Figure 3.23)

3.5.4 Graphic Overlays and Image Reconstructions

A variety of graphical representations of anatomical and pathological features were assessed in the laboratory. These were derived from the clinical data sets employed for image-guidance during the validation phase. Whilst early experiments with these overlays attempted to provide three-dimensional information of the target position, the complexity of these graphical representations illustrated the importance of simplicity and clarity. More complex overlays proved not only unsuccessful but also confusing. Later overlays were therefore restricted to simple outlines and symbols (Figure 3.24).

Laboratory phantom investigation into the accuracy of graphical overlay projection was also undertaken. A skull phantom with internal anatomical features, including optic nerves, was imaged and registered with the neuronavigation system. The Image-Guided Neuroendoscope was brought in to visualise the internal features, clamped in position and the endoscopic images captured. The centre of each optic nerve was segmented from the CT data set and, following application of the distortion correction algorithm, was superimposed over the captured endoscope image (Figure 3.25). The mean offset of the overlay points from the corresponding captured image
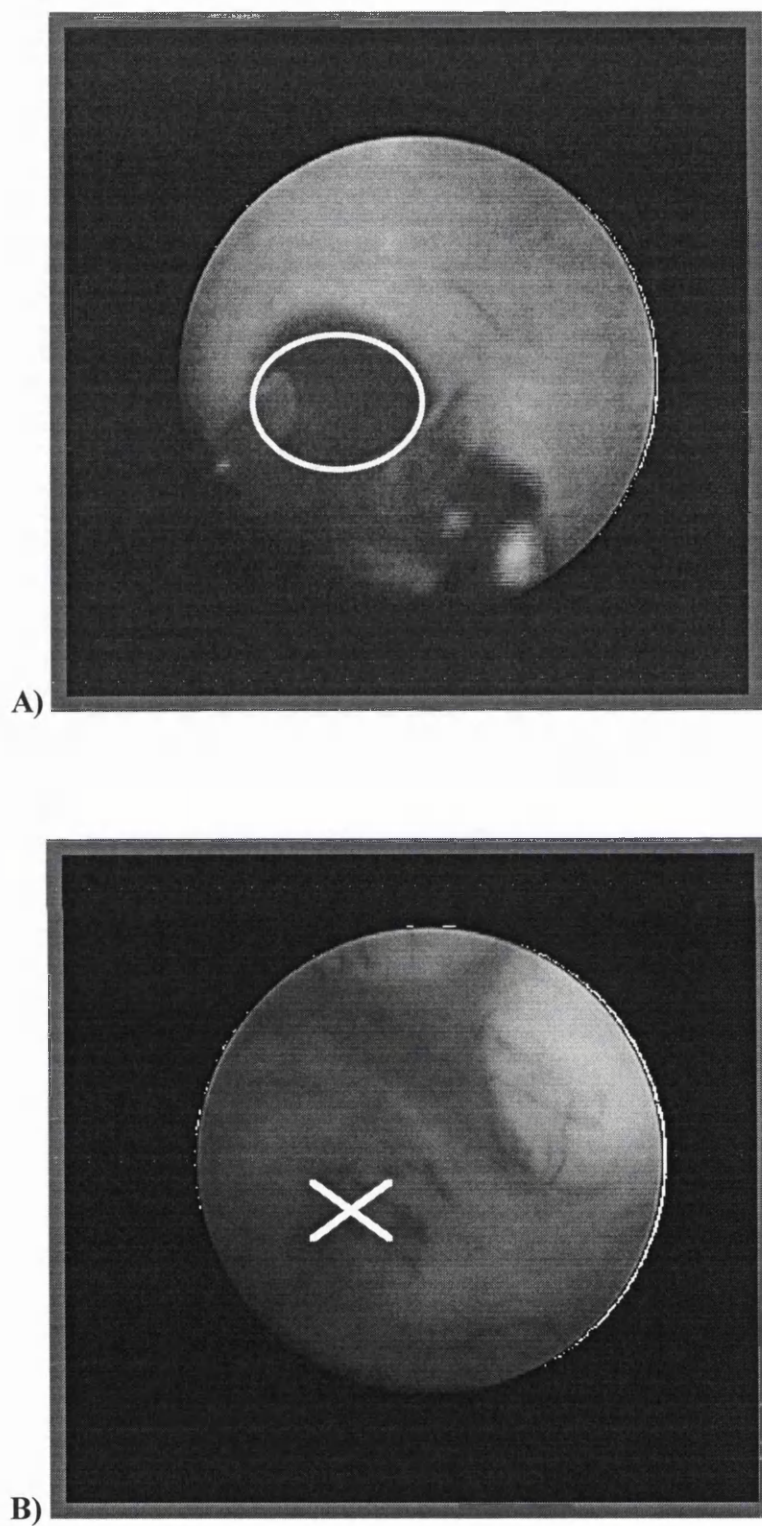
Figure 3.24: Endoscope views with overlaid graphics. A) The position of the foramen of Munro (circle) and B) the site selected for third ventriculostomy (cross).
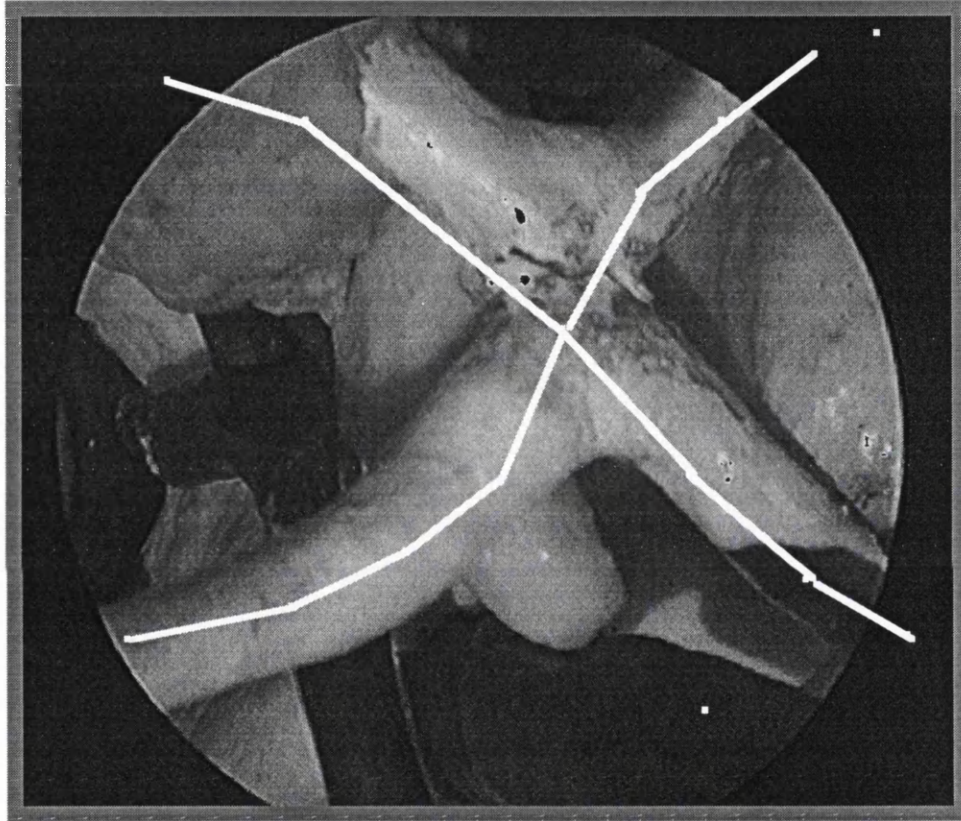
Figure 3.25: Corrected endoscope image of a skull phantom with anatomical internal features. A simple linear graphics overlay representing the centre of the optic nerves, segmentated from a CT data set of the phantom, is shown.

position was determined. This revealed a mean error of phantom graphics overlay guidance of 2.2mm (SD 0.9mm).

When the ventricular surface anatomy was segmented from high definition clinical image data sets and three-dimensional renderings produced, the results were uniformly disappointing. Whilst the ependyma could be thresholded and an accurate representation resulted, the depth perception and surface contour visibility was far below that available in real endoscope images. With these limitations it became clear that such images would not be appropriate for intra-operative guidance, particularly if corrected endoscopic images could be provided in real time.

DISCUSSION

DISCUSSION

In conception, the development of Image-Guided Neuroendoscopy appeared a simple matter of attaching LED's to a rigid endoscope and loading a model of this arrangement into the workstation. However, wider experience and a deeper knowledge of the complexities of neuronavigation brought additional questions to the introduction of this novel technique. The necessity for a truly stereotactic method of endoscope insertion became apparent and this in turn made the development of an adjustable, locking instrument holder mandatory. Similarly, the potential impact of post-imaging brain distortion on all image-guided surgery was recognised and required investigation, both to determine the magnitude of shift and to discover pre-operative predictors of this. In addition, the degree of optical distortion inherent in the endoscope became apparent, which necessitated image correction to enable registration of the endoscope images and scan data for accurate graphics overlays. Thus, the concept for the development of Image-Guided Neuroendoscopy grew into a larger undertaking with a wider scope, greater complexity and larger reward than at first envisaged.

4.1 LABORATORY STUDIES OF NEURONAVIGATION SYSTEM ACCURACY

The neuronavigation system selected for the development of IGN was a prototype system, developed in collaboration with the manufacturers, Philips Medical Systems. Whilst the theoretical accuracy and sensitivity of the infrared detection method had been determined by the development group (Fuchs et al 1996), the application accuracy of the system required independent assessment in laboratory phantom investigations and the system required validation in clinical use. The issues addressed in the laboratory phantom studies were; the impact of imaging parameters on registration accuracy, the accuracy of pointer tracking and the effects of pointer design and rotation on this.

The determination of accuracy in stereotaxy requires the definitive identification of identical points in the image data set and in physical space. Whilst some groups have employed the registration RMSE or surgeon-selected points during surgery to describe system accuracy (Doshi et al 1995, Golfinos et al 1995) these are inadequate as neither method can determine the actual discrepancy between the localised position of a target and the physical position in space. In contrast, the methods employed here closely reproduced those of established researchers into the accuracy of frame-based stereotaxy (Maciunas et al 1994) with image localisers implanted into the phantom to enable reliable error assessments to be undertaken. Indeed, these markers were similar to those employed by the Vanderbilt group, who have shown that the centre of each attachment

is identified with a mean error of 0.4mm in the images and 0.3mm in physical space (Maurer et al 1997).

4.1.1 Registration

The objective of image to physical space registration is to align the scanner co-ordinate system precisely with the physical object that was imaged. All image-guidance systems, whether frame-based or frameless, perform this registration by matching a relatively small number of physical points with their image correlates and extrapolation of this fit to the entire data set. Whilst this method is both simple and effective, there are inherent potentials for error, which should be appreciated. However, when the principles of point-based registration are understood, the errors may be minimised and the vagaries of the method exploited to best advantage. The fiducial-based registration utilised by the neuronavigation system employed here exemplifies these principles.

With the fiducial method registration is performed through the identification of the fiducial positions, both in the images and in physical space. These two sets of points are aligned through rigid body transformations, the final solution being determined by the least squares error method. The accuracy with which the two sets have been aligned is presented as the Root Mean Square Error of registration. However, the RMSE must not be confused with the error of point localisation, because the accuracy of registration will seldom be uniform throughout the registered volume. This inhomogeneity arises because the target, images and fiducial positions are not constant. If the object were spherical, with multiple evenly distributed fiducials, each imaged and

registered with uniform accuracy, then the RMSE of registration would be a good indicator of point accuracy throughout the volume. Conversely, if the fiducials were placed in a ring around the sphere, laying in one plane, the registration RMSE would apply to that plane only, with increasing error of localisation towards each pole.

Naturally the ideal fiducial arrangement is not applicable to the head, which is not spherical, has skin of varying mobility and thickness and where the fiducials are irregularly placed. Thus, in clinical practice there may be regions of the head in which the error of registration is lower than the RMSE as well as regions where the error is greater. For example, to plan a small craniotomy and resect a convexity meningioma the fiducials should be placed widely across the vault with a cluster over the region of interest. The wide spacing ensures that there are no major skews to the registration whilst the cluster ensures that the registration is biased towards the area of the lesion. However, a fiducial with a high error in the cluster would adversely affect the registration in this region and should be removed. Conversely, when the target is toward the centre of the head, such as for the Image-Guided Neuroendoscopy cases, the best fit at the target site will be achieved through the even distribution of fiducials across the whole cranium and exclusion of fiducials with registration errors markedly different from the average. As the target lies at the epicentre of the part of a sphere described by the fiducials, the registration in this region is likely to be more accurate than that at the surface.

An allied consideration is that whilst a high RMSE indicates a poor correlation between the two sets a low RMSE does not necessarily indicate a good correlation. For

example, a small number of fiducials may be registered with a low RMSE but the point error will be large throughout the data set. Thus, the RMSE of registration provides a guide to the accuracy of fit for the volume only when sufficient fiducials have been employed and when these are evenly distributed. In addition, reliable comparison of RMSE values between registrations is only possible when the same number of fiducials are used for registration and the fiducials are in identical positions. Therefore, the registration experiments undertaken during this investigation were performed in this manner.

Whilst the overall mean registration RMSE in the phantom registration experiments was 1.4mm and this compares favourably with the claims for other image-guidance systems, such absolute values should be interpreted with caution because they are certain to underestimation the error experienced in clinical practice. Of particular note in these experiments were the differences in registration error demonstrated between imaging modalities and protocols. Thus, the finding that registration with the CT data sets resulted in a significantly lower RMSE than registration with MRI, confirmed the expectation that the smaller voxel sizes of the CT scans and lower geometric distortion would make guidance with this modality more accurate. Similarly, the finding that registration with 2mm sequential CT was significantly more accurate than with 3mm CT was in accord with this expectation.

In contrast, the greater RMSE of registration discovered for images acquired with the 1.5T MR scanner and with the Fine Vectra sequence than with Standard Vectra data was not expected. The explanation for the reduced accuracy of Signa registration,

despite a smaller voxel size, is likely to be the higher level of geometric distortion seen at the periphery of the field with this magnet. In view of this finding the distortion visible in images of linear phantoms was compared for the two MRI scanners. This confirmed the greater distortion in the 1.5T magnet, with in excess of 5mm distortion at the periphery of the Signa field and less than 2mm with the Vectra. The explanation for the lower than expected accuracy of registration with the Fine Vectra data is likely to be the poor image definition which resulted from this sequence. Thus, determination of the position for the centre of each fiducial was found to be much more difficult in these images than for the Standard Vectra images. On the other hand, the finding that there was no significant difference in registration RMSE for 6 versus 11 fiducial tests was not surprising as the minimum number with which this system will register is 5 and errors in registration would be expected to increase sharply below this number.

4.1.2 Point Localisation

The phantom laboratory investigations into the accuracy of point localisation revealed an overall error of 1.6mm with the short pointer and an overall mean error for CT of 0.8mm. Whilst this is recognised to underestimate the clinical errors, useful comparisons can be made with similar experiments into frame-based localisation and between imaging protocols. Interestingly the laboratory investigations of Vrionis, Robertson et al (1997) on cadaveric temporal bone, with CT-guidance, revealed rather greater localisation errors of between 1.2 and 1.38mm. However, the method employed required the identification of targets on anatomical features which inevitably introduced

uncertainty. Of greater significance is the finding, in the landmark investigations of Maciunas and Galloway, that the minimum error for CT-guided frame-based localisation was 1.8mm (SD 1.1mm). This was achieved with 2mm axial CT images and 0° of gantry tilt. The comparable result for the phantom experiments of neuronavigation accuracy described here was an error of 0.7mm (SD 0.4mm). Whilst this appears impressive, the underestimation of registration errors in clinical practice is likely to be greater for the fiducial-based registration process than the frame-based method. This arises through fiducial movement on mobile skin, errors in localising the epicentre of the fiducial and difficulties in the identification of fiducial centre in the image data set. Therefore, the frame-based and neuronavigation techniques are likely to achieve more equal accuracies in clinical use.

The finding that the neuronavigation system accuracy at least equalled, and probably exceeded, that for frame-based guidance is supported by reported accuracy assessments in the literature. For example, localisation error for an ultrasound-based system in clinical use has been reported as 1.5mm with 1mm CT slices (Barnet et al 1993b). Clearly the prototype infrared system employed in the development of IGN achieved considerably better accuracy and this also supports the theoretical superiority of optical guidance over other methods. Similarly, the mean error of point localisation with the ISG Wand has been reported variously as 1.8mm (Doshi et al 1995) and 1.5mm (Drake et al 1994). Supportive experimental accuracy results for an articulated arm, demonstrating an error less than or equal to the best stereotactic frames, has been

described by Zinreich et al (1993). However, none of these completely reproduce the errors arising in clinical practice.

In the investigations described here comparison of the error in point localisation between imaging protocols revealed the expected superiority of CT-directed over MRI-directed localisation. This again reflects both the smaller voxel size of the CT data sets and lower geometric distortion of CT compared to MRI. Similarly, the expected rise in error with slice thickness was also found within the CT subgroup, between 2mm and 3mm data sets. When the impact of pointer design on point localisation accuracy was investigated, across scanning modalities and within each subtype, the error of localisation was found to be significantly greater with the long and bayonet pointers than with the short pointer. This result was expected as the geometric relationship of the handle LED's to the pointer tip will result in accentuation of any error of localisation of the LED's when the distance to the tip is increased. Whilst many of these findings had been predicted prior to these investigations, confirmation of these features enabled the logical selection of the optimum arrangement for each clinical situation. In addition, the relatively low errors achieved with the long pointer provided a bench mark for the localisation of the endoscope, provided the distance form LED carrier to tip was similar.

The findings for MRI-directed point localisation were less predictable than those for CT. Whilst the errors of localisation of the image markers and baseplate holes were significantly lower for Signa and Fine Vectra data sets than for the Standard Vectra data set, the pattern was reversed when spare surface fiducials were employed. The latter

pattern was also that found in the registration accuracy experiments. The explanation of this apparent paradox is most likely that the greater peripheral field distortion of the Signa scanner uniformly impairs the accuracy of fiducial localisation without degrading the recognition of more central targets. For these, the smaller voxel size and higher definition images enable more accurate point localisation. Conversely, the explanation for the pattern discovered for the Fine Vectra protocol is most likely related to the difficulty experienced in defining some of the targets with this protocol. Although the overall results confirmed that error increased as voxel size decreased, the subgroup analysis highlighted the importance of the nature of the target also.

4.1.3 Pointer Rotation, Movement and Reproducibility

The finding that rotation of the pointer away from the perpendicular camera view altered the detected position of the pointer has demonstrated the importance of maintaining this relationship. At 90° this reached 0.5mm with the Signa data, representing an astonishing 33% increase in phantom point localisation error. However, as phantom laboratory experiments underestimate errors, the relative increase in error associated with pointer rotation will inevitably be reduced in clinical practice.

The tests of reproducibility of pointer localisation revealed a very high level of concordance. However, there was a significant difference between the pointer types with reduced reproducibility for the bayonet pointer compared with the straight pointers. This is in accordance with the findings of the point localisation experiments and reflects the increased potential for error with the longer, more flexible bayonet

pointer design. However, the level of error of reproducibility detected was considerably lower than that reported in the literature for other systems. For example, Barnett et al (1993b) reported pointer reproducibility of 0.6mm.

The micrometer advance experiments revealed that movement of the pointer was consistently detected at 0.4mm increments. For the image data sets employed in neuronavigation this is equal to the smallest CT voxel dimension and is less than half of any MRI voxel dimension. Thus, in clinical practice the detection of positional movement within the data set will be limited by the resolution of the images rather than the ability of the system to detect movement.

4.2 CLINICAL EVALUATION OF THE NAVIGATION SYSTEM

The achievement of navigation is to bring the exquisite detail of contemporary neuro-imaging into the operating theatre, in a form that enables interactive planning and guided surgery. The advantages of intra-operative guidance are increasingly recognised with claims of improved completeness of safe tumour resection (Maciunas et al 1996), reduced hospital stay (Henderson et al 1997) and less operative morbidity (Spetzger et al 1995). In addition, the advantages of these systems are not restricted to cases previously performed with the stereotactic frame but are more widely applicable (Sandeman et al 1994). The prototype system employed throughout this investigation proved reliable in clinical practice, was intuitive to use and the operative experience gained led to an initial synthesis of the relative strengths of navigation in various pathological conditions. For example, in meningioma and high-grade glioma surgery the major impact of navigation has been the accurate placement of the scalp flap and craniotomy, whereas in low-grade glioma not only may collateral injury be limited by guidance but also a maximal resection can be achieved more safely.

4.2.1 Patient Data

The navigation system was employed in a consecutive series of 100 open neurosurgical operations and the underlying pathological diagnoses in these cases were particularly diverse. During the course of this series just four patients were unable to undergo neuronavigation-assisted surgery, either due to failures to undergo imaging or

removal of the fiducials. There were neither irretrievable system failures during surgery nor instances in which the system was felt to be misleading. However, some difficulty was experienced initially with data transfer through failure of the communication network infrastructure of the hospital.

The variety of procedures undertaken imposed widely differing demands on the navigation system, from fiducial placement to imaging protocols, patient registration and location of fallback markers. The optimum arrangement of fiducials was determined in each case through reference to the planned operation, the lesion position and the intended position of the patient during surgery. This proved particularly important in the unusual mid-face, maxillotomy, extreme lateral and transpetrous approaches to the skull base. In some of these skull base procedures fallback marker placement in the standard manner was not possible and a technique was developed whereby bone screws were placed peripherally to perform this function. Thus, this series was undertaken to clinically evaluate the navigation system. This was achieved and considerable additional experience gained in the clinical aspects of neuronavigation.

4.2.2 Visual Analogue Scales

The visual analogue scale questionnaire revealed the perceptions of the operating surgeons and enabled numerical analysis of these. Ranking of the median response for each question showed that neuronavigation was considered to be most useful for localising the lesion followed by increasing the surgeon's confidence, improved planning, better appreciation of the anatomy and safety of surgery. However, two issues receiving

markedly different results were the effect of neuronavigation on the extent of safe resection and duration of surgery. As the majority of the mass lesions were well-circumscribed or benign, the extent of resection would not be expected to be affected by neuronavigation and the operation time study confirms the overall lack of significant effect upon duration of surgery. Therefore, the surgeons' impression of operation duration changes appeared to be accurate.

4.2.3 Duration of Surgery and Navigation Time Analysis

Although duration of surgery is just one aspect of quality assessment in surgery and is dependent upon multiple factors, a prolongation of operating time is undesirable. Therefore the impact of the introduction of neuronavigation on duration of surgery was assessed. At the same time frequency and duration of intraoperative system usage was recorded. For the cases with neuronavigation less than 10 minutes of operation time was consumed in setting up the hardware and performing the patient to image registration. The finding that there was no significant difference in the duration of matched conventional and neuronavigation cases demonstrated that, as a small time penalty was paid at the commencement of surgery, the surgical time must have been slightly reduced. It is most interesting that the surgeon's perception of impact on duration of surgery was in complete accord with this (i.e. a minimal overall reduction in operation time). The finding that intraoperative system usage occurred with a median frequency of 7 and a median duration of 1 minute for each application was most informative. This demonstrated how little time was required to gain useful information through

neuronavigation. In addition, the finding that the navigation system was used less in meningioma surgery than for other tumours was interesting and in accord with the impression that whilst neuronavigation is helpful in planning and placing an accurate flap, guidance is less helpful in meningioma resection.

4.2.4 Accuracy in the Clinical Environment

Whilst the mean RMSE of registration in clinical practice of 3.7mm was certainly comparable with that achieved by other neuronavigation systems (Golfinos et al 1995), the limitation of this measure has already been stressed. Of greater importance was the finding that the mean application accuracy with this system, measured through bone surface offset in 48 cases, was 2.2mm. This result was comparable with the error determined in the laboratory examinations of the temporal bone, when imaging modalities are allowed for, as this later study employed 1mm CT (Vrionis et al 1997). The greater errors reported in the small series of intraoperative tumour localisation by Ryan et al (1996), which determined a mean error of 4.8mm ±3.5mm, are likely to reflect their use of imprecisely selected targets on difficult anatomical contours.

The clinical accuracy achieved by the prototype optical navigation system is clearly adequate for the purposes of general image-guidance and is particularly reassuring when considering the number of prone and skull base cases included in these figures. In addition, analysis of the error associated with each fiducial position determined that the standard Evaluation Protocol positions were associated with lower errors than additional markers. The underlying explanation is presumed to be the

increased distortion of skin in the more mobile regions of the neck and face, where many

of the additional markers were placed.

4.3 POST-IMAGING BRAIN DISTORTION

Although per-operative brain distortion has been noted by a number of authors (Drake et al 1994, Golfinos et al 1995, Spetzger et al 1995) the critical issues of the magnitude of such shifts, changes with depth and impact upon neuronavigation have not previously been addressed. Despite this, concern over the effects of post-imaging brain distortion on accuracy of image-guidance has prompted the development of elaborate methods to circumvent this perceived problem. These include insertion of ball bearings or catheters to correct for shifts during tumour resection (Kelly 1993), image updating with ultrasound (Bucholz et al 1996, Koivukangas et al 1993, Trobaugh et al 1994), CT (Kwoh et al 1988, Lunsford et al 1996) and even intra-operative MRI (Tronnier et al 1997).

The underlying causes of post-imaging brain distortion are likely to be both pharmacological and surgical. Pharmacological factors include manipulations of total and cerebral blood volume, diuretic administration and mechanical ventilation. Whilst the effects of such manipulations on intracranial pressure have been extensively studied, the specific effect of these upon the volumes of grey matter, white matter, CSF, tumour and oedematous brain is not clear. What is more, differential effects on such tissues would inevitably lead to complex post-imaging brain distortion rather than simple total brain volume changes. The major surgical factors giving rise to brain distortion are pressure changes on skull opening, the action of unopposed gravity, CSF withdrawal, retraction and tissue removal. However, the impact of these is neither well understood nor

extensively researched, most particularly with regard to the impact upon accuracy in Image-Guided Neuroendoscopy.

Although analysis of pre-operative MRI features for the lesions in the study group revealed such banal findings as that meningiomas are superficial and provoke oedema, this data was vital to the later analysis of correlations between these features and the recorded shifts. Similarly, the finding that overall brain shift increased through the operation was expected and the magnitude of shifts, for example the mean shift at opening of 4.6mm, was unremarkable. However, analysis of the brain shifts according to pathological groups did reveal some important and educational findings.

4.3.1 Brain Distortion According to Surgical Pathology

Whilst the magnitude and correlations of post-imaging brain distortion described here provides data highly pertinent to open neurosurgical procedures, the relevance of these to IGN may be less transparent. The importance of these measurements is three-fold. Firstly the provision of data on the potential magnitude of shift for pathologies amenable to endoscopic surgery. Secondly the identification of predictive factors, which enable lesions which will produce marked shift to be identified prior to surgery. Thirdly the advent of endoscope-assisted neurosurgery for a variety of lesions and the potential for IGN to be employed on solid tumours indicates the importance of understanding these shifts in all pathological groups. Furthermore, shift measurements taken during epilepsy cases, with opening of the lateral ventricle, served to assess the impact of CSF escape.

Meningioma

This group displayed relatively consistent and group-specific patterns of brain distortion, which can be exploited. Thus, in meningiomas shift of the cortex on opening was found to be modest whilst shift at depth and shift of the cortex at completion were significantly greater than in other groups. The direction of shift also followed a consistent pattern in meningiomas with bulging on opening, bulging at the deepest tumour margin and infalling at completion in the majority. The implication for image-guidance is that during meningioma surgery flap positioning and tumour margin delineation can be relied upon, but the deep tumour margin will be elevated towards the surgeon and encountered sooner than indicated on the image-guidance system – a potentially serious discrepancy. However, it should be noted that in this group deep tumour margin represents compressed cortex and the method of measuring tumour bed shift after complete tumour removal may over-estimate the shift during resection, when the bulging of normal brain is inhibited by the presence of residual tumour.

Cerebral Gliomas

Gliomas exemplify the desirability of accurate image-guidance at depth when tumour margins are poorly demarcated, maximal removal desired and when eloquent brain abuts the lesion. Fortunately the pattern of shifts revealed by this study complement this role for navigation during glioma surgery. Thus, shift of the deepest tumour margin was significantly less in gliomas than that seen in meningiomas and was less than both the shift of cortex on opening and at completion in gliomas. In addition

correlations were identified between the magnitude of shift at depth and both the pre-operative image measures of tumour volume and midline shift. The implication for neuronavigation in glioma surgery is that image-guided resection is feasible and reliable but should be used with caution where pre-operative images reveal a particularly large mass with marked deviation of the midline.

Non-Gliomatous Intra-Axial Lesions

These lesions were significantly smaller, produced significantly less midline shift and provoked less oedema than those of other groups. Therefore, it is not surprising that the shift at depth in this group was significantly less than for the other groups. But, despite both the small mean size and the low associated shifts, there was a strong correlation between tumour volume and shift at depth. The implication is that post-imaging brain distortion is small in these cases, is least at depth and that image-guidance should be highly reliable. In addition, reduced accuracy may be predicted if the lesion is unusually large in size on the pre-operative MRI. These findings are most encouraging as such lesions would be particularly amenable to future developments of IGN.

Skull Base Lesions

The characteristics of these lesions are remarkable for the low incidence of oedema and the small magnitude of each shift, both of which were significantly lower than all other groups. These factors predict good reliability during neuronavigation and IGN for skull base lesion.

4.3.2 Error Prediction in Clinical Practice

The determination of correlations between intra-operative brain shifts and features on the pre-operative images enabled prediction of the relative magnitude of shift expected in an individual case. Thus, shift at depth is correlated with shift of the cortex on opening, tumour volume and presence of oedema. Therefore, increased shift is predicted when these features are above the average for the group. The most important results in relation to Image-Guided Neuroendoscopy are the Group III findings. Endoscopy is currently aimed at such non-gliomatous deeply seated pathologies and is minimally invasive in nature. These factors result in low predicted values for post-imaging brain distortion in IGN for these cases. However, the potential application of IGN to a wider range of indications makes the findings for other groups highly relevant also.

4.4 FRAMELESS STEREOTAXY

Whilst neuronavigation has become widely accepted as advantageous in open cranial surgery the technique has, until now, had little impact on traditionally frame-based stereotactic procedures. The reasons for this included the initial presumption that neuronavigation was intrinsically less accurate than frame-based stereotaxy and the absence of satisfactory instrument-guides for frameless stereotaxy. Laboratory investigations have now demonstrated a high degree of accuracy for both optical and arm-based image-guidance systems (Fuchs et al 1996, Maurer et al 1997, Rohling et al 1995) and the inadequacies of adapted neurosurgical arms have been overcome by the adjustable, locking, adaptable instrument holder (Dorward et al 1997). The resultant method of frameless stereotaxy has combined flexibility, simplicity and unimpeded access to the skull with precise and undeviating instrument guidance. The surgeon may select from virtually infinite entry points, trajectories and targets whilst viewing corresponding image reformats. This has enabled rapid and intuitive selection of the optimum approach to any target.

4.4.1 Phantom Accuracy Measurements

The phantom tests of localisation accuracy showed that the magnitude of error for frameless stereotaxy was at least comparable with that accompanying frame-based stereotaxy. The investigations of Maciunas, Galloway and co-workers (Maciunas et al 1992, Maciunas et al 1994) revealed that the application accuracy of the Cosman-Roberts-Wells system was to 1.8mm with a standard deviation of 1.1mm giving a 95%

confidence limit (CI) of 3.6 mm. By comparison the error of phantom frameless stereotaxy, with the same scanning parameters, was 1.1mm with a SD of 0.5mm giving a 95% CI of 2.1mm. The phantom frameless stereotaxy experiments described here also revealed that error with CT was significantly lower than for MR-directed procedures. This is in agreement with the findings for frame-based stereotaxy and reflects both the greater geometric stability of CT and the smaller voxel sizes. Similarly, 2mm CT slices provided significantly more accurate guidance than 3mm slices in frameless stereotaxy and slice thickness has been shown to be the major determinant of error in CT-directed frame-based stereotaxy (Bucholz et al 1993, Maciunas et al 1994). Once again, the finding that 3mm helical CT was significantly more accurate than 3mm axial CT was in accordance with the expected improvement in accuracy with smaller voxel volumes. It is interesting to note that in these experiments the mean error of phantom frameless stereotaxy closely mirrored the MID for that imaging study, implying that the limiting factor to accuracy of frameless stereotaxy was voxel size.

The phantom measurements of MRI-directed frameless stereotactic localisation revealed a mean error of 1.4mm. Reports in the literature of comparable phantom accuracy measurements for MRI-directed frame-based stereotaxy reveal localisation errors of up to 5 to 10mm (Burchiel et al 1996, Derosier et al 1991, Walton et al 1997). The superior accuracy of frameless MRI-directed stereotaxy may be explained through reductions in image distortions. Thus, frame registration with peripheral N-fiducials is inherently less accurate than when the more central skin surface fiducials are used. In addition, the size of some MRI-compatible frames precludes the use of a head coil, the

frames themselves cause field distortions (Burchiel et al 1996, Maciunas et al 1996), and frame geometry may distort during pin tightening (Kamiryo & Laws 1996).

4.4.2 Advantages in Clinical Practice and In vivo Accuracy

The clinical series of frameless stereotactic biopsies demonstrated several of the advantages of this method over classical frame-based stereotactic techniques. Firstly, patients were imaged without anaesthetic, reducing scanning time, medical personnel requirements and patient risk. Secondly, compared with frame-based biopsy, theatre time was significantly reduced (Alberti et al 1996). Thirdly, the frameless method could be applied equally to the guidance of biopsy needles, biopsy forceps, ventricular catheters, depth electrodes or endoscopes and might readily be adapted to guide further instruments. Fourthly, MRI-directed stereotaxy could be undertaken without MRI-compatible surgical equipment. Fifthly, additional targets could be selected at any point during the procedure, without further imaging. Sixthly, surgical access to the skull was unimpeded and a burr-hole procedure could be converted to an open operation without difficulty and with continued guidance. The clinical series also served to validate the frameless method of biopsy retrieval as all specimens were diagnostic and no complications were encountered.

When the early post-operative MRI studies were obtained, to determine the in vivo error of frameless stereotactic biopsy, the biopsy site was found to be visible with remarkable clarity. Image fusion enabled the biopsy error to be determined by simple subtraction of the co-ordinate values for the intra-operative target and the biopsy site.

This provided linear x, y and z measurements, with a reassuringly low mean error of 2.3mm. The method employed for image fusion is well established with an accuracy of less than 1.5mm (West et al 1997) for CT to MRI fusion. Thus, the fusion of identical MRI scans, as performed here, would be expected to achieve considerably better accuracy. In addition, the use of surface fiducials, which were retained in position for the majority of the post-operative MRI scans, has been demonstrated to allow image fusion with an error of 0.25mm (Ellis et al 1996). Whilst the method is simple to apply it is dependent upon the anatomical knowledge of the operator, but this was not foreseen as a difficulty in this investigation. Whilst a variety of more elaborate methods have been developed (Kall et al 1996) these were neither available nor considered necessary to the completion of the task.

Whilst there are no directly comparable studies of in vivo accuracy for frame-based stereotactic biopsy in the literature, the phantom accuracy results imply that these would be at least as great for frame-based systems. Such values provide a valuable indication of the confidence with which a structure may be reached in clinical practice. Thus, with the frameless method, to avoid a nearby structure with 95% confidence when selecting a biopsy target from an axial image slice the target must lie on average 4.3mm distant (mean error + 2 SD). When three dimensions are considered, such as when the target is an anatomical structure in functional neurosurgery, the error measurements obtained should be converted to vectors, which are ipso facto much greater than their constituent linear errors. Thus, the mean in vivo Euclidean error for frameless stereotactic biopsy was 4.8mm, which represents an error volume of 0.46cm^3

and a mean volume of 95% confidence of $2.75cm^3$. Such values have clear clinical

significance and in this light it is important to appreciate that all phantom frameless

stereotaxy accuracy measurements were Euclidean.

4.5 IMAGE-GUIDED NEUROENDOSCOPY

Neuroendoscopy has become established as a valuable instrument in the contemporary practice of neurosurgery. The scope and indications of endoscopic procedures continue to broaden and endoscopic techniques are adopted ever more widely. With the development of image-guidance and the frequency of disorientation during endoscopy, the combination of navigation with neuroendoscopy was a natural progression. The envisaged advantages were of both providing guidance during standard endoscopic cases and of enabling expansion of the possible indications for endoscopy. Frame-based stereotactic guidance of the endoscope has been advocated as this enables targeted insertion and ensures orientation (Caemert & Abdullah 1993, Goodman 1993, Grunert et al 1994, Hellwig et al 1994). However, this method is cumbersome, invasive, time-consuming and severely restricts the freedom of movement during surgery. Ultrasound-guided endoscopy (Auer 1992, Yamakawa et al 1994) has also been developed to aid orientation and identification of anatomical relations, but ultrasound provides a markedly distorted image, of relatively low resolution and is highly operator-dependent. In contrast, neuronavigation systems provide image-guidance that is interactive, rapid and ergonomic.

Attachment of a rigid endoscope to the articulated arm of the Viewing Wand has been reported (Drake et al 1994) but the arm again limits movement, range and rotation of the endoscope. In addition the arm does not lock in position, making the combined tools heavy and awkward, and no assessment of accuracy was described. The combination of a sonic digitiser with an endoscope has also been reported (Rhoten et al

1997), but this suffered from tracking interference (Bucholz & Smith 1993) and required the pointer to occupy the instrument channel, precluding guidance during endoscopic surgery. in contrast, the system developed for Image-Guided Neuroendoscopy during this investigation involved the coupling of an optical tracking system with an operating endoscope, which combined the freedom of movement of freehand endoscopy, flexibility of interactive image display and accurate real time tracking with direct endoscopic visualisation.

4.5.1 Phantom Accuracy Measurements

When the accuracy of point localisation by the tracked endoscope was examined, in the series of laboratory phantom investigations, the mean error was found to be 1.8mm for all imaging modalities and protocols. Whilst this level of error was encouraging, the finding that the mean error of point localisation with 2mm Sequential CT was just 0.9mm indicated that a highly accurate instrument had been developed. However, the tracked endoscope was significantly less accurate than the short straight system pointer, achieving an accuracy similar to that for the bayonet pointer. These findings are consistent with the expectation that pointer accuracy will be reduced as the distance from LED's to tip increases, this length being similar for the endoscope and bayonet pointer. Whilst again acknowledging the underestimation of clinical error by phantom experiments, the magnitude of error discovered would be expected to provide an accurate and reliable clinical tool. This is supported when these results are compared with the error inherent in frame-based stereotaxy. As previously described, the lowest

mean error achieved by stereotactic frames in the experiments of Maciunas and Galloway was 1.8mm with 2mm axial CT-guidance. With this level of error, stereotactic frames have proven reliable and accurate clinical tools with low associated complication rates. Therefore, with a lower mean phantom error for similar imaging, Image-Guided Neuroendoscopy would be expected to perform equally well in clinical practice.

4.5.2 Impact of IGN on Surgical Practice

The clinical series of five Image-Guided Neuroendoscopic operations was undertaken to evaluate the developed technique. This was highly successful as each case was completed without undue difficulty, the system performed well and the guidance appeared accurate at all stages of the procedures. In addition, the availability of image-guidance during several of these endoscopic procedures proved extremely valuable. Indeed, at least two of the five cases could not have been completed without guidance and the novel Image-Guided Neuroendoscope provided this interactively, in real time and accurately.

Clinical application of the Image-Guided Neuroendoscope also highlighted some of the advantages of this instrument. The interactive orthogonal display of volumetric data sets enabled precise pre-planning of entry point, target and trajectory. Image to patient registration and pointer guidance led to accurate transfer of the entry plan to the patient, and guidance of the endoscope during insertion enabled the optimum ventricular cannulation to be achieved. Intra-operative tracking ensured that orientation was maintained throughout the procedures and anatomical relations were demonstrated,

which were not directly visible. Furthermore, these advantages were obtained without compromise of the freedom of movement so essential to endoscopic surgery.

Thus, the envisaged impacts of IGN are; firstly, the provision of guidance during insertion and orientation during endoscopy, reducing the risks of misplacement and disorientation without losing the freedom of movement required for effective surgery. Secondly, the provision of image-guidance is expected to enable difficult endoscopic procedures to proceed safely where previously they may have been abandoned. Thirdly, the registered scan data will enable obscured peri-ventricular structures to be operated upon with confidence and accuracy where previously transventricular biopsy has been somewhat capricious. Finally, image-guidance, along with continued improvements in instrumentation, has the potential to facilitate the endoscopic resection of intra-parenchymal lesions. The envisaged method would be stereotactic implantation and, initially, blind debulking of the lesion centre, progressing to endoscopic and image-guided resection when a cavity has been developed. The putative advantages of such a technique would be those of minimal access and stereotactic guidance. Whilst the overall number of adult cases currently requiring such an approach is small the increasing acceptance of endoscopy and application of IGN in paediatrics may significantly raise the potential caseload.

4.5.3 Correction of Optical Distortion

Distortion of the image in endoscopy is both troublesome during surgical intervention and precludes registration of the endoscope image with reformatted scan

data. The surgeon is most aware of optical distortion when an instrument is advanced into the endoscopic view from a side port in the endoscope carrier. The instrument tip appears to move in an arc across the operative field, usually missing the central target by some millimetres. The instrument may be moved onto the target by adjusting the endoscope position, with the instrument tip stationary, but this risks inadvertent snagging of susceptible structures. This surgical inadequacy and the intention to experiment with graphics necessitated the development of a method for the correction of the endoscope image distortion.

The method chosen for image distortion correction proved straightforward and reliable, successfully correcting the grid pattern, both when perpendicular and at an angle. Whilst minute imperfections were still discernible in the corrected grid image these errors were insufficient to seriously impair later registration or surgical guidance. These residual distortions are presumed to arise from some non-radial lens distortions, which are not addressed with the method of correction described. Whilst further correction might be achieved through the addition of another correction technique, such as decentering distortion correction (Weng et al 1992), the increased cost in computing time and the minor level of inaccuracy addressed make this unlikely to be rewarding.

4.5.4 Graphic Overlays and Image Reconstructions

Although virtual endoscopic images of the ventricular surface were reconstructed from segmentations of several image data sets this was found to be both highly time-consuming and disappointing. The level of anatomical detail visible in such surface

renderings was so far inferior to the endoscope video image as to be unhelpful and was certainly insufficient to conduct a surgical procedure safely. Therefore, this investigation demonstrated that the better solution to the provision of anatomical information from scan data was the overlay of graphics onto the corrected endoscope image, which remained the surgical view. However, reconstruction of the entire surface (phantom, skin of the head or brain) did provide useful information on the orientation of the endoscope and proved a worthwhile display to employ in the fourth viewport of the navigation system during insertion and freehand endoscopy.

Trials of various graphic outlines and representations rapidly demonstrated the need for simplicity and clarity rather than detail or perspective views. Therefore, single outlines of important structures and targets were adopted for the assessment of graphic overlay accuracy. This required endoscope tracking, video capture, distortion correction, image segmentation, graphic overlay and offset measurement. The mean error of graphic overlay was just 2.2mm, in these phantom experiments. This appears an acceptable level of error for clinical introduction of this technique, where graphic overlay would provide supplementary information, relating to structures not visible within the field of view. However, such additional anatomical information, in conjunction with the array of neuronavigation tools, may enable the wider application of Image-Guided Neuroendoscopy to procedures previously outside the remit of endoscopy.

5.1 CONCLUSIONS

The overall aim of this investigation was the development of Image-Guided Neuroendoscopy, with additional aims of assessing graphic overlays and virtual endoscopy. These aims have been successfully accomplished and supplementary investigations undertaken to establish the accuracy of the novel instrument in clinical use. The novel IGN tool was validated through a series of clinical cases, performing far beyond expectation and, in certain cases, enabling procedures to proceed where previously they would not. The enthusiasm of the operating surgeons for this instrument, following these experiences, has been a great source of gratification.

At the outset of this project a prototype navigation system was selected. This was an appropriate type of system, enabled the addition of the required tools for the project and was accompanied by a close collaboration with the system software engineers. However, the prototype itself required assessment, development and clinical validation. These tasks were accomplished through the series of laboratory phantom investigations, development planning with the software engineers and the application of the system to a wide variety of clinical procedures. Through all phases of the project the navigation system performed up to and beyond expectation, was reliable and has become a testament to the success of this collaboration.

Through experience with the navigation system in clinical use and analysis of the factors that could impair IGN, the issue of brain shift became prominent, and the dearth of quantitative data on this subject became apparent. Therefore, the additional study of post-imaging brain distortion was designed and undertaken to rectify this deficit in the

understanding of image-guidance, and to enable a logical approach to the estimation of brain shift. Whilst the magnitude of shift in certain cases was large, the overall results confirmed the impression that distortion need not negate the reliability of neuronavigation. More importantly, the discovery of differences between pathological groups demonstrated in which cases, and when, neuronavigation could be relied upon and when not. The encouraging aspect for endoscopic surgery was that shift was minimal in the cases amenable to endoscopic resection and in the pathologies that are potentially operable via IGN, or IGN-assisted microsurgery. Therefore, the conclusion from the brain shift studies is that post-imaging brain distortion does not negate image-guidance, that each pathology has a characteristic pattern of behaviour and that excessive shift may be predicted pre-operatively in many cases.

The introduction of IGN also required the development, assessment and validation of the novel technique of frameless stereotaxy. This was accomplished through the introduction of the adjustable, locking arm and the results of the laboratory phantom investigations into accuracy were extremely encouraging. Recognition that these may be seriously underestimating clinical errors and the desire to investigate the true accuracy of stereotaxy led to the planning and execution of the in vivo accuracy study. The results of this were most informative and of importance to both frameless and frame-based stereotaxy. Thus, the conclusion from these frameless stereotaxy studies was that the method employed was accurate, appropriate and clinically valid. In addition, frameless stereotaxy was shown to provide some noticeable advantages over the traditional frame-based procedure.

The final phase of this project was the correction of endoscope image distortion for registration to scan data, input of graphic overlays and the assessment of virtual endoscopy. Unfortunately the latter proved to be so far inferior to true endoscopic images that the segmentation of ventricular surfaces to reconstruct endoscope views was abandoned. However, simple outlines of anatomical structures appeared to provide an excellent method of enhancing the information available to the operating surgeon, within the endoscope image, making virtual endoscopy an unnecessary complication. Whilst graphics injection was not achieved in real time during the project, the process was achieved and the accuracy of the overlay determined to be sufficient. The conclusion of this section was that a very valuable method of information presentation had been achieved, with a good level of accuracy, and that this method has wide potential in several fields of surgery.

REFERENCES

Abdullah J, Caemaert J. (1995) Endoscopic management of craniopharyngiomas: a review of 3 cases. Minim Invasive Neurosurg 38(2): 79-84

Alberti O, Dorward NL, Kitchen ND, et al: (1996) Neuronavigation - impact on operating time. XIIth Meeting of the World Society for Stereotactic and Functional Neurosurgery. Lyon, July 1-4, 1997. Stereotact Funct Neurosurg 67:100-101.

Apuzzo MLJ, Chandrasoma PT, Cohen D Zee CS, Zelman V. (1987) Computed imaging stereotaxy: experience and perspective related to 500 procedures applied to brain masses. Neurosurgery 20:930-937.

Auer LM. (1985) Endoscopic evacuation of intracerebral haemorrhages. High-tech surgical treatment – a new approach to the problem? Acta Neurochir (Wien) 74:124-128.

Auer LM, Deinsberger W, Niederkorn K, Gell G, Kleinert R, Schneider G, Holzer P, Bone G, Mokry M, Korner E et al. (1989) Endoscopic surgery versus medical treatment for spontaneous intracerebral hematoma: a randomized study. J Neurosurg 70:530-535.

Auer LM. (1992) Ultrasound stereotaxic endoscopy in neurosurgery. Acta Neurochir (Wien) Suppl 54:34-41.

Bale RJ, Vogele M, Freysinger W, Gunkel AR, Martin A, Bumm K, Thumfart WF. (1997) Minimally invasive head holder to improve the performance of frameless stereotactic surgery. Laryngoscope 107:373-377.

Barnett GH, Kormos DW, Steiner CP Weisenberger J. (1993a) Use of a frameless, armless stereotactic wand for brain tumour localization with 2-D and 3-D neuroimaging. Neurosurgery 33:674-678.

Barnett GH, Kormos DW, Steiner CP Weisenberger J. (1993b) Intraoperative localization using an armless, frameless stereotactic wand: Technical note. J Neurosurg 78: 510-514

Barnett GH, Steiner CP, Weisenberger J: (1996) Target and trajectory guidance for interactive surgical navigation systems. Stereotact Funct Neurosurg 66:91-95.

Bradford R, Thomas DGT, Bydder GM. (1987) MRI-directed stereotactic biopsy of cerebral lesions. Acta Neurochir Suppl Wien 39:25-27.

Brown RA. (1979) A computerized tomography-computer graphics approach to stereotactic localization. J Neurosurg 50:715-720.

Brown RA, Roberts TS, Osborne AG. (1980) Stereotaxic frame and computer software for CT-directed neurosurgical localization. Investigative Radiology 15(4): 308-312.

Bucholz RD, Ho HW, Rubin JP: (1993) Variables affecting the accuracy of stereotactic localization using computerized tomography. J Neurosurg 79:667-673.

Bucholz RD, Pittman T. (1991) Endoscopic coagulation of the choroid plexus using the Nd:YAG laser: initial experience and proposal for management. Neurosurgery 28:421-426.

Bucholz RD, Smith KR. (1993) A comparison of sonic digitizers versus light emitting diode-based localization. In: Maciunas RJ. (ed) Interactive image-guided neurosurgery AANS Publications, Park Ridge, IL, USA, pp179-200.

Bucholz R, Sturm C, Henderson J. (1996) Detection of brain shift with an image guided ultrasound device. Acta Neurochirurgica 138(5): 627

Burchiel KJ, Nguyen TT, Coombs BD, et al: (1996) MRI distortion and stereotactic neurosurgery using the Cosman-Roberts-Wells and Leksell frames. Stereotact Funct Neurosurg 66:123-136.

Caemert J, Abdullah J. (1993) Diagnostic and therapeutic stereotactic cerebral endoscopy. Acta Neurochir (Wien) Suppl 124(1): 11-13

Clarke RH, Horsley V. (1906) On a method of investigating the deep ganglia and tracts of the nervous system (cerebellum). Br Med J ii:1799-1800

Cohen AR. (1994) Ventriculoscopic surgery. Clin Neurosurg 41:546-562.

Cohen AR, Perneczky A, Rodiewicz GS, Gingold SI. (1995) Endoscope-assisted craniotomy: approach to the rostral brain stem. Neurosurgery 36:1128-1129.

Colchester ACF, Zhao J, Holton-Tainter KS, et al. (1996) Development and preliminary evaluation of VISLAN, a surgical planning and guidance system using intra-operative video imaging. Medical Image Analysis 1:1-18.

Dandy WE. (1922) An operative procedure for hydrocephalus. Johns Hopkins Hosp Bull 33:189-190.

Derosier C, Delegue G, Munier T, et al: (1991) MRI, geometric distortion of the image and stereotaxy. Journal de Radiologie 72:349-353.

Dorward NL, Alberti O, Dijkstra A, et al: (1997) Clinical Introduction of an Adjustable Rigid Instrument-holder for Frameless Stereotactic Interventions. Computer Aided Surgery 2:180-185.

Doshi PK, Lemieux L, Fish DR, Shorvon SD, Harkness WH, Thomas DGT. (1995) Frameless stereotaxy and interactive neurosurgery with the ISG Viewing Wand. Acta Neurochir (Wien) Suppl 64: 49-53

196

Drake JM. (1993) Ventriculostomy for treatment of hydrocephalus. Neurosurg Clin N Am 4:657-666.

Drake JM, Prudencio J, Holowaka S, Rutka JT, Hoffman HJ, Humphreys RP. (1994) Frameless stereotaxy in children. Paediatr Neurosurg 20:152-159

Drake JM, Rutka JT, Hoffman HJ. (1994) ISG Viewing Wand system. Neurosurgery 34:1094-1097.

Ellis RE, Toksvig-Larsen S, Marcacci M, Caramella D, Fadda M. (1996) A biocompatible fiducial marker for evaluating the accuracy of CT image registration. In: Lemke HU et al (eds) Computer Assisted Radiology, Elsevier Science BV, Amsterdam, pp693-698.

Fuchs M, Wischmann HA, Neumann A, Weese J, Zylka W, Sabczynski J, Kuhn MH, Schmitz G, Gieles PMC. (1996) Accuracy analysis for image-guided neurosurgery using fiducial skin markers, 3D CT imaging and an optical localizer system. In: Lemke HU et al (eds) Computer Assisted Radiology, Elsevier Science BV, Amsterdam, pp 770-775.

Fukushima T. (1978) Endoscopic biopsy of intraventricular tumors with the use of a ventriculofiberscope. Neurosurgery 2:110-113.

Fukushima T, Ishijima B, Hirakawa K, Nakamura N, Sano K. (1973) Ventriculofiberscope: a new technique for endoscopic diagnosis and operation. Neurosurgery 38:251-256.

Galloway RL, Maciunas RJ, Edwards CA. (1992) Interactive image-guided surgery. IEEE Trans Biomed Eng 39:1226-1231.

Gill SS, Thomas DGT, Warrington AP, Brada M. (1991) Relocatable frame for stereotactic external beam radiotherapy. Int J Radiat Oncol Biol Phys 20:599-603.

Golfinos JG, Fitzpatrick BC, Smith LR, Spetzler BSE, Spetzler RF. (1995) Clinical use of a frameless stereotactic arm: results of 325 cases. J Neurosurg 83:197-205.

Goodman RR. (1993) Magnetic resonance imaging-directed stereotactic endoscopic third ventriculostomy. Neurosurgery 32:1043-1047.

Gomez H, Barnett GH, Estes ML, Palmer J, Magdinec M. (1993) Stereotactic and computer-assisted neurosurgery at the Cleveland Clinic: review of 501 consecutive cases. Cleve Clin J Med 60(5): 399-410

Griffith HB. (1986) Endoneurosurgery: Endoscopic intracranial surgery. In Symon L, Brihaye J, Guidetti B, Loew F, Miller JD, Nornes H, Pásztor E, Pertuiset B, Yasargil MG (eds) Advances and Technical Standards in Neurosurgery. Springer Verlag, Wien, pp2–24.

Grunert P, Perneczky A, Resch K. (1994) Endoscopic procedures through the foramen interventriculare of Munro under stereotactical conditions. Minim Invasive Neurosurg 37:2-8.

Haneishi H, Yagihashi Y, Miyake Y. (1995) A new method for distortion correction of electronic endoscope images. IEEE Trans Med Imaging 14(3): 548-555

Hellwig D, Bauer BL. (1991) Endoscopic procedures in stereotactic neurosurgery. Acta Neurochir (Wien) Suppl 52:30-32.

Hellwig D, Bauer BL, Dauch WA. (1994) Endoscopic stereotactic treatment of brain abscesses. Acta Neurochir (Wien) Suppl 61:102-105.

Hellwig D, Bauer BL, List-Hellwig E. (1995) Stereotactic endoscopic interventions in cystic brain lesions. Acta Neurochir (Wien) Suppl 64:59-63.

Henderson JM, Eicholz KM, Bucholz RD. (1997) Decreased length of stay and hospital costs in patients undergoing image-guided craniotomies. J Neurosurg 86:367A.

Henderson JM, Smith KR, Bucholz RD.(1994) An accurate and ergonomic method of registration for image-guided neurosurgery. Computerized Medical Imaging & Graphics 18:273-277.

Hirato M, Watanabe K, Takahashi A, Hayase N, Inoue HK, Ohye C. (1994) Use of a frameless isocentric stereotactic system (NEURO-SAT) combined with the intraoperative microrecording. Stereotact Funct Neurosurg 63:80-83.

Horsley V, Clarke RH. (1908) The structure and functions of the cerebellum examined by a new method. Brain 31:45-124.

Huewel N, Perneczky A, Urban V, Fries G. (1992) Neuroendoscopic technique for the operative treatment of septated syringomyelia. Acta Neurochir (Wien) Suppl 54:59-62.

Jho HD, Carrau RL. (1997) Endoscopic endonasal transsphenoidal surgery: experience with 50 patients. Journal of Neurosurgery 87:44-51.

Jones RF, Kwok BC, Stening WA, Vonau M. (1994) The current status of endoscopic third ventriculostomy in the management of non-communicating hydrocephalus. Minimally Invasive Neurosurgery 37:28-36.

Kall BA, Goerss SJ, Stiving SO, Davis DH, Kelly PJ. (1996) Quantitative analysis of a non-invasive stereotactic image registration technique. Stereotact Funct Neurosurg 66:69-74.

Kamiryo T, Laws ERJ: (1996) Stereotactic frame-based error in magnetic-resonance-guided stereotactic procedures: A method for measurement of error and standardization of technique. Stereotact Funct Neurosurg 67:198-209.

Kandel EI, Schavinsky YV. (1972) Stereotaxic apparatus and operations in Russia in the 19th century. J Neurosurg 37:407-411.

Kato A, Yoshimine T, Hayakawa T, Tomita Y, Ikeda T, Mitomo M, Harada K, Mogami H. (1991) A frameless, armless navigational system for computer-assisted neurosurgery. J Neurosurg 74:845-849.

Kelly PJ. (1993) Stereotactic excision of brain tumours. In: DGT Thomas (ed). Stereotactic and Image Directed Surgery of Brain Tumours, Churchill Livingstone, Edinburgh, pp89-109.

Kelly PJ, Kall B, Goerss S, Earnest F. (1986) Computer assisted stereotaxic resection of intra-axial brain neoplasms. J Neurosurg 64:427-439.

Kelly PJ, Kall BA, Goerss SJ. (1988) Results of computed tomography-based computer-assisted stereotactic resection of metastatic intracranial tumours. Neurosurgery 22:7-17.

Koivukangas J, Louhisalmi Y, Alakuijala J, Oikarinen J. (1993) Ultrasound-controlled neuronavigator-guided brain surgery. J Neurosurg 79:36-42.

Kosugi Y, Watanabe E, Goto J, Watanabe T, Yoshimoto S, Takakura K, Ikebe J (1988) An articulated neurosurgical navigation system using MRI and CT images. IEEE Trans Biomed Eng 35:147-52.

Kwoh YS, Hou J, Jonckheere EA, Hayati S. (1988) A robot with improved absolute positioning accuracy for CT guided stereotactic brain surgery. IEEE Trans Biomed Eng 35:153-60.

Laborde G, Klimek L, Harders A, Gilsbach J. (1993) Frameless stereotactic drainage of intracranial abscesses. Surg Neurol 40:16-21.

Leksell L. (1950) A stereotaxic apparatus for intracerebral surgery. Acta Chir Scand 99:229-233.

Lewis AI, Crone KR, Taha J, van Loveren HR, Yeh HS, Tew JM. (1994) Surgical resection of third ventricle colloid cysts. Preliminary results comparing transcallosal microsurgery with endoscopy. J Neurosurg 81:174-178.

Lewis AI, Keiper GL, Crone KR. (1995) Endoscopic treatment of loculated hydrocephalus. J Neurosurg 82:780-785.

Lunsford LD, Kondziolka D, Bissonette DJ. (1996) Intraoperative imaging of the brain. Stereotact Funct Neurosurg 66: 58-64.

Maciunas RJ. (1993) In: Interactive Image-Guided Neurosurgery, AANS Publications, Park Ridge, IL USA.

Maciunas RJ, Berger MS, Copeland B, Mayberg MR, Selker R, Allen GS. (1996) A technique for interactive image-guided neurosurgical intervention in primary brain tumors. Neurosurgery Clinics of North America 7:245-466.

Maciunas RJ, Fitzpatrick JM, Gadamsetty S, Maurer CRJr. (1996) A universal method for geometric correction of magnetic resonance images for stereotactic neurosurgery. Stereotact Funct Neurosurg 66:137-140.

Maciunas RJ, Galloway RL, Latimer JW, et al: (1992) An independent application accuracy evaluation of stereotactic frame systems. Stereotact Funct Neurosurg 58:103-107.

Maciunas RJ, Galloway RLJ, Latimer JW: (1994) The application accuracy of stereotactic frames. Neurosurgery 35:682-694.

Maurer CRJ, Fitzpatrick JM, Wang MY, Galloway RLJr, Maciunas RJ, Allen GS. (1997) Registration of head volume images using implantable fiducial markers. IEEE Transactions on Medical Imaging 16:447-462.

Mixter WJ. (1923) Ventriculoscopy and puncture of the third ventricle. Boston Med Surg J 188:277-278.

Nakajima S, Atsumi H, Kikinis R, Moriarty TM, Metcalf DC, Jolesz FA, Black PM. (1997) Use of cortical surface vessel registration for image-guided neurosurgery. Neurosurgery 40:1201-1208.

Neal JH. (1995) An endoscopic approach to cysticercosis cysts of the posterior third ventricle. Neurosurgery 36:1040-1043.

Oka K, Yamamoto M, Ikeda K, Tomonaga M. (1993) Flexible endoneurosurgical therapy for aqueductal stenosis. Neurosurgery 33:236-242.

Ostertag CB, Mennel HD, Kiessling M. (1980) Stereotactic biopsy of brain tumours. Surg Neurol 14:275-283.

Pople IK, Ettles D. (1995) The role of endoscopic choroid plexus coagulation in the management of hydrocephalus. Neurosurgery 36:698-701.

Putnam TJ. (1935) Results of the treatment of hydrocephalus by endoscopic coagulation of the choroid plexus. Arch Pediatr 52:676-685.

Redfern RM. (1989) History of stereotactic surgery for Parkinson's disease. Br J Neurosurg 3:271-304.

Regis J, Bouillot P, Rouby-Volot F, Figarella-Branger D, Dufour H, Peragut JC. (1996) Pineal region tumours and the role of stereotactic biopsy: review of the mortality, morbidity and diagnostic rates in 370 cases. Neurosurgery 39:907-912.

Reinhardt HF, Horstmann GA, Gratzl O. (1993) Sonic stereometry in microsurgical procedures for deep-seated brain tumors and vascular malformations. Neurosurgery 32:51-57.

Rhoten, RLP, Luciano MG, Barnett GH. (1997) Computer-assisted endoscopy for neurosurgical procedures: technical note. Neurosurgery 40:632-637.

Roberts DW, Strohbehn JW, Hatch JF, Murray W, Kettenberger H. (1986) A frameless stereotaxic integration of computerized tomographic imaging and the operating microscope. J Neurosurg 65:545-549.

Roessler K, Ungersboeck K, Dietrich W, Aichholzer M, Hittmeir K, Matula C, Czech T, Koos WT. (1997) Frameless stereotactic guided neurosurgery: clinical experience with an infrared based pointer device navigation system. Acta Neurochirurgica 139:551-559.

Rohling R, Munger P, Hollerbach JM, Peter T. (1995) Comparison of relative accuracy between a mechanical and an optical position tracker for image-guided neurosurgery. Journal of Image Guided Surgery 1:30-34.

Ryan MJ, Erikson RK, Levin DN Pelizzari CA, Macdonald RL, Dohrmann GJ. (1996) Frameless stereotaxy with real-time tracking of patient head movement and retrospective patient-image registration. J Neurosurg 85:287-292.

Sandeman DR, Patel N, Chandler C, Nelson RJ, Coakham HB, Griffith HB. (1994) Advances in image-directed neurosurgery: preliminary experience with the ISG Viewing Wand compared with the Leksell G frame. Br J Neurosurg 8:529-544.

Sandeman DR, Gill SS. (1995) The impact of interactive image guided surgery: the Bristol experience with the ISG/Elekta viewing Wand. Acta Neurochirurgica (Suppl) 64:54-58.

Scarff JE. (1951) Treatment of obstructive hydrocephalus by puncture of the lamina terminalis and floor of the third ventricle. J Neurosurg 8:204-213.

Sheldon CH, McCann G, Jaques S, et al. (1980) Development of computerised microstereotaxic method for localization and removal of minute CNS lesions under direct 3-D vision: technical report. J Neurosurg 52:21-27.

Silverman SG, Collick BD, Figueira MR, Khorasani R, Adams DF, Newman RW, Topulos GP, Jolesz FA. (1997) Interactive MR-guided biopsy in an open-configuration MR imaging system. Radiology Vol 1:181.

Sipos EP, Tebo SA, Zinreich SA, Long DM, Brem H. (1996) In vivo accuracy testing and clinical experience with the ISG Viewing Wand. Neurosurgery 39:194-202.

Smith KR, Frank KJ, Bucholz RD. (1994) The NeuroStation - a highly accurate, minimally invasive solution to frameless stereotactic neurosurgery. Comput Med Imaging Graph 18:247-256.

Smith WE, Vakil N, Maislin SA. (1992) Correction of distortion in endoscope images. IEEE Transactions on Medical Imaging 11:117-122.

Spetzger U, Laborde G, Gilsbach JM. (1995) Frameless neuronavigation in modern neurosurgery. Minimally Invasive Neurosurgery 38:163-6.

Spiegel EA, Wycis HT, Marks M, Lee AJ. (1947) Stereotaxic apparatus for operations on the human brain. Science 106:349-350.

Tan KK, Grzeszczuk R, Levin DN, Pelizzari CA, Chen GT, Erickson RK, Johnson D, Dohrmann GJ. (1993) A frameless stereotactic approach to neurosurgical planning based on retrospective patient-image registration. Technical note. J Neurosurg 79:296-303.

Teo C, Rahman S, Boop FA, Cherny B. (1996) Complications of endoscopic neurosurgery. Childs Nervous System 12:248-253.

Thomas DGT, Nouby RM. (1989) Experience in 300 cases of CT-directed stereotactic surgery for lesion biopsy and aspiration of haematoma. Br J Neurosurg 3:321-326.

Trobaugh JW, Richard WD, Smith KR, Bucholz RD. (1994) Frameless stereotactic ultrasonography: method and applications. Comput Med Imaging Graph 18:235-246.

Tronnier VM, Wirtz CR, Knauth M, Lenz G, Pastyr O, Bonsanto MM, Albert FK, Kuth R, Staubert A, Schlegel W, Sartor K, Kunze S. (1997) Intraoperative diagnostic and interventional magnetic resonance imaging in neurosurgery. Neurosurgery 40:891-900.

Tutino M. (1996) Exploration of intracranial structures endoscopically through minimal craniotomies. Plastic and Reconstructive Surgery 97:1027-1033.

Ungersböck K, Aicholzer M, Günther M, Rössler K, Koos W. (1996) Cavernous Malformations: Frame-based versus frameless stereotactic localisation. Acta Neurochirurgica 138:627.

Vinas FC, Zamorano L, Lis-Planells M, Buciuc R, Diaz FG. (1996) Interactive intraoperative localization during resection of intraventricular lesions. Minim Invas Neurosurg 39:65-70.

Vrionis FD, Robertson JH, Foley KT, Gardner G. (1997) Image-interactive orientation in the middle cranial fossa approach to the internal auditory canal: an experimental study. Computer Aided Surgery 2:34-41.

Vrionis FD, Foley KT, Robertson JH, Shea JJ. (1997) Use of cranial surface anatomical fiducials for interactive image-guided navigation in the temporal bone: a cadaveric study. Neurosurgery 40:755-764.

Walker ML, MacDonald J, Wright LC. (1992) The history of ventriculoscopy: where do we go from here? Pediatr Neurosurg 18:218-223.

Walton L, Hampshire A, Forster DC, Kemeny AA, Maciunas RJ, Fitzpatrick JM, Adler JR, Roberts DW, Favre J, Burchiel K. (1997) Stereotactic localization with magnetic resonance imaging: A phantom study to compare the accuracy obtained using two-dimensional and three- dimensional data acquisitions. Neurosurgery 41:131-139.

Watanabe E, Watanabe T, Manaka S, Mayanagi Y, Takakura K. (1987) Three-dimensional digitizer (neuro-navigator): A new equipment for CT-guided stereotaxic surgery. Surg Neurol 27:543-547.

Weng J, Cohen P, Herniou M. (1992) Camera calibration with distortion models and accuracy evaluation. IEEE Trans Med Imaging 14:vol10.

West J, Fitzpatrick JM, Wang MY, Dawant BM, Maurer CRJr, Kessler RM, Maciunas RJ, et al. (1997) Comparison and evaluation of retrospective intermodality brain image registration techniques. J Computer Assisted Tomography 21:554-566.

Westermann B, Trippel M, Reinhardt H. (1995) Optically-navigable operating microscope for image-guided surgery. Minim Invasive Neurosurg 38:112-116.

Wild AM, Xuereb JH, Marks PV, Gleave JRW. (1990) Computerized tomographic stereotaxy in the management of 200 consecutive intracranial mass lesions. Analysis of indications, benefits and outcome. Br J Neurosurg 4:407-415.

Yamakawa K, Kondo T, Yoshioka M, Takaura K. (1994) Ultrasound guided endoscopic neurosurgery - new surgical instrument and technique. Acta Neurochir (Wien) Suppl 61:46-48.

Yeh HS, Taha JM, Tobler WD. (1993) Implantation of intracerebral depth electrodes for monitoring seizures using the Pelorus stereotactic system guided by magnetic resonance imaging. J Neurosurg 78:138-141.

Zamorano LJ, Nolte L, Kadi AM, Jiang Z. (1994) Interactive intraoperative localization using an infrared based-system. Stereotact Funct Neurosurg 63:84-88.

Zinreich SJ, Tebo SA, Long DM, Brem H, Mattox DE, Loury ME, Vander Kolk CA, Koch WM, Kennedy DW, Bryan RN. (1993) Frameless stereotaxic integration of CT imaging data: accuracy and initial applications. Radiology 188:735-742.

APPENDICES

APPENDIX I:

CLINICAL EVALUATION PROTOCOL

1. Patient information

Name   :   ....

Registration number   :   ⊔⊔ ⊔⊔ ⊔⊔ ⊔⊔ ⊔⊔ ⊔⊔

Sex   :   G male
                                          G female

Date of birth (mm - dd - yy)   :   ⊔⊔ - ⊔⊔ - ⊔⊔

**Has the patient signed
informed consent?**   :   ☐ no
                                          ☐ yes

⌐ IF ANSWER IS ' NO' STOP PROCEDURE HERE

History   :   ....
....
....
....
....
....
....
....
....
....
....
....
....

Examination at Presentation   :   ....
....
....
....
....
....
....

Date of admission   :   ⊔⊔ - ⊔⊔ - ⊔⊔

2. Preliminary diagnosis

2.1 *Type of lesion*   :   ☐ tumor:
                                      ☐ meningioma
                                      ☐ glioma
                                      ☐ metastasis
                                      ☐ unknown
                                      ☐ other: ....

                              ☐ vascular:
                                      ☐ avm
                                      ☐ aneurysm
                                      ☐ other:...

                              ☐ epilepsy :

                              ☐ other: ....

2.2 *Number of lesions :*   ☐ 1
                              ☐ multiple: ......

2.3 *Location of lesion(s): hemisphere* ☐ left
                              ☐ right
                              ☐ midline

                 region   ☐ frontal
                              ☐ parietal
                              ☐ temporal
                              ☐ occipital
                              ☐ base of skull
                              ☐ extrensic :
                                               ☐ cerebellar
                                               ☐ brainstem
                 depth   ☐ cortical
                              ☐ subcortical
                              ☐ deep-seated

                              ☐ other :..
                                           ....

3. Patient preparation and marker placement

Stereotactic frame used   :   □ no
                                    □ yes. Frame type: □ Leksell
                                                          □ BRW
                                                          □ CRW
                                                          □ other:...........................

Type of markers used   :   □ fiducial
                                        □ Philips CT
                                        □ Philips MR
                                        □ other, viz.:...
                                    □ anatomical markers, *location to be indicated in Fig.1!*

Location of markers: *Please use recommended marker placement, and indicate in Table 1.*

☞   *In addition use 2 - 3 markers in the area of the craniotomy, at least 5 cm apart from eachother.*
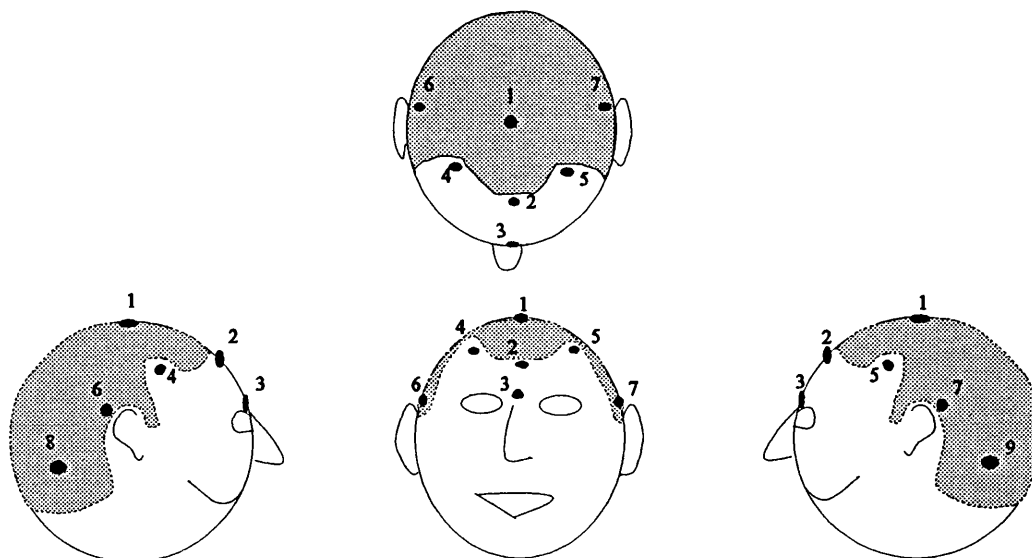
Fig 1. The numbers indicate the recommended position of the fiducial markers in the scan protocol.

218

Table 1. Marker location (*) L=left, R=right, F=frontal, P=parietal, T=temporal, O=occipital

marker in Fig.1	used on patient (indicate "Y" if used, "X" if not used)	additional markers used: (indicate in Fig. 1)	location of the additional markers (*)	
			L/R	F/P/T/O
1		10		
2		11		
3		12		.
4		13		
5				
6				
7				
8				
9				

No. of markers placed   :   ⌊⌊⌋

Markers were placed by   :   ....(name)

Date of markerplacement (dd - mm - yy)   :   ⌊⌊⌋ - ⌊⌊⌋ - ⌊⌊⌋

3. Scan information

Type of scanner : ....

□ *CT:*   [default]

scantype	:	□ slice-to-slice □ volume	[volume]
orientation	:	□ HF/S □ HF/P	[HF/S]
matrix	:	□ 256 □ 320 □ 512	[320]
field of view	:	⊔⊔⊔ mm	
nr of slices	:	⊔⊔	[50]
slice thickness	:	□ 1.5 mm □ 3 mm □ 5 mm □ other: ⊔.⊔ mm	[3]
reconindex (mm)	:	⊔	[2]
kV	:	⊔⊔⊔	[120]
mAs	:	⊔⊔⊔	[175]
angulation	:	⊔⊔	[0]
CF	:	⊔	[1]
contrast agent	:	□ no □ yes	[yes]
		type of contrast :......................................	[Omnipaque 300]
		amount : ⊔⊔⊔ ml	[100]
		flow : ⊔⊔ ml/s	[0]
		delaytime : ⊔ min.	[2]

injection   : ☐ manual   [manual]
                          ☐ motorized
                          ☐ combined manual and motorized

CT head support :   ☐ normal
                      ☐ adapted support for EasyGuide
                      ☐ other:......................................

Date of scan (dd - mm - yy)   : ⊔⊔ - ⊔⊔ - ⊔⊔

Patient arrival in scanner   : ⊔⊔ : ⊔⊔ hrs

Patient departure from scanner   : ⊔⊔ : ⊔⊔ hrs

Actual scan time   : ⊔⊔   min.

Were there any problems during scan?
     ☐ no
     ☐ yes: ☐ patient movement
                       ☐ poor scan quality
                       ☐ skin movement in head support
                       ☐ inadequate coverage
                       ☐ lesion(s) not/badly visible
                       ☐ other:..

Radiologist present   :...(name)
X-ray technician present   :...(name)
Philips support present   :...(name)

□ *MR (standard brain 3D protocol T1):*

Type of scanner : □ **General Electric Vectra 0,5 T**
    □ **General Electrc Signa 1,5 T**

		[default]		[0,5 T]	[1,5 T]
TR	: ⊔⊔,⊔			[45]	[14,2]
TE	: ⊔⊔,⊔			[15]	[3,3]
Flip	: ⊔⊔			[50]	[30]
echo	: ⊔			[1]	----
Matrix	: ⊔⊔⊔ x ⊔⊔⊔			[192 x 192]	[256 x 256]
NEX	: ⊔			[1]	[1]
FOV	: ⊔⊔	[25]	[24]		
Thickness	: ⊔⊔⊔,⊔			[180]	[1,5]
Slices	: ⊔⊔⊔			----	[124]

contrast agent : □ no
    □ yes
        type of contrast : .... [Gaudolineum]

        amount : ⊔⊔⊔ ml   [15 ml]

        delaytime : ⊔ min   [2- 4]
        (inject - scan)
        injection : □ Intravenus
        □ other :..

Date of scan (dd - mm - yy)   : ⊔⊔ - ⊔⊔ - ⊔⊔

Patient arrival in scanner   : ⊔ ⊔:⊔ ⊔ hrs

Patient departure from scanner   : ⊔ ⊔:⊔ ⊔ hrs

Actual scan time   : ⊔ ⊔   min.

Were there any problems during scan?
    ☐ no
    ☐ yes: ☐ patient movement
                    ☐ poor scan quality
                    ☐ skin movement in head support
                    ☐ inadequate coverage
                    ☐ lesion(s) not/badly visible
                    ☐ other:..

Radiologist present   :...(name)
X-ray technician present   :...(name)
Philips support present   :...(name)

5. Image transport

Image transfer to OR by   :   ☐ ODR
                                       ☐ network

Date of transfer (dd-mm-yy) :   ⊔⊔ - ⊔⊔ - ⊔⊔

Were there any problems with the image transfer?
     ☐ no
     ☐ yes :   ☐ took too long time
                             ☐ network problems
                             ☐ incomplete transfer
                             ☐ optical disc problem
                             ☐ other,viz...

6. Surgery, general information

6.1 Administrative data

Surgeon's name : ....

                   ☐ Consultant
                   ☐ Senior Registar
                   ☐ Registar

Assistent's name : ....
OR nurse : ....
Philips attendee : ....

Date of surgery (dd - mm - yy) : ⎿⎿� - ⎿⎿� - ⎿⎿�

6.2 Patient position
☐ supine
☐ prone
☐ sitting
☐ lateral, left side up
☐ lateral, right side up

☐ head turned to right
☐ head turned to left

6.3 Type of procedure
☐ craniotomy
☐ frameless stereotactic procedure
☐ framebased stereotactic procedure
☐ posterior fossa craniectomy
☐ endoscopy
☐ functional procedure :viz.:...
☐ other, viz..

Timings :
    Induction   : ⎿� ⎿�:⎿� ⎿�:⎿� ⎿� hrs

    On table   : ⎿� ⎿�:⎿� ⎿�:⎿� ⎿� hrs

    Knife to skin   : ⎿� ⎿�:⎿� ⎿�:⎿� ⎿� hrs

225

6.4 Theatre lay-out :

Mark with an "--------"the position of the camara array and a "+++"the position of the workstation.

Draw on : 1. Patient orientation
2. Anaesthetst
3. Surgeon
4. Scrub nurse
5. Microscope

7. Registration procedure

7.1 Image markers:

The image markers were found:

☐ **automatically** :

Table 2. *Results of automatic marker search*

marker number in 4th viewport (see Note *1)	corresponds to marker number in protocol (see Fig. 1)	identified marker rejected (if so indicate Y = yes)	state reason for rejection (BIS, OT, see Note *2)
1			
2			
3			
4			
5			
6			
7			
8			
9			
10			
11			
12			
13			
14			
15			
16			

Notes:
*1 the 4th viewport can show 16 slices as maximum (1 is upper left, 16 is lower right). Normally less than 16 markers will be identified. Then only fill in the corresponding part of the table.
*2 BIS = bony landmark in skull, OT = other reason: *please specify !*

The number of markers identified automatically : ⊔ ⊔

□ **manually** :

Table 3. Results of manual marker search

marker number in 4th viewport	corresponds to marker number in protocol (see Fig. 1)	anatomical marker (if yes, indicate Y) * see note 1
1		
2		
3		
4		
5		
6		
7		
8		
9		
10		
11		
12		
13		
14		
15		
16		

Note: *1 indicate anatomical markers additionally in Fig. 1.

Time needed to identify markers manually : ⎵⎵ min.

7.2 Pointer used for registration:
- □ 100 mm straight
- □ 100 mm small bajonet
- □ 130 mm straight
- □ 130 mm strong bajonet
- □ Bipolar forceps
- □ other, viz.:...

identification of pointer:
- □ Philips steel   number: ⎵⎵
- □ EasyGuide   number: ⎵⎵
- □ Other   ....

7.3 Patient-to-image registration and accuracy assessment

Table 4. Registration results

marker nr in 4th Viewport	reason why marker was not usable *see note 1 (NV, SH,	registration 1		registration 2		registration 3	
		marker used ? (Y/N)	nearest marker after registration (see note 2) (mm)	marker used ? (Y/N)	nearest marker after registration (see note 2) (mm)	marker used ? (Y/N)	nearest marker after registration (see note 2) (mm)
1							
2							
3							
4							
5							
6							
7							
8							
9							
10							
11							
12				·			
13							
14							
15							
16							
RMSE and AVERAGE in mm		RMSE: ⊔.⊔	AVERAGE: ⊔.⊔	RMSE: ⊔.⊔	AVERAGE: ⊔.⊔	RMSE: ⊔.⊔	AVERAGE: ⊔.⊔

Note 1: NV = marker not visible for cameras due to patient position   SH = marker shifted too much due to Mayfield clamp
    MR = marker removed before registration   OT = other reason. **Please specify !**

Note 2: Use at least 3 points for assessment of the accuracy
If more than one registration was performed, state reason(s):
  □ unacceptable RMSE
  □ trying to improve RMSE
  □ an error occurred during registration. Specify type of error:..
  ....

8. Registration checkpoints

8.1 Pointer for sterile use:
- ☐ 100 mm straight
- ☐ 100 mm small bajonet
- ☐ 130 mm straight
- ☐ 130 mm strong bajonet
- ☐ Bipolar forceps
- ☐ other, viz.:...

identification of pointer:
- ☐ Philips steel   number: ⊔ ⊔
- ☐ EasyGuide   number: ⊔ ⊔
- ☐ Other   :..

8.2 ☐ *Checkpoints at craniotomy site (**at least 4**)*
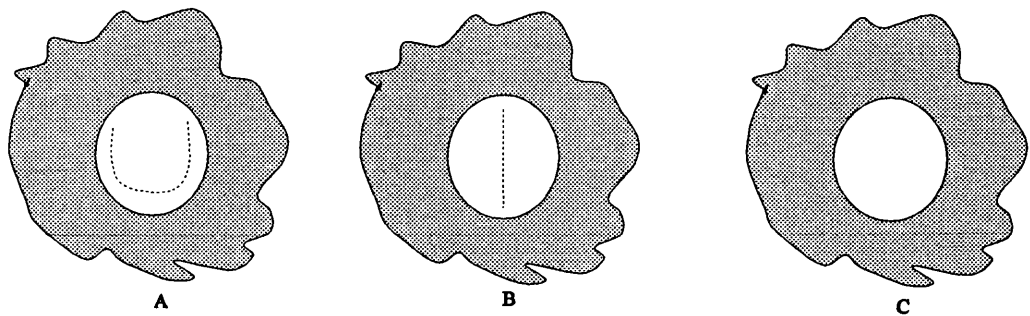
Figure 2. ☐ *A U-shaped incision*   ☐ *B linear incision* ☐ *C indicate other incisionline*
The shaded area is the area (expectedly to be) covered by sterile clo

8.3 Initial checkpoint verification

Please indicate the check points (at least 4) in Fig. 2 or Fig. 3, and store the pointer positions in the system (this will become set 2).

Table 5. Initial verification:

checkpoint number	nearest marker (mm)
1	
2	
3	
4	
5	
6	
AVERAGE :	⊔.⊔ mm

Note: if average value exceeds 3 mm, reregister on set 1!

8.5. Registration result

What was your subjective impression of accuracy after registration during verification?

☐ bad
☐ reasonable
☐ good
☐ excellent

Comment in case of bad:...
....

231

8.6. Tracking
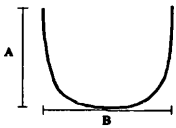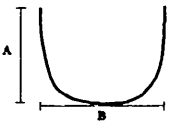
Place   : ☐ Mayfield
                     ☐ Skin
                     ☐ Bone
                     ☐ Mayfield and Skin
                     ☐ Mayfield and Bone

Moment   : ☐ Pre-registration
                     ☐ Before covering
                     ☐ Before skin incision
                     ☐ Before drilling
                     ☐ After removal of boneflap

9. Craniotomyplanning

Please indicate results of planning in Table 6.

Lenght in : ☐ cm

conventional planning			EasyGuide planning		
☐	linear incision	length : ⊔⊔.⊔	☐	linear incision	length : ⊔⊔.⊔
☐	U-shaped incision	A = ⊔⊔.⊔ B = ⊔⊔.⊔	☐	U-shaped incision	A = ⊔⊔.⊔ B = ⊔⊔.⊔
☐	other	describe shape and dimensions	☐	other	describe shape and dimensions

Distance between freehand lesion locus and EasyGuide locus : ☐☐,☐ cm

Plan photo   : ☐ No
                 ☐ Yes

233

10. Intra-operative monitoring : surface checks on bone at craniotomy site

Note : the average nearest distance of checkpoints should be < 3 mm, using 4 points. If not then reregister

TIME(HH:MM) ☞	⊔⊔ : ⊔⊔	⊔⊔ : ⊔⊔	⊔⊔ : ⊔⊔	⊔⊔ : ⊔⊔
checkpoint nr. ⇓	nearest marker (mm)	nearest marker (mm)	nearest marker (mm)	nearest marker (mm)
1	⊔.⊔	⊔.⊔	⊔.⊔	⊔.⊔
2	⊔.⊔	⊔.⊔	⊔.⊔	⊔.⊔
3	⊔.⊔	⊔.⊔	⊔.⊔	⊔.⊔
4	⊔.⊔	⊔.⊔	⊔.⊔	⊔.⊔
5	⊔.⊔	⊔.⊔	⊔.⊔	⊔.⊔
6	⊔.⊔	⊔.⊔	⊔.⊔	⊔.⊔
AVERAGE (mm)	⊔.⊔	⊔.⊔	⊔.⊔	⊔.⊔
reregistered (Y/N) If average is >3.0 mm				
New RMSE (mm) after reregistration	⊔.⊔	⊔.⊔	⊔.⊔	⊔.⊔

TIME(HH:MM) ☞	□ □ : □ □	□ □ : □ □	□ □ : □ □	□ □ : □ □
checkpoint nr. ⇓	distance to nearest checkpoint (mm)	distance to nearest checkpoint (mm)	distance to nearest checkpoint (mm)	distance to nearest checkpoint (mm)
1	□ . □	□ . □	□ . □	□ . □
2	□ . □	□ . □	□ . □	□ . □
3	□ . □	□ . □	□ . □	□ . □
4	□ . □	□ . □	□ . □	□ . □
5	□ . □	□ . □	□ . □	□ . □
6	□ . □	□ . □	□ . □	□ . □
AVERAGE (mm)	□ . □	□ . □	□ . □	□ . □
reregistered (Y/N) If average is >3.0 mm				
New RMSE (mm) after reregistration	□ . □	□ . □	□ . □	□ . □

11. Miscellaneous

Number of burrholes made   : ⊔

Maximum diameter of lesion   : ⊔⊔.⊔ mm

Distance skin - proximal part of the lesion   : ⊔⊔.⊔ mm

Distance skin - distal part of the lesion   : ⊔⊔.⊔ mm

12. Complications and delays in management

Complications   :
- ⊔ Bleeding
- ⊔ Infection
- ⊔ Operative
- ⊔ Neurological deficit
- ⊔ CSF lekkage

Delays in discharge   :
- ⊔ Social
- ⊔ Neurological
- ⊔ Administrative

Total No. of days   : ⊔⊔

13. Surgeon's report

1. Outpatient Review : ⊔⊔ - ⊔⊔ - ⊔⊔

2. Date of discharge : ⊔⊔ - ⊔⊔ - ⊔⊔

3. Nights on ITU : ⊔⊔ nights

4. Estimated total extra time due to EasyGuide :
   ☐ < 5 minutes

   ☐ 5 - 10 minutes

   ☐ > 10 minutes :
   viz...
   ....
   ....
   ....

5. Imaging Requirements :

   Extra scan   : ☐ No
                                         ☐ Yes :   ☐ MRI
                                                          ☐ CT
   Extra hardcopies   : ☐ No
                                         ☐ Yes

   Reduction of scan and hardcopies   :☐ No
                                         ☐ Yes

6. Did you discontinue the use of EasyGuide Neuro prior to the end of surgery?
   ☐ no
   ☐ yes , please explain
       ☐ error in EasyGuide Neuro
       ☐ too much brain shift
       ☐ other, viz...
       ....

237

7. Were differences observed between conventional planning and EasyGuide planning?
- ☐ no

- ☐ yes. Nature of difference:
    - ☐ EasyGuide planning better centered
    - ☐ conventional planning better centered
    - ☐ no difference in centering

    - ☐ EasyGuide planning led to a smaller craniotomy
    - ☐ conventional planning led to a smaller craniotomy
    - ☐ no difference in craniotomy size

    - ☐ EasyGuide planning led more direct towards the target
    - ☐ EasyGuide planning did not lead more directly towards the target

    - ☐ other differences, viz..
    ....

8. Which of the plans seems most appropriate to the specific patient situation?
- ☐ conventional planning
- ☐ EasyGuide Neuro planning

9. Indicate which of the following were improved via the use of EasyGuide Neuro :
- ☐ defining the location of the skin incisionline
- ☐ defining the size of the skin incisionline
- ☐ defining the shape of the skin incisionline

- ☐ defining the location of the craniotomy:
- ☐ defining the size of the craniotomy
- ☐ defining the shape of the craniotomy

- ☐ reduced the number of burrholes compared to conventional planning

- ☐ avoiding critical structures (safety and precision). These criticial structures were:
    - ☐ artery:..
    - ☐ vene:..
    - ☐ functional area:...

- ☐ help decide the extent of resection

10. Were there any signs that EasyGuide was misleading?
- ☐ no
- ☐ yes, explain:...
....

APPENDIX II:

RESULTS RAW DATA

II.I: LABORATORY STUDIES OF NEURONAVIGATION SYSTEM ACCURACY

ii.i.i: Phantom Registration Results

Scan Type	Test Number	RMSE	Mean Nearest Marker	Number of Fiducials
Standard Vectra MRI	1	1.1	1.1	6
	2	1.2	1.0	6
	3	0.9	0.9	6
	4	1.0	0.9	6
	5	1.1	1.1	6
	6	1.3	1.3	11
	7	1.2	1.1	11
	8	1.0	0.9	11
	9	1.1	1.1	11
	10	1.3	1.3	11
	11	0.9	1.1	11
	12	0.9	1.1	11
	13	0.9	1.0	11
	14	0.9	0.8	7
	15	1.0	0.8	10
Signa MRI	1	1.3	1.2	7
	2	1.2	1.2	7
	3	1.6	1.4	11
	4	1.8	1.7	6
	5	1.7	1.5	6
	6	1.9	1.8	6
	7	1.6	1.3	6
	8	1.7	1.5	6
	9	1.8	1.8	6
	10	1.8	1.7	11
	11	1.8	1.6	11
	12	1.9	1.6	11
	13	1.8	1.6	11
	14	1.7	1.4	11
	15	1.6	1.4	11
	16	1.6	1.4	11
	17	1.8	1.6	11
	18	2.2	1.6	9
Fine Vectra MRI	1	1.4	1.3	5
	2	1.4	1.2	5
	3	1.4	1.2	6
	4	1.7	1.4	6
	5	1.4	1.1	6
	6	1.5	1.4	10
	7	1.3	1.3	10
	8	1.6	1.5	10
	9	1.7	1.5	10
	10	1.5	1.3	10
	11	0.9	1.0	6
	12	1.4	1.3	10

ii.i.ii: Point Localisation Experiments; Image Localiser Screw Attachments

Fine Vectra MRI					
Screw No.	Short Pointer	Short Pointer	Short Pointer	Short Pointer	Short Pointer
1	1.1	1.1	1.2	1.3	1.1
2	1.6	1.5	1.6	1.6	1.5
3	1.6	1.6	1.6	1.6	1.6
4	2.0	2.0	1.9	1.9	2.0
5	1.2	1.1	1.1	1.2	1.0
6	1.0	0.9	1.0	1.0	0.9
7	1.8	1.6	1.7	1.7	1.6
8	2.7	2.8	2.7	2.8	2.7
9	1.0	0.9	0.9	0.9	0.9
10	1.6	1.7	1.9	1.7	1.4
11	1.2	1.2	1.4	1.4	1.2
12	2.6	2.7	2.7	2.4	2.6
13	2.0	1.9	2.0	1.8	1.9
14	1.1	1.2	1.2	1.2	1.3
15	0.9	0.8	0.9	0.9	0.9
16	0.9	0.9	0.9	1.0	0.9
17	0.7	0.7	0.7	0.7	0.7
18	1.5	1.6	1.6	1.5	1.6
19	1.3	1.4	1.3	1.5	1.4
	Long Pointer	Long Pointer	Long Pointer	Long Pointer	Long Pointer
1	1.5	1.7	1.6	1.8	1.4
2	1.8	1.7	1.8	1.8	1.7
3	1.8	1.6	1.6	1.4	1.7
4	2.3	2.2	2.3	2.1	2.2
5	1.6	1.6	1.3	1.5	1.4
6	1.0	1.0	1.0	1.1	1.0
7	2.0	2.0	2.0	1.9	2.0
8	2.9	3.0	3.0	2.8	2.8
9	1.5	1.2	1.1	1.3	1.3
10	1.9	1.7	1.7	1.8	1.8
11	1.5	1.8	1.2	1.4	1.5
12	2.9	3.2	3.1	3.1	3.0
13	2.3	2.1	2.1	2.1	2.1
14	1.3	1.4	1.3	1.2	1.2
15	1.0	1.0	1.1	1.0	1.1
16	1.1	1.0	1.6	1.3	1.2
17	1.0	1.1	1.1	1.2	1.4
18	1.8	1.7	1.7	1.9	1.8
19	1.7	1.7	1.7	1.5	1.6

Fine Vectra MRI Continued					
Pointer:	Bayonet Pointer	Bayonet Pointer	Bayonet Pointer	Bayonet Pointer	Bayonet Pointer
1	1.9	1.7	1.7	1.8	1.7
2	1.3	1.3	1.2	1.4	1.3
3	2.5	2.3	2.3	2.4	2.3
4	2.9	3.0	3.1	2.9	2.8
5	1.1	1.0	0.7	0.8	1.0
6	2.3	2.2	2.2	2.2	2.2
7	3.3	3.3	3.3	3.3	3.1
8	3.2	3.1	2.9	2.8	3.0
9	2.6	2.3	2.6	2.3	2.4
10	3.0	3.1	2.7	3.1	2.9
11	2.6	2.0	2.3	2.5	2.4
12	3.9	4.0	4.2	3.9	4.0
13	2.8	2.5	2.7	2.5	2.5
14	2.6	2.3	2.6	2.7	2.5
15	1.8	2.1	1.9	1.9	2.0
16	2.4	2.6	2.5	2.2	2.2
17	2.1	2.3	2.0	2.0	2.1
18	2.4	2.5	2.2	2.2	2.4
19	2.3	2.1	1.9	2.1	2.1

Standard Vectra MRI					
Screw Number	Short Pointer	Short Pointer	Short Pointer	Short Pointer	Short Pointer
1	2.0	1.7	2.0	2.0	1.7
2	1.6	2.0	1.8	1.8	1.7
3	2.1	2.2	2.2	2.2	2.3
4	2.5	2.4	2.4	2.4	2.4
5	2.0	1.8	2.1	2.0	2.1
6	1.7	1.6	1.8	1.8	1.9
7	2.3	2.4	2.4	2.4	2.3
8	2.9	3.0	2.9	2.9	2.8
9	1.7	1.8	1.8	1.9	1.8
10	1.1	1.2	1.2	1.3	1.3
11	0.6	0.9	1.0	0.7	0.9
12	2.2	2.2	2.3	2.4	2.4
13	2.3	2.3	2.3	2.3	2.3
14	2.5	2.4	2.5	2.5	2.4
15	1.3	1.4	1.4	1.4	1.4
16	2.3	2.2	2.3	2.3	2.3
17	1.5	1.3	1.4	1.4	1.4
18	1.5	1.4	1.5	1.5	1.5
19	2.5	2.6	2.8	2.7	2.7

	Long Pointer	Long Pointer	Long Pointer	Long Pointer	Long Pointer
			Standard Vectra MRI Continued		
1	2.1	2.3	2.3	2.1	2.3
2	2.1	2.2	2.0	2.3	1.9
3	2.3	2.3	2.2	2.3	2.2
4	2.4	2.5	2.5	2.6	2.5
5	1.9	2.5	2.6	2.6	2.7
6	1.9	1.7	1.5	1.6	2.0
7	2.5	2.6	2.6	2.5	2.6
8	3.1	2.8	2.9	2.9	2.8
9	2.0	1.8	2.1	2.1	2.2
10	1.3	1.2	1.2	1.3	1.2
11	0.9	1.2	1.2	1.0	1.2
12	2.6	2.8	2.9	2.8	2.8
13	2.4	2.4	2.4	2.5	2.5
14	2.6	2.5	2.5	2.5	2.5
15	1.5	1.5	1.5	1.4	1.5
16	2.3	2.3	2.2	2.4	2.4
17	1.7	1.6	1.5	1.9	1.7
18	1.7	1.7	1.7	1.7	1.9
19	2.9	3.0	3.0	3.0	3.1
	Bayonet Pointer				
1	2.9				
2	2.4				
3	2.4				
4	3.0				
5	2.0				
6	1.7				
7	2.9				
8	3.3				
9	2.0				
10	1.5				
11	1.4				
12	3.0				
13	3.0				
14	2.7				
15	1.8				
16	2.7				
17	2.1				
18	2.0				
19	3.3				

Signa MRI					
Screw Number	Short Pointer	Short Pointer	Short Pointer	Short Pointer	
1	1.5	0.8	1.0	0.9	
2	1.5	1.2	1.5	1.3	
3	2.7	2.8	2.6	2.6	
4	1.9	1.8	2.0	2.0	
5	0.6	0.7	0.5	0.9	
6	1.0	1.0	0.9	1.0	
7	1.8	1.5	2.0	2.1	
8	1.8	1.9	1.8	1.9	
9	1.4	1.5	1.4	1.5	
10	1.7	1.7	1.7	1.7	
11	1.1	1.1	1.0	0.9	
12	1.6	1.3	1.5	1.5	
13	1.6	1.5	1.7	1.6	
14	1.9	1.7	1.7	1.7	
15	1.6	1.4	1.1	1.4	
16	1.6	1.5	1.6	1.3	
17	1.3	1.4	1.4	1.2	
18	1.0	0.9	0.9	1.0	
19	1.1	1.1	1.1	1.1	
	Long Pointer	Long Pointer	Long Pointer	Long Pointer	Long Pointer
1	1.5	1.9	1.6	1.5	1.4
2	2.0	2.3	2.0	1.8	2.2
3	2.9	2.9	2.8	2.7	2.8
4	2.1	2.4	2.3	2.6	2.5
5	1.1	1.0	0.8	1.0	0.7
6	1.3	1.2	1.2	1.1	1.3
7	2.3	2.4	2.5	2.4	2.2
8	2.0	1.8	1.9	2.0	2.0
9	1.8	1.7	1.8	1.7	1.9
10	1.8	1.8	1.8	1.9	1.9
11	1.5	1.3	1.3	1.5	1.7
12	1.8	1.9	2.0	2.0	2.1
13	2.2	2.2	2.2	2.1	2.2
14	2.2	2.1	2.1	1.8	2.0
15	2.0	1.9	1.7	1.7	1.8
16	2.1	2.0	2.0	2.1	1.9
17	2.0	1.8	2.0	1.8	1.8
18	1.5	1.8	1.5	1.6	1.5
19	1.7	1.7	1.8	1.5	1.7

	Signa MRI Continued				
	Bayonet Pointer	Bayonet Pointer	Bayonet Pointer	Bayonet Pointer	Bayonet Pointer
1	0.9	1.1	0.8	0.8	0.7
2	1.7	2.2	2.0	1.7	1.5
3	2.9	3.0	2.7	3.0	2.7
4	2.7	2.4	2.7	2.5	2.9
5	0.3	0.9	0.5	0.5	0.8
6	1.0	1.0	1.1	1.1	1.0
7	2.7	2.5	2.4	2.6	2.8
8	2.5	2.2	2.1	2.2	2.1
9	1.7	1.7	1.6	1.6	1.4
10	1.8	1.8	1.8	1.8	1.8
11	1.5	1.7	2.0	1.9	1.6
12	2.1	2.3	2.4	2.5	2.1
13	2.5	2.4	2.6	2.6	2.7
14	2.4	2.7	2.6	2.6	2.3
15	2.3	2.0	2.4	2.1	2.2
16	2.3	2.3	2.2	2.4	2.4
17	2.4	2.3	2.4	2.3	2.3
18	1.7	1.8	2.0	2.1	2.2
19	1.6	1.7	1.8	1.7	1.9

ii.i.ii: Point Localisation Experiments (CT); Image Localiser Screw Attachments

	2mm Sequential CT				
Hole No.	Short Pointer	Short Pointer	Short Pointer	Short Pointer	Short Pointer
1	1.0	0.7	0.9	0.6	1.1
2	0.9	0.8	0.6	0.7	0.7
3	0.6	0.7	0.6	0.6	0.6
4	0.4	0.9	0.5	0.7	0.6
5	1.5	1.7	1.4	1.6	1.7
6	0.9	0.6	0.6	0.4	0.6
7	1.1	0.4	0.2	0.4	0.3
8	1.7	0.5	0.8	1.0	0.9
9	0.9	0.9	0.7	0.8	0.6
10	0.8	0.5	0.7	0.7	0.8
11	1.0	0.8	0.5	0.8	0.8
12	0.3	0.4	0.7	0.8	0.3
13	0.4	0.6	0.3	0.5	0.4
14	0.6	0.5	0.6	0.7	0.6
15	0.3	0.2	0.3	0.4	0.1
16	0.3	0.3	0.3	0.3	0.1
17	0.3	0.3	0.3	0.3	0.3
18	0.6	0.3	0.4	0.6	0.8

3mm Sequential CT					
Hole No.	Short Pointer	Short Pointer	Short Pointer	Short Pointer	Short Pointer
1	0.9	1.2	1.3	1.0	1.8
2	1.0	1.2	1.3	0.6	1.5
3	0.8	0.7	0.6	0.7	0.4
4	0.3	0.6	0.6	0.3	0.7
5	1.9	1.9	2.1	1.5	2.5
6	1.2	1.4	1.3	1.0	1.5
7	0.3	0.2	0.1	1.1	0.3
8	1.0	1.4	1.1	1.0	0.8
9	1.0	0.9	1.1	0.6	1.1
10	1.1	1.2	1.2	0.7	1.4
11	0.7	0.9	0.7	0.6	0.6
12	0.4	0.2	0.3	0.4	0.7
13	0.4	0.6	0.5	0.3	0.4
14	0.8	0.6	0.6	0.6	0.3
15	0.5	0.5	0.5	0.4	0.4
16	0.3	0.4	0.4	0.1	0.3
17	0.7	0.4	0.3	0.2	0.5
18	1.0	0.8	0.8	0.8	1.2
3mm Helical CT					
Hole No.	Short Pointer	Short Pointer	Short Pointer	Short Pointer	Short Pointer
1	1.5	1.2	1.0	1.6	1.5
2	0.9	1.2	0.7	1.2	1.2
3	0.7	0.6	0.3	0.8	0.8
4	0.5	0.5	0.5	0.7	0.6
5	1.7	1.9	1.2	2.1	2.3
6	1.2	1.3	0.6	1.2	1.4
7	1.4	0.4	0.3	0.5	0.5
8	0.9	0.8	0.8	1.3	1.3
9	0.9	1.2	0.5	0.8	1.1
10	1.3	1.3	0.9	1.2	1.2
11	0.9	0.8	0.6	0.9	1.1
12	0.6	0.4	0.8	0.7	0.5
13	0.4	0.4	0.5	0.3	0.7
14	0.6	0.4	0.7	0.4	0.6
15	0.6	0.5	0.3	0.4	0.8
16	0.3	0.4	0.1	0.3	0.3
17	0.4	0.3	0.2	0.2	0.4
18	0.4	0.7	0.3	0.8	1.1

ii.i.iii: Point Localisation Experiments: Baseplate Holes

	Signa MRI				
Hole No.	Short Pointer	Short Pointer	Short Pointer	Short Pointer	Short Pointer
1	1.2	1.2	1.2	1.3	1.2
2	1.0	0.8	1.0	0.9	1.0
3	1.1	1.1	1.1	1.1	1.2
4	1.0	1.1	1.2	1.2	1.2
5	0.8	0.9	0.8	0.9	0.8
6	1.7	1.5	1.5	1.8	1.5
7	1.4	1.6	1.5	1.4	1.5
8	1.8	1.5	1.6	1.7	1.6
9	1.4	1.4	1.3	1.4	1.4
10	1.3	1.4	1.3	1.2	1.4
13	1.1	1.2	1.1	1.0	1.1
14	1.2	1.2	1.3	1.4	1.2
17	1.3	1.2	1.3	1.3	1.4
18	1.6	1.6	1.5	1.5	1.6
19	1.5	1.5	1.5	1.5	1.6
20	1.5	1.4	1.5	1.5	1.4
	Long Pointer	Long Pointer	Long Pointer	Long Pointer	Long Pointer
1	1.3	1.3	1.4	1.6	1.4
2	1.2	1.2	1.2	1.2	1.2
3	1.2	1.1	1.3	1.2	1.2
4	1.4	1.5	1.3	1.3	1.4
5	1.4	1.2	1.4	1.4	1.3
6	2.1	1.9	1.9	1.9	2.0
7	1.8	1.7	1.9	1.9	1.8
8	2.3	2.1	2.0	2.1	2.1
9	1.6	1.7	1.6	1.5	1.6
10	1.4	1.4	1.4	1.3	1.4
13	1.9	1.8	1.9	1.7	1.7
14	2.0	1.8	1.7	1.8	2.1
17	1.6	1.6	1.5	1.5	1.4
18	1.9	1.7	1.7	1.7	1.5
19	1.9	1.9	1.9	1.9	2.0
20	1.8	1.7	1.8	1.9	1.6

Signa MRI Continued					
	Bayonet Pointer	Bayonet Pointer	Bayonet Pointer	Bayonet Pointer	Bayonet Pointer
1	2.0	2.1	2.1	2.0	2.1
2	1.5	1.8	2.0	1.8	1.9
3	1.5	1.6	1.8	1.8	1.8
4	2.2	2.0	1.7	2.3	2.1
5	1.8	1.8	2.0	2.0	1.9
6	2.8	2.7	2.5	2.2	2.9
7	2.3	2.3	2.4	2.3	2.3
8	2.4	2.7	2.8	2.3	2.9
9	1.8	2.1	2.5	2.0	2.2
10	1.9	2.0	1.9	1.8	2.2
13	2.2	2.5	2.2	2.2	2.3
14	2.1	2.3	2.3	2.2	2.3
17	2.0	2.1	2.3	2.1	2.1
18	2.3	2.3	2.4	2.3	2.4
19	2.4	2.5	2.3	2.7	2.3
20	2.3	2.4	2.4	2.0	2.3

Fine Vectra MRI					
Hole No.	Short Pointer	Short Pointer	Short Pointer	Short Pointer	Short Pointer
1	2.2	2.2	2.3	2.3	2.2
2	2.2	2.2	2.2	2.3	2.4
3	2.0	2.0	2.0	1.9	1.9
4	2.0	2.0	2.0	2.0	2.0
5	1.9	1.9	1.9	1.8	1.8
6	2.1	2.1	2.1	2.2	2.1
7	1.9	1.9	1.9	1.9	1.9
8	1.5	1.5	1.5	1.5	1.5
9	1.5	1.4	1.4	1.4	1.4
10	1.5	1.4	1.5	1.4	1.4
13	1.5	1.4	1.5	1.4	1.4
14	1.0	1.1	1.1	1.1	1.1
17	1.5	1.8	1.6	1.5	1.5
18	1.7	1.7	1.7	1.7	1.8
19	1.6	1.6	1.5	1.6	1.6
20	1.8	1.8	1.8	1.7	1.8

	Fine Vectra MRI Continued				
	Long Pointer	Long Pointer	Long Pointer	Long Pointer	Long Pointer
1	2.5	2.4	2.5	2.3	2.3
2	2.5	2.4	2.4	2.3	2.4
3	2.1	2.1	2.2	2.1	2.2
4	2.3	2.3	2.3	2.3	2.2
5	2.2	2.3	2.3	2.2	2.2
6	2.4	2.4	2.4	2.4	2.4
7	2.1	2.1	2.1	2.0	2.1
8	1.7	1.7	1.6	1.7	1.7
9	1.5	1.5	1.5	1.5	1.5
10	1.7	1.6	1.8	1.6	1.7
13	1.6	1.6	1.5	1.6	1.5
14	1.5	1.5	1.5	1.5	1.5
17	1.8	1.7	1.8	1.8	1.8
18	1.9	2.0	1.9	2.0	2.1
19	1.7	1.8	1.8	1.8	1.8
20	2.0	2.0	2.0	2.0	2.1
	Bayonet Pointer	Bayonet Pointer	Bayonet Pointer	Bayonet Pointer	Bayonet Pointer
1	3.3	3.2	3.1	3.3	3.4
2	3.1	3.5	3.5	3.3	3.3
3	2.6	2.8	2.9	2.8	2.8
4	2.5	2.7	2.7	2.5	2.6
5	2.8	2.8	2.8	2.8	2.9
6	2.8	2.9	2.8	2.9	2.9
7	2.4	2.7	2.6	2.6	2.9
8	2.3	2.2	2.2	2.2	2.3
9	2.1	2.4	2.3	2.3	2.1
10	2.1	2.2	2.2	2.0	2.1
13	2.3	2.1	2.1	2.2	2.0
14	2.2	2.3	2.0	2.0	2.0
17	2.3	2.3	2.3	2.5	2.2
18	2.3	2.5	2.3	2.4	2.7
19	2.4	2.3	2.2	2.2	2.2
20	2.8	2.8	2.6	2.8	2.8

Standard Vectra MRI					
Hole No.	Short Pointer	Short Pointer	Short Pointer	Short Pointer	Short Pointer
1	0.7	0.6	0.7	0.6	
2	0.6	0.6	0.5	0.5	
3	0.6	0.4	0.7	0.4	
4	0.7	0.7	0.6	0.7	
5	0.7	0.6	0.6	0.6	
6	1.2	1.1	1.2	1.0	
7	0.7	0.7	0.6	0.7	
8	1.4	1.4	1.4	1.4	
9	1.4	1.4	1.4	1.4	
10	0.7	0.7	0.6	0.7	
13	0.6	0.5	0.7	0.5	
14	0.5	0.5	0.5	0.4	
15	0.6	0.7	0.7	0.7	
16	0.6	0.7	0.6	0.6	
17	1.2	1.1	1.2	1.2	
18	0.7	0.7	0.7	0.7	
19	1.4	1.4	1.4	1.4	
20	1.5	1.4	1.4	1.4	
	Long Pointer	Long Pointer	Long Pointer	Long Pointer	Long Pointer
1	0.8	0.7	0.8	0.6	0.6
2	0.4	0.4	0.4	0.4	0.4
3	0.8	0.6	0.8	0.8	0.7
4	0.8	0.9	0.8	1.0	0.9
5	0.9	1.1	0.7	0.9	1.0
6	1.0	1.1	1.1	1.0	1.0
7	0.9	0.9	0.9	0.7	0.8
8	1.4	1.4	1.4	1.4	1.4
9	1.5	1.5	1.5	1.5	1.5

ii.i.iv: Point Localisation Experiments; Spare Fiducials

	Signa MRI				
Fiducial No.	Short Pointer	Short Pointer	Short Pointer	Short Pointer	Short Pointer
2	0.7	0.6	0.7	0.5	0.6
9	2.4	2.4	2.4	2.3	2.3
12	1.4	1.4	1.6	1.2	1.3
13	2.1	2.1	2.3	2.7	2.3
	Long Pointer	Long Pointer	Long Pointer	Long Pointer	Long Pointer
2	0.5	0.7	0.6	0.5	0.5
9	2.4	2.4	2.5	2.5	2.3
12	0.9	0.7	0.6	0.9	0.8
13	1.9	1.9	2.3	1.7	1.9
	Bayonet Pointer	Bayonet Pointer	Bayonet Pointer	Bayonet Pointer	Bayonet Pointer
2	0.5	0.7	0.5	0.4	0.3
9	3.0	2.8	2.8	3.0	2.9
12	1.5	1.4	1.3	1.6	1.3
13	1.4	1.6	1.6	1.6	1.8
	Fine Vectra MRI				
	Short Pointer	Short Pointer	Short Pointer	Short Pointer	Short Pointer
2	1.3	1.6	1.6	1.5	1.9
9	2.4	2.3	2.4	2.4	2.4
12	1.7	2.0	2.0	2.0	2.0
13	0.8	0.8	0.8	0.9	0.8
	Long Pointer	Long Pointer	Long Pointer	Long Pointer	Long Pointer
2	1.1	1.3	1.2	1.4	1.3
9	2.5	2.5	2.4	2.4	2.6
12	2.1	2	1.9	1.7	1.6
13	0.6	0.7	0.6	0.8	0.7
	Bayonet Pointer	Bayonet Pointer	Bayonet Pointer	Bayonet Pointer	Bayonet Pointer
2	0.6	0.4	0.5	0.9	0.9
9	2.9	2.7	2.8	2.8	2.8
12	1.8	1.3	1.2	0.9	1.3
13	1.0	1.1	0.7	1.1	1.0
	Standard Vectra MRI				
	Short Pointer	Short Pointer	Short Pointer	Short Pointer	Short Pointer
2	0.4	0.4	0.2	0.2	0.2
9	1.6	1.7	1.6	1.7	1.5
12	1.0	1.2	0.7	0.9	0.7
13	0.6	0.6	0.9	0.9	0.7
	Long Pointer	Long Pointer	Long Pointer	Long Pointer	Long Pointer
2	0.7	0.5	0.4	0.7	0.7
9	1.1	1.2	1.1	1.1	1.3
12	1.2	1.2	0.9	1.2	1.4
13	0.4	0.8	0.5	0.3	0.7
	Bayonet Pointer	Bayonet Pointer	Bayonet Pointer	Bayonet Pointer	Bayonet Pointer
2	1.4	0.8	1.2	1.2	0.9
9	1.7	1.9	2.1	1.7	1.9
12	1.8	1.5	1.8	2.3	1.7
13	0.7	0.6	0.9	0.8	0.9

ii.i.v: Pointer Reproducibility Experiments

Standard Vectra MRI					
Trial Number	Short Pointer	Trial Number	Short Pointer	Trial Number	Short Pointer
1	2.6	22	2.6	43	2.6
2	2.6	23	2.6	44	2.6
3	2.6	24	2.6	45	2.6
4	2.6	25	2.6	46	2.6
5	2.6	26	2.7	47	2.6
6	2.6	27	2.6	48	2.6
7	2.6	28	2.6	49	2.6
8	2.6	29	2.6	50	2.6
9	2.6	30	2.6	51	2.6
10	2.7	31	2.6	52	2.6
11	2.6	32	2.6	53	2.6
12	2.6	33	2.6	54	2.6
13	2.6	34	2.6	55	2.6
14	2.6	35	2.6	56	2.6
15	2.6	36	2.6	57	2.6
16	2.6	37	2.6	58	2.6
17	2.6	38	2.6	59	2.6
18	2.6	39	2.6	60	2.6
19	2.6	40	2.6	61	2.6
20	2.6	41	2.6	62	2.6
21	2.6	42	2.6	63	2.6
Trial Number	Long Pointer	Trial Number	Long Pointer	Trial Number	Long Pointer
1	2.5	47	2.6	93	2.7
2	2.6	48	2.6	94	2.7
3	2.6	49	2.6	95	2.7
4	2.6	50	2.6	96	2.7
5	2.6	51	2.6	97	2.7
6	2.6	52	2.6	98	2.7
7	2.6	53	2.6	99	2.7
8	2.6	54	2.6	100	2.7
9	2.6	55	2.6	101	2.7
10	2.6	56	2.6	102	2.7
11	2.6	57	2.6	103	2.7
12	2.6	58	2.6	104	2.7
13	2.6	59	2.6	105	2.7
14	2.6	60	2.6	106	2.7
15	2.6	61	2.6	107	2.7
16	2.6	62	2.6	108	2.7
17	2.6	63	2.6	109	2.7
18	2.6	64	2.6	110	2.7
19	2.6	65	2.6	111	2.7
20	2.6	66	2.6	112	2.7
21	2.6	67	2.6	113	2.7
22	2.6	68	2.6	114	2.7
23	2.6	69	2.6	115	2.7
24	2.6	70	2.6	116	2.7
25	2.6	71	2.6	117	2.7

Reproducibility Experiments Continued					
Trial Number	Long Pointer	Trial Number	Long Pointer	Trial Number	Long Pointer
26	2.6	72	2.6	118	2.7
27	2.6	73	2.6	119	2.7
28	2.6	74	2.6	120	2.7
29	2.6	75	2.6	121	2.7
30	2.6	76	2.6	122	2.7
31	2.6	77	2.6	123	2.7
32	2.6	78	2.6	124	2.7
33	2.6	79	2.6	125	2.7
34	2.6	80	2.6	126	2.7
35	2.6	81	2.6	127	2.7
36	2.6	82	2.6	128	2.7
37	2.6	83	2.6	129	2.7
38	2.6	84	2.6	130	2.7
39	2.6	85	2.6	131	2.7
40	2.6	86	2.6	132	2.7
41	2.6	87	2.6	133	2.7
42	2.6	88	2.6	134	2.7
43	2.6	89	2.6	135	2.7
44	2.6	90	2.6	136	2.7
45	2.6	91	2.6	137	2.8
46	2.6	92	2.7		
Trial Number	Bayonet Pointer	Trial Number	Bayonet Pointer	Trial Number	Bayonet Pointer
1	2.6	36	2.6	71	2.6
2	2.6	37	2.6	72	2.6
3	2.6	38	2.6	73	2.6
4	2.6	39	2.6	74	2.6
5	2.6	40	2.6	75	2.5
6	2.6	41	2.6	76	2.5
7	2.6	42	2.6	77	2.5
8	2.6	43	2.6	78	2.5
9	2.6	44	2.6	79	2.5
10	2.6	45	2.6	80	2.5
11	2.6	46	2.6	81	2.5
12	2.6	47	2.6	82	2.5
13	2.6	48	2.6	83	2.5
14	2.6	49	2.6	84	2.5
15	2.6	50	2.6	85	2.5
16	2.6	51	2.6	86	2.5
17	2.6	52	2.6	87	2.5
18	2.6	53	2.6	88	2.5
19	2.6	54	2.6	89	2.5
20	2.6	55	2.6	90	2.5
21	2.6	56	2.6	91	2.5
22	2.6	57	2.6	92	2.5
23	2.6	58	2.6	93	2.5
24	2.6	59	2.6	94	2.5
25	2.6	60	2.6	95	2.5

Reproducibility Experiments Continued					
Trial Number	Bayonet Pointer	Trial Number	Bayonet Pointer	Trial Number	Bayonet Pointer
26	2.6	61	2.6	96	2.5
27	2.6	62	2.6	97	2.7
28	2.6	63	2.6	98	2.7
29	2.6	64	2.6	99	2.7
30	2.6	65	2.6	100	2.7
31	2.6	66	2.6	101	2.7
32	2.6	67	2.6	102	2.7
33	2.6	68	2.6	103	2.7
34	2.6	69	2.6	104	2.8
35	2.6	70	2.6		

ii.i.vi: Detection of Pointer Movement Experiment

Standard Vectra MRI			
Test Number	Micrometer Start Position	Micrometer at Detection	Travel (mm)
1	27.25	27.14	-0.11
2	27.14	26.80	-0.34
3	26.80	26.41	-0.39
4	26.41	25.91	-0.50
5	25.91	25.46	-0.45
6	25.46	25.00	-0.46
7	25.00	24.56	-0.44
8	24.56	24.12	-0.44
9	24.12	23.72	-0.40
10	23.72	23.29	-0.43
11	23.29	22.85	-0.44
12	22.06	21.77	-0.29
13	21.77	21.39	-0.38
14	21.39	21.08	-0.31
15	21.08	20.73	-0.35
16	20.73	20.25	-0.48
17	20.25	20.08	-0.17
18	20.08	19.66	-0.42
19	19.66	19.04	-0.62
20	19.04	18.81	-0.23

ii.i.vii: Pointer Rotation Experiment

	Standard Vectra MRI				
	Nearest Marker Distance (mm)				
Trial Number	90° Right	45° Right	0°	45° Left	90° Left
1	51.4	50.7	50.6	50.6	51.0
2	51.4	50.6	50.4	50.4	51.0
3	51.4	50.6	50.6	50.6	50.9
4	51.3	50.6	50.4	50.6	50.9
5	51.5	50.6	50.5	50.6	51.0
6	51.5	50.6	50.5	50.6	51.0
7	51.4	50.6	50.4	50.6	50.9
8	51.2	50.7	50.4	50.6	51.0
9	51.5	50.7	50.4	50.6	51.0
10	51.3	50.7	50.4	50.6	51.0
11	51.5	50.6	50.5	50.6	51.0
12	51.4	50.7	50.4	50.6	51.0
13	51.5	50.6	50.4	50.6	50.9
14	51.2	50.7	50.4	50.6	50.9
15	51.6	50.7	50.5	50.6	51.0
16	51.5	50.6	50.4	50.7	51.0
17	51.5	50.6	50.3	50.6	50.9
18	51.4	50.6	50.5	50.5	51.1
19	51.4	50.5	50.3	50.7	51.0
20	51.2	50.6	50.4	50.6	51.0

II.II: Clinical Evaluation of the Neuronavigation System
ii.ii.i: 100 Cases; General Data, & Duration of Surgery

Case No.	Age	Sex	Pathology	Site	Diameter (mm)	Scan Type	Operation	Number of Fiducials	RMSE (mm)	Mean Nearest Marker	Time (hrs)
1	39	M	Aneurysm	ST	47.1	MR(V)	Clipping	8	4.6	3.2	3.83
2	46	F	Glioma	ST	43.1	MR(V)	Craniotomy(D)	7	4.0	3.5	1.25
3	74	M	Metastasis	IT	22.2	MR(V)	Craniectomy(E)	6	4.6	3.8	1.16
4	32	M	Meningioma	ST	71.7	MR(V)	Craniotomy(E)	10	4.2	3.0	8.83
5	51	M	Glioma	ST	45.9	MR(V)	Craniotomy(D)	10	3.9	2.5	1.75
6	46	M	Metastasis	ST	33.8	MR(V)	Freehand Biopsy	10	3.9	3.5	1.25
7	38	F	Metastasis	ST	24.0	MR(H)	Craniotomy(E)	8	3.7	3.4	1.67
8	43	M	Epilepsy	ST	50.0	MR(H)	Hippocampectomy	7	4.8	4.3	3.00
9	60	F	Glioma	ST	66.5	MR(V)	Craniotomy(D)	9	3.0	2.8	1.75
10	60	F	Epidermoid	IT	59.9	MR(H)	Craniectomy(E)	9	4.1	3.5	2.75
11	32	F	Cavernoma	ST	57.5	MR(V)	Craniotomy(E)	8	2.9	2.1	2.08
12	45	F	Metastasis	ST	43.8	MR(H)	Craniotomy(E)	8	3.3	2.7	2.17
13	34	M	Glioma	ST	31.3	MR(H)	Craniotomy(D)	9	3.6	3.2	1.58
14	43	M	Epilepsy	ST	21.4	MR(H)	Lesionectomy	8	2.3	2.9	2.42
15	28	M	Glioma	ST	71.9	MR(V)	Craniotomy(D)	9	3.2	2.6	1.83
16	55	M	Glioma	ST	64.9	MR(H)	Craniotomy(D)	8	3.6	3.1	2.08
17	43	M	Glioma	ST	57.4	MR(H)	Craniotomy(D)	9	4.8	4.5	1.17
18	35	M	AVM	ST	17.6	MR(H)	Craniotomy(E)	9	3.9	2.9	3.00
19	52	F	Meningioma	ST	52.6	MR(H)	Craniotomy(E)	7	2.6	2.4	3.33
20	31	F	Cavernoma	ST	19.6	MR(H)	Craniotomy(E)	5	1.8	1.3	1.67
21	66	M	Glioma	ST	50.7	MR(H)	Craniotomy(D)	8	3.7	2.9	1.92
22	73	M	Glioma	ST	56.8	MR(H)	Craniotomy(D)	9	5.0	4.2	1.75
23	33	F	Epilepsy	ST	20.7	MR(H)	Hippocampectomy	8	3.4	2.8	2.80
24	39	F	Meningioma	ST	75.0	MR(V)	Craniotomy(E)	10	4.3	3.3	2.75
25	41	F	Meningioma	ST	34.4	MR(V)	Craniotomy(E)	9	3.7	3.0	1.17
26	60	M	Glioma	ST	40.3	MR(H)	Craniotomy(D)	10	3.8	2.7	1.75
27	53	F	Meningioma	ST	55.5	MR(V)	Craniotomy(E)	6	2.3	3.7	2.00
28	50	F	Epidermoid	IT	58.8	MR(H)	Craniectomy(E)	5	7.3	5.7	2.50
29	28	M	Epilepsy	ST	29.3	MR(H)	Lesionectomy	8	3.3	2.5	3.00

				SP							
30	49	M	Neuroma	IT	40.0	MR(H)	Laminectomy(E)	7	6.8	3.5	1.83
31	15	F	Granuloma	IT	29.0	MR(V)	Transpetrous(D)	7	4.3	2.0	2.42
32	60	F	Meningioma	ST	57.2	MR(V)	Craniotomy(E)	8	5.9	4.0	2.75
33	46	F	Meningioma	IT	31.6	MR(V)	Far Lateral(E)	8	3.9	4.6	3.25
34	34	M	Meningioma	IT	43.7	MR(V)	Transpetrous(E)	9	2.1	1.9	5.33
35	55	M	Glioma	ST	47.5	MR(V)	Craniotomy(D)	10	2.9	2.8	1.83
36	58	F	Osteo. Imperfect	IT	53.2	MR(V)	Maxillotomy(D)	12	3.0	2.9	4.42
37	60	M	Glioma	ST	20.4	MR(V)	Craniotomy(D)	7	2.3	2.7	1.30
38	29	M	Meningioma	IT	48.5	MR(V)	Far Lateral(D)	7	3.9	3.2	5.00
39	41	M	Meningioma	ST	46.4	MR(V)	Craniotomy(E)	7	4.4	4.4	3.00
40	62	M	Meningioma	ST	55.5	MR(V)	Craniotomy(E)	8	3.3	3.0	4.60
41	40	M	Neuroma	IT	44.3	MR(H)	Transpetrous(E)	9	2.9	3.1	4.50
42	32	M	Epilepsy	ST	15.8	MR(H)	Lesionectomy	9	2.1	1.8	2.08
43	36	F	Arachnoid cyst	IT	30.4	MR(H)	Craniectomy(E)	8	2.5	2.0	1.83
44	27	M	Meningioma	ST	27.0	MR(H)	Craniotomy(E)	8	4.3	3.9	2.20
45	26	M	Granuloma	ST	20.5	MR(H)	Craniotomy(D)	6	3.7	2.7	2.25
46	30	M	Epilepsy	ST	22.0	MR(H)	Electrodes	7	3.0	2.5	1.75
47	36	F	Meningioma	ST	31.4	MR(H)	Craniotomy(E)	10	4.5	5.2	2.50
48	50	F	Meningioma	IT	29.6	MR(H)	Transpetrous(E)	9	3.5	2.9	4.80
49	29	M	Arachnoid cyst	IT	39.8	MR(V)	IV Shunt	7	3.7	3.5	1.75
50	30	M	Epilepsy	ST	22.0	MR(H)	Lesionectomy	5	4.2	2.6	2.25
51	51	M	Meningioma	ST	13.4	MR(H)	Craniotomy(E)	9	3.5	3.8	2.25
52	67	M	Meningioma	ST	65.0	MR(H)	Craniotomy(E)	10	5.0	3.8	2.20
53	34	M	Glioma	ST	19.5	MR(V)	Craniotomy(D)	8	3.0	2.8	1.50
54	49	M	Meningioma	ST	26.0	MR(H)	Craniotomy(E)	9	2.3	1.9	1.50
55	59	F	Plexus papilloma	IT	42.5	MR(V)	Craniectomy(E)	6	3.8	3.4	2.75
56	17	M	Chondrosarcoma	ST	105.6	MR(H)	MidfaceDeglov.(D)	7	3.0	3.1	4.25
57	55	M	Granuloma	ST	14.0	MR(H)	Craniotomy(D)	7	2.2	2.7	1.25
58	60	M	Meningioma	ST	58.4	MR(V)	Craniotomy(E)	8	5.6	4.8	5.20
59	38	F	Haemangioblastoma	IT	17	MR(V)	Craniectomy(E)	6	3.2	3.7	5.50
60	36	M	Glioma	ST	44.7	MR(V)	Craniotomy(D)	9	2.9	2.8	1.16
61	60	F	Glioma	ST	38.6	MR(V)	Craniotomy(D)	9	3.9	3.0	2.25
62	51	F	Ependymoma	IT	35.2	MR(V)	Craniectomy(D)	9	3.7	2.8	5.20
63	23	F	Chordoma	IT	55.9	MR(V)	Far Lateral(D)	9	2.9	2.7	5.00

64	F	69	Meningioma	ST	46.9	MR(V)	Craniotomy(E)	9	3.6	3.2	1.50
65	M	58	Glioma	ST	46.0	MR(V)	Craniotomy(D)	9	4.7	4.7	1.33
66	F	52	Meningioma	ST	45.5	MR(V)	Craniotomy(E)	8	4.0	3.3	2.00
67	F	47	Chordoma	IT	16.2	MR(V)	Transoral(E)	11	2.7	2.3	2.00
68	M	47	Neurilemmoma	IT	61.6	MR(V)	Transpetrous(E)	10	4.8	3.4	5.10
69	F	49	Meningioma	ST	64.2	MR(V)	Craniotomy(E)	11	2.6	2.2	3.67
70	M	48	Chordoma	IT	29.0	MR(H)	Maxillotomy(D)	11	2.9	2.8	2.75
71	M	35	Epilepsy	ST	69.0	MR(H)	Craniotomy(E)	10	4.8	3.8	3.67
72	M	76	Glioma	ST	38.6	MR(V)	Craniotomy(D)	13	2.3	2.1	0.83
73	F	20	Colloid cyst	ST	15.5	MR(V)	Craniotomy(E)	9	3.9	3.6	3.25
74	F	26	Colloid cyst	ST	10.1	MR(V)	Craniotomy(E)	8	2.8	2.6	3.50
75	M	43	Glioma	ST	18.0	MR(V)	Craniotomy(D)	8	3.7	3.9	1.25
76	F	18	Epilepsy	ST	2.5	MR(H)	Electrodes	10	3.6	3.7	1.75
77	F	18	Epilepsy	ST	2.5	MR(H)	Lesionectomy	5	8.5	8.3	2.25
78	F	56	Glioma	ST	65.4	MR(H)	Craniotomy(D)	7	2.6	2.6	2.00
79	M	42	Abscess	ST	43.5	MR(V)	Craniotomy(E)	12	3.9	2.9	2.50
80	M	30	Epilepsy	ST	6.0	MR(V)	Corticectomy	8	2.8	3.2	2.25
81	F	27	Glioma	ST	28.1	MR(V)	Craniotomy(D)	10	2.8	2.3	1.60
82	M	60	Glioma	ST	51.4	MR(H)	Craniotomy(D)	7	5.6	5.2	3.00
83	F	50	Meningioma	ST	58.8	MR(V)	Craniotomy(E)	11	3.0	3.2	2.80
84	F	29	Glioma	ST	83.0	MR(V)	Craniotomy(D)	9	3.0	2.3	3.30
85	M	45	Subependymoma	IT	16.2	MR(V)	Craniectomy(E)	9	4.6	4.1	2.10
86	M	45	Haemangioblastoma	IT	39.4	MR(V)	Craniectomy(E)	7	4.0	3.5	4.00
87	M	36	Epilepsy	ST	20.5	MR(H)	Craniotomy(E)	8	3.5	2.7	2.80
88	M	40	Metastasis	ST	43.0	MR(V)	Craniotomy(E)	10	4.3	3.7	1.50
89	M	35	Epilepsy	ST	12.8	MR(H)	Craniotomy(E)	10	3.1	3.2	3.67
90	M	69	Meningioma	ST	74.6	MR(H)	Craniotomy(E)	11	4.7	4.3	2.00
91	F	74	Meningioma	ST	61.2	MR(V)	Craniotomy(E)	10	3.7	2.7	4.75
92	M	27	Glioma	ST	29.6	MR(H)	Craniotomy(D)	12	2.4	2.9	3.00
93	F	77	Meningioma	ST	31.7	MR(V)	Craniotomy(E)	9	3.3	4.1	1.50
94	M	33	Glioma	ST	17.4	MR(H)	Craniotomy(D)	8	2.6	1.9	3.00
95	F	23	Glioma	ST	28.5	MR(V)	Craniotomy(D)	10	3.1	2.2	2.50
96	F	55	Meningioma	ST	29.8	MR(H)	Craniotomy(E)	6	5.1	3.8	3.25
97	F	38	Cavernoma	ST	30.6	MR(V)	Craniotomy(E)	8	4.7	4.8	1.75

98	51	M	DNT	ST	10.6	MR(V)	Craniotomy(D)	9	2.7	2.3	2.00
99	57	M	Neuroma	IT	41.4	MR(H)	Craniotomy(E)	8	3.7	3.3	4.00
100	49	M	Meningioma	ST	32.5	CT	Craniotomy(E)	9	3.3	3.3	5.00

ST = Supratentorial,
IT = Infratentorial,
SP = Spinal,
(D) = Debulking,
(E) = Excision.

ii.ii.ii: Visual Analogue Scale Results

Case No.	Question Number									
	1	2	3	4	5	6	7	8	9	10
1	3.9	3.0	0.0		2.0	2.1	0.0	2.6		
2	0.7	2.0	0.7	4.0	0.5	0.5	0.0	0.9		
3	2.5	2.6	4.5	0.0	0.4	4.0	4.0	3.9		
4	2.4	3.5	3.4	0.0	2.0	5.0	0.2	2.6		
5	2.0	2.2	0.0	3.4	3.0	4.0	0.9	3.1		
6	0.4	0.4	4.4	0.0	0.6	-0.6	-0.6	1.2		
7	0.0	1.0	3.0	0.0	1.5	1.6	0.0	1.0		
8	0.1	1.2	0.4	0.0	2.0	1.3	-0.6	1.8		
9	3.4	4.5	4.3	0.5	2.6	3.5	0.5	4.3		
10	3.5	3.5	1.4	0.0	2.4	2.6	0.2	3.5		
11	1.0	1.9	3.0	0.0	1.5	1.6	-0.9	0.9		
12	4.0	4.0	4.0	0.0	1.0	4.0	1.0	4.0		
13	2.5	2.5	2.4	0.0	1.3	2.5	0.2	3.3		
14	3.0	3.0	3.0	2.0	1.0	3.0	0.0	3.0		
15	3.5	2.6	3.4	3.5	3.5	3.5	0.9	3.5		
16	2.0	0.8	1.3	3.5	3.3	3.6	-1.1	2.5		
17	2.6	2.6	2.5	0.0	0.1	-0.1	-2.7	1.3		
18	0.7	0.4	1.4	0.0	1.2	3.2	1.0	0.9		
19	3.1	3.6	0.6	0.0	2.5	3.3	0.6	3.5		
20	4.5	4.5	4.7	4.8	4.8	4.8	2.5	5.0		
21	0.6	0.5	2.2	0.0	0.9	0.5	0.0	0.8		
22	2.0	5.0	5.0	0.0	3.5	4.0	3.6	4.3		
23	0.9	1.6	2.0	0.0	2.1	3.6	0.0	0.9		
24	1.5	-1.0	0.5	-3.0	0.5	1.0	-1.4	0.0		
25	0.0	1.2	1.2	2.5	0.0	0.0	-1.1	1.4		
26	1.1	3.9	5.0	3.0	2.1	4.0	2.1	4.0		
27	0.6	2.2	3.4	0.0	1.6	1.6	2.2	2.4		
28	4.3	4.4	1.6	4.3	4.4	4.2	0.5	4.4		
29	2.6	2.5	3.7	0.0	2.0	3.0	2.0	3.0		
30	2.8	3.6	2.5	0.0	3.2	2.8	1.0	3.1		
31	0.0	5.0	5.0	5.0	5.0	5.0	3.0	5.0		
32	1.3	3.2	3.2	0.1	1.5	0.1	1.3	2.0		
33	2.3	0.0	1.5	0.0	-0.2	0.0	-2.0	0.0		
34	3.8	0.0	3.4	0.0	2.6	3.4	0.0	3.3		
35	1.0	1.0	1.2	4.0	3.9	4.0	1.5	3.6		
36	3.4	3.4	3.6	3.5	3.3	3.6	-1.7	3.3		
37	3.3	3.8	3.9	0.3	2.6	2.5	3.5	3.6		
38	2.1	2.3	2.6	1.2	1.9	2.3	0.5	2.6		
39	1.0	4.1	5.0	0.1	1.0	3.8	3.0	2.9		
40	0.8	2.5	1.3	0.0	2.2	0.8	0.1	1.0		
41	3.8	0.0	3.8	3.9	0.0	3.5	0.2	2.7		
42	2.0	0.0	3.0	4.0	4.0	4.0	2.0	2.0		
43	1.2	2.0	1.0	0.0	1.2	1.3	1.3	0.6		
44	1.0	3.1	3.0	0.0	2.0	3.0	1.0	3.0		
45	0.4	2.4	3.7	1.5	0.1	1.6	0.5	2.5		
46	2.6	2.6	4.0	0.0	1.6	3.1	1.7	3.7		
47	-0.8	-1.3	-2.0	-1.2	-2.7	-1.0	-1.1	-3.9		
48	0.6	0.0	0.0	1.5	2.5	2.5	-0.5	0.8		
49	0.3	0.2	2.4	0.0	1.2	-0.3	-0.5	1.3		

50	2.3	2.1	1.9	2.6	1.4	4.0	0.6	2.4		
51	0.6	0.6	0.4	0.0	0.3	0.0	-0.8	1.3		
52	0.0	2.5	3.5	0.0	1.6	3.7	-0.5	3.6		
53	5.0	5.0	5.0	0.0	3.0	4.0	-3.0	4.0		
54	1.6	2.5	3.9	2.3	3.0	3.0	2.0	4.0		
55	0.0	1.2	2.3	0.0	1.0	0.0	-1.0	0.8		
56	1.5	1.5	2.5	3.0	3.0	3.0	2.0	2.5		
57	3.0	4.2	1.0	0.0	2.0	0.0	-2.2	2.0		
58	1.5	1.5	0.0	0.6	3.0	2.0	0.0	1.3	1.2	
59	1.6	3.6	3.6	0.1	2.1	2.5	1.6	3.6	1.6	
60	1.5	1.5	3.7	0.1	2.7	3.4	-0.6	3.3	0.5	
61	3.0	1.0	3.0	0.2	1.0	3.0	-0.1	3.2	2.2	1.4
62	0.0	0.0	0.0	1.8	0.1	0.1	-1.6	1.3	0.0	
63	1.7	0.1	0.1	2.6	1.0	-0.2	-1.5	2.0	0.0	
64	1.0	2.0	0.0	0.0	0.0	1.0	-0.6	0.8	0.9	
65	4.2	4.2	4.2	4.1	3.8	4.2	3.8	3.9	3.3	
66	3.5	4.5	4.4	0.0	2.4	4.4	-0.5	2.5	4.7	4.3
67	1.7	0.9	1.3		1.7	1.4	-3.2	1.3	1.3	3.0
68	2.5	2.6	2.5	0.0	2.0	0.8	-1.2	1.8	0.0	0.0
69	4.5	4.4	3.7	2.6	3.4	4.5	0.6	4.6	4.4	
70	3.6	3.5	3.2	3.3	3.3	3.4	3.2	3.2	2.5	
71	4.5	2.5	4.3	4.2	4.3	4.2	1.5	4.3		
72	3.6	3.6	4.3	1.6	2.5	4.3	-0.7	4.5	2.5	
73	3.5	3.4	3.5	3.2	3.2	3.2	2.8	3.5	2.8	3.3
74	0.0	0.0	0.0	0.0	0.0	1.5	-0.6	0.0	0.0	
75	1.8	1.0	1.1	0.0	0.0	0.0	0.0	0.0	0.0	
76	2.5	0.5	3.5	0.0	2.0	3.0	-1.0	2.0	0.0	0.0
77	0.5	1.5	1.5		0.5	0.0	-0.6	2.4	0.2	0.7
78	1.2	1.4	1.5	0.0	1.5	1.1	1.6	1.8	1.3	2.0
79	1.2	1.5	2.5	0.0	1.5	1.6	1.6	1.7	2.5	1.6
80	1.4	0.5	1.2	0.0	0.3	0.2	0.3	1.5	1.6	
81	0.0	2.3	3.2		1.6	0.6	0.7	3.3	2.5	
82	1.7	2.2	1.6	1.0	0.5	1.6	-0.2	1.9	0.3	1.0
83	4.5	4.5	4.5		3.5	4.5	4.6	4.8	4.6	4.7
84	3.5	3.5	4.6	2.5	2.5	3.4	2.5	4.6	2.5	
85	3.5	3.5	4.6	2.5	2.5	3.4	2.5	4.6	2.5	
86	1.6	0.0	1.5	0.0	0.0	1.6	-0.4	1.6	1.4	
87	2.6	3.5	3.4	0.0	2.4	0.3	1.2	3.3	1.5	
88	3.3	3.3	3.3		1.6	0.0	-1.6	1.4	0.6	0.6
89	1.6	1.6	0.5		0.6	1.7	0.0	2.4	1.6	
90	1.4	1.4	1.3	1.3	1.5	-0.2	0.3		0.0	
91	2.0	2.0	2.0	0.0	1.3	0.9	-0.4	2.0	1.0	
92	3.5	3.5	3.5	0.0	0.0	4.1	0.0	4.6	3.6	
93	4.6	4.7	4.8	4.5	4.5	4.5	-1.5	4.6	4.8	4.6
94	4.4	4.5	4.9	0.0	4.6	4.7	-0.6	4.8	4.5	
95	4.6	4.7	4.4	4.5	2.6	4.5	0.6	4.3	4.5	
96	0.0	0.0	0.0	0.0	0.0	0.0	0.0	1.2	0.7	
97	0.0	0.0	0.8	3.6	0.2	0.8	0.2	1.5	2.3	
98	3.5	3.5	4.6	3.5	4.5	3.5	2.5	3.5	2.5	
99	1.6	3.0	3.3	0.0	2.2	2.3	2.4	2.9	2.4	
100	2.6	2.6	3.5	3.5	3.5	3.5	1.6	3.6		

ii.ii.iii: **Registration Fiducial Accuracy Results**

Case No.	Registration Fiducial Position																
	1	2	3	4	5	6	7	8	9	10	11	12	13	14	15	16	17
1		3.0	4.4	1.2	3.6	5.5				8.4		0.9	2.3				
2	3.2	2.6	4.0	4.6		0.9			1.5	1.9	5.2	2.8	2.2				
3	3.0			5.8		2.7	4.4	3.0	4.1								
4	3.5	3.2	4.7	1.5	3.5	3.5				1.3	1.8	4.4	1.0				
5	4.0	1.3	2.2	1.5	2.4	4.7	2.1				4.0	2.4	1.0				
6	1.4	1.9	4.0	2.3	3.1	4.7		4.8		3.3	4.5	5.1					
7	2.8	3.6	1.1		4.4		1.6		3.1	4.9	3.8						
8		1.1	4.1	5.2		5.5				6.7	3.8	4.0					
9	3.0	0.7	2.5	2.9	5.2	2.0				2.8	2.3	3.0					
10	3.6	2.1			2.6		5.7	3.4	1.6	3.3	3.1	6.5					
11	3.6	1.4	1.7	0.8		2.6				2.0	1.9	3.1					
12	3.2	2.8	2.6	3.1		2.4		2.1		3.2	2.4						
13	1.2	4.1	0.5	3.7	5.5	4.3				2.6	5.8	1.2					
14	3.2	2.3	2.3	3.6	4.7	3.1				2.5	2.2						
15	2.1	2.6	2.9	2.7	3.2		2.6		2.6	2.3							
16	2.3		4.0	1.7		2.2		4.6		4.8	2.2	3.3					
17	1.7	2.1	4.5	4.6	6.3	5.2		3.7		5.3	7.0						
18	3.4	3.3	5.1	4.1	3.0		5.2			2.2	3.3	4.6	2.9	3.1			
19		4.0	2.0	2.0	2.5	0.9				3.4							
20		0.3	2.0	0.8	1.8					1.7							
21	3.0	1.6	1.0		2.7		5.1		1.5	3.3	5.0						
22	4.0	2.2	2.3	3.2	2.1	4.9				8.0	1.9	9.9					
23		1.8		3.2	3.7	2.8	0.0			1.0	5.2	1.4	4.3				
24	2.4	1.6	3.0	3.1	3.0	1.0		5.7		7.2	2.7	2.8					
25	4.7	2.1	1.4		2.6		3.8				1.5	3.2	2.2				
26	1.2	1.0	1.6	2.9	3.2		5.3		4.2	2.3	3.2	2.4					
27	4.0	4.2			3.6		3.7				1.5	5.2					
28	2.0					7.0		9.9	3.6		6.1						
29	2.7	2.5	4.9	3.4	2.7	3.6		3.0		0.8							
30						2.0	2.6	3.4	6.6	5.4	2.5	5.6					
31			4.4		3.1		5.0			3.4	6.6	0.5	3.0				
32	4.0	2.9	3.3		7.4		9.1			6.4	4.9	4.7					
33		5.1	4.2	2.7		1.7				4.0	7.0	2.5	7.0				
34	2.9	1.9	1.3		0.9		1.5		2.7	2.8	1.7	1.7					
35	4.8	1.4	1.5	2.2	3.1	4.6		2.0		3.5	1.7	2.7					
36	2.4	2.0	2.4	1.7	3.9	2.5	3.5			2.8	3.8	2.3	3.7	1.6			
37	1.0	2.1	1.0	2.9	4.0	3.8	5.3										
38		1.8	4.1				3.2	1.9	2.6		4.9		4.3				
39	5.0				2.4		3.6		5.0	5.8	5.0	3.7					
40	2.8	2.4	2.2	1.7	5.8	2.5	5.0			1.9							
41	0.9	3.6	2.9	3.1		0.8		5.5		3.2	4.7						
42	1.7	0.6	1.1		1.9		2.4			3.0	1.5	1.6	3.1				
43	2.1	3.1			2.2		0.5		1.7	1.3	3.3	2.1					
44	2.7	3.6		4.2	4.4		3.8			3.6	4.2	4.6					
45	2.8	4.3		2.2	3.0		2.0					2.3					
46	2.0			1.6	1.2	2.2	1.6			2.4	6.2						
47	5.4	5.6	7.0	4.7	3.0	4.5	6.7			4.3	5.3	6.3					
48		1.2	2.8		4.3		1.0	2.3	3.1	2.4	5.0	4.8					
49	3.5	1.5	4.6			3.5	2.3	1.1	4.9								

50	2.5	1.9	1.0	3.1	4.4	2.4	2.8	5.6	4.4							
51	4.6	4.9	4.1	4.1	5.4		1.7			3.0	3.1	3.8				
52	2.0	1.8	6.0	2.4	3.2		4.2		5.4	3.6	5.2	4.6				
53	5.0	1.7		1.2	2.2	1.8	2.2			1.3	4.2	3.7				
54	4.2	2.2			1.6		1.4			6.2	2.4	1.8	2.3			
55	1.0	0.4	1.5		2.2		2.0		2.7	2.6	2.2	2.7				
56	2.2			5.6			2.4			1.7	4.2	4.6				
57	2.3	1.4		2.5	5.3	2.1	2.0			2.8	5.0	5.7				
58	2.6	2.5	5.4	1.1	3.7	1.2					5.3					
59	2.2															
60	2.4	3.2	1.6		2.8			3.4	3.2							
61				2.7		3.5				2.8	6.6		3.2	3.2		
62	1.6	2.4	2.6	3.1	2.9	3.7		3.4		3.2	2.3					
63	2.8	1.6		4.0	2.0		2.0			2.0	3.1	2.9	6.0	6.1		
64		4.0		2.6		1.7		2.9	0.8	2.6		4.2	2.5	4.5		
65		2.9	2.0	2.5		1.4				2.2	2.0	3.9	4.1	3.3		
66	3.4			2.5	4.0	4.4	5.2	3.6	2.4	2.6	0.8					
67	4.9	3.3		4.3	4.2	4.1							4.0	7.1		
68	3.4			5.1		3.5		5.3		5.4	3.6	5.7	5.0	4.9		
69		5.7			4.1		1.0	2.5	4.3	3.8	3.0		2.0			
70			1.9		3.0	1.6			2.6	2.6	3.2	4.4	1.8	1.9	1.1	1.1
71		2.1	1.2	2.4		1.7			2.2	7.8	2.6	9.9	2.8	1.7		
72	1.8	2.5	2.6	3.4	1.7	0.9			4.3	3.3	1.3	1.2	1.8			
73		1.2	3.1	1.6		1.4	4.3	4.7		2.6	4.6	2.2	3.8	1.5		
74	4.8	3.2	2.0	2.6	1.8		7.2			7.9	5.2	1.6	2.3			
75	0.9	0.5	1.0	0.7	3.0	4.0	2.8	2.7	2.8	2.6	3.7	2.9	0.3			
76	1.8		3.1			4.8	2.8			3.2	3.5	4.9	4.8	3.1		
77	2.1	1.2	1.6	0.8	1.2	3.2	3.4			2.4	2.6	4.6	4.2			
78	4.7	1.5	2.1	1.8	4.9	5.0					3.4					
79		0.9	1.3	2.9	3.7		1.6		4.5	1.6		3.8	2.9			
80	1.8	2.1	2.3	2.5	4.4	2.8				2.8	3.2					
81	2.3	2.7	3.0	0.6	0.3	1.1	4.6	4.6	4.7	2.8	1.6					
82	3.3	1.3	4.6	4.6		2.6	4.3		2.5	4.7						
83	4.0	1.4		4.5	2.2	4.0		3.5	5.1	0.9	3.4	5.9	3.5			
84	1.8	2.5		4.8			3.3	3.7	4.0	3.8	4.4	4.4	4.0			
85	3.0	3.2	2.2	4.0	2.3		5.5				2.8	6.5				
86	2.8	2.6		1.6	1.8	0.6		1.4	2.8	6.9						
87	1.8	2.1		1.6	4.2		1.6	3.8	4.6	0.6	5.0	3.8	2.9	4.6		
88	2.3	1.8	2.1	1.6	1.4	3.4	2.8			2.8	3.2	1.4				
89	4.2	3.6	2.8	3.2	4.4	1.6				2.4	3.6					
90		3.8	0.6	1.2	1.6	2.1	3.1	3.2	2.4	3.1	2.6					
91		3.0		3.8	7.7	4.5			4.8	3.4	9.1					
92	2.5	2.7	2.1	2.4	1.3	5.5	4.3		5.7	2.1	3.2	3.3				
93	2.6	1.9	1.6	3.8	3.1		1.0	1.4		3.9	4.4	3.5				
94	3.1	2.4	1.0	2.4	2.9		1.8	3.6	1.3	2.1						
95	2.3	1.1		3.1	4.7		3.2			2.5	1.8	1.6	1.8			
96	4.5	1.3		4.0	4.4		4.1	4.3	5.9		5.5	3.2				
97					2.4		3.2	1.8	2.4	4.6		5.4	4.8			
98			4.1	1.2	0.8	3.6	2.8	3.6			1.9	6.4				
99	1.5	2.2			3.3	4.2	4.3	5.6	3.5	1.3	3.7	7.1				
100	4.0	2.8	0.8	4.1	2.3		3.2		4.4	2.9	4.0			3.8		

II.III: POST-IMAGING BRAIN DISTORTION
ii.iii.i: Pre-Operative Image Analysis

	Age	Group	Depth*	Volume (cm³)	Midline Shift	Oedema	RMSE	Time (min)
1	52	1	25.7	27.0	4.1	+	2.6	200
2	31	3	36.1	2.6	0.0	-	1.8	100
3	66	2	34.6	46.3	11.9	+	3.7	55
4	73	2	28.7	60.8	0.0	+	5.0	105
5	33	3	54.1	2.4	0.0	-	3.4	168
6	39	1	35.1	41.0	9.1	+	4.3	165
7	41	1	22.2	12.3	3.0	+	3.7	70
8	60	2	48.0	37.5	1.9	+	3.8	105
9	53	1	30.5	24.6	4.9	+	2.3	117
10	50	4	51.2	37.5	4.1	-	7.3	150
11	60	1	40.6	20.3	6.8	+	5.9	165
12	55	2	26.3	30.2	11.2	+	2.9	170
13	60	2	30.9	4.6	0.0	-	2.3	90
14	62	1	14.1	59.0	7.5	+	3.3	265
15	32	2	50.0	2.1	0.0	-	2.1	245
16	36	4	54.0	7.0	3.6	-	2.5	108
17	26	3	22.9	3.9	4.8	+	3.7	135
18	50	4	63.5	4.7	1.8	-	3.5	290
19	30	3	59.3	1.8	0.0	-	4.2	145
20	67	1	38.0	58.0	13.5	+	5.0	252
21	34	2	26.9	2.8	2.9	+	3.0	90
22	49	1	26.2	5.3	5.3	+	2.3	84
23	59	3	63.0	10.3	0.0	-	3.8	166
24	60	2	33.3	8.8	4.5	+	3.9	135
25	51	3	48.9	8.0	2.9	-	3.7	311
26	69	1	35.9	33.0	1.8	+	3.6	215
27	58	2	30.4	42.2	8.2	+	4.7	130
28	52	1	24.9	24.6	11.2	+	4.0	118
29	47	4	66.1	10.0	3.5	-	4.8	305
30	49	1	40.6	76.4	19.9	+	2.6	220
31	47	4	21.1	5.2	0.0	-	2.9	165
32	20	3	69.5	1.4	0.0	-	3.9	195
33	26	3	71.9	0.5	0.0	-	2.8	210
34	25	2	37.1	8.2	4.1	+	3.4	105
35	43	2	31.1	3.6	3.6	+	3.7	75
36	32	2	47.4	55.7	9.4	+	2.6	120
37	42	3	58.3	19.6	5.9	+	3.9	153
38	47	2	32.3	4.1	0.0	-	2.8	96
39	61	2	35.7	24.0	5.9	+	4.7	180
40	50	1	43.6	51.3	7.6	+	3.0	170
41	29	2	34.3	140.5	12.9	-	3.0	207
42	45	3	66.2	14.8	7.6	+	4.0	235
43	36	2	53.3	1.1	0.0	+	3.5	170
44	40	3	36.4	40.3	2.3	+	4.3	90
45	36	2	52.1	0.9	0.0	-	3.1	160
46	75	4	40.9	47.5	8.3	+	3.7	285
47	27	2	23.8	8.4	2.3	-	2.4	182
48	77	1	29.0	14.5	2.5	+	3.3	90

ii.iii.ii: Post-Imaging Brain Distortion; Magnitude of Distortion

No.	Age	Bone	Measurements			Corrected Values		
			Opening	Tx Bed	Completion	Opening	Tx Bed	Completion
1	52	0.0	3.0	11.7	1.0	3	11.7	1
2	31	1.8	3.8	3.0	-9.0	2	1.2	7.2
3	66	0.0	9.0	0.0	0.0	9	0	0
4	73	1.0	4.5	3.9	5.1	3.5	2.9	4.1
5	33	-1.0	-1.3	1.4	-4.4	2.3	2.4	5.4
6	39	3.6	15.7	18.5	-10.2	12.1	14.9	6.6
7	41	0.0	5.8	10.0	0.6	5.8	10	0.6
8	60	4.8	0.0	3.2	1.0	-4.8	-1.6	-3.8
9	53	3.6	3.2	12.6	-5.4	-0.4	9	1.8
10	50	3.9	0.3	0.5	0.0	-3.6	-3.4	-3.9
11	60	-2.0	2.6	22.2	-21.7	4.6	24.2	23.7
12	55	4.5	11.9	11.4	-2.6	7.4	6.9	-1.9
13	60	-0.9	4.3	3.5	-1.4	5.2	4.4	2.3
14	62	-0.9	0.8	5.4	-10.2	1.7	6.3	11.1
15	32	5.5	0.0	2.2	0.3	-5.5	-3.3	-5.2
16	36	1.3	0.0	0.0	1.2	-1.3	-1.3	-0.1
17	26	0.2	4.7	2.5	7.7	4.5	2.3	7.5
18	50	-1.2	2.1	-0.5	-4.1	3.3	1.7	5.3
19	30	1.4	-1.7	-0.7	-14.0	0.3	-0.7	12.6
20	67	-1.6	3.9	5.5	-5.3	5.5	7.1	6.9
21	34	-7.9	3.9	-1.4	1.2	11.8	9.3	9.1
22	49	3.4	4.3	4.2	2.6	0.9	0.8	-0.8
23	59	0.7	4.0	0.4	-6.3	3.3	-0.3	5.6
24	60	1.0	5.5	0.0	-2.1	4.5	-1	1.1
25	51	0.0	3.4	0.5	-14.2	3.4	0.5	14.2
26	69	2.4	7.8	16.3	-8.4	5.4	13.9	6
27	58	0.5	20.9	3.5	-5.5	20.4	3	5
28	52	3.7	0.0	9.8	-9.4	-3.7	6.1	5.7
29	47	0.0	1.6	0.0	0.5	1.6	0	0.5
30	49	-1.1	1.6	15.3	-21.0	2.7	16.4	22.1
31	47	0.0	2.0	0.6	-1.1	2	0.6	1.1
32	20	-1.1	1.5	-0.3	-4.6	2.6	1.4	5.7
33	26	-3.8	-7.3	-3.7	-20.0	11.1	7.5	23.8
34	25	-2.5	3.5	-2.2	-5.4	6	4.7	7.9
35	43	3.0	5.9	2.1	-4.7	2.9	-0.9	1.7
36	32	-2.5	5.8	8.6	1.7	8.3	11.1	4.2
37	42	-1.3	1.8	3.5	7.2	3.1	4.8	8.5
38	47	-8.4	-3.9	-4.1	-5.6	12.3	12.5	14
39	61	3.3	8.0	2.6	0.0	4.7	-0.7	-3.3
40	50	4.7	-1.6	0.0	-7.6	-3.1	-4.7	2.9
41	29	-2.7	2.8	11.0	-10.9	5.5	13.7	13.6
42	45	4.1	3.7	2.4	13.3	-0.4	-1.7	9.2
43	36	0.0	0.0	0.0	-10.5	0	0	10.5
44	40	2.3	12.4	14.4	12.3	10.1	12.1	10
45	36	1.8	2.0	2.4	5.1	0.2	0.6	3.3
46	75	1.9	2.9	1.2	1.9	1	-0.7	0
47	27	0.0	-1.7	-0.8	-3.3	-1.7	-0.8	-3.3
48	77	0.0	1.0	5.1	-6.6	1.0	5.1	-6.6

265

II.IV: FRAMELESS STEREOTAXY
ii.iv.i: Phantom Accuracy Measurements

Screw No.	Signa MRI				
1	0.6	1.0	1.2	0.6	0.7
2	1.3	1.7	1.7	1.0	1.9
3	2	2.8	1.6	1.9	2.0
4	1.3	1.8	1.5	1.8	1.1
5	0.5	1.1	0.8	0.6	0.6
6	0.4	0.9	1.6	0.5	1.3
7	1.9	2.0	1.8	1.0	1.5
8	1.6	2.2	1.5	2.2	2.9
9	0.8	1.9	0.5	1.5	0.9
10	0.8	1.9	1.6	0.7	0.6
11	0.8	2.2	1.8	1.6	1.2
12	1.4	1.4	1.0	1.6	0.5
13	1.7	2.7	0.3	1.4	0.8
14	2.1	2.2	0.8	0.6	1.8
15	1.4	1.9	0.9	0.5	0.6
16	2.3	1.5	1.4	0.6	0.9
17	1.0	2.0	0.7	1.5	1.5
18	0.9	1.5	1.6	1.0	0.4
19	0.8	1.3	0.9	0.3	0.5
Screw No.	**Standard Vectra MRI**				
1	1.2	2.5	1.8	0.9	
2	1.6				
3	1.3				
4	1.9	1.3	1.8	1.5	
5	2.4				
6	0.7	2.0	2.7	1.0	
7	2.0				
8	4.1	0.0	0.0	0.0	
9	1.4				
10	2.1	1.4	2.4	1.8	
11	1.8				
12	2.8	2.2	2.4	1.8	
13	1.2				
14	0.5	1.7	1.7	2.8	
15	1.9				
16	1.5	2.1	1.9	2.0	
17	1.2				
18	1.0				
19	1.7				
Screw No.	**3mm Sequential CT**				
1	0.8	1.8	1.8	1.4	1.5
4	1.2	1.1	0.6	0.6	1.1
6	2.0	2.2	0.4	0.9	0.7
8	0.8	1.6	1.5	1.0	2.0
10	2.5	1.8	0.8	0.9	1.6
12	1.4	1.3	1.6	2.6	1.1
14	0.8	2.6	1.4	1.9	1.5
16	0.8	1.2	0.9	0.9	1.1

Screw No.	2mm Sequential CT				
1	1.4	0.8	0.5	1.0	0.2
4	0.8	0.4	0.8	1.7	0.9
6	0.4	1.4	1.1	0.7	0.4
8	1.7	1.7	1.2	0.9	0.8
10	1.9	0.9	0.9	0.4	1.0
12	2.4	0.8	1.5	1.4	1.2
14	1.6	0.8	1.6	1.4	0.6
16	0.6	1.2	2.2	0.0	1.2
Screw No.	3mm Helical CT				
1	1.0	0.6	0.7	0.0	1.8
4	1.2	0.9	0.0	0.6	0.9
6	1.3	0.8	0.6	0.9	0.9
8	1.2	1.6	0.8	0.7	0.9
10	0.8	1.5	1.1	1.8	0.9
12	0.9	0.7	0.8	0.6	0.2
14	1.5	2.0	1.3	1.2	0.4
16	0.0	1.1	1.3	0.9	0.8

ii.iv.ii: Frameless Stereotaxy; In Vivo Accuracy Assessment

Case No.	Slice	Target X	Target Y	Target Z	Biopsy X	Biopsy Y	Biopsy Z	X Error	Y Error	Z Error
1	Axial	-18.8	-67.9	138.6	-18.3	-65.6	132.6	-0.5	-2.3	6.0
1	Sagittal	-19.4	-67.9	138.3	-18.9	-65.6	132.6	-0.5	-2.3	5.7
1	Coronal	-18.8	-68.2	138.3	-18.3	-65.6	132.6	-0.5	-2.6	5.7
2	Axial	-17.7	-70.8	137.8	-17.6	-68.9	140.5	-0.1	-1.9	-2.7
2	Sagittal	-18.0	-70.8	137.7	-17.6	-68.9	139.9	-0.4	-1.9	-2.2
2	Coronal	-17.7	-71.0	137.7	-17.6	-69.6	139.9	-0.1	-1.4	-2.2
3	Axial	7.1	-6.0	252.4	7.5	-7.1	249.1	-0.4	1.1	3.3
3	Sagittal	7.0	-6.0	252.4	6.8	-7.1	248.4	0.2	1.1	4.0
3	Coronal	7.1	-6.2	252.4	7.5	-7.1	248.4	-0.4	0.9	4.0
4	Axial	38.5	-12.0	173.1	40.9	-12.3	166.3	-2.4	0.3	6.8
4	Sagittal	38.3	-12.0	172.7	40.3	-11.7	166.3	-2.0	-0.3	6.4
4	Coronal	38.5	-12.1	173.3	40.9	-12.9	166.3	-2.4	0.8	7.0
5	Axial	-24.6	-4.0	142.4	-26.9	-9.4	144.4	2.3	5.4	-2.0
5	Sagittal	-24.8	-4.0	142.3	-26.9	-8.8	145.0	2.1	4.8	-2.7
5	Coronal	-24.6	-4.4	142.3	-26.9	-9.4	144.4	2.3	5.0	-2.1
6	Axial	-21.7	-13.6	156.5	-27.5	-12.1	156.8	5.8	-1.5	-0.3
6	Sagittal	-22.1	-13.6	156.4	-28.1	-12.1	156.1	6.0	-1.5	0.3
6	Coronal	-21.7	-13.6	156.4	-27.5	-12.1	156.1	5.8	-1.5	0.3
7	Axial	23.1	7.2	83.1	22.3	7.1	82.2	0.8	0.1	0.9
7	Sagittal	22.8	7.2	82.5	22.3	7.1	81.6	0.5	0.1	0.9
7	Coronal	23.1	6.9	82.5	22.3	6.5	81.6	0.8	0.4	0.9
8	Axial	45.8	26.5	30.1	44.0	24.6	29.6	1.8	1.9	0.5
8	Sagittal	45.2	26.5	29.6	43.4	24.6	29.6	1.8	1.9	0.0
8	Coronal	45.8	26.1	29.6	44.0	24.6	29.6	1.8	1.5	0.0
9	Axial	23.7	4.4	79.8	23.7	6.1	79.9	0.0	-1.7	-0.1
9	Sagittal	23.6	4.4	79.5	23.7	6.1	79.9	-0.1	-1.7	-0.4
9	Coronal	23.7	4.1	79.5	23.7	6.1	79.9	0.0	-2.0	-0.4
10	Axial	19.3	12.8	30.1	14.5	15.4	33.8	4.8	-2.6	-3.7
10	Sagittal	19.0	12.8	30.1	14.5	15.4	33.8	4.5	-2.6	-3.7
10	Coronal	19.3	12.5	30.1	14.5	15.4	33.1	4.8	-2.9	-3.0
11	Axial	30.6	57.4	21.8	31.2	60.9	20.2	-0.6	-3.5	1.6
11	Sagittal	30.1	57.4	21.4	31.2	60.9	20.2	-1.1	-3.5	1.2
11	Coronal	30.6	57.1	21.4	31.2	60.9	19.5	-0.6	-3.8	1.9
12	Axial	-3.5	4.2	25.4	-4.0	9.3	31.6	0.5	-5.1	-6.2
12	Sagittal	-4.0	4.2	24.9	-4.0	9.3	30.9	0.0	-5.1	-6.0
12	Coronal	-3.5	3.6	24.9	-4.0	9.3	30.9	0.5	-5.7	-6.0
13	Axial	40.7	-13.6	-5.1	39.2	-9.7	-3.3	1.5	-3.9	-1.8
13	Sagittal	40.4	-13.6	-5.6	39.2	-9.7	-3.5	1.2	-3.9	-2.1
13	Coronal	40.7	-13.6	-5.6	39.2	-9.7	-3.5	1.5	-3.9	-2.1
14	Axial	-30.6	-9.3	29.4	-36.4	-8.6	30.3	5.8	-0.7	-0.9
14	Sagittal	-31.1	-9.3	29.1	-36.4	-8.6	29.7	5.3	-0.7	-0.6
14	Coronal	-30.6	-9.8	29.1	-36.4	-9.2	30.3	5.8	-0.6	-1.2
15	Axial	-43.9	34.9	43.9	-47.9	38.0	42.5	4.0	-3.1	1.4
15	Sagittal	-44.5	34.9	43.6	-47.9	38.0	41.8	3.4	-3.1	1.8
15	Coronal	-43.9	34.7	43.6	-48.5	37.3	41.8	4.6	-2.6	1.8

268

II.V: IMAGE-GUIDED NEUROENDOSCOPY
ii.v.i: Phantom Accuracy Assessment

Screw Number	Tracked Endoscope Pointer				
	Fine Vectra MRI				
1	1.80	1.60	1.80	1.70	1.80
2	1.40	1.30	1.30	1.30	1.30
3	2.20	2.40	2.30	2.30	2.40
4	2.70	2.20	1.70	1.80	2.00
5	0.80	0.80	1.00	1.00	0.80
6	2.10	2.30	2.30	2.20	2.20
7	1.90	1.90	2.20	2.40	2.30
8	1.90	1.90	1.80	2.00	2.10
9	2.50	2.20	2.50	2.40	2.30
10	1.80	1.90	1.60	1.90	1.80
11	1.90	2.20	2.40	2.40	2.30
12	1.80	2.10	1.80	2.00	2.00
13	1.60	1.60	1.60	1.50	1.60
14	2.40	2.50	2.80	2.50	2.20
15	1.80	1.70	1.90	2.00	1.70
16	1.70	1.60	1.50	1.20	1.40
17	2.00	2.90	2.00	2.10	2.00
18	2.40	2.30	2.30	2.40	2.30
19	2.20	2.00	1.90	2.10	2.20
	Standard Vectra MRI				
1	2.70	2.80	3.00	3.00	2.80
2	2.30	2.40	2.30	2.50	2.50
3	2.50	2.50	2.50	2.30	2.40
4	2.80	2.80	2.90	2.90	2.80
5	2.10	2.10	1.90	2.00	2.10
6	1.50	1.50	1.60	1.50	1.50
7	2.80	2.80	2.90	2.80	2.90
8	3.10	2.90	2.90	3.00	3.00
9	1.70	1.80	1.70	1.70	1.60
10	1.60	1.50	1.80	1.80	1.60
11	1.20	1.20	1.10	1.00	1.30
12	2.90	3.00	2.90	3.10	3.10
13	3.00	3.20	3.10	3.00	3.10
14	2.50	2.50	2.40	2.40	2.50
15	1.50	1.50	1.50	1.60	1.50
16	2.50	2.60	2.60	2.40	2.50
17	1.80	1.70	1.90	1.80	3.20
18	1.70	1.70	1.80	1.70	1.70
19	2.70	2.90	2.90	3.00	2.70

		Signa MRI			
1	1.20	1.00	1.00	1.00	1.10
2	1.90	2.00	2.10	2.00	2.00
3	2.70	2.70	2.70	2.90	2.80
4	2.80	3.00	2.80	3.00	3.00
5	1.00	0.80	0.80	0.80	1.60
6	0.90	1.10	1.20	1.00	0.50
7	2.80	2.80	2.90	2.90	2.90
8	2.20	2.30	2.20	2.30	2.40
9	1.80	1.90	1.90	1.90	1.90
10	2.00	1.70	1.80	2.00	0.90
11	1.80	1.60	2.10	2.00	1.80
12	1.90	2.20	2.50	2.40	2.50
13	1.70	1.80	1.80	1.80	1.90
14	2.60	2.60	2.70	2.70	2.40
15	2.50	2.70	3.40	2.60	2.70
16	2.10	2.00	2.40	2.60	2.20
17	2.40	2.50	2.50	2.20	2.30
18	2.00	1.90	1.90	2.20	2.30
19	1.80	1.80	1.80	1.80	1.70
		2mm Sequential CT			
1	1.50	1.00	1.00	0.90	1.00
2	0.80	0.70	0.80	0.90	0.90
3	0.80	0.80	0.90	0.70	0.70
4	0.60	0.80	0.40	0.50	0.60
5	0.50	0.60	0.40	0.70	0.60
6	0.50	0.70	0.70	0.90	1.30
7	1.30	1.50	0.90	1.00	1.40
8	0.40	0.90	1.00	1.20	0.60
9	0.50	1.30	1.20	1.50	1.10
10	0.20	0.20	0.10	0.30	1.40
11	1.70	1.60	2.80	2.70	1.90
12	1.40	1.50	1.30	0.90	1.00
13	0.80	0.30	0.40	0.30	0.50
14	1.10	1.20	0.90	0.50	0.80
15	0.50	0.30	0.50	0.50	0.20
16	0.10	0.40	0.20	0.20	0.20
17	1.10	0.70	0.90	0.60	0.50
18	0.40	0.10	0.20	0.50	0.60

3mm Sequential CT				
1	1.30	0.50	0.50	0.30	0.70
2	1.60	2.00	1.40	1.80	0.10
3	1.00	0.80	0.80	1.10	0.30
4	0.70	1.80	1.20	1.00	1.60
5	0.20	0.30	1.60	1.00	0.80
6	0.80	0.60	0.70	0.90	1.00
7	0.50	0.80	1.00	0.70	0.60
8	1.30	1.50	1.50	1.80	1.40
9	2.00	1.70	1.30	1.50	1.20
10	1.60	1.20	1.60	1.00	1.70
11	1.00	0.60	0.60	0.40	0.90
12	0.30	0.60	0.40	0.30	0.60
13	0.20	0.90	0.40	1.00	0.30
14	0.50	1.00	0.60	0.30	0.50
15	1.70	1.80	2.50	1.70	2.40
16	0.50	0.60	0.30	0.40	0.20
17	1.10	0.50	0.60	1.00	0.60
18	0.30	0.20	0.30	0.20	0.30

3mm Helical CT				
1	1.80	1.90	1.10	1.40	1.30
2	0.30	0.40	0.10	0.50	0.40
3	0.30	0.50	0.40	0.20	0.60
4	1.00	1.30	1.20	1.50	0.90
5	0.60	0.20	0.40	0.30	0.60
6	1.20	1.10	1.50	0.80	1.10
7	0.20	0.50	0.30	0.40	0.40
8	0.40	0.60	0.30	0.80	0.70
9	1.30	1.50	1.20	1.20	1.40
10	0.90	1.40	1.10	1.70	1.90
11	1.00	0.50	1.20	0.90	0.70
12	0.40	0.60	1.20	0.80	0.80
13	1.60	1.10	0.70	0.60	0.70
14	1.50	1.40	1.40	1.60	1.50
15	0.30	0.50	0.70	0.40	0.70
16	1.10	0.80	0.70	0.10	0.70
17	1.40	1.80	1.70	0.90	0.70
18	0.30	0.40	0.60	0.50	0.20

APPENDIX III

DESCRIPTIVE STATISTICS OF RAW DATA

III.I: LABORATORY STUDIES OF NAVIGATION

SYSTEM ACCURACY

iii.i.i: Phantom Registration Results

Phantom Registration (MRI)
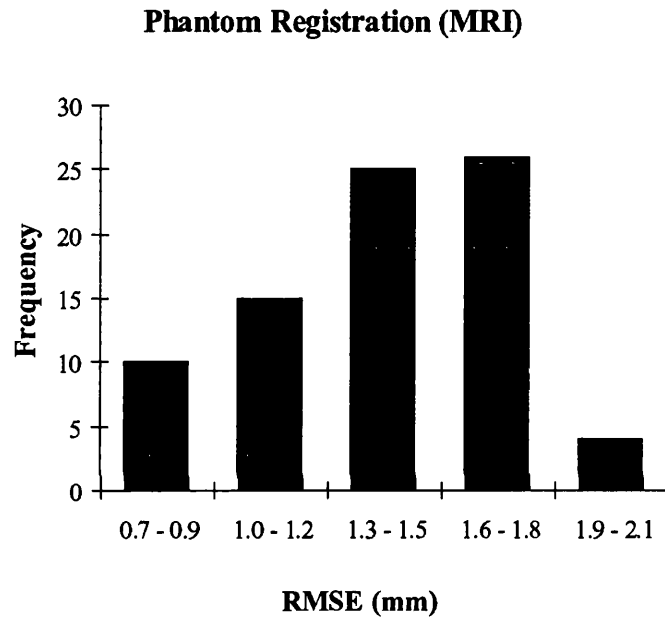
Phantom Registration (MRI)	
Mean	1.40
Standard Error	0.03
Median	1.40
Mode	1.40
Standard Deviation	0.31
Sample Variance	0.09
Minimum	0.90
Maximum	1.90
Count	80.00

Phantom Registration (CT)
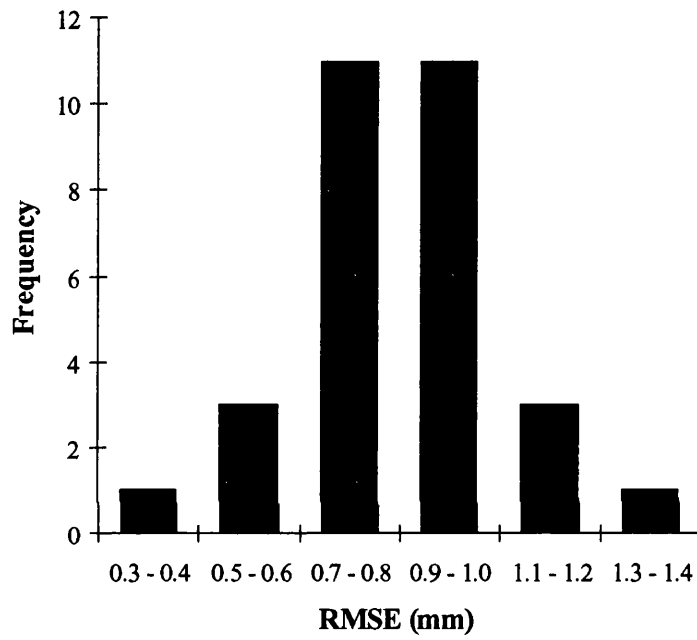
Phantom Registration (CT)	
Mean	0.84
Standard Error	0.04
Median	0.85
Mode	0.90
Standard Deviation	0.19
Sample Variance	0.04
Minimum	0.40
Maximum	1.30
Count	30.00

Point Localisation (Short Pointer, MRI)
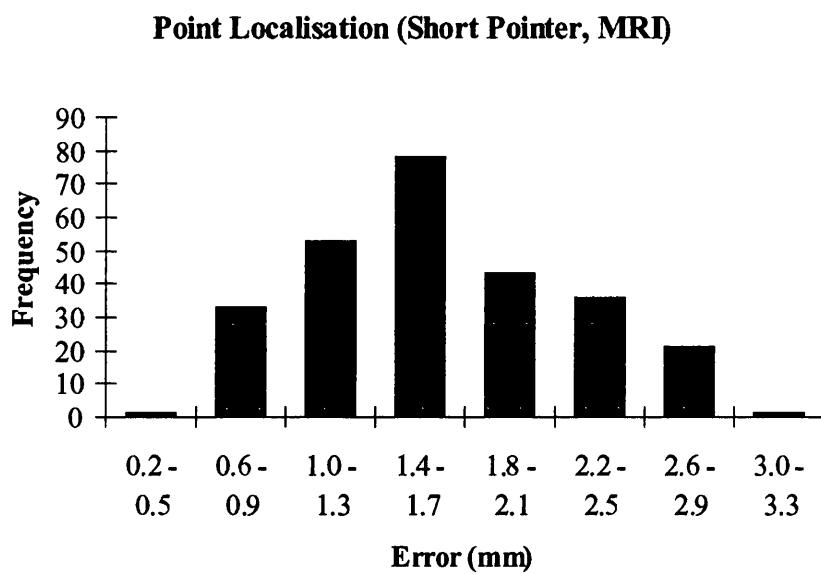
Point Localisation (Short Pointer)	
Mean	1.64
Standard Error	0.04
Median	1.60
Mode	1.60
Standard Deviation	0.57
Sample Variance	0.33
Minimum	0.50
Maximum	3.00
Count	266.00

Point Localisation (Long Pointer, MRI)
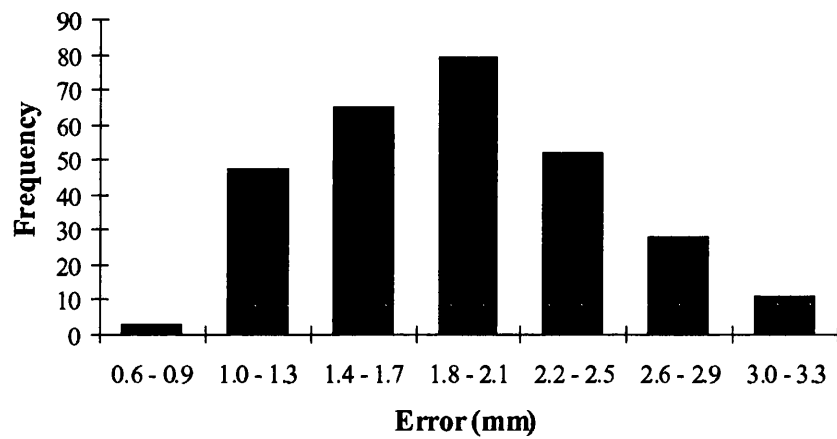
Point Localisation (Long Pointer)	
Mean	1.91
Standard Error	0.03
Median	1.90
Mode	1.70
Standard Deviation	0.55
Sample Variance	0.30
Minimum	0.70
Maximum	3.20
Count	285.00

276

Point Localisation (Bayonet Pointer, MRI)
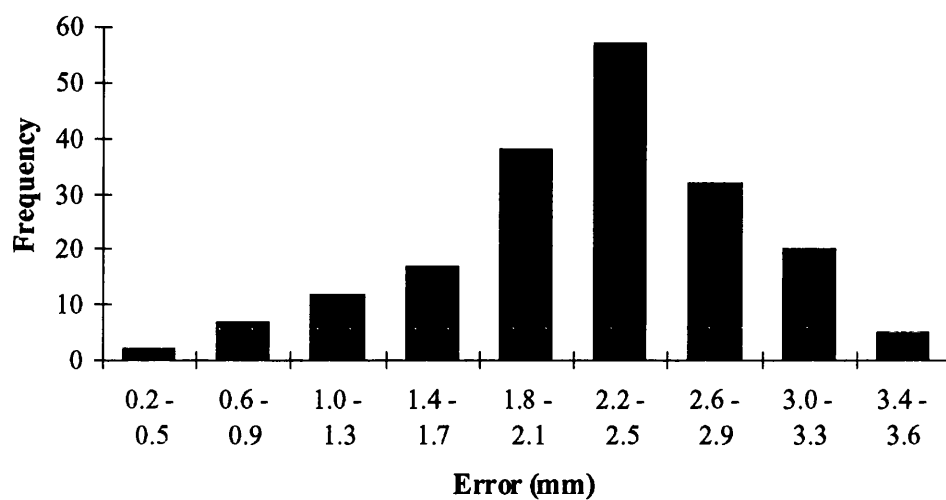
Point Localisation (Bayonet Pointer)	
Mean	2.24
Standard Error	0.05
Median	2.30
Mode	2.40
Standard Deviation	0.68
Sample Variance	0.46
Minimum	0.50
Maximum	4.20
Count	190.00

Point Localisation (CT)
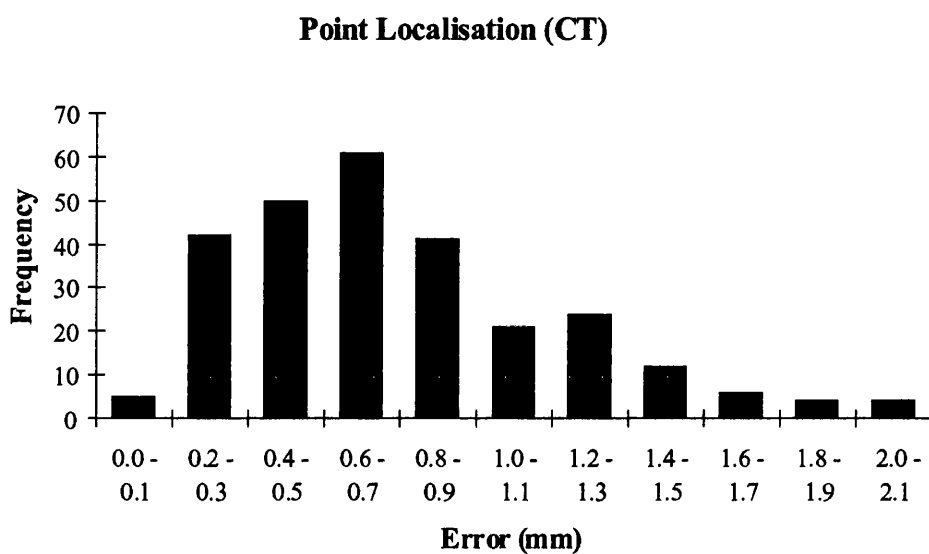
Point Localisation (CT)	
Mean	0.75
Standard Error	0.03
Median	0.70
Mode	0.60
Standard Deviation	0.43
Sample Variance	0.19
Minimum	0.10
Maximum	2.50
Count	270.00

Point Localisation (MRI)
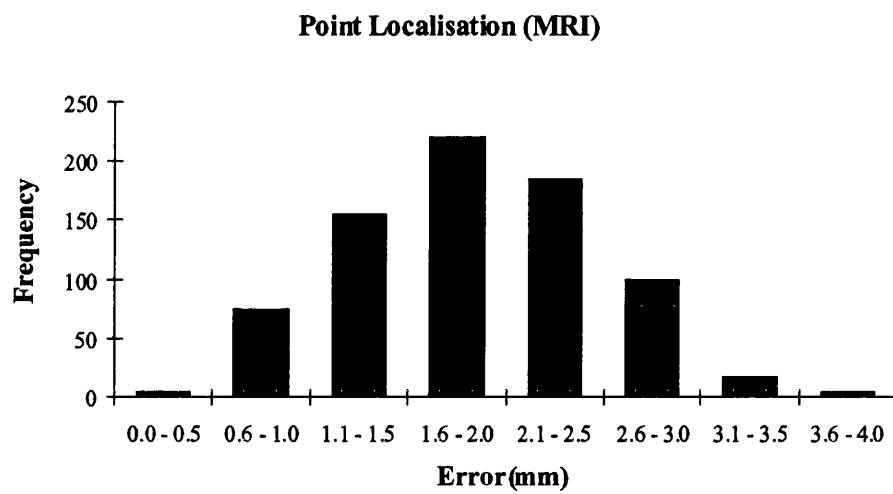
Point Localisation (MRI)	
Mean	1.90
Standard Error	0.02
Median	1.90
Mode	1.70
Standard Deviation	0.64
Sample Variance	0.41
Minimum	0.30
Maximum	4.20
Count	760.00

iii.i.iii: Pointer Reproducibility Experiments
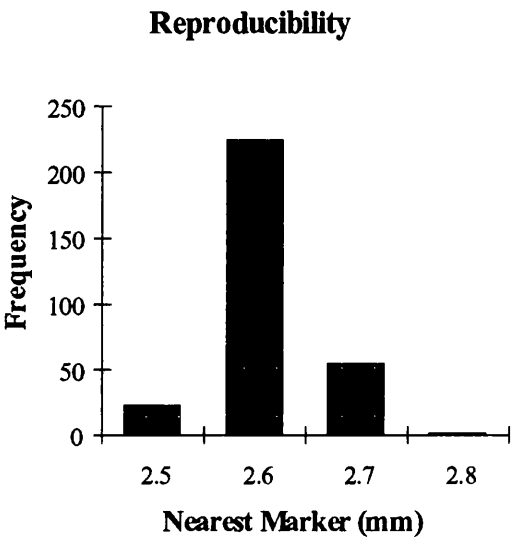
Reproducibility

Reproducibility	
Mean	2.61
Standard Error	0.00
Median	2.60
Mode	2.60
Standard Deviation	0.05
Sample Variance	0.00
Minimum	2.50
Maximum	2.80
Count	303.00

iii.i.iv: Detection of Pointer Movement Experiment

Micrometer Advance
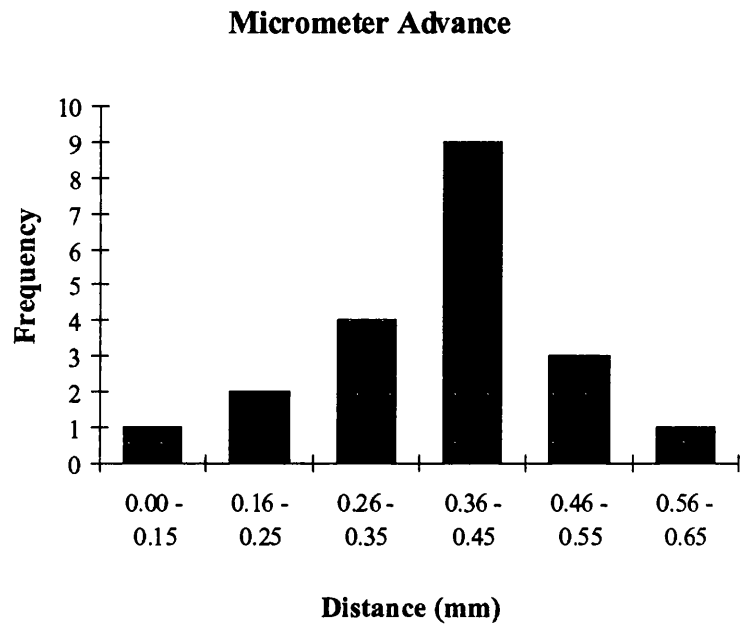
Micrometer Advance	
Mean	0.38
Standard Error	0.03
Median	0.41
Mode	0.44
Standard Deviation	0.12
Sample Variance	0.01
Minimum	0.62
Maximum	0.11

iii.i.v: Pointer Rotation Experiment

Pointer Rotation

Nearest Marker (mm)
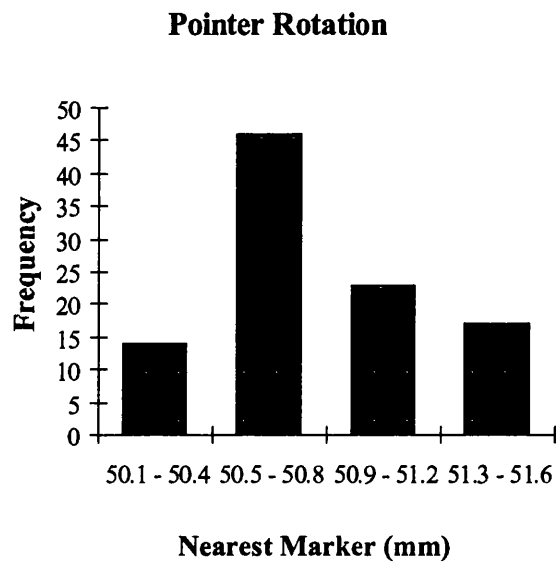
Rotation	
Mean	50.81
Standard Error	0.04
Median	50.60
Mode	50.60
Standard Deviation	0.36
Sample Variance	0.13
Minimum	50.30
Maximum	51.60
Count	100.00

III.II: CLINICAL EVALUATION OF THE

NEURONAVIGATION SYSTEM

iii.ii.i: 100 Cases; General Data & Duration of Surgery
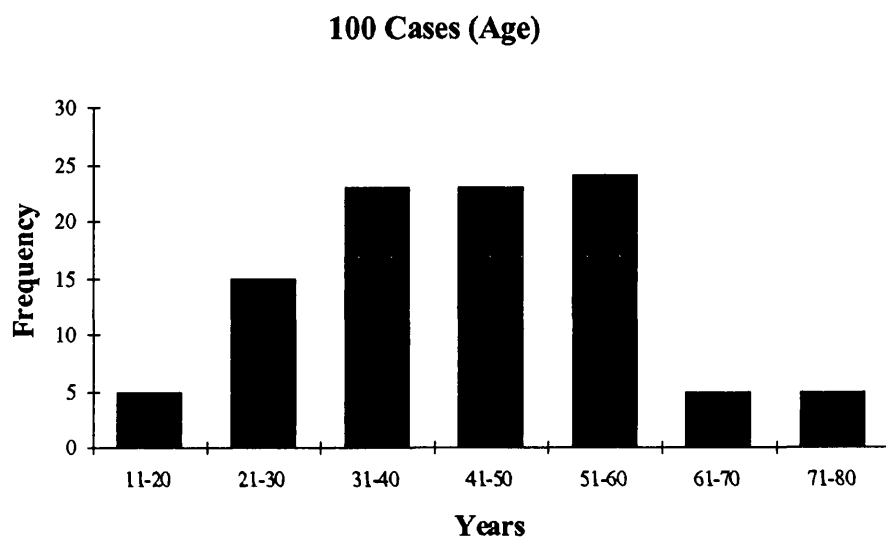
100 Cases (Age)

100 Cases (Age)	
Mean	44.29
Standard Error	1.46
Median	44.00
Mode	60.00
Standard Deviation	14.56
Sample Variance	211.97
Minimum	15.00
Maximum	77.00
Count	100.00

100 Cases (Lesion Diameter)
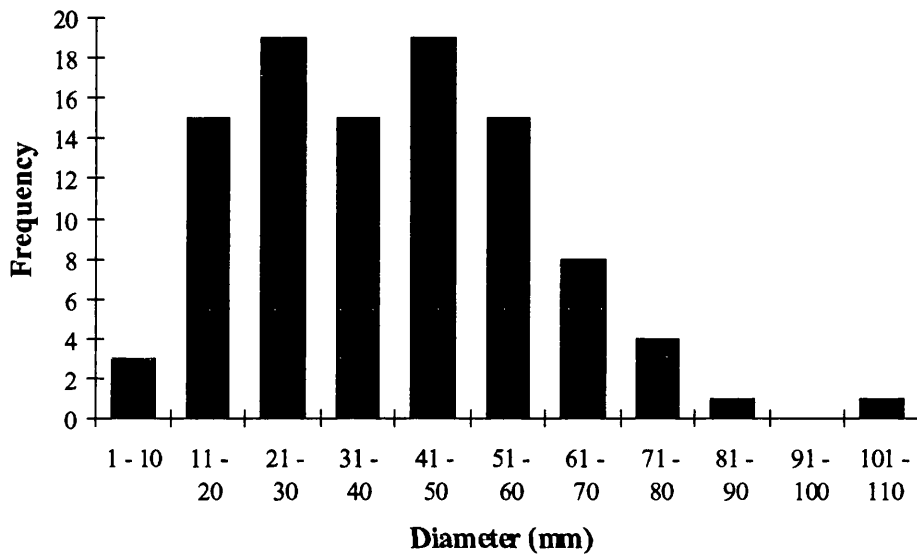
100 Cases (Lesion Diameter)	
Mean	39.37
Standard Error	1.96
Median	39.60
Mode	55.50
Standard Deviation	19.61
Sample Variance	384.46
Minimum	2.50
Maximum	105.60
Count	100.00

100 Cases (Duration of Surgery)
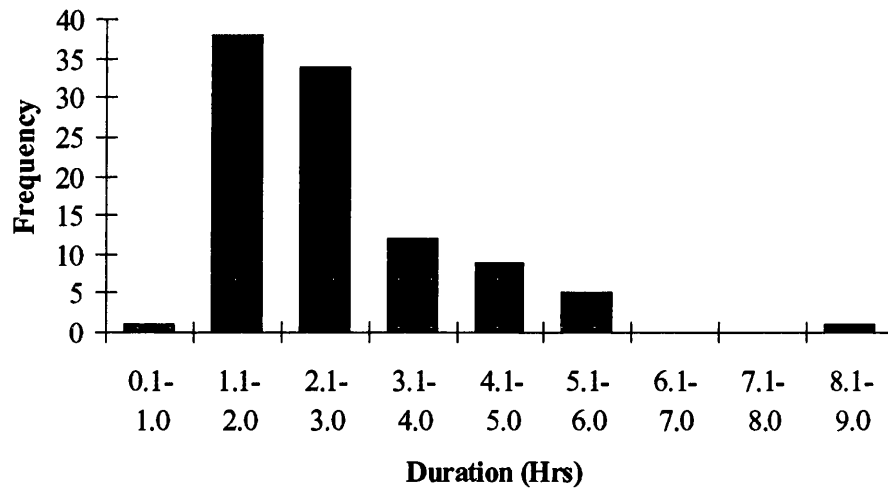
100 Cases (Duration of Surgery)	
Mean	2.69
Standard Error	0.13
Median	2.25
Mode	1.75
Standard Deviation	1.32
Sample Variance	1.74
Minimum	0.83
Maximum	8.83
Count	100.00

100 Cases (Number of Fiducials)
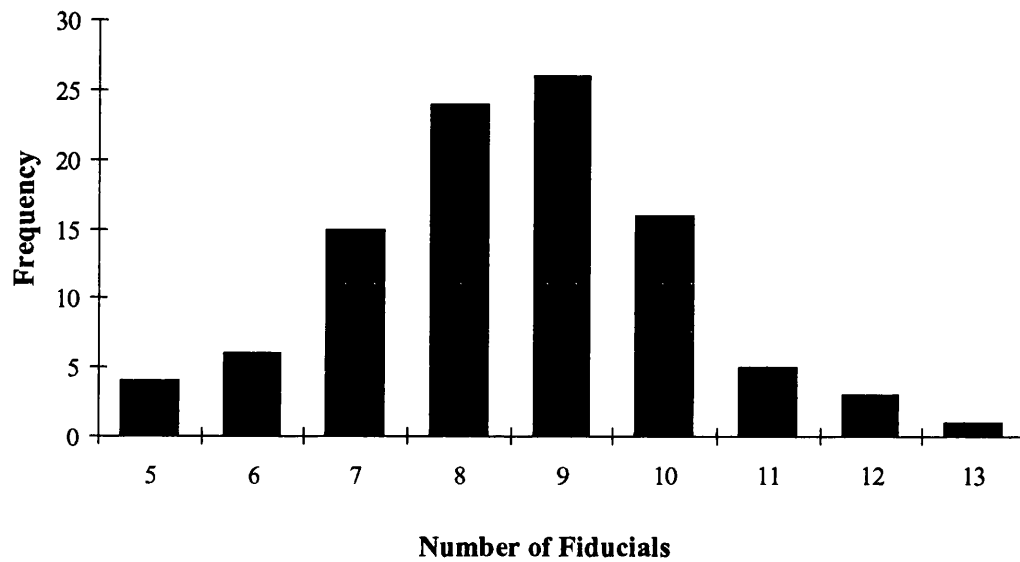
100 Cases (Number of Fiducials)	
Mean	8.51
Standard Error	0.16
Median	9.00
Mode	9.00
Standard Deviation	1.61
Sample Variance	2.60
Minimum	5.00
Maximum	13.00
Count	100.00

Analogue Scales (Q1 - 10)
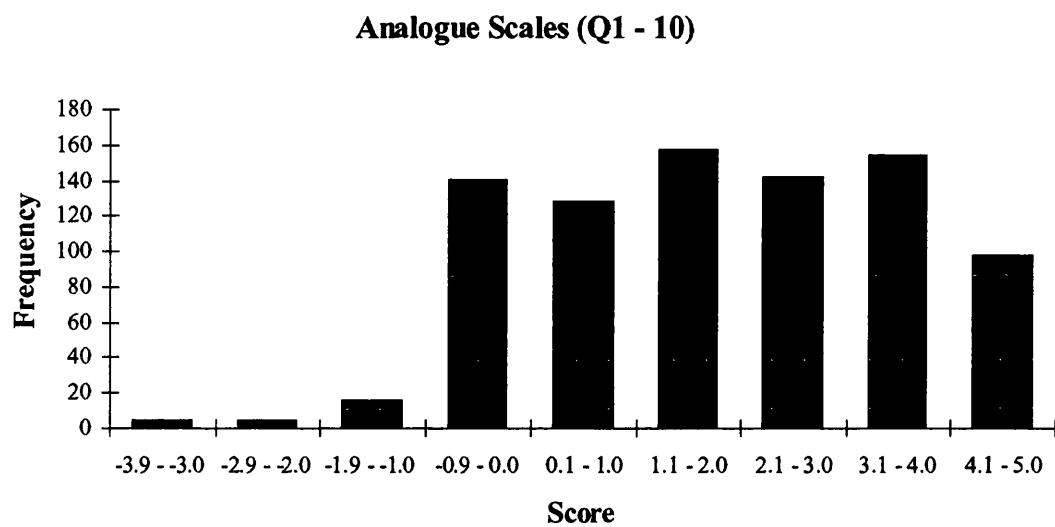
Analogue Scales (Q1-10)	
Mean	1.93
Standard Error	0.06
Median	2.00
Mode	0.00
Standard Deviation	1.68
Sample Variance	2.82
Minimum	-3.90
Maximum	5.00
Count	846.00
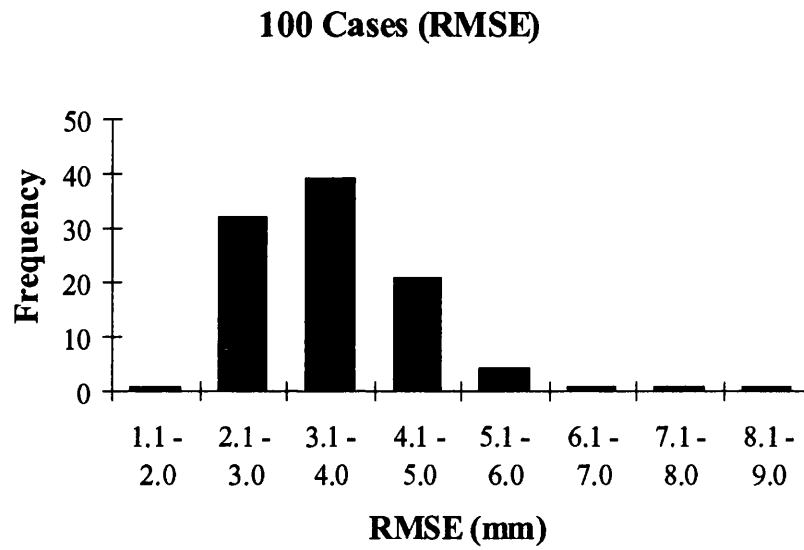
100 Cases (RMSE)

100 Cases (RMSE)	
Mean	3.69
Standard Error	0.11
Median	3.65
Mode	3.70
Standard Deviation	1.10
Sample Variance	1.21
Minimum	1.80
Maximum	8.50
Count	100.00

III.III: POST-IMAGING BRAIN DISTORTION

iii.iii.i Pre-Operative Image Analysis
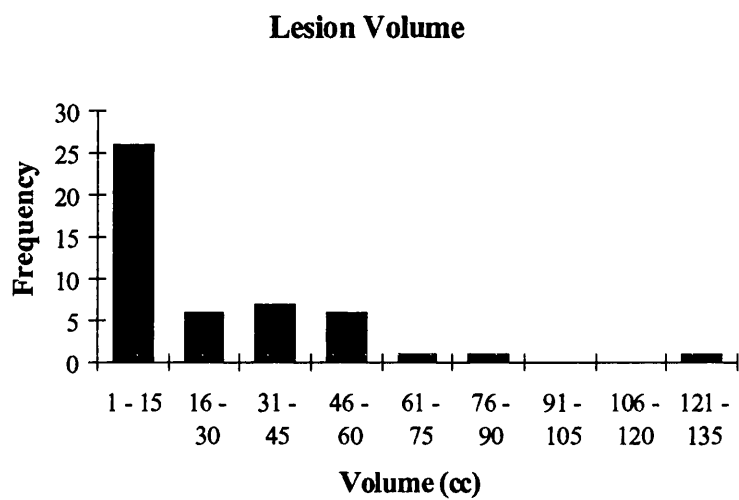
Lesion Volume

Lesion Volume (cc)	
Mean	23.89
Standard Error	3.85
Median	13.40
Mode	37.50
Standard Deviation	26.64
Sample Variance	709.90
Minimum	0.50
Maximum	140.50
Count	48.00

iii.iii.ii: Magnitude of Post-Imaging Brain Distortion

Shift of Cortex at Opening
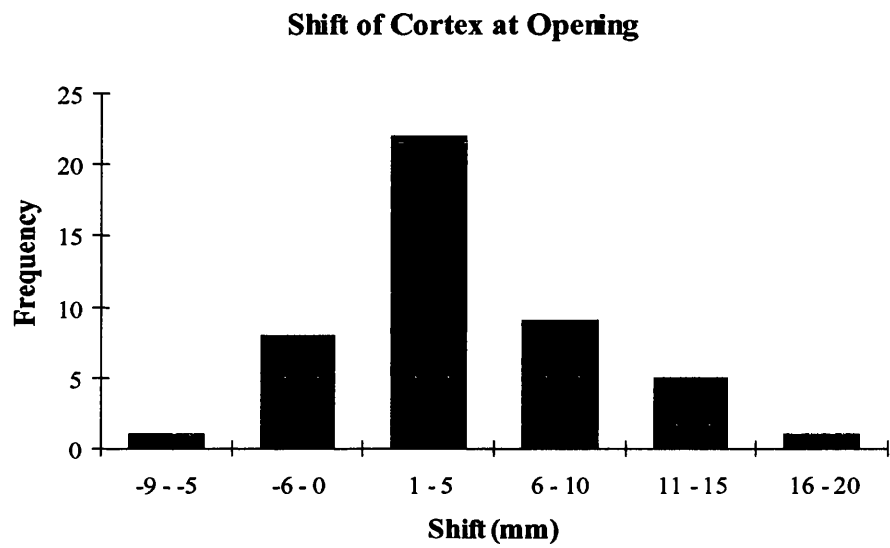
Shift of Cortex at Opening	
Mean	3.72
Standard Error	0.73
Median	3.20
Mode	4.50
Standard Deviation	4.98
Sample Variance	24.77
Minimum	-5.50
Maximum	20.40
Count	46.00
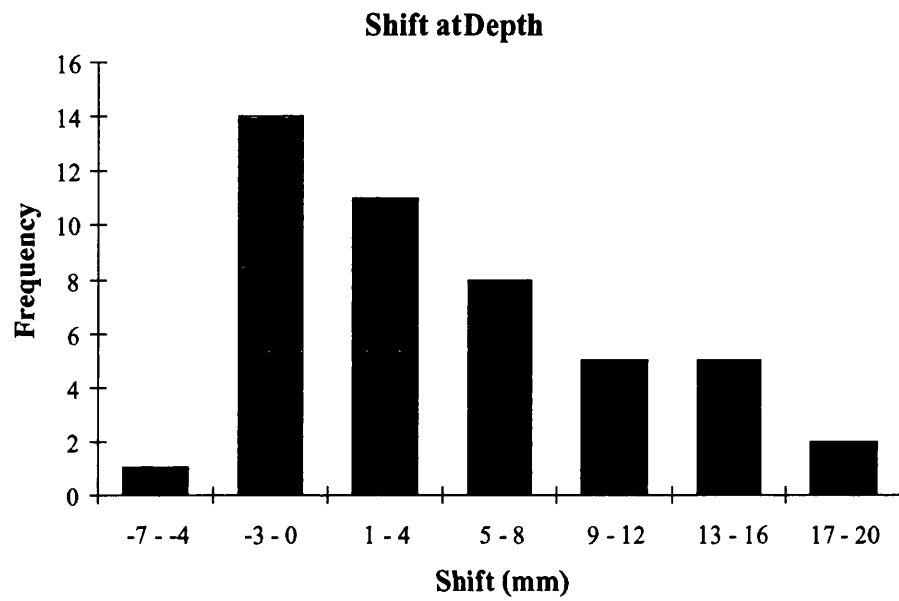
Shift atDepth

Shift at Depth	
Mean	4.43
Standard Error	0.93
Median	2.35
Mode	0.00
Standard Deviation	6.28
Sample Variance	39.40
Minimum	-4.70
Maximum	24.20
Count	46.00

Shift of Cortex at Completion
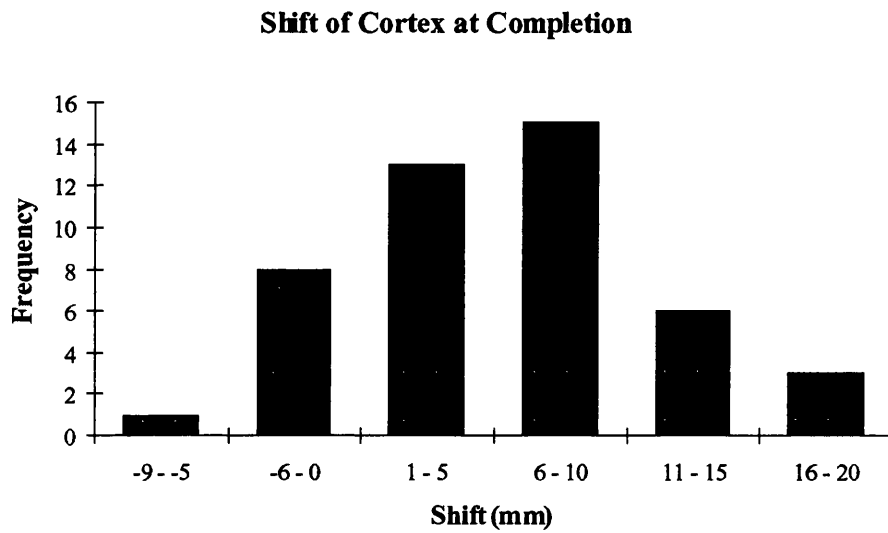
Shift of cortex at Completion	
Mean	5.71
Standard Error	0.99
Median	5.35
Mode	0.00
Standard Deviation	6.74
Sample Variance	45.49
Minimum	-5.20
Maximum	23.80
Count	46.00

III.IV: FRAMELESS STEREOTAXY

iii.iv.i: Phantom Accuracy Measurements

Point Localisation (MRI)
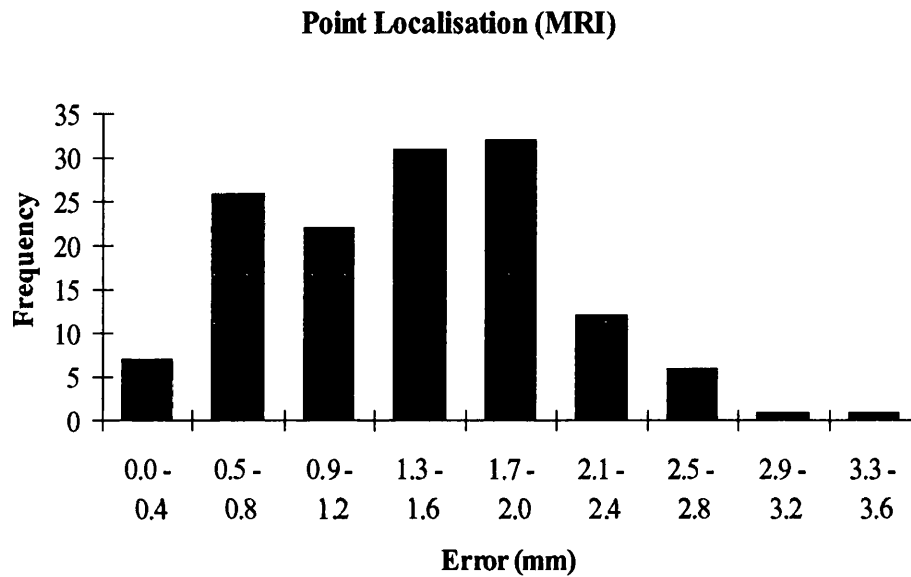
Point Localisation (MRI)	
Mean	1.42
Standard Error	0.06
Median	1.50
Mode	1.80
Standard Deviation	0.69
Sample Variance	0.47
Minimum	0.00
Maximum	4.10
Count	138.00

Point Localisation (CT)
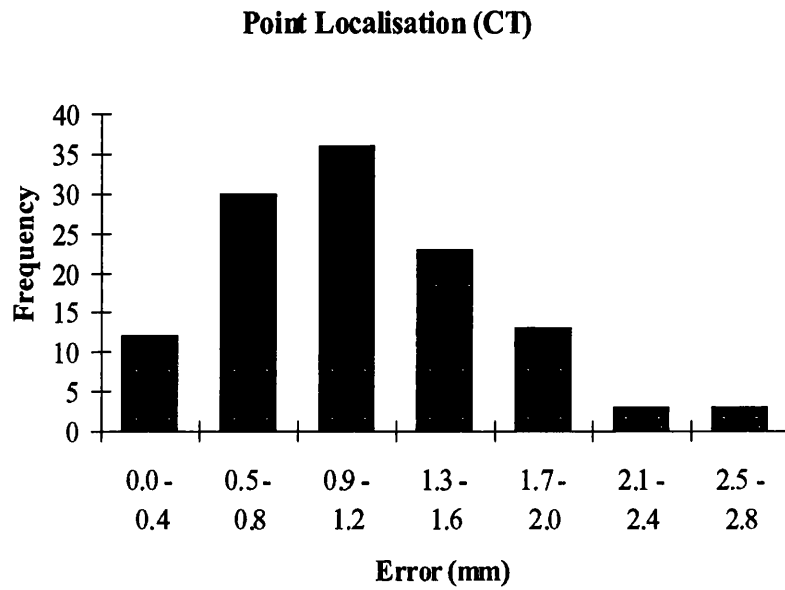
Point Localisation (CT)	
Mean	1.11
Standard Error	0.05
Median	1.00
Mode	0.80
Standard Deviation	0.55
Sample Variance	0.30
Minimum	0.00
Maximum	2.60
Count	120.00

iii.iv.ii: In Vivo Accuracy Assessment
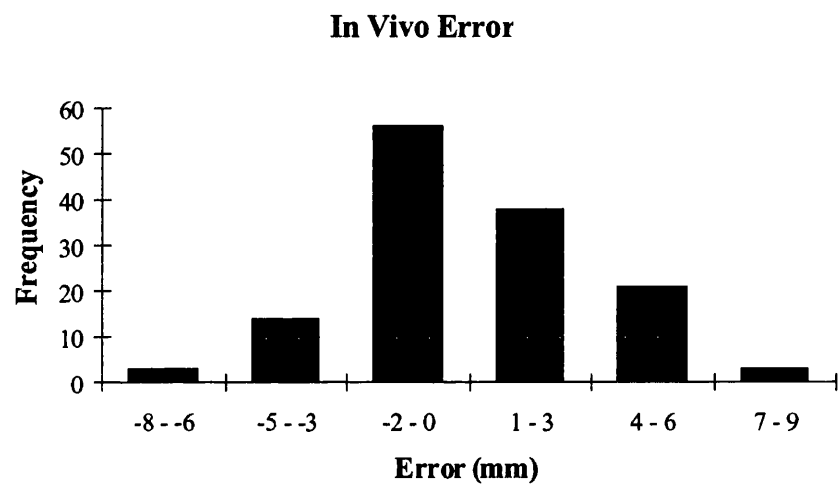
In Vivo Error

In Vivo Error	
Mean	0.17
Standard Error	0.26
Median	-0.10
Mode	0.00
Standard Deviation	3.00
Sample Variance	9.01
Minimum	-6.20
Maximum	7.00
Count	135.00

III.V: IMAGE-GUIDED NEUROENDOSCOPY

iii.v.i: Phantom Accuracy Assessment

Point Localisation (MRI)
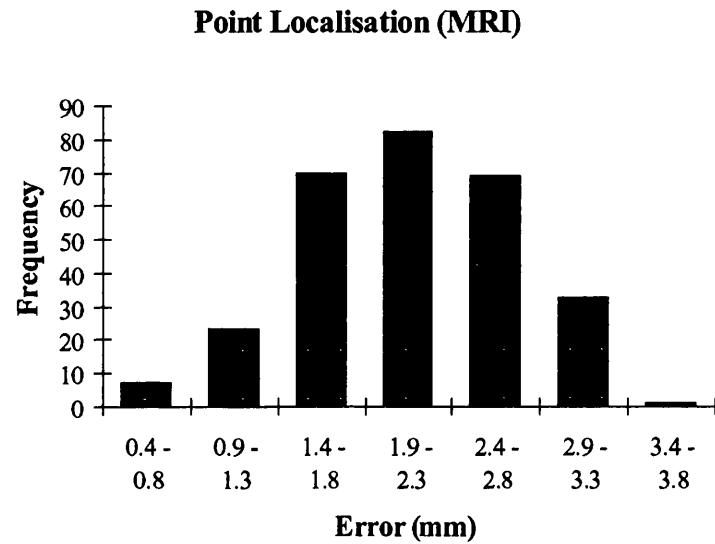
Point Localisation (MRI)	
Mean	2.10
Standard Error	0.03
Median	2.10
Mode	1.80
Standard Deviation	0.58
Sample Variance	0.34
Minimum	0.50
Maximum	3.40
Count	285.00

Point Localisation (CT)
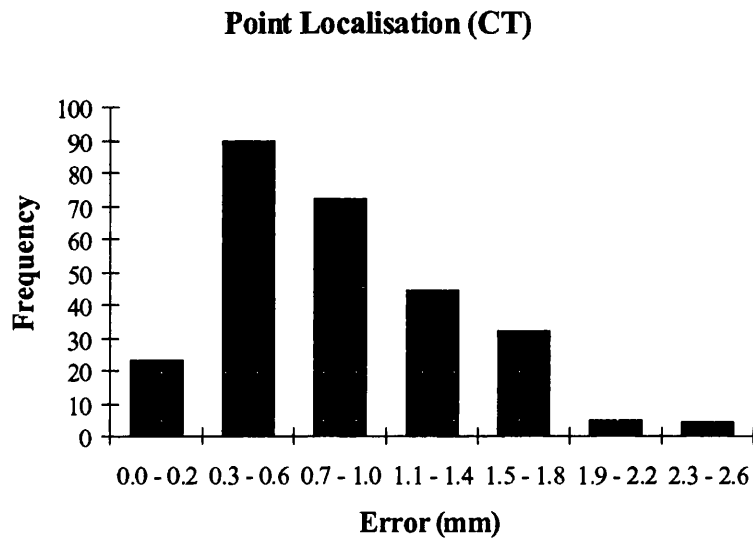
Point Localisation (CT)	
Mean	0.86
Standard Error	0.03
Median	0.80
Mode	0.60
Standard Deviation	0.52
Sample Variance	0.27
Minimum	0.00
Maximum	2.80
Count	270.00

APPENDIX IV:

LIST OF ABBREVIATIONS

BRW   Brown-Roberts-Wells

CD   Compact Disk

Cl   Confidence limit

cm   Centimetres

CRW   Cosman-Roberts-Wells

CSF   Cerebrospinal fluid

CT   Computed Tomography

DICOM   Digital Imaging and Communications in Medicine

DNT   Dysembryoblastic Neuroepithelial Tumour

EASI   European Applications for Surgical Interventions

ENT   Ear, Nose and Throat

fMRI   Functional Magnetic Resonance Imaging

FOV   Field Of View

hrs   Hours

Hz   Hertz (cycles per second)

IGN   Image-Guided Neuroendoscopy

IQR   Inter-Quartile Range

LED   Light emitting diode

MID   Mean Intervoxel Distance

min   Minutes

mm	Millimetres
MR	Magnetic Resonance
MRI	Magnetic Resonance Imaging
p	Probability
PC	Personal Computer
PET	Positron Emission Tomography
PMS	Philips Medical Systems
PPU	Philips Processing Unit
r	Correlation coefficient
RMSE	Root Mean Square Error
ROM	Read-Only Memory
SD	Standard Deviation
SPGR	Spin Echo Gradient
T	Tesla
TIFF	Tag Image File Format
TR	Time between excitation pulses
TE	Echo time
VP	Ventriculo-peritoneal
3D	Three-dimensional

APPENDIX V:

PUBLICATIONS ARISING FROM THE THESIS

Dorward NL, Alberti O, Velani B, Gerritsen FA, Harkness WFJ, Kitchen ND, Thomas DGT. (1998) Post-imaging brain distortion; magnitude, correlates and impact on neuronavigation. J Neurosurg 88:656-662.

Dorward NL, Alberti O, Velani B, Buurman J, Dijkstra A, Kitchen N, Gerritsen FA, Thomas DGT. (1998) Early clinical experience with the EasyGuide neuronavigation system and measurement of intraoperative brain distortion. In: Hellwig D, Bauer BL (eds) Minimally Invasive Techniques for Neurosurgery, Springer Verlag, Berlin, pp193-196.

Dorward NL. (1998) Frameless stereotactic biopsy with the EasyGuide. Medica Mundi 41:33-37.

Dorward NL, Alberti O, Zhao J, Dijkstra A, Buurman J, Palmer JD, Hawkes D, Thomas DGT. (1998) Interactive image-guided neuroendoscopy; development and early clinical experience. Minimally Invasive Neurosurgery 41:31-34.

Dorward NL. (1997) Neuronavigation – the surgeon's sextant. Editorial, Br J Neurosurg 11:101-103.

Dorward NL, Alberti O, Dijkstra A, Buurman J, Kitchen ND, Thomas DGT. (1997) Clinical introduction of an adjustable rigid instrument-holder for frameless stereotactic interventions. Computer Aided Surgery 2:180-185.

Thomas DGT, Dorward NL, Kingsley D et al. (1997) Clinical experience with the EasyGuide Neuro navigation system. In: HU Lemke, MW Vannier & K Inamura (eds). Computer Assisted Radiology and Surgery, Elsevier Science, Amsterdam pp757-761.

Abstracts:

Dorward NL, Alberti O, Kitchen ND, Thomas DGT. (1998) Frameless stereotactic biopsy: accuracy in phantom studies and in clinical practice. Proceedings of the 131st Meeting of the Society of British Neurological Surgeons, Bristol, 3-5 September 1997. Br J Neurosurg 12:83-84.

Dorward NL, Wadley J, Alberti O, Gerritsen FA, Buurman J, Harkness WFJ, Kitchen ND, Thomas DGT. (1997) One hundred consecutive cases with EasyGuide Neuro. Proceedings of the 1st International Congress on Computer Integrated Surgery, Linz 1-5 September 1997. Computer Aided Surgery 2:209

Dorward NL, Alberti O, Kitchen ND, Thomas DGT. (1997) Measurement of brain distortion in tumour surgery by a neuronavigation system. Proceedings of the 130th Meeting of the Society of British Neurological Surgeons, Cambridge, 2-4 April 1997. Br J Neurosurg 11:462-463.

APPENDIX VI:

ACKNOWLEDGEMENTS

Whilst I was able to derive the novel concepts addressed in this thesis by myself, their realisation would not have been possible without the considerable assistance and co-operation which I received. Therefore, I wish to express my gratitude to all who were instrumental in the completion of this project. In particular Professor David GT Thomas, Mr Neil Kitchen, Dr Olaf Alberti and Binti Velani for their parts in the project and Dr. Dave Hawkes and Jason Zhao, of the Radiological Sciences Department at Guy's Hospital, for their invaluable assistance with the image computing aspects of neuronavigation. In addition, I thank my wife, Libby, for her long-suffering support during the protracted process of writing up this thesis.